.

Exoplanet Characterisation through Transit Timing Variations



Laurel Kaye

Worcester College

University of Oxford

A thesis submitted for the degree of

Doctor of Philosophy

Trinity 2023

0.1 Acknowledgements

Lumos. When I sat in my first astrophysics class in September of 2011, Professor Ronen Plesser of Duke University impressed upon me that astronomy is almost solely a study of light, and light's absence. Unlike other physical or biological or social sciences with chemicals to manipulate, organisms to interrogate, or conditions to alter and test before our hands, eyes, noses, and ears, that with which astronomers chose to interest themselves is and remains unreachably far, often leaving its host before those perceiving it now were born. We build shrines to this light, collecting it in massive mirrors and fibers and discs, we launch telescopes on rockets to seek out a more undiluted form of this light, send astronauts up to fix and poke at these, build supercomputers to predict and prod and process what this light might show. I want to thank Ronen, who first told me the story of light and its absence, as well as the more amazing epic tale of the universe we have compiled from it through the centuries. Though this thesis will form one small leaflet in the narrative of otherworldly light, it would not have begun without these initial moments of awe.

I am so fortunate in that many more have helped me along the way. I would be absolutely nowhere without my supervisor Suzanne Aigrain, who is as patient and thoughtful a mentor as she is a brilliant role model. Suzanne, it has been such a privilege to grow under your guidance through these five years of pandemic and shifting sands and progress, and I don't have words to fully voice my appreciation. I didn't expect anything other than a 'no' when I came into your office halfway through the academic year to ask whether I could switch from an HIV research lab to working with exoplanets, but that was one of the best 'yes's I have ever heard. The entire SPLOX team has been like a family, starting with Rebecca and Nora who have continued to shine their light from afar through spacey doodles and covid calls. The group in Oxford has been a home, a place of creativity, support and excitement.

I have also been guided along the way by Garret Cotter, who seeded the excitement for research that has carried me through the last decade. I want to thank the Clarendon Scholarship for making it possible to pursue this dream, and for making this experience such a rich one. A massive thanks to the strong women of the Oxford University Boat Club: you have in turn depleted and restored my sanity, and have dragged me many a time from the river to the library, sometimes with a shower, and always with love. A big thanks to my family, who has probably not understood all of my academic silliness but has tolerated it nonetheless and still sent me cookies. To Megan, your love and friendship has been the truest and has gotten me through more crises than there are pages in this thesis. Finally, a tremendous and heartfelt thanks to Lisa and Laura and Rebekah who are my chosen sisters at the pen and keyboard. May all of your stars continue to burn bright.

0.2 Abstract

Transit Timing Variations (TTVs) arise in exoplanetary systems as a result of nonlinear perturbations from Keplerian orbits. Their presence provides a valuable tool for examining the characteristics and architectures of such systems and enable measurements of mass and eccentricity as well as the detection of new planets.

In this thesis, I start with the work presented in Kaye et al. (2022), taking an in-depth look at TOI- 270, a system of three transiting planets orbiting near 5:3 and 2:1 mean-motion resonances. Following an extensive observing campaign using 8 different space-based and ground-based observatories between 2018 and 2020, I report a clear detection of TTVs for planets c and d, with amplitudes of ∼10 minutes and a super-period of ∼3 years. When incorporating recently published constraints from radial velocity (RV) observations, we obtain precise masses and eccentricities for all three planets as well as significantly refine estimates of the radii and mean orbital periods of all three planets. Our findings imply an Earth-like rocky composition for the inner planet, and Earth-like cores with an additional He/H_2O atmosphere for the outer two. TOI- 270 is now one of the best-constrained systems of small transiting planets, and it remains an excellent target for atmospheric characterisation.

After this in-depth look at TOI- 270, I then step out and take a broader look, presenting a catalogue of transiting exoplanetary systems discovered in Kepler or K2 data that were observed again by TESS (Kaye & Aigrain, paper in prep). I refine ephemerides and orbital parameters, as well as look for long-term non-linear trends in their transit times indicative of TTVs. In total, I reexamine 121 planets in 117 systems. Of these, 19 were known previously to show TTVs. I additionally find evidence for either periodic timing residuals or non-linear trends in the ephemerides of 24 systems for which variation was not previously detected. Of particular interest are Kepler-522 b, which shows TTVs of 20 minutes in amplitude, and K2-348, which contains of two Neptune-sized planets for which TESS data shows long-term second order trends. Many systems further experienced an improvement in their linear ephemerides by a factor of 2-10. I perform further analysis on a few of these interesting systems, fitting the TTVs of Kepler-522 b to reveal a potential non-transiting companion and assessing the limits of detecting tidal decay in several of Kepler and K2's hot Jupiters.

I then present several case studies of systems in which TTV analysis complements the greater work of exoplanet discovery and characterisation. We start with a system of two transiting Neptune-sized planets around the bright, young M-dwarf AU Mic, presented in Zicher et al. (2022) and Wittrock et al. (2022). With data from a 1-year, intensive monitoring campaign of the system's RV using 91 observations with the HARPS spectrograph, and use of a multidimensional Gaussian Process

framework to model the stellar and planetary signals simultaneously, we arrived at mass estimates for both planets. I modeled TTVs for this system to show that these masses are consistent with the scatter in observed transit times and help guide future observations.

Finally, we discuss the role of TTVs in rounding out the discovery and validation of a two-planet system around a bright early G dwarf through the Planet Hunters TESS project (Eisner et al., 2021). Modelling of the transits combined with RV data from Nicholson et al. (in prep) yields periods for each planet that put them in 5:3 orbital resonance. Using the mass estimates from RV data I model TTVs and find reasonable agreement to the scatter seen in transit points. The potential to better characterise the system's TTVs combined with the brightness of the host star and the strong likelihood of an extended H/He atmosphere on both planets, this system offers excellent prospects for atmospheric characterisation and comparative planetology.

Declaration

The work in this thesis is based on research I carried out at the University of Oxford between Trinity Term 2019 and Trinity Term 2023.
Chapter 2 is primarily taken from my first-author, peer reviewed paper (see list below). While the majority of the work in the paper is my own, certain analyses were performed and the relevant sections of the paper were written by co-authors and adapted for this thesis, and this chapter has its own declaration to note these contributions. Chapter 3 presents content from a paper near submission, and is primarily my work and writing with input from Suzanne Aigrain.

Chapter 4 represents the summary of several papers on which I was co-author. The section on AU-Mic presents the work from Zicher et al. (2022) and Wittrock et al. (2022) on which I am co-author (see below). All data extraction, photometric, and RV analysis was carried out by other members of the research teams. For Norbert Zicher's paper I forward-modelled TTVs using the extracted transit times and for Justin Wittrock's paper, I helped conceive of, design and monitor the TTV analysis, though fits were performed by Justin. In the HD 152843system, I similarly carried out all TTV modelling for the papers by Nora Eisner and Belinda Nicholson listed below, while other members of the research team performed photometric and RV analysis. Relevant declarations are found as reminders at the head of each section in Chapter 4. The remainder of Chapter 4 in which I analyse Kepler-522 as well as several hot Jupiters is solely my own work.

Code used in this research has been written by myself or is publicly available and referenced in the relevant places.

List of publications that present work from this thesis

1. Kaye et al. (2022) Transit timing variations in the three-planet system: TOI-270, , MNRAS, 510, 5464.

2. Kaye & Aigrain (in prep), *Transit Ephemerides and Timing Variations from Kepler and K2 to TESS*

3. Eisner et al. (2021), *Planet Hunters TESS III: two transiting planets around the bright G dwarf HD 152843*,, MNRAS, 505, 1827.

4. Zicher et al. (2022), One year of AU Mic with HARPS - I. Measuring the masses of the two transiting planets, MNRAS, 512, 3060.

5. Wittrock et al. (2022), *Transit Timing Variations for AU Microscopii b and c*, , AJ, 164, 1.

6. Nicholson et al. (in prep) HD152843 b & c: measuring masses of a unique planetary system.

Acronyms

LC ..... Light curve

MAST ..... Mikulski Archive for Space Telescopes

MCMC ..... Markov chain Monte Carlo

RV ..... Radial velocity

TTV ..... Transit Timing Variation

TESS ..... Transiting Exoplanet Survey Satellite

TOI ..... TESS object of interest

KOI ..... Kepler object of interest

TFOP ..... TESS Follow-up Observing Program

MMR ..... Mean Motion Resonance

TDV ..... Transit duration variation

SPOC ..... Science Processing Operations Cente

TPF ..... Target Pixel File

FAP ..... False Alarm Probability

SNR ..... Signal to Noise Ratio

LS ..... Lomb-Scargle

HARPS-N ... High Accuracy Radial velocity Planet Searcher in the Northern hemisphere

LCO(GT) .... Las Cumbres Observatory Global Telescope

NGTS ..... Next Generation Transit Survey

PEST ..... Perth Exoplanet Survey Telescope

Contents

0.1 Acknowledgements ii
0.2 Abstract iii

1 Introduction **1**
1.1 A History of Exoplanet Discovery 1
1.2 Methods of Detection 5
1.2.1 Radial Velocity 5
1.2.2 Transit Method 7
1.2.3 Transit Timing Variations 9
1.2.4 Astrometry 10
1.2.5 Gravitational Microlensing 11
1.2.6 Direct Imaging 12
1.3 Transit Searches 13
1.3.1 Kepler 13
1.3.2 K2 16
1.3.3 The Transiting Exoplanet Survey Satellite (TESS) 17
1.3.4 Targeted Space-Based Transit Observatories 18
1.3.5 Ground-Based Transit Observatories 19
1.4 Orbital motion 20
1.4.1 Kepler's laws 25
1.4.2 Orbits in two-dimensions 27
1.4.3 Orbit in three-dimensions 28
1.5 Transit equations 30
1.5.1 Quadratic limb darkening model 34
1.5.2 Stellar Parameter Determination 36

1.6 TTV Equations . . . 38
1.6.1 Chopping . . . 42
1.6.2 Transit Duration Variations . . . 43
1.6.3 Discoveries . . . 44
1.7 Atmosphere, composition and evolution . . . 48
1.8 Summary and Outline of Thesis . . . 51

2 Transit Timing Variations in the 3-planet system TOI-270 53
2.1 Introduction . . . 53
2.2 Observations . . . 59
2.2.1 *TESS* . . . 63
2.2.2 *LCO* . . . 64
2.2.3 *TRAPPIST*-South . . . 65
2.2.4 *ASTEP* . . . 65
2.2.5 *NGTS* . . . 67
2.2.6 *PEST* . . . 67
2.2.7 *Spitzer* . . . 68
2.3 Light curve analysis . . . 69
2.3.1 Model implementation . . . 73
2.3.2 *TESS* . . . 75
2.3.3 Spitzer . . . 76
2.3.4 Ground based observatories . . . 79
2.4 Dynamical Analysis . . . 80
2.4.1 TTV Retrieval . . . 80
2.4.2 Long-term Stability . . . 84
2.5 Results and Discussion . . . 91
2.5.1 Combined TTV and RV Analysis . . . 91
2.5.2 Evolution and Additional Planets . . . 92
2.5.3 Atmospheric and Composition . . . 93
2.5.4 Potential for Atmospheric Characterization . . . 93
2.6 Conclusion and Future Work . . . 94

3 Transit Timing Variations from Kepler and K2 to TESS 96
3.1 Introduction . . . 96
3.2 Target Selection . . . 98
3.3 Observations . . . 101
3.3.1 Kepler . . . 101
3.3.2 K2 . . . 102
3.3.3 *TESS* . . . 102
3.4 Light curve analysis . . . 103

3.4.1 Overview . . . 103
3.4.2 Normalization . . . 104
3.4.3 Cross Correlation . . . 105
3.4.4 Planetary Parameter Fits . . . 108
3.4.5 Timing Fits . . . 109
3.5 Transit Timing Analysis . . . 110
3.6 Results . . . 112
3.6.1 Systems with Previous TTVs . . . 115
3.6.2 New Periodic TTVs . . . 117
3.6.3 Systems with Second Order Trends . . . 123
3.6.4 Large Corrections to Ephemerides . . . 123
3.7 Discussion . . . 125
3.8 Conclusion . . . 130

4 Transit Timing Analysis and Prediction of Selected Systems 132
4.1 Introduction . . . 132
4.2 AU Mic . . . 133
4.3 Discovery and Analysis of the HD 152843 system . . . 139
4.4 Further Work on TOI-270 . . . 145
4.4.1 Transit and TTV Analysis . . . 145
4.4.2 Results and Discussion . . . 147
4.5 Systems from Catalogue paper . . . 152
4.5.1 Hot Jupiters . . . 152
4.5.2 Analysis of Kepler-522 b . . . 160
4.5.3 Concluding Remarks . . . 169

5 Conclusion 170
5.1 Concluding Remarks . . . 170
5.2 Future Work . . . 176
5.3 The Direction of Future Exoplanet Searches . . . 180

A TOI-270 183

B Appendix: TTV Catalogue 191

C Appendix: Further Work 208
C.1 Follow-up Spectroscopy of GY326 . . . 208
C.1.1 Background: GY326 and Dippers . . . 209
C.1.2 Analysis . . . 212
C.1.3 Concluding GY326 . . . 221
C.2 Cloudie: Searching for inhomogeneous cloud cover on hot Jupiters . 222

C.2.1 Analysis 224
C.2.2 Continuing Work 229

D Meet the Planets **232**

Bibliography **237**

Bibliography **237**

Do not go gentle into that good night

— Dylan Thomas

CHAPTER 1

Introduction

1.1 A History of Exoplanet Discovery

Humanity has long posited the existence of other worlds. Ancient civilizations observed the motion of celestial objects in the night sky, recognizing the Sun, the Moon, and the brightest planets, such as Venus, Mars, Jupiter, and Saturn, as distinct wanderers against the backdrop of the fixed stars. With the advent of the telescope in the 17th century, Galileo Galilei pioneered a series of revolutionary discoveries, for the first time beholding the four largest moons of Jupiter, now known as the Galilean moons, and observing the phases of Venus, providing evidence for a heliocentric model of the solar system. These discoveries challenged the prevailing geocentric view and laid the foundation for a new understanding of planets.

While the work of Galileo and his predecessor, Copernicus, laid the groundwork for contemplating the existence of planets around stars other than our sun, or exoplanets, it would take several centuries before scientific advancements and technological capabilities allowed for their detection. However, in the following centuries, astronomers made significant progress in uncovering the secrets of our more closely neighboring worlds within our own solar system. Observations and calculations by Johannes Kepler and Isaac Newton led to the formulation of the

laws of planetary motion, providing a mathematical framework to describe the orbits and dynamics of the planets. Later advancements in telescopes, such as the discovery of Uranus by William Herschel in 1781 (Herschel & Dreyer, 1912) and Neptune by Johann Galle in 1846 (Miner & Wessen, 2002), expanded our knowledge of the outer reaches of the solar system.

In the early 1990s, Aleksander Wolszczan and Dale Frail discovered the first two exoplanets orbiting a millisecond pulsar, a rapidly rotating neutron star, with the creative title of PSR B1257+12 (Wolszczan & Frail, 1992). This was an unexpected discovery, as it was thought that planets could not survive the intense radiation in the late phases of stellar evolution that give rise to such objects. A pulsar is a highly magnetized supernova remnant that emits beams of radiation from its poles like a beacon, which produce a regular pattern of pulses as the star rotates that can be detected by radio telescopes.

Wolszczan and Frail detected the planets using a technique called pulsar timing variations, which involves measuring the precise arrival times of the pulsar's radio pulses over a long period of time. As the pulsar obits the centre of mass of the system, the light-travel time to the observer varies, causing small changes in the arrival times of the pulses. These periodic timing variations provide evidence for the presence of the planets. While they were named according to what would later become convention, adding letters to their hosts names to get PSR B1257+12b and PSR B1257+12c, the two planets, along with a third planet discovered a few years later in 1994 (Wolszczan, 1997), were given the colloquial names Draugr, Poltergeist and Phobetor. Their host pulsar was named Lich, meaning an undead creature, rounding out a set of fitting names for a once-exploded star and a family of planets likely formed from the remains (Wang et al., 2006). While such objects as PSR B1257+12b have proven rare (Niţu et al., 2022), the method of analysisng timing variations has since formed an important component of the toolbox of exoplanet discovery and characterisation.

The first exoplanet discovered orbiting a main-sequence star was 51 Pegasi b, which was detected in 1995 by Swiss astronomers Michel Mayor and Didier Queloz

using the radial velocity method (Mayor & Queloz, 1995). Located about 50 light-years away in the constellation Pegasus, the planet is a gas giant, similar in size to Jupiter, and orbits its star at a distance of only 0.05 AU. This small distance gives the planet a very short orbital period of only 4.2 Earth days, which again came as a surprise to astronomers, who had not expected to find a flaming hot ball of gas in so tight an orbital embrace (Guillot et al., 1996).

However surprising, the discovery of 51 Pegasi b was a major breakthrough in astronomy, as it was the first confirmation that planets could exist around main sequence stars other than our Sun. It sparked a new era of exoplanet discovery, as astronomers began using the same method to search for planets around other stars and in 1999, a team of astronomers led by Geoffrey Marcy and Paul Butler announced the discovery of several new exoplanets using the radial velocity method (Cochran et al., 1997; Marcy et al., 1999). This marked the beginning of a rapid increase in the number of known exoplanets.

In 2000, the first transiting exoplanet was discovered, when the planet HD 209458 b was observed passing in front of its star (Charbonneau et al., 2000; Henry et al., 2000). Because this method involves observing the slight dip in the star's brightness as the planet passes in front of it, it allowed the planet's size and orbit to be determined for the first time. After several small-scale ground-based surveys, the Kepler spacecraft was launched in 2009, with the goal of detecting exoplanets using the transit method (Borucki et al., 2010). The Kepler mission was hugely successful, taking the number of discovered exoplanets from a few hundred, to several thousand, as well as adding many multi-planet systems to the mix. A successor came in the form of the Transiting Exoplanet Survey Satellite, or TESS Ricker et al. (2014), which is continuing to top up the number of discoveries to where it stands today, in the 5,000s (Akeson et al., 2013).

Such cataloging also enabled astronomers to start identifying trends in the population. While detection methods favour certain populations, a few distinct patterns have emerged. Contrary to expectations, most of the planetary systems discovered look very different from the Solar System: giant planets in very close

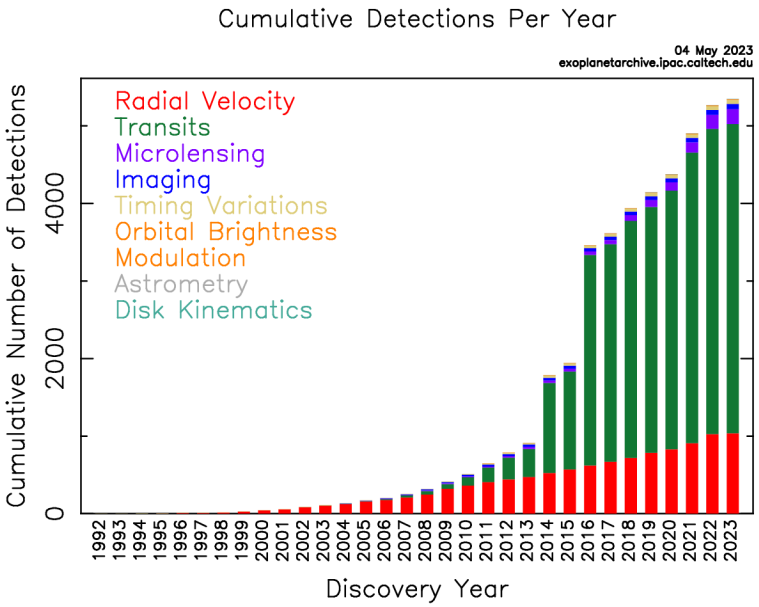


Figure 1.1: Exoplanet discoveries by year. The different methods of detection will be discussed in greater detail in Section 1.2

orbits smaller than that of Mercury, multiple planet systems with planets of similar size and mass, and systems with planets orbiting in retrograde or highly eccentric orbits (Buchhave et al., 2012; Barnes et al., 2011; Sanchis-Ojeda et al., 2012). Searches starting with Kepler have revealed that in spite of the tendency of most detection methods to favour larger planets, the frequency of planets increases with decreasing size (Wittenmyer et al., 2011). This suggests that smaller planets may be more common than larger ones, which is consistent with theories of planet formation (Williams & Cieza, 2011).

Beyond the detection of exoplanets, astronomers became increasingly interested in characterising these other worlds, learning about their compositions, atmospheres, and evolution. In 2005, the Spitzer Space Telescope was used to observe the thermal emission of exoplanets, allowing their temperatures and atmospheric compositions to be determined (Werner et al., 2004; Deming et al., 2005; Charbonneau et al., 2005). This marked a new era in exoplanet characterization, wherein we know not only of the existence of these alien planets, but what they might be like, and how they evolve or differ from our own.

For example, the hot Jupiter mentioned above as the first exoplanet to be detected by transit, HD 209458 b, has subsequently had its atmosphere studied using transit spectroscopy (Vidal-Madjar et al., 2003; Brogi & Line, 2019; Alonso-Floriano et al., 2019). These observations have revealed the presence of water vapor, carbon monoxide, and other molecules, as well as a layer of high-altitude clouds that reflects starlight. The planet's atmosphere is also highly extended, with a size that is much larger than its physical radius.

Other systems more closely echo our own, such as the TRAPPIST-1 system, first discovered in 2016 by Gillon et al. (2017). This is a system of seven Earth-sized exoplanets that orbit a red dwarf star about 40 light-years away. The atmospheres of several of these planets have been studied using transit spectroscopy, which has has made no clear detections, but does not rule out the presence of carbon dioxide-dominated, oxygen-dominated or water-dominated atmospheres (de Wit et al., 2016; Lustig-Yaeger et al., 2019; Zhang et al., 2018). Spectrographs like that of the James Webb Space Telescope (JWST) will provide further insight into the planets' atmospheric compositions and temperatures in the near future that will hopefully enable comparative planetology within this fascinating system.

In recent years, new techniques such as direct imaging and gravitational microlensing have been used to discover new exoplanets, further expanding our knowledge of the universe beyond our solar system. These techniques will be described in more detail below. Overall, exoplanet discovery has come a long way in just a few decades, and we can expect many more exciting discoveries in the years to come.

1.2 Methods of Detection

1.2.1 Radial Velocity

As mentioned above, the radial velocity (RV) method was the earliest method to yield exoplanet discoveries around main sequence stars. It is based on the principle that as a planet orbits its star, its gravity causes the star to move towards and away from us along our line of sight. This motion causes a periodic Doppler shift in

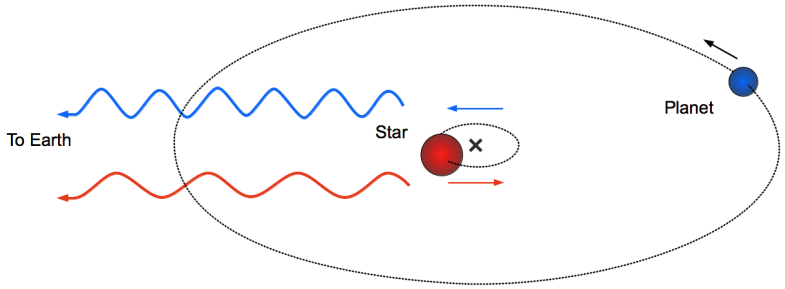


Figure 1.2: Light from a star with an exoplanet will be periodically red and blue shifted along the line of sight to an observer.

the star's spectral lines as seen in Figure 1.2, which can be detected using a high-resolution spectrograph. By measuring the periodic variations in the star's radial velocity over time, we can infer the presence of an orbiting planet and determine its properties, such as its mass and orbital period.

Several high resolution spectroscopic facilities play large roles in the discovery and characterisation of exoplanets by this method. One of these is HARPS (High Accuracy Radial Velocity Planet Searcher), a high-resolution spectrograph installed on the 3.6-meter telescope at the La Silla Observatory in Chile, which has been used to discover hundreds of exoplanets, including many of the first rocky planets around other stars (Pepe et al., 2000). Another facility is HIRES (High-Resolution Echelle Spectrometer), which is installed on the Keck I telescope at the W. M. Keck Observatory in Hawaii (Marconi et al., 2021).

ESPRESSO (Echelle SPectrograph for Rocky Exoplanet and Stable Spectroscopic Observations) is another high-resolution spectrograph installed on the VLT (Very Large Telescope) in Chile. It has a very high radial velocity precision of a few centimeters per second, capable of detecting Earth-sized planets (Pepe et al., 2021a). Finally, CARMENES (Calar Alto high-Resolution search for M dwarfs with Exoearths with Near-infrared and optical Échelle Spectrographs) is a high-resolution spectrograph installed on the 3.5-meter telescope at the Calar Alto Observatory in Spain which specializes in detecting planets around low-mass M dwarf stars (Quirrenbach et al., 2014).

These high-resolution spectrographs have played a critical role in the discovery and characterization of exoplanets using the radial velocity method. They have enabled astronomers to measure the masses and orbital parameters of exoplanets with unprecedented precision, and have helped to advance our understanding of the diversity and formation of planetary systems in the universe.

The RV method is particularly effective for detecting massive planets that orbit close to their host stars, as these planets induce a larger gravitational tug on their host stars, resulting in larger radial velocity variations. This leaves it less effective for discovering detecting small, Earth-like planets, or planets on wide orbits, as their gravitational tug on their host stars is much smaller and more difficult to detect, inducing sub-m/s velocities that have historically been buried in systematic errors from instruments, analysis, and as instruments continue improving, in the noise from stellar photospheric velocities (Fischer et al., 2016).

RV measurements also give rise to a degeneracy between mass and inclination as the amplitude of the radial velocity variation depends on the planet's mass and the angle between the planet's orbital plane and the observer's line of sight. This degeneracy can be partially resolved using additional information, but it remains a challenge for accurately characterizing exoplanets using RVs alone, and the masses achieved through RV methods are lower limits, unless other methods such as transits, or transit timing variations can constrain either the inclination or mass independently.

1.2.2 Transit Method

While RV studies have proved incredibly useful for the detection and characterisation of exoplanets, the most fruitful of detection methods is the transit method, which relies on planets in edge-on configurations falling in our line of sight eclipsing their host stars. To detect exoplanets using this method, we must observe a star over an extended period of time, typically weeks to months, and measure its brightness continuously. When a planet transits its host star, it blocks a fraction of the star's light, causing a dip in the observed brightness, as can be seen in Figure 1.3.

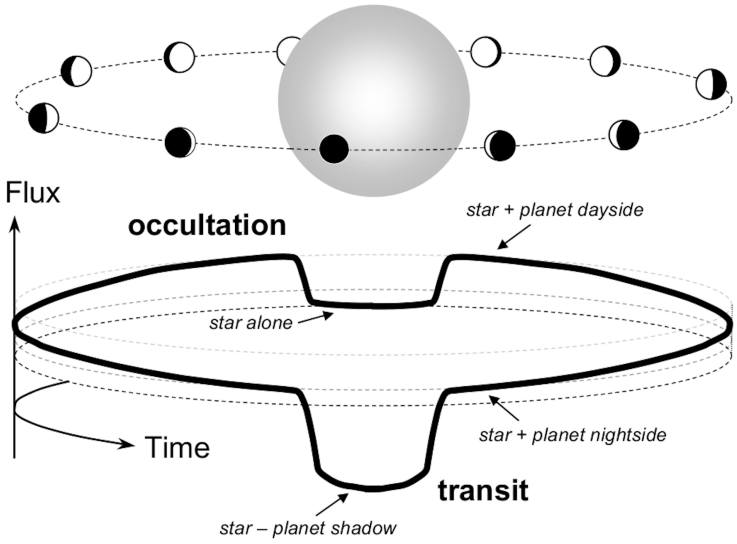


Figure 1.3: An exoplanet transiting its host star gives rise to a distinct dip in flux. From Winn (2014) 1.2

By analyzing the changes in brightness during a transit, we can construct a light curve representing the relative flux (brightness) of the star as a function of time. The depth and shape of the transit signal provide valuable information about the properties of the planet, such as its size and orbital period.

The duration and depth of a transit provides information about the size and orbital characteristics of the planet, including the ratio of the orbital radius to the stellar radius ($a/R_\star$), the inclination (i), impact parameter (b), and period (P). While a single transit can place limits on a period, multiple transits are needed to validate this parameter. The duration of a transit (t_{dur}) is related to the size of the planet and the distance from the star, with larger, further out planets producing longer transits. The depth of the transit, equivalent to the fraction of light blocked by the planet, is related to the planet's size relative to its host star. Geometric and physically based calculations of each of these parameters will be described in further detail in Section 1.5. In order to pin down absolute dimensions of the planet, more information is needed about the star, which can be supplied from its spectrally-derived photospheric properties including its luminosity, effective temperature, surface gravity, and metallicity, as well as through making comparisons

to evolutionary models. An important factor in getting accurate stellar parameters today is the availability of parallaxes from GAIA which allows us to translate the apparent luminosity to absolute luminosity, which can be coupled with T_{eff} (from spectra) to get precise stellar radii. More accurate stellar properties can sometimes result from the analysis of interferometry (Glindemann, 2011), asteroseismology (García & Ballot, 2019), and eclipsing binary companions (Mayer, 1971).

This approach is often combined with radial velocity as a means of candidate confirmation, as well mass estimation, however this mass estimation is limited for smaller planets, as discussed above. Overall, the transit method of detection, through ground based observatories and through satellite transit searches (see Section 1.3) is responsible for nearly 4,000 of the over 5,000 exoplanets that have been discovered to date. The dynamical and geometric equations of transits will be described in further detail in Sections 1.4 and 1.5

1.2.3 Transit Timing Variations

The bulk of this thesis is focused on transit timing variations (TTVs), therefore Section 1.6 will delve into considerably more depth on this method of detecting and characterising exoplanets. For now we will introduce them as a concept before returning later in this chapter when we have laid the other mathematical groundwork for the physics and geometry of orbits. Transit Timing Variations, while responsible for only a small number of new exoplanet discoveries, provide a powerful tool for mass measurement (Agol et al., 2005; Holman & Murray, 2005). TTVs refer to deviations from strictly periodic transits of a planet caused by gravitational interactions between multiple planets in a system. When multiple planets orbit the same star, their mutual gravitational interactions affect each other's orbits. These perturbations can lead to changes in the timing of their eclipses as measured photometrically from earth, as can be seen in Figure 1.4.

TTVs are studied through the careful analysis of observed transits, and comparing these to predictions based on a regular, unperturbed orbit. If there are TTVs, the observed transit times will deviate from the predicted times. By characterising

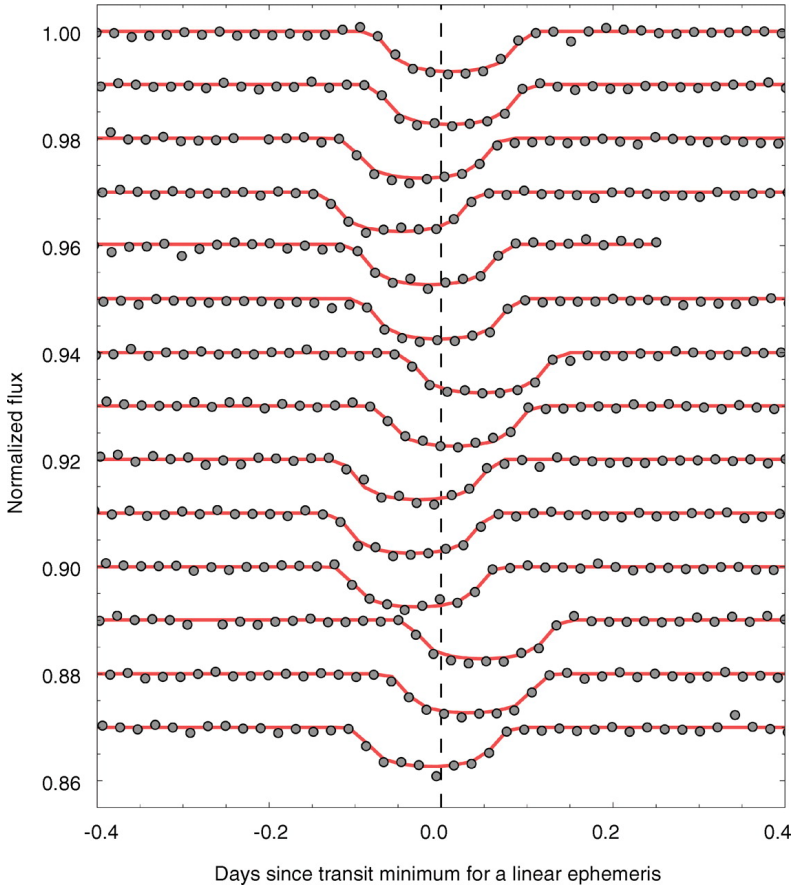


Figure 1.4: The transits of KOI-872 b showing large TTVs. The dotted line shows the average expected transit time, while it is clear that the planet regularly transits earlier or later than this average. From Nesvorný et al. (2012)

the magnitude and pattern of these TTVs, we can infer the presence, masses, and orbital characteristics of additional planets.

TTVs can be modeled as perturbations to a Keplerian orbit. Equations detailing their approximations and computations will be discussed in greater detail in Section 1.6.

1.2.4 Astrometry

Astrometry is the astronomical discipline concerned with accurately measuring the distances and positions of celestial objects, which lends itself to several uses in the study of exoplanets. Because the presence of a planetary companion causes a star to revolve around the system's centre of mass, this manifests as a measurable change

in position (Muterspaugh et al., 2010; Sahlmann et al., 2015). While obtaining accurate parallax measurements from the ground is extremely challenging owing to the effects of Earth's atmosphere, Gaia is a space telescope that was launched in 2013 with the aim of accurately measuring the three-dimensional spatial and the three-dimensional velocity distribution of stars, determining their astrophysical properties, and detecting exoplanets (Gaia Collaboration et al., 2016a).

Through observing millions of stars on average 70 times each every five years, Gaia will become sensitive to Jupiter-mass planets, including those in multiyear orbits around their host stars. Further, the astrometric data of Gaia allow actual masses (rather than lower limits) to be measured, which is critical for both demographic as well as atmospheric follow-up studies (see Section 1.7). The third Gaia data release (Gaia DR3) includes the first Gaia astrometric orbital solutions whose sensitivity in terms of estimated companion mass extends down to the planetary-mass regime (Gaia Collaboration et al., 2023; Holl et al., 2023). This third data release is able to confirm and sometimes refine the orbits of known orbital companions as well as identify new candidates, showing great promise for continued discovery from DR4 and future data releases.

1.2.5 Gravitational Microlensing

Like direct imaging, the method of gravitational microlensing is only responsible for a small fraction of exoplanet discoveries. This method employs Einstein's theory of general relativity, in that a gravitating body bends the spacetime around it. Gravitational microlensing occurs when the gravitational field of a massive object, such as a star, bends the path of light from a distant source object (e.g., a background star). As a result, the light is magnified and forms a brightening or amplification pattern known as a microlensing event. In the context of exoplanet detection, the presence of a planet around the lensing star can be inferred from characteristic features in the microlensing light curve (Griest & Safizadeh, 1998). As the planet moves along its orbit, it produces a distinct perturbation in the light curve, causing temporary deviations from the typical symmetric magnification pattern.

Gravitational microlensing offers several advantages in exoplanet detection. It is sensitive to a wide range of planet masses and can detect planets at larger distances from their host stars compared to other methods (Cassan et al., 2012). Microlensing is particularly effective at discovering cold and low-mass planets, including free-floating "rogue" planets not bound to any star (Bond et al., 2004; Gould et al., 2006; Sumi et al., 2011). Several dedicated microlensing surveys have been conducted, such as the Microlensing Observations in Astrophysics (MOA) (Bond et al., 2001), Optical Gravitational Lensing Experiment (OGLE) (Udalski et al., 2004), and Korea Microlensing Telescope Network (KMTNet) (Hwang et al., 2015). These surveys monitor a large number of stars to identify and characterize microlensing events and search for exoplanets.

1.2.6 Direct Imaging

Direct imaging is a technique whereby we capture actual images of exoplanets, separate from their host stars. While challenging due to the vast contrast between the bright star and the faint planet, several methods and technologies have been developed to accomplish this task. Adaptive optics (AO) is a technique used to correct for the distortion caused by Earth's atmosphere that involves measuring the atmospheric turbulence in real-time and using deformable mirrors to counteract the distortion, resulting in sharper images (Macintosh et al., 2007). Coronagraphs are optical devices or techniques designed to block or suppress the light from the central star, allowing the faint light from nearby exoplanets to be observed. They typically use occulting masks or apodized optical elements to create a region of darkness around the star, enabling the detection of nearby planets.

Direct imaging has been successful in capturing images and spectra of several tens of exoplanets, all gas giants. For example, HR 8799 is a young star located around 129 light-years away in the constellation Pegasus, which hosts a planetary system with at least four directly imaged gas giants, all several times more massive than Jupiter and located at considerable distances from their host star (Marois et al., 2010). While

direct imaging favours larger planets on wide orbits like HR 8799 b-e, advances in imaging techniques will enable us to increasingly probe and expand this domain.

1.3 Transit Searches

Exoplanet transit searches rely on precise and continuous monitoring of stellar brightness. Exoplanet transit surveys have been conducted using ground-based telescopes, such as the WASP (Wide Angle Search for Planets) and HAT (Hungarian-made Automated Telescope) networks, but space based programs have had a great deal of success in getting high quality photometry without the earth's atmosphere (Bakos et al., 2004). Launched in 2006, CoRoT was the first space mission capable of detecting transiting rocky planets, discovering dozens of exoplanets in its observing run (Rauer et al., 2009). Now, two space spaced transit survey telescopes, Kepler and TESS (Transiting Exoplanet Survey Satellite) are responsible for the majority of exoplanet discoveries and monitoring, and form a large basis for the work in this thesis.

These surveys have uncovered a diverse range of exoplanets, from hot Jupiters to rocky Earth-sized planets. Statistical analyses of transit data have provided valuable insights into exoplanet demographics, including the occurrence rates of different types of planets and the prevalence of multi-planet systems. Furthermore, transit observations can be combined with other techniques, such as radial velocity measurements and atmospheric characterization, to obtain a more comprehensive understanding of exoplanets and their properties.

1.3.1 Kepler

Launched in 2009, the Kepler space satellite specifically targeted a ∼115 square degree field of stars in the constellations Cygnus and Lyra (see Figure 1.5 with the primary goal of detecting and characterizing exoplanets. Kepler monitored the brightness of over 150,000 stars simultaneously for four years in its primary mission, with a higher degree of precision and cadence than any ground-based facility. Its

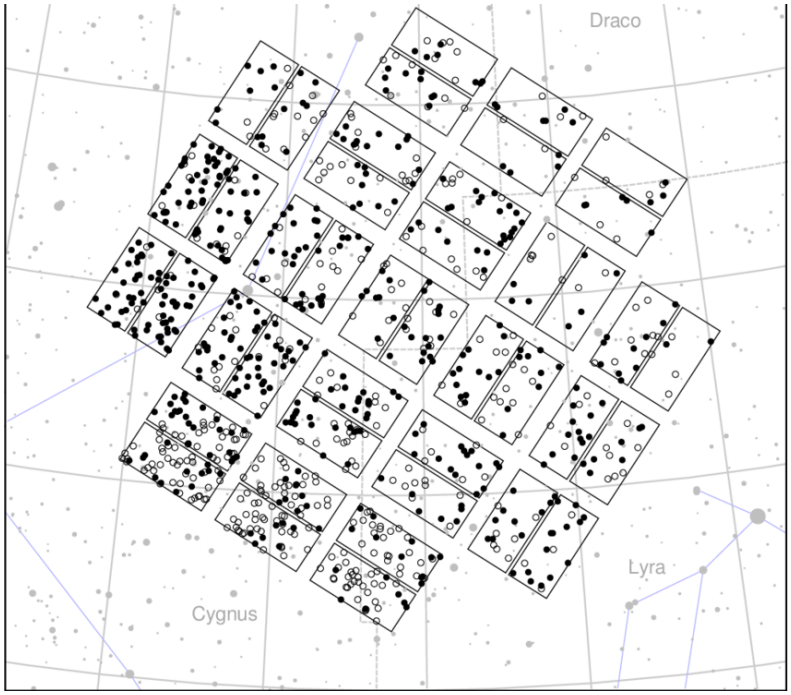


Figure 1.5: The Kepler field with rectangles showing the limits of Kepler's 42 CCDs Pigulski et al. (2009)

discoveries number in the thousands and include everything from hot Jupiters to earth-sized planets located in the habitable zone of their stars.

Kepler employed two different observation modes: short and long cadence. In short cadence mode, Kepler took measurements with a higher frequency, capturing the brightness of stars with integrations every minute (Van Cleve & Caldwell, 2016). Short cadence observations were primarily used to study stellar variability, asteroseismology, and phenomena that required a higher time resolution. In long cadence mode, Kepler took measurements at a lower cadence, typically every 30 minutes. The exoplanet transit searches normally employed long cadence mode, as the longer integration time allowed for the detection of larger numbers of exoplanets.

Transit detection algorithms were employed to identify potential exoplanet candidates from light curves. Several key methods were developed for use by Kepler such as the Box-fitting Least Squares (BLS) algorithm, which fits transit models to the data along a set of hypothetic periods, and minimises the chi-square to identify transit-like signals (Kovács et al., 2002; Aigrain & Irwin, 2004). After initial

transit detection, a Signal Verification and Validation (V&V) pipeline was used to assess the authenticity of transit signals. This involved performing additional analyses to filter out false positives caused by instrumental noise, stellar variability, or other astrophysical phenomena.

Kepler's observations demonstrated that small, planets are common, and they can orbit a wide range of stellar types, including M-dwarfs and Sun-like stars (Thompson et al., 2018). Kepler also revealed the existence of planetary systems with multiple exoplanets, some of which exhibit compact and resonant orbital configurations (Latham et al., 2011; Mills et al., 2016a; Borucki et al., 2013). Additionally, the mission discovered a diverse range of exoplanet sizes, orbital periods, and orbital architectures, further expanding our knowledge of planetary formation and evolution. The range of exoplanet discoveries originating in this time can be appreciated in Figure 1.8. Beyond exoplanets, the Kepler mission had broader impacts in stellar astrophysics and other fields, providing unprecedented data on stellar variability, stellar asteroseismology, and activity cycles.

The radius gap and photo-evaporation

Another trend that was first noticed in Kepler data is the appearance of a "radius valley" that can also be appreciated in Figure 1.8. Fulton et al. (2017) used the precise radii of 2024 Kepler planets to uncover a relative scarcity of planets falling in the range of $1.5 \lesssim R_{\rm p} \lesssim 2\,R_{\oplus}$. Models would suggest that this gap may be due in part to photo-evaporation, in which close-in ($a \lesssim 0.1$ AU) sub-Neptune planets with extended atmospheres would lose their atmosphere within a few hundred Myr due to the intense level of photo-ionising radiation from their host stars, forming bare rocky cores, and leaving a gap in which a planet's gravitation is not strong enough to match this stripping effect (Lopez & Fortney, 2014; Ginzburg et al., 2018).

A follow-up by Van Eylen et al. (2018) incorporated precise stellar parameters from asteroseismology to revise the presence, location, and shape of such a valley detecting a clear bimodal distribution, with super-Earths ($R_{\rm p} = 1.5\,R_{\oplus}$) and sub-Neptunes ($R_{\rm p} = 1.5\,R_{\oplus}$) separated by a deficiency around $2\,R_{\oplus}$. They found that

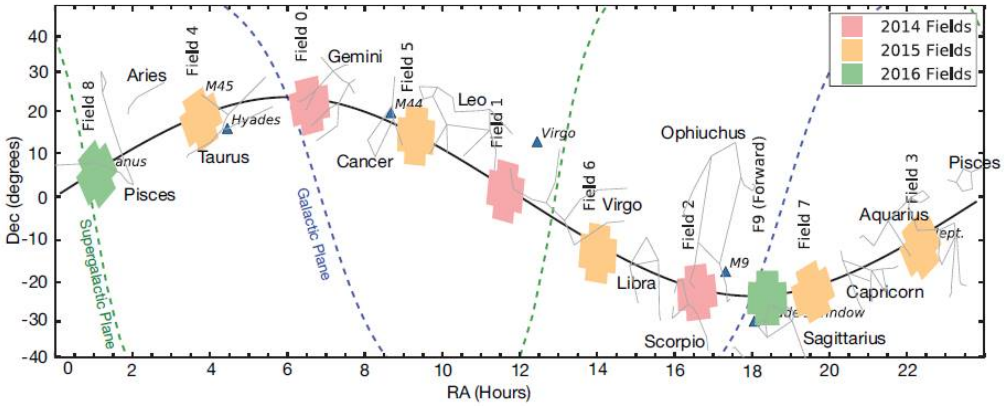


Figure 1.6: The K2 fields broken down by year of observation.

the valley is characterised as a power law $R \propto P^{\gamma}$ with $\gamma \approx -0.09$. The negative slope further suggests that photo-evaporation is the main mechanism behind the radius gap. Further characterising this trend and analysing its significance in the context of evolutionary models is an ongoing area of focus in the field.

1.3.2 K2

In 2013, the failure of two of the four reaction wheels used to stabilize Kepler's orientation stopped functioning correctly. This rendered the original Kepler mission unable to maintain the required precision pointing necessary for its primary exoplanet science. However, astronomers deployed a creative solution that allowed Kepler to continue its operations under a modified mission called K2. To overcome the loss of precise pointing, the K2 mission utilized the remaining two functioning reaction wheels along with incident solar radiation pressure to stabilize the spacecraft. This allowed for continuous observations of the sky, albeit with reduced pointing precision compared to the original Kepler mission (Van Cleve & Bryson, 2017).

Although the two functional reaction wheels provided stability, the torque exerted by the solar radiation pressure caused small changes in the spacecraft's pointing. To mitigate this effect, K2 observed specific regions of the sky where these small pointing variations would have minimal impact on the science objectives. Unlike the original Kepler field, these were located along the ecliptic, providing a rich and diverse new set of observations, as can be seen in Figure 1.6. The spacecraft

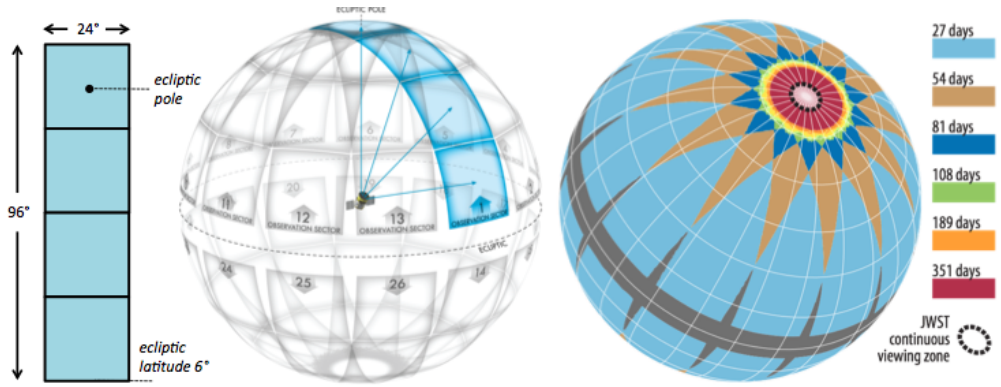


Figure 1.7: TESS sectors in Cycle 1 and 2 showing areas of continuous viewing.

was periodically repositioned to counteract any drift caused by the combination of solar pressure and reaction wheel operations, observing its series of different target fields over sectors lasting approximately 80 days. Although K2 had many limitations compared to the original mission, it continued to make significant discoveries and steadily add to the growing number of known transiting exoplanets.

1.3.3 The Transiting Exoplanet Survey Satellite (TESS)

As mentioned earlier, the Transiting Exoplanet Survey Satellite (TESS) is a space-based mission launched by NASA in 2018 with the primary goal of discovering exoplanets around nearby bright stars (Ricker et al., 2014). Unlike Kepler, which focused on a fixed field of view, or K2 which was confined to the ecliptic, TESS surveys the entire sky by dividing it into 26 sectors. Each sector covers an area of sky, approximately 24 degrees by 96 degrees, with each sector being monitored continuously for about 27 days before moving on to the next adjacent field. This survey strategy allows TESS to capture a large number of exoplanet candidates and other astronomical phenomena. TESS also recaptures significant portions of the Kepler and K2 fields, so brighter Kepler stars with higher signal-to-noise ratios (SNR) can be monitored across observing campaigns.

With a smaller aperture than Kepler, TESS specifically targets nearby, bright stars, which enables further detailed characterization of any newly discovered exoplanets using ground-based telescopes and other observatories. TESS employs a

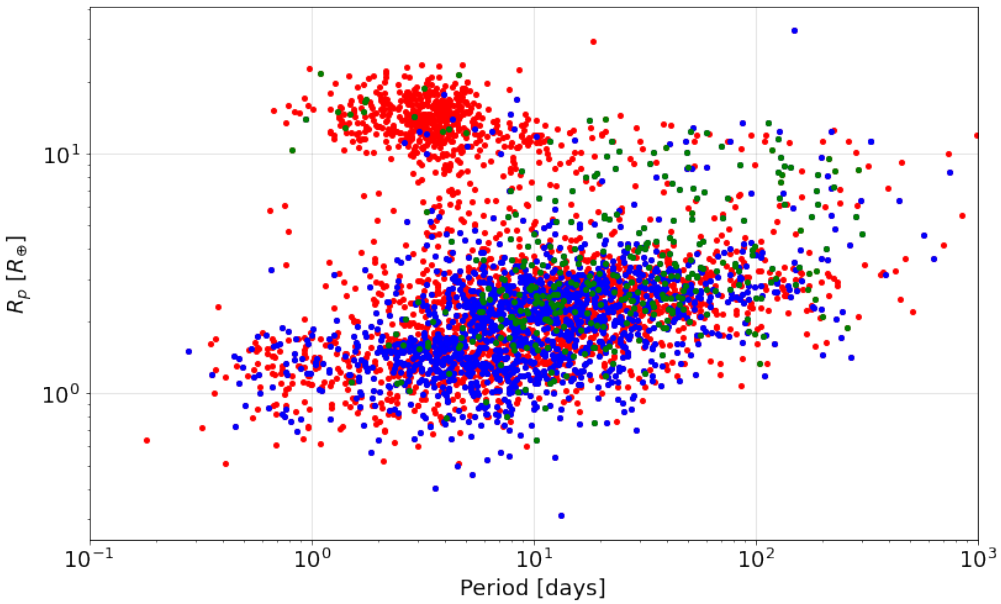


Figure 1.8: Known transiting exoplanets as of June 2023. Transit surveys have revealed many multiple planet systems with smaller radii. Multi-planet systems are marked in blue, and systems with TTV measurements are marked in green.

cadence of 30-minute exposure full frame images (FFIs) of the entire sector, which is well-suited for the discovery and characterization of exoplanets as it provides sufficient SNR for precise transit measurements. It also has a 2-minute cadence mode, which is used for specific target stars of interest, and allows for a more precise determination of the exoplanet's orbital parameters, detection of stellar oscillations (asteroseismology), and the study of rapidly rotating stars and other short-term variability. Overall, the TESS mission complements the work of Kepler and K2 by surveying a larger portion of the sky, targeting nearby bright stars, and focusing on exoplanets with shorter orbital periods.

1.3.4 Targeted Space-Based Transit Observatories

While Kepler, K2 and TESS have provided the motherlode of transiting exoplanet discoveries, several other space-based and ground-based telescopes have their eyes trained on other-worldly eclipses. The work of these other observatories is typically to follow-up on transits detected by TESS or Kepler, often providing higher resolution photometry, further transit times, or spectroscopic measurements.

Assisting TESS from space, is the Hubble Space Telescope (HST). While it was primarily designed for many varied astronomical observations unrelated to exoplanet science, HST has been used to study exoplanets and their atmospheres through transit observations. Its successor, the James Webb Space Telescope (JWST) launched in 2021 and has already furthered transit spectroscopy, with its Near Infrared Spectrograph (NIRSpec) enabling 0.6-5.3 μm spectroscopy at resolving powers of ∼100, ∼1000, and ∼2700 in 4 observing modes (Böker et al., 2023). Its increased sensitivity to infrared radiation allows it to better detect and study thermal emission, which is particularly useful for observing hot Jupiters. By analyzing thermal emission, we can estimate the temperature profiles and thermal properties of exoplanet atmospheres.

The Spitzer Space Telescope, with its infrared capabilities, has also been instrumental in observing exoplanet transits and characterizing their atmospheres. It has helped identify molecules in exoplanet atmospheres and provided information about their temperature profiles. Finally, the newest addition to exoplanet-focused optical space-based observing is the Characterizing Exoplanet Satellite (CHEOPS). Launched by the ESA in 2019 and achieving first light in 2020, CHEOPS is a dedicated space telescope designed to perform high-precision photometric measurements of transiting exoplanets.

1.3.5 Ground-Based Transit Observatories

While Earth's atmosphere severely limits the photometric precision needed for exoplanet searches, several ground based facilities have augmented exoplanet discovery and characterisation. One of the earliest is WASP (Wide Angle Search for Planets), a collaboration between several ground-based observatories located in the Canary Islands and South Africa (Pollacco et al., 2006). Using wide-field cameras, the project has been successful in discovering numerous transiting exoplanets. Observatories involved in WASP include the SuperWASP North and South, as well as the Las Cumbres Observatory (LCO (Brown et al., 2013)). Another is HATNet (Hungarian Automated Telescope Network), a network of small automated

telescopes primarily located in Arizona and Hawaii that has been successful in the discovery of several exoplanets, including hot Jupiters and Neptune-sized planets (Bakos et al., 2004).

Joining these is KELT (Kilodegree Extremely Little Telescope), which uses two small-aperture telescopes—one in the northern hemisphere and one in the south, and has primarily discovered hot-Jupiters (Pepper et al., 2007). Another facility, SPECULOOS (Search for habitable Planets Eclipsing Ultra-cool Stars), is a network of telescopes located at multiple sites, including Paranal Observatory in Chile and Teide Observatory in the Canary Islands (Gillon et al., 2013). It is designed to search for Earth-sized exoplanets orbiting nearby, ultra-cool dwarf stars. Also located at Paranal is NGTS (the Next-Generation Transit Survey), which consists of an array of several 20 cm aperture telescopes and performs follow-up transit observations (Wheatley et al., 2018).

While not an exhaustive list, many of these facilities are involved in the TESS Follow-up Observing Program or TFOP, an initiative that aims to facilitate and coordinate follow-up observations of exoplanet candidates discovered by TESS, conducting additional measurements and analyses to confirm or refute the presence of exoplanets and refine their properties.

1.4 Orbital motion

Now equipped with the knowledge of the mechanisms of discovery and observatories in place, we turn to understanding the physical underpinnings of what we can observe. We start with Newton's equations of motion before turning to Keplerian orbits. We then describe the geometry of transits, and discuss how transit timing variations arise.

We'll start with the motion of two bodies, a star and planet in this case, governed by a single Newtonian form of gravity, in which the attraction between two bodies is directly proportional to the product of their masses m_1 and m_2 and inversely proportional to the square of the distance r between them. This is given by

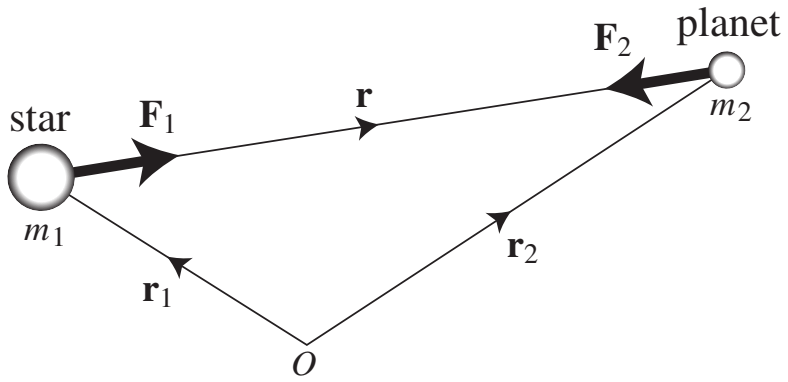


Figure 1.9: Diagram of forces acting on a star (m_1) and on a planet (m_2) with respective position vectors r_1 and r_2. (from Murray & Correia, 2010).

$$F = -\frac{\mathrm{G}m_1m_2}{r^2}, \tag{1.1}$$

where $\mathrm{G} = 6.67428 \times 10^{-11}\mathrm{m}^3\,\mathrm{kg}^{-1}\,\mathrm{s}^{-2}$ is the universal gravitational constant. These two bodies will rotate around a point in space that is the centre of mass of the system, known as the barycenter. The force on a single body, in this case a planet is therefore

$$\mathbf{F} = \frac{k}{r^3}\mathbf{r}, \tag{1.2}$$

Where k is the gravitational constant multiplied by the product of the masses of the two orbital bodies, m_1 (the star) and m_2 (the planet) with position vectors $\mathbf{r}_1$ and $\mathbf{r}_2$ with respect to an inertial frame whose origin is the point **O** as described by (Murray & Correia, 2010) and displayed in Figure 1.9.

The relative motion of the two orbital bodies is therefore $\mathbf{r} = \mathbf{r}_2 - \mathbf{r}_1$, and by following Newton's second law of motion, the gravitational forces acting on both bodies are

$$\mathbf{F}_1 = m_1\ddot{\mathbf{r}}_1 = +\frac{\mathrm{G}m_1m_2}{r^3}\,\mathbf{r}, \tag{1.3}$$

$$\mathbf{F}_2 = m_2\ddot{\mathbf{r}}_2 = -\frac{\mathrm{G}m_1m_2}{r^3}\,\mathbf{r}. \tag{1.4}$$

We can now write an equation for the relative acceleration of the planet (m_2) with respect to the star (m_1) as $\ddot{\mathbf{r}} = \ddot{\mathbf{r}}_2 - \ddot{\mathbf{r}}_1$. Putting this together with equations (1.3) and (1.4), we arrive at

$$\ddot{\mathbf{r}} + \mathrm{G}\ (m_1 + m_2)\,\frac{\mathbf{r}}{r^3} = 0. \tag{1.5}$$

Taking a vector product from $\mathbf{r}$ and this equation and integrating leads to the constant vector $\mathbf{h}$, known as the angular momentum vector. This vector is perpendicular to both the position vector $\mathbf{r}$ and $\dot{\mathbf{r}}$ and allows us to define the planetary motion in the orbit plane.

To solve equation 1.5, the coordinates are translated from Cartesian coordinates x and y into polar coordinates (r, θ), with θ being the reference direction as seen in Figure 1.9. The position $\mathbf{r}$, velocity $\dot{\mathbf{r}}$, and acceleration $\ddot{\mathbf{r}}$ vectors can be written in polar coordinates as

$$\mathbf{r} = r\hat{\mathbf{r}}, \tag{1.6}$$

$$\dot{\mathbf{r}} = \dot{r}\hat{\mathbf{r}} + r\dot{\theta}\hat{\theta}, \tag{1.7}$$

$$\ddot{\mathbf{r}} = (\ddot{r} - r\dot{\theta}^2)\hat{\mathbf{r}} + \left[\frac{1}{r}\frac{\mathrm{d}}{\mathrm{d}t}\left(r^2\dot{\theta}\right)\right]\hat{\theta}, \tag{1.8}$$

where $\hat{\mathbf{r}}$ and $\hat{\theta}$ denote unit vectors along and perpendicular to the radius vector, respectively. By combining Eqs (1.6) and (1.8) with Eq. (1.5) we have

$$(\ddot{r} - r\dot{\theta}^2)\hat{\mathbf{r}} + \left[\frac{1}{r}\frac{\mathrm{d}}{\mathrm{d}t}\left(r^2\dot{\theta}\right)\right]\hat{\theta} + \mathrm{G}\ (m_1 + m_2)\,\frac{r}{r^3}\hat{\mathbf{r}} = \mathbf{0}. \tag{1.9}$$

In order to solve Eq. (1.9) for the positions of orbital motion we need to separate its $\hat{\mathbf{r}}$ and $\hat{\theta}$ components. Using Eq. 1.7 above, we can now write

$$\mathbf{h} = \mathbf{r} \times \dot{\mathbf{r}} = r^2\dot{\theta}\hat{\mathbf{z}}, \tag{1.10}$$

where $\hat{\mathbf{z}}$ is a unit vector perpendicular to the orbital plane forming a right-handed triad with $\hat{\mathbf{r}}$ and $\hat{\theta}$.

Following on from Eq. (1.10), the derivative of h appears in the $\hat{\theta}$ component in Eq. (1.9). This implies that the $\hat{\theta}$ component in Eq. (1.9) has to be zero. Therefore the orbital motion can be simplified to the following equation

$$(\ddot{r} - r\dot{\theta}^2) = -\mathrm{G}\ (m_1 + m_2)\,\frac{1}{r^2}. \tag{1.11}$$

Equation (1.11) can be solved following the procedure described by Murray & Correia (2010). This is done by first making the u substitution $u = 1/r$, and using $h = r^2\dot{\theta}$, which allows us to rewrite $\ddot{r}$ as

$$\ddot{r} = -(r^2\dot{\theta})^2 u^2 \frac{\mathrm{d}^2 u}{\mathrm{d}\theta^2} = -h^2 u^2 \frac{\mathrm{d}^2 u}{\mathrm{d}\theta^2}, \tag{1.12}$$

We can then rewrite Eq. (1.11) as

$$\frac{\mathrm{d}^2 u}{\mathrm{d}\theta^2} + u = \frac{\mathrm{G}(m_1 + m_2)}{h^2}. \tag{1.13}$$

Equation (1.13) is called Binet's equation. It has a general solution of

$$u = \frac{\mathrm{G}(m_1 + m_2)}{h^2}\left[1 + e\cos\left(\theta - \varpi\right)\right], \tag{1.14}$$

where the two constants of integration are e, an amplitude and ϖ, a phase. Reversing the u substitution and rewriting Eq. (1.14) in terms of r, gives

$$r = \frac{p}{1 + e\cos\left(\theta - \varpi\right)} \tag{1.15}$$

Where $p = h^2/\mathrm{G}(m_1 + m_2)$. Equation (1.15) now gives the general equation of a conic section curve in polar coordinates. For this set of curves, the variable e is called *eccentricity* and p is referred to as the *semi-latus rectum*. If $e = 0$, the curve is a circle, if $0 < e < 1$, it is an ellipse, if $e = 1$, it's a parabola, and if $e > 1$, a hyperbola, as shown in Figure 1.10. For planetary systems, we are interested in cases where the planet and star are gravitationally bound in closed orbits ($e < 1$).

Consequently, throughout this thesis we concentrate on elliptical motion. In this case the semi-latus rectum relates with the ellipse properties as

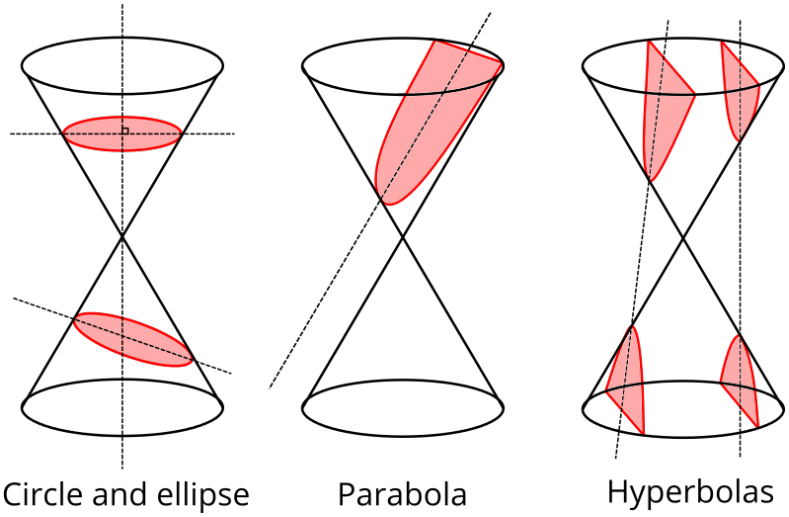


Figure 1.10: Possible solutions to Binet's Equation giving conic sections for various values of e.

$$p = a(1 - e^2), \tag{1.16}$$

and

$$b^2 = a^2(1 - e^2), \tag{1.17}$$

where the constant a is the semi-major axis of the ellipse and b is the semi-minor axis (Fig. 1.11). For any value of θ this now gives a radius of

$$r = \frac{a\,(1 - e^2)}{1 + e\cos(\theta - \varpi)}. \tag{1.18}$$

The angle θ, called the *true longitude*, is the angle on the orbital plane between a reference line and the planet's position. The maximum (*apoastron*) and minimum (*periastron*) values of the radius can be found when $\theta = \varpi$ or $\theta = \varpi \pm \pi$ respectively, giving a minimum of $a(1 - e)$ and $a(1 + e)$ to be the maximum. The angle ϖ is called the *longitude of periastron*, defined as the angle on the orbital plane between the reference line and the periastron. It is usually more convenient to refer the angular coordinate to the periastron rather than to the arbitrary reference line. This leads to the definition of the *true anomaly* as $\nu \equiv \theta - \varpi$ (see Fig. 1.11), such that Equation (1.15) can now be rewritten as

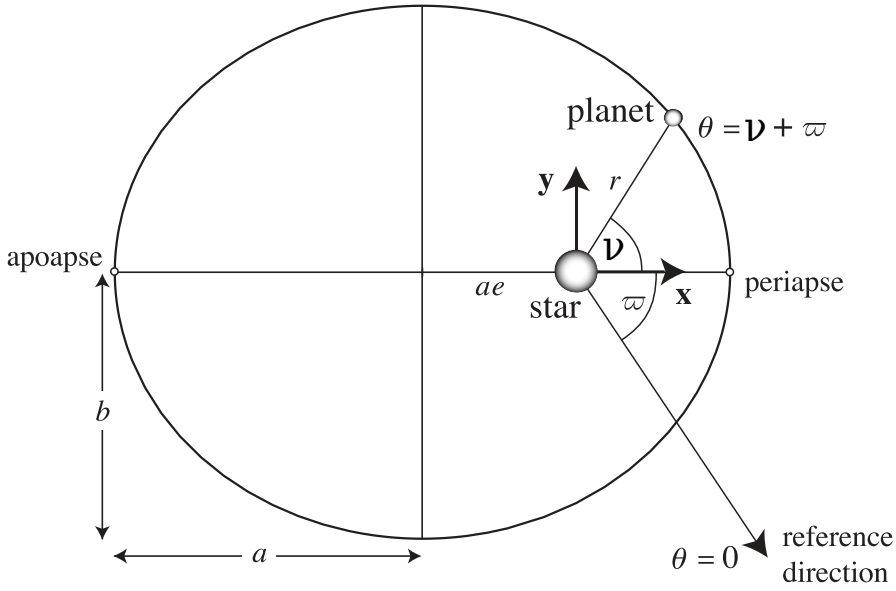


Figure 1.11: The geometry of the ellipse of semi-major axis a, semi-minor axis b, eccentricity e and longitude of periapse ϖ (from Murray & Correia, 2010) .

$$r = a\frac{(1-e^2)}{1+e\cos\nu}. \tag{1.19}$$

1.4.1 Kepler's laws

Kepler's first law states that for a gravitationally bound system, Eq. (1.19) describes the relative orbit of a planet about a star as an ellipse, with the star at one of two foci of the ellipse. This comes as we've showed above as a direct consequence of the inverse square law of gravitation. Figure 1.11 show a diagram of the elliptical orbit of the planet.

Kepler's second law, as alluded to above, refers to the area swept out radially by the planet with respect to the star. It can be arrived at by considering the motion of the mass m_2 during the time interval $\mathrm{d}t$. The area $\mathrm{d}A$ swept out by the radius vector r in time $\mathrm{d}t$, or areal velocity $\dot{A}$, is given by

$$\dot{A} \equiv \frac{\mathrm{d}A}{\mathrm{d}t} = \frac{1}{\mathrm{d}t}\int_0^r r\mathrm{d}r\mathrm{d}\theta \tag{1.20}$$

By integrating Eq. (1.20) with respect to r and using $h = r^2\dot{\theta}$, we get

$$\dot{A} = \frac{1}{2} r^2 \dot{\theta} = \frac{1}{2} h. \tag{1.21}$$

Since h is a constant this implies that equal areas are swept out in equal times and hence Eq. (1.21) is the mathematical form of Kepler's second law of planetary motion.

For gravitational bound systems, based on Eq. (1.19), of elliptical motion, the planet occupies the same position after the radius vector r has turned through an angle of 2π, implying a set periodicity. The time P needed by the planet to complete a full orbit is called the *orbital period*. By integrating Eq. (1.21) over an orbital period P we obtain

$$A = \frac{1}{2} hP. \tag{1.22}$$

where A is the area enclosed by the ellipse. We know that the area of an ellipse is also given by $A = \pi ab$, where the semi-minor axis b is related to the semi-major axis a and the eccentricity e through $b^2 = a^2(1 - e^2)$. Combining this with Eq. (1.17) gives us

$$A^2 = \frac{1}{4} h^2 P^2 = \pi^2 a^4 \left(1 - e^2\right). \tag{1.23}$$

By combining the above equation with Eq. (1.3), we arrive at

$$P^2 = \frac{4\pi^2}{\mathrm{G}(m_1 + m_2)} a^3. \tag{1.24}$$

Which is known as Kepler's Third Law, which states that the square of the orbital period P^2 is directly proportional to the cube of the semi-major axis a^3. We can see that P is independent of e and is a function of the sum of the two masses $m_1 + m_2$ and the semi-major axis a only. In most cases of orbiting planets, $m_2 \ll m_1$ and $m_1 + m_2 \approx m_1$. This therefore simplified to $(4\pi^2)/(\mathrm{G}\, m_1)$ a constant.

1.4.2 Orbits in two-dimensions

Kepler's laws on top of Newton's law of gravitation give us the shape of orbits and some guiding principals of the behaviour of gravitationally bound bodies. However, we don't yet have a direct way of determining a planet's position as a function of time. As stated above, the true anomaly ν is an angular measure that determines the position of an object along its orbit relative to its pericenter, measured as the angle between the periapsis, the star, and the current position of the orbiting object, as seen in Figure 1.12. While we have so far shown that the orbital radius can be calculated if we know the value of the eccentricity e, the semi-major axis a and the true anomaly, in order to describe the planetary orbit as function of time we need define two additional angles: the eccentric anomaly ϵ and the mean anomaly μ.

The eccentric anomaly is geometrically defined as the angle between the periapsis, the central body, and an imaginary point on an auxiliary circle known as the *eccentric circle*, a reference circle used to determine the position of the orbiting object based on its distance from the center of the ellipse. Following the derivation by Murray & Correia (2010), the true and eccentric anomalies are related as

$$\nu = 2 \arctan \left[\sqrt{\frac{1+e}{1-e}} \tan \left(\frac{\epsilon}{2} \right) \right], \tag{1.25}$$

whereas the eccentric anomaly relates to the mean anomaly μ as

$$\mu = \epsilon - e \sin(\epsilon). \tag{1.26}$$

The mean anomaly is defined as the fraction of the orbital period that has elapsed since the object last passed its pericenter, giving it an explicit dependence on time t defined by

$$\mu = \frac{2\pi}{P} (t - T_{\mathrm{p}}). \tag{1.27}$$

Also, $\mu = 0$ when $t = T_{\mathrm{p}}$ or $t = T_{\mathrm{p}} + P$ which implies a zero time of periastron passage. It is further the case that $\mu = \pi$ when $t = T_{\mathrm{p}} + P/2$, which is the apoastron

passage. The true anomaly can then be obtained in terms of t by solving Eqs. (1.27), (1.26), and (1.25) to give us the orbital position as function of time.

Further combining Eq 1.27, Eq 1.26 and Kepler's second law, we can get

$$\mathrm{d}\nu = \frac{2\pi}{P}\sqrt{1-\epsilon^2}\left(\frac{a}{r}\right)^2 \mathrm{d}t = \sqrt{1-\epsilon^2}\left(\frac{a^2}{r}\right)\mathrm{d}\mu \tag{1.28}$$

Integrating to find an average over a full orbit gives

$$\frac{1}{r^2} = \frac{1}{2\pi}\int_0^{2\pi}\frac{\mathrm{d}\mu}{r^2} = \frac{1}{a^2\sqrt{1-\epsilon^2}} \tag{1.29}$$

to give the mean longitude λ as

$$\lambda = \mu + \varpi \tag{1.30}$$

1.4.3 Orbit in three-dimensions

In order to fully understand the basics of orbits and lay the groundwork for perturbations caused by additional bodies, there is one more dimension to consider. We can specify the orbital plane in which the above measures of λ and μ are defined as linear functions as having a coordinate system of (x, y, z), while the plane of the observer can lie along a different reference direction. The orbital plane is inclined with respect to this observational frame at an angle i called the *inclination*, which ranges from $0 \leq i \leq 180°$, with an orbit said to be prograde if $i \leq 90°$, and retrograde if $i > 90°$. At this difference in inclination, the planetary coordinates can be defined with respect to axes (X, Y, Z). This is pictured in (Fig. 1.12)

The planet's position vector in the orbital coordinate system is given by

$$\mathbf{r} = (x, y, 0) = x\,\hat{\mathbf{x}} + y\,\hat{\mathbf{y}} + 0\,\hat{\mathbf{z}} \tag{1.31}$$

where $\hat{\mathbf{x}}$, $\hat{\mathbf{y}}$, and $\hat{\mathbf{z}}$ are orthogonal unit vectors. The orbital plane does not have a preferred projection and intersects the reference plane X-Y in a line called *line of nodes*. The *longitude of the ascending node* is an angle that specifies the location of the line of nodes within the reference plane. It is measured along the reference plane, starting from a defined reference direction and ranges from

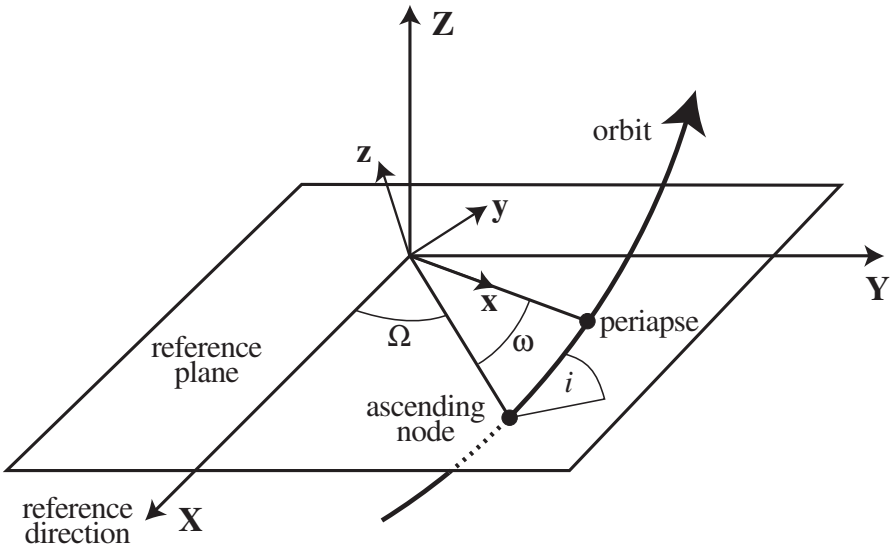


Figure 1.12: Relating the (x,y,z) orbital and (X,Y,Z) observer coordinate systems and the angles ω, i and Ω (from Murray & Correia, 2010).

$0 \leq i \leq 360°$. Figure 1.12 shows the ascending node, the three angles (Ω, ω and i), the reference plane X-Y, and the reference direction X. This growing list of parameters is summarised in Table 1.1.

These two coordinate systems are helpful for understanding the relation of the angles discussed, ω, i and Ω. Several of these angles can be understood and interchanged by utilising rotation matrices about each axis. One rotation occurs through the angle of ω about the z-axis to coincide with the line of nodes, one rotates through angle i about the x-axis and one through an angle Ω around the z-axis.

Using the relations $x = r\cos(f)$, $y = r\sin(f)$ and $z = 0$ in the orbital plane to relate to the reference plane, X, Y, Z is written as:

$$X = r\left[\cos\Omega\cos(\nu+\omega) - \sin\Omega\sin(\nu+\omega)\cos i\right], \tag{1.32}$$

$$Y = r\left[\sin\Omega\cos(\nu+\omega) + \cos\Omega\sin(\nu+\omega)\cos i\right], \tag{1.33}$$

$$Z = r\sin(\nu+\omega)\sin i. \tag{1.34}$$

The reference plane X-Y is usually taken to be the plane of the sky perpendicular to the line of sight, with the Z-axis oriented towards the observer. The reference X axis is usually oriented towards the celestial North pole. For this case we do

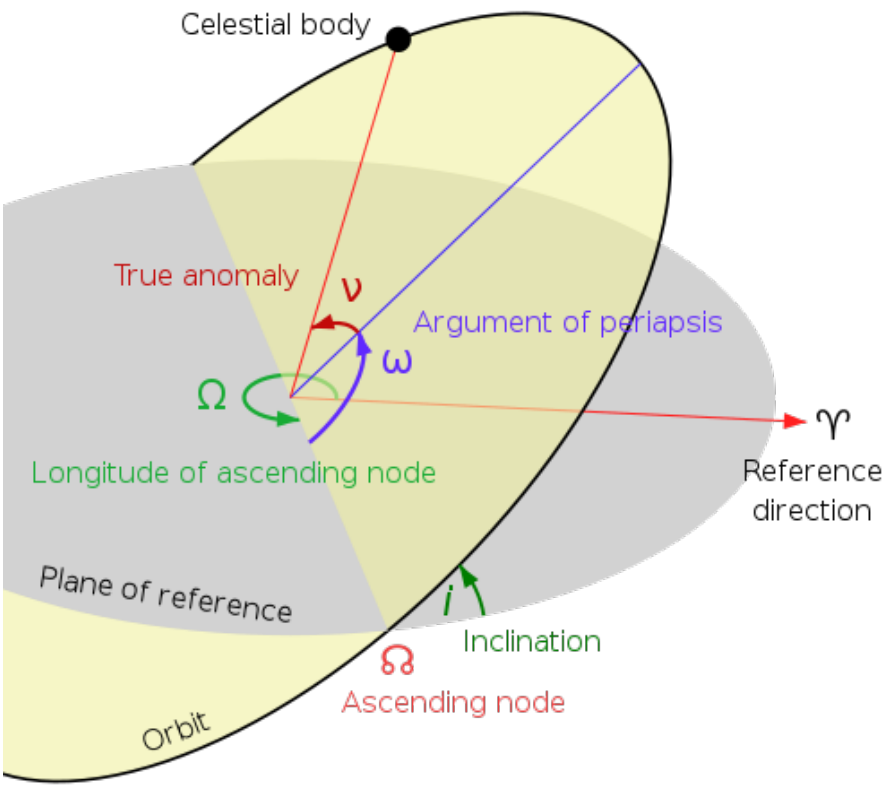


Figure 1.13: Further visualisation of the orbital plane with respect to the observer's plane

not have a preferred direction and so we can assume $\Omega = \pi$. Equations (1.32), (1.33) and (1.34) can thus be rewritten as

$$X = -r\cos(\nu + \omega) \tag{1.35}$$

$$Y = -r\sin(\nu + \omega)\cos i \tag{1.36}$$

$$Z = r\sin(\nu + \omega)\sin i \tag{1.37}$$

Equations (1.35), (1.36) and (1.37) form the basis to describe the orbital motion in the two-body system as seen from Earth. A summary of this is shown in Figure 1.13.

1.5 Transit equations

In order to put this orbital geometry into play in a useful manner for observing from our corner of the galaxy, we must translate these properties into transit parameters. In Section 1.2.2 we described the basic principles of the transit method

of exoplanet detection wherein we look for periodic dips in a photometric time series from a star corresponding to the planet crossing in front of and occluding a portion of the star's flux. Generally, five parameters constrain a system with a transiting planet: Stellar mass M_*, stellar radius R_*, planet radius R_P, semi-major axis a and orbital inclination i.

In order to describe planetary transits it helps to defined the distance in the $X-Y$ plane between the star and planet. Combining equations (1.19), (1.36), and (1.35), this distance is written as

$$d = \sqrt{X^2 + Y^2} = \sqrt{r^2 \cos^2(\nu + \omega_\star) + r^2 \sin^2(\nu + \omega_\star) \cos^2 i}. \tag{1.38}$$

Note that d depends on the true anomaly $\nu(t)$, which in turn is a function of time according to Eqs. (1.25), (1.26), and (1.27). Following Eastman et al. (2013), the projected distance δ is defined using the argument of periastron of the star $\omega_\star$ instead of the argument of periastron of the planet ω_p. Following the definition of r given in Eq. (1.19), we can now define the scaled projected distance as the ratio of the distance d and the stellar radius $R_\star$, as

$$\delta = \frac{a}{R_\star} \frac{1 - e^2}{1 + e \cos \nu} \sqrt{1 - \sin^2(\nu + \omega_\star) \sin^2 i}. \tag{1.39}$$

If we define

$$r_{\rm p} \equiv \frac{R_{\rm p}}{R_\star}, \tag{1.40}$$

as the planet-to-star radius ratio, from equation (1.39), the transit of an exoplanet occurs only when $\delta < 1 + r_{\rm p}$ and $\sin(\nu + \omega_\star) > 0$ (star behind the planet). On the other hand, the planet's occultation (or secondary eclipse) occurs if $\delta < 1 + r_{\rm p}$ and $\sin(\nu + \omega_\star) < 0$ (planet behind the star).

Assuming a circular orbit, the probability of a transit happening is proportional to the ratio of the area of the planet's transit path to the total area of the sky

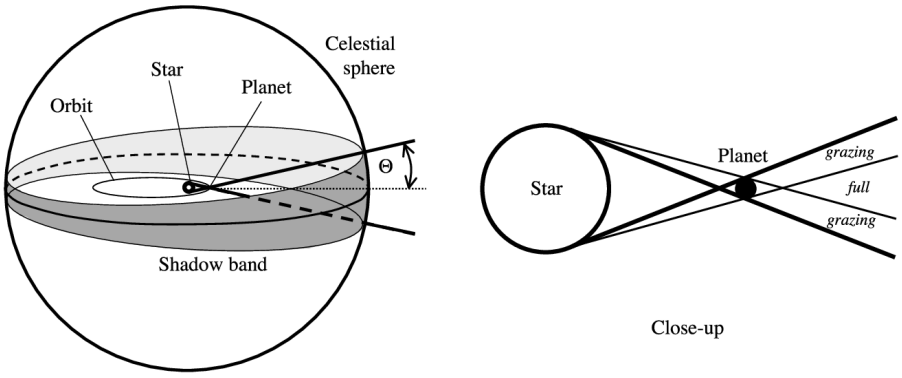


Figure 1.14: The dark shadow corresponds to the portion of the celestial sphere where a full transit is visible, while the lightly shaded area corresponds to grazing transits. From Winn et al. (2003).

that the planet can cross in its orbit, as seen in Figure 1.14. The probability of a planet transiting can be therefore be expressed approximately as

$$p \simeq \frac{R_\star + r_\mathrm{p}}{a \cos i} \simeq 0.005 \frac{R_\star}{R_\odot} \frac{1\mathrm{AU}}{a} \tag{1.41}$$

For the case that $r_\mathrm{p} \ll R_\star$.

In order to analytically describe how the total flux $F(t)$ changes as a function of time due to the presence of a transiting planet, we need to account for the disc-integrated stellar flux $F_\star(t)$, the planet flux $F_\mathrm{p}(t)$ (both, reflected light and thermal emission), and the loss of light when transits/occulations occur $\lambda(\delta, r_\mathrm{p})$. The total flux $F(t)$ is given by

$$F(t) = F_\star(t) + F_\mathrm{p}(t) - \lambda(\delta, r_\mathrm{p}). \tag{1.42}$$

We will assume that the stellar flux $F_\star(t)$ is constant and equal to 1, and that any variation can be expressed as a fraction of the stellar light. We also assume that the planet contribution to the light curve is negligible ($F_\mathrm{p} = 0$), i.e., we assume that occulations and phase curve have no effect on the observed light curve. Under these assumptions, Eq. (1.42) can be re-written as

$$F(t) = 1 - \lambda(\delta, r_\mathrm{p}). \tag{1.43}$$

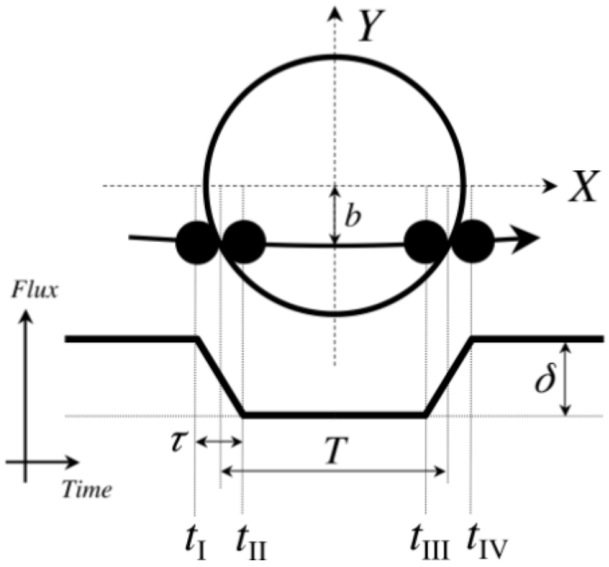


Figure 1.15: The flux at the ingress, full occultation, and egress of a transit, from Winn (2014)

By definition $\lambda = 0$ when $\delta > 1 + r_p$. For cases where $\delta < 1 + r_p$, the change of light depends on the analytical form of λ, which accounts for the loss of light as the planet crosses the stellar disc. There are different approaches to define the analytical form of $\lambda(\delta, r_p)$. To start, we can treat the star as an uniform source of light where the stellar flux is described by a constant function $I = I_0$. The transit λ can then be modelled as in Mandel & Agol (2002) as

$$\lambda(\delta, r_p) = \begin{cases} 0 & : \delta > 1 + r_p \\ \frac{1}{\pi}\left[r_p^2\kappa_0 + \kappa_1 - \sqrt{\frac{4\delta^2 - \left(1+\delta^2-r_p^2\right)^2}{4}}\right] & : 1 - r_p < \delta < 1 + r_p \\ r_p^2 & : \delta < 1 - r_p \end{cases} , \quad (1.44)$$

where $\kappa_0 = \cos^{-1}\left[(r_p^2 + \delta^2 - 1)/(2r_p\delta)\right]$ and $\kappa_1 = \cos^{-1}\left[(1 - r_p^2 + \delta^2)/(2\delta)\right]$. By examining Eq. (1.44) we can see several features of the transit. First, in order to change the flux, the planet must occult the stellar disc ($\delta < 1 + r_p$). During the transit ingress and egress ($1 - r_p < \delta < 1 + r_p$), the light decreases and increases continuously. Finally, in the fraction of the transit where the entire planet is occulting the star ($\delta < 1 - r_p$), the change in flux is constant and equal to the planet-to-star area ratio, $r_p^2 = (R_p/R_\star)^2$.

Figure 1.15 shows the stellar flux for different values of $r_{\rm p}$ as function of δ. For non-grazing transits where $r_{\rm p} \ll R_\star$, a, the impact parameter b can be approximated through

$$b^2 = \frac{\left(1-\sqrt{\delta}\right)^2 - \left(\tau_{\rm full}/\tau_{\rm tot}\right)^2 \left(1+\sqrt{\delta}\right)^2}{1-\left(\tau_{\rm full}/\tau_{\rm tot}\right)^2} \tag{1.45}$$

Where τ is the time of ingress and egress, $\tau_{\rm full}$ is the time that the entire planet is occulting the star, and $\tau_{\rm tot}$ is the total time including the full eclipse plus ingress and egress. In turn b is related to inclination, i through

$$b = \frac{a}{R_\star}\cos i \tag{1.46}$$

1.5.1 Quadratic limb darkening model

The neat linear appearance of each section of the transit curve so far has assumed that stars are uniform sources of light. However, this is decidedly not the case: several principals govern the specific shape of transits, and one of major features is a stellar effect known as *limb darkening*, where variations in temperature and opacity across a star make them look brighter in the centre and fainter at the edge (the limb) (Mandel & Agol, 2002; Giménez, 2006). This causes the intensity to vary, even when the planet has fully passed in front of the stellar disk. It also means a larger total decrease in flux is observed when the planet transits close to the centre of the star rather than near the edge.

To account for the effects of limb darkening, the intensity of the stellar disc I can be parameterised by laws $I = I(\mu)$ which depend on $\mu = \cos\theta$, where θ is the angle between the line of sight and the normal to a given point of the stellar surface. Some of the most widely used limb darkening laws in exoplanet transit light-curve fitting are given by linear, logarithmic or exponential equations (Heyrovsky, 2007). These are attempts to capture the specific stellar intensity using a small number of parameters, typically two limb darkening coefficients. We will likewise adopt two coefficients and implement light curve functions that use a quadratic limb darkening

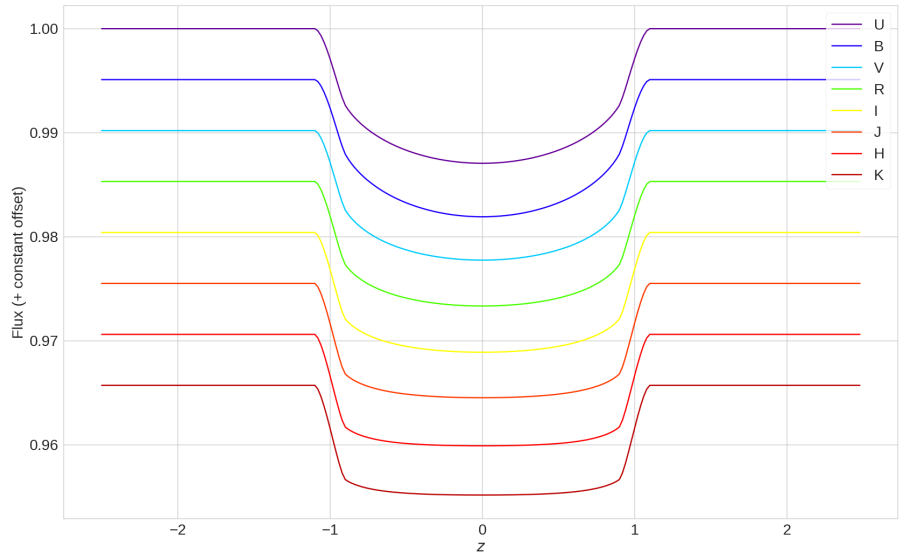


Figure 1.16: Theoretical light curves of a Sun-like star transited by a planet 10% its size. Different colours show a different Johnson-Cousins' filter.

model as described by Mandel & Agol (2002), wherein the flux in the stellar disc can be parameterised as a quadratic function in terms of μ as

$$I = 1 - u_1(1-\mu) - u_2(1-\mu)^2, \tag{1.47}$$

where u_1 and u_2 are limb darkening coefficients constrained to $u_1 + u_2 < 1$. These coefficients depend on the stellar type and wavelength. Following this approach, the light curve function has the form

$$F = F(\delta, r_\mathrm{p}, u_1, u_2), \tag{1.48}$$

for a given wavelength bandpass. The parameters r_p, u_1 and u_2 are different for different bandpasses.

Figure 1.16 shows synthetic transit light curves at different wavelengths for a Jupiter-size planet passing in front of a Sun-like star. The adopted bandpass correspond to those of the U, B, V, R, U, J, H, and K Johnson-Cousins filters with limb darkening coefficients for each bandpass are extracted from Claret & Bloemen (2011). It is possible to see how the effects of limb darkening are significantly stronger at shorter wavelengths (Claret & Bloemen, 2011).

This addition to light curves of limb darkening is still a simplification: the granular nature of stars, features such as spots and plagues, and various activity cycles add components to the in and out of transit light curves. Some of these features and their corrections will be discussed in greater detail later on.

In this thesis, lightcurves are modeled using BATMAN (Kriedberg, 2015). This PYTHON package incorporates the equations of planetary transits presented above and calculates the fraction of stellar flux blocked by a transiting planet. It integrates the intensity and overlap in area as a function of separation between the stellar and planetary centers, adjusting the step size near the limbs, since typical stellar intensity profiles have larger gradients near the limb of the star than at the center (Claret, 2000). BATMAN enables the calculation uniform, linear, quadratic, square-root, logarithmic, exponential, and four-parameter nonlinear stellar intensity profiles, and in this thesis, quadratic limb darkening is adopted.

Integration can be tuned to match accuracy needs, with greater integration steps resulting in better area but slowing down the processing time. Accurate transit light curve calculation is essential for modeling the high precision timing measurements a carried out in this work and BATMAN light curves can be calculated with accuracy better than 0.001 ppm transit observations. Further details of implementation will be discussed in the relevant sections of the thesis.

1.5.2 Stellar Parameter Determination

An important limiting factor in obtaining accurate measurements of any of the planetary parameters explored above is the the quality of the host star properties. The Kepler Input Catalog (KIC; Brown et al. (2011)) provided the first homogeneous catalog of properties of Kepler field stars derived through photometry constraints, providing stellar effective temperatures and radii good to about 200 K and 30-40% radius uncertainty. These parameters limit the precision of planet size and incident stellar flux measurements, obscuring important features. Any fine details in the radius distribution of planets are blurred out by the uncertainties associated with photometric stellar radii.

A more accurate approach is a spectroscopic one. In this approach, theoretical models of stellar structure and evolution are used to compile grids of stellar properties ($R_\star$, $T_{\rm eff}$, etc.) as functions of $M_\star$, [Fe/H], and age. A set of models at constant metallicity and age is commonly called an "isochrone." Thus, the measured spectroscopic properties of $T_{\rm eff}$, log$g$, and [Fe/H] can be converted into $M_\star$, $R_\star$, and age by fitting against such isochrones. For example, Petigura et al. (2017) and Johnson et al. (2017) combined spectroscopic constraints with stellar interior modeling to estimate stellar radii to within 11% for 1305 Kepler Objects of Interest hosting 2025 planet candidates observed as part of the California-Kepler Survey. These approaches are still widely employed and comprise a significant fraction of the stellar parameters employed in exoplanetary study.

A further method for making even more accurate determinations of stellar properties is asteroseismology, the study of stellar oscillations, which are dependant on a star's internal structure and are thus able to determine the mass and radius (see, e.g., Brown & Gilliland (1994), Christensen-Dalsgaard et al. (2010), Gilliland et al. (2010)). The Kepler mission's influx of photometric data made it possible to obtain significantly more accurate stellar parameters for a larger population of planets (Huber et al., 2013; Aguirre et al., 2015; Lundkvist et al., 2016), determining typical uncertainties on radius of ∼3-4% and on mass of ∼7-11%. Continued constraining asteroseismological measurements will be taken in the coming decade with PLATO (Planetary Transits and Oscillations of Stars), a mission proposed to launch in 2026, which will follow in the footsteps of Kepler and TESS, by observing a large sample of stars with high precision photometry over an extended period of time, searching up to 1,000,000 stars (Rauer et al., 2014).

Beyond asteroseismology, Gaia parallaxes have proved instrumental for refining stellar properties and will continue to do so (Johnson et al., 2017; Gaia Collaboration et al., 2023). With accurate distances combined with frequent photometry, each new Gaia data release updates an extensive catalogue of uniformly inferred stellar parameters (Fouesneau et al., 2023). Further, with hundreds of millions of stellar measurements being accurate enough to derive high-quality colour-magnitude

diagrams we can continue to fine tune stellar models to feed back into photometric and spectroscopic approaches.

1.6 TTV Equations

Up to this point, we have discussed gravitationally bound systems consisting of two bodies and the transits that arise when these bodies cross in front of a star along a line of sight. When a third or n^{th} body is introduced, gravitational perturbations occur in an interaction that leads to periodic changes in the timing of the transits of both planets. While mentioned as a method of detection in Section 1.2, TTVs can be used as a tool for confirming and characterizing exoplanets, identifying additional unseen planets in a system of known transiting planets, and studying the dynamical stability of planetary systems. However, the first TTVs to be discovered appeared not in exoplanetary systems but but in our own solar system: the orbits of Jupiter and Saturn challenged early astronomers and in the form of "The Great Inequality", a disobedience of the careful records of Tycho Brahe to the emerging Newtonian and Keplerian physical understanding of orbits (Wilson, 1985). The perturbation theory of Laplace led to a solution in 1985 in the form of a phenomenon that would later be given the name Transit Timing Variations.

While the nonlinear dynamics of perturbations give rise to complicated equations whose solutions must be arrived at analytically, we can start to understand the mathematical basis of TTVs following Agol & Fabrycky (2018) by writing Kepler's equations above in the form of a potential as

$$\phi = \frac{-GM}{r} \tag{1.49}$$

Where M is a reduced mass of $M = M_\star + m_\mathrm{p}$ and $\mu \equiv M_\star m_\mathrm{p}/M$. With this notation, Newton's force law can be written as

$$\mathbf{F} = \mu\ddot{\mathbf{r}} = \frac{-G\mu M_\star}{r^2}\hat{\mathbf{r}} \tag{1.50}$$

In a three body problem, however, we can start by adding a term corresponding to the force of a second planet on the first, so that Eq. 1.50 becomes

$$\mathbf{F}_1 = \frac{-G\mu_1 M_\star}{r_1^2}\,\hat{\mathbf{r}}_1 + \mathbf{F}_{12} \tag{1.51}$$

where we have the addition of a force $\mathbf{F}_{12}$ of planet 2 on planet 1. This force is in turn made up of two terms, the direct gravitational acceleration on planet 1 due to planet 2, and a second term which accounts for the gravitational effect of planet 2 on the star, and can therefore be modeled as acceleration of the reference frame of planet 1 when the star is fixed at zero, which acts as an acceleration on planet 1 in the opposite direction. These are written as

$$\mathbf{F}_{12} = \mu_1 \ddot{\mathbf{r}}_1 = G\mu_1 m_2 |r_2 - r_1|^{-3} (\mathbf{r}_2 - \mathbf{r}_1) - G\mu_1 m_2 r_2^{-2} \hat{\mathbf{r}}_2 \tag{1.52}$$

The detection of such an extra force and constraining its solution is a trickier task. Orbital transit times are usually expressed in a table called an ephemeris that is a linear function of time, or epoch number, E as defined by

$$C = T_0 + P \tag{1.53}$$

where T_0 is the time of the 0^{th} transit and P is the constant orbital period. The C stands for "calculated" while we designate O for the actual observed transit times. This gives us a commonly used designation of $O - C$ to examine and characterise residuals to the average linear ephemeris (Sterken, 2005). An example of a system with significant $O - C$ residuals to a linear ephemeris is shown in Figure 1.17. This figure also portrays one common way TTVs manifest in observational data, appearing as approximately sinusoidal residuals to a linear ephemeris of transit times, wherein a planet will arrive slightly earlier and then slightly later than its average transit time. Where there are two transiting planets, these sinusoidal trends will be anti-correlated, so that as one planet arrives earlier, the other arrives later. This can be further appreciated for two planets in Figure 1.18.

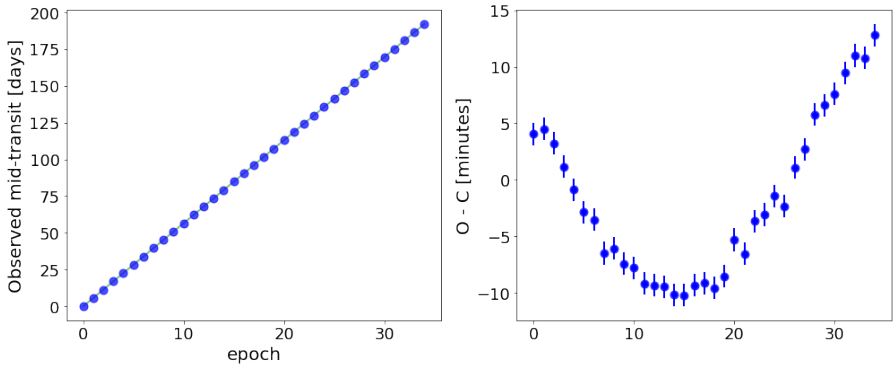


Figure 1.17: An example of timing data (simulated), where the left panel shows possible observed transit midtimes of an exoplanet, to which a line is fit by least squares. The right panel shows the residuals of that fit, which is the conventional $O-C$ diagram

To arrive at the specific timing offset for each planet, we write the $O-C$ formulae as

$$\delta t_1 = P_1 \frac{m_2}{m_0} f_{12}\left(\alpha_{12}, \theta_{12}\right), \delta t_2 = P_2 \frac{m_1}{m_0} f_{21}\left(\alpha_{12}, \theta_{21}\right), \tag{1.54}$$

Where m_0, m_1, and m_2 are the masses of the star and each of the planets respectively, f_{ij} refers to the perturbations of planet j on planet i, which is a function of semimajor axis ratio $\alpha_{ij} = min\left(a_i/a_j, a_j/a_i\right)$ and angular orbital elements $\theta_{ij} = (\lambda_i, e_i, \omega_i, I_i, \Omega_i, \lambda_j, e_j, \omega_j, I_j, \Omega_j)$. These functions can be evaluated analytically through perturbation theory (Nesvorný & Morbidelli, 2008; Nesvorný, 2009; Nesvorný & Beaugé, 2010; Agol & Deck, 2016; Deck & Agol, 2016). Because of Newton's second law, the mass of the planet being perturbed does not enter into the lowest order timing offsets.

The term TTV was coined by Agol et al. (2005), who also investigated the effect of mean motion resonance (MMR), in which the orbital periods of gravitationally interacting planets are close to small integer ratios of one another, on the presence and amplitude of TTVs. The amplitude in such a case can be computed through energy trades (see Agol et al. 2005; Holman et al. 2010). Following Kepler's relation of $a \propto P^{3/2}$, which gives

$$\delta a = (3/2)\, a_1 \delta P_1 / P_1 \tag{1.55}$$

and by differentiating the orbital energy equation as follows we get

$$E_1 = \frac{-GMm_1}{2a_1} \tag{1.56}$$

$$\delta E_1 = \frac{GMm_1}{2a_1^2}\delta a_1 = \delta E_2 = \frac{GMm_2}{2a_2^2}\delta a_2 \tag{1.57}$$

where we have set $\delta E_1 = \delta E_2$ due to energy conservation. Using Eq 1.55 and Kepler's Second Law, this leads to

$$\delta P_2 = -\delta P_1 \frac{m_1}{m_2}\left(\frac{P_2}{P_1}\right)^{5/3} \tag{1.58}$$

Because there is a factor of P_2/P_1 more epochs for the inner planet than for the outer planet in the same amount of time, the timing offset builds up by an extra factor of this ratio for the inner planet. Therefore Eq 1.59 becomes

$$\delta t_2 = -\delta t_1 \frac{m_1}{m_2}\left(\frac{P_2}{P_1}\right)^{2/3} \tag{1.59}$$

Analytic work has been done in resonant (Nesvorný & Vokrouhlický, 2016) and near-resonant cases (Lithwick et al., 2012; Hadden & Lithwick, 2016) to confirm the scaling and anticorrelation of the two TTV curves. This proximity to and perturbation from resonance results in small shift in eccentricity and semi-major axis and gives rise to the majority of observed TTVs. In these cases, $O-C$ residuals cycle through in a periodic quasi-sinusoidal manner of early than average and later than average over a number of epochs called the "superperiod"

$$P_{\mathrm{TTV}} = \left|\frac{j}{P_{\mathrm{inner}}} - \frac{k}{P_{\mathrm{outer}}}\right|^{-1} \tag{1.60}$$

where j and k are small integers defining the resonance $j:k$ of outer to inner orbital periods. Observationally, this superperiod can be perceived as a full sinusoidal cycle through earlier and later transits before the pattern repeats. For example, in Figure 1.18, the two planets cycle through two and a half TTV super-periods.

The amplitude of TTVs is correlated to the planetary eccentricities to the power of the one minus the order of resonance. So first-order resonance results in TTVs even in non-eccentric systems, while higher order resonances only produce

observable TTVs in cases of higher eccentricity. While the amplitude dependence on proximity to mean motion resonance makes it more likely for TTVs to be detected in these systems as opposed to non-resonant systems, planets are rarely if ever in perfect MMR. These configurations result in dynamical chaos and are therefore unlikely to be found (Holman & Murray, 2005)

Non-resonant systems can give rise to TTVs as well. In systems where there is a very large planet orbiting close to the star, shifts to the barycentre cause the outer planet to arrive either early or late to its moving target. Although this effect hasn't yet been observed in multi-planet systems, it has been seen in the case of circumbinary planets (Doyle et al., 2011). Another less common effect that gives rise to TTVs, is when a larger outer companion tidally influences its inner companion, either slowing it down if the two are coplanar, or speeding it up if they are significantly mutually inclined (Borkovits, T. et al., 2003; Agol et al., 2005; Dawson et al., 2014). Non-periodic long-term trends can also indicate other effects such as orbital evolution from disk friction or tidal orbital decay (Christ et al., 2019; Birkby et al., 2014; Patra et al., 2017). However, periodic TTVs due to the gravitational perturbations of planetary companions will largely be the focus of this thesis.

1.6.1 Chopping

While there is a degeneracy between planetary mass ratios and eccentricity in TTV analysis, this degeneracy can sometimes be broken by the presence of a "chopping" signal. This short-term variation on top of a more sinusoidal trend arises from the variation of the synodic period of two interacting planets, that is, the time it takes for them to line up in their orbits in conjugation. This synodic period is equal to $P_{syn} = (1/P_1 - 1/P_2)^{-1}$. Because these alignments do not occur coherently, the TTVs they produce are smaller in amplitude than the primary TTV signal. However, in the case of low eccentricity and high mass difference, these effects can appear like "zig-zags" on top of a smooth periodic trend (see Figure 1.18) and can help break degeneracies Nesvorný & Vokrouhlický (2016); Schmitt et al. (2014).

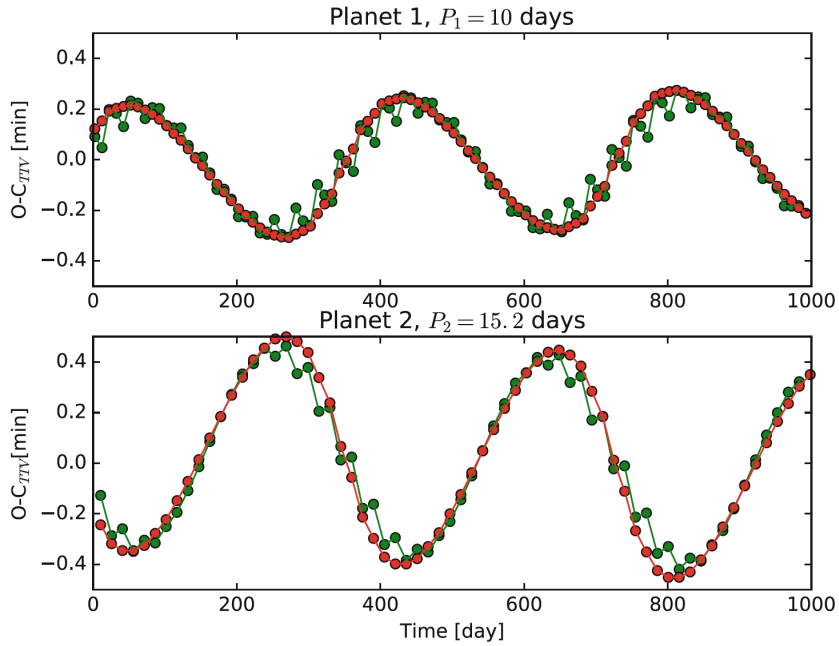


Figure 1.18: Shown are simulated data for two and a half superperiods of a system near 2:3 MMR. Green points show $O - C$ TTVs of two low-eccentricity planets with larger mass ratios, compared with red points showing two higher eccentricity planets with smaller mass ratios. Zig-zag "chopping" is apparent in the high-mass/low-eccentricity case while less apparent in the low-mass/high-eccentricity case. From Agol & Fabrycky (2018)

1.6.2 Transit Duration Variations

Transit duration variations (TDVs) are similarly the effects of dynamical orbital evolution, that like TTVs are caused by anything that changes a, e, ω as well as i, and in some cases can be seen to "mimic" the effects of TTVs (Boley et al., 2020). When the inclination changes, it is known as "orbital plane reorientation". In essence it causes the planet to pass across a smaller or larger fraction of the stellar disk and trace a shorter or longer chord, which changes the amount of time an occlusion lasts.

Three major mechanisms causes TDVs

1. Stellar Tides: Tidal forces from the host star can affect the orientation of an exoplanet's orbit (Szabó et al., 2012; Barnes et al., 2013). These forces arise due to the gravitational torque of the oblate star on the planet. They are also a controversial explanation for transit shape anomalies (Barnes et al., 2013).

2. Kozai-Lidov Mechanism: The Kozai-Lidov mechanism is a gravitational effect

that can cause significant changes in the inclination and eccentricity of an exoplanet's orbit (Shevchenko, 2017). It occurs when a planet is perturbed by a companion planet or star leading to large oscillations in the orbital inclination, resulting in the reorientation of the orbital plane (Almenara et al., 2015; Mills & Fabrycky, 2017).

3. Star-Planet Interactions: Magnetic interactions between a planet and its host star can also influence the orientation of the planet's orbit (Spalding & Batygin, 2015). These interactions can cause the planet's orbit to precess over time, leading to changes in the orbital plane. The strength of these interactions depends on the magnetic properties of both the planet and the star.

While the effects of TDVs are often subtle and typically occur on longer timescales than the TTVs arising from near-resonant interactions (Boley et al., 2020), it is important to consider TDVs when performing planetary fits and extracting mid-transit times.

1.6.3 Discoveries

The first system to show proper TTVs arising from orbital resonance was the Kepler-9 system, which contains two Saturn-sized planets and displays TTVs of 4 and 39 minutes respectively (Holman et al., 2010). This heralded a wave of TTV detections in the Kepler multi-planet systems, notably in Kepler-36 (Carter et al., 2012), Kepler-62 (Borucki et al., 2013), and Kepler-223 (Mills et al., 2016a) a system with four exoplanets in a resonant chain. Of these, one of the best characterised is Kepler-36, where precise measurement of transit times, as well as a stellar density from asteroseismic variability have enabled precise mass measurements of less than 8%. The periodic anticorrelated TTVs of this system can be easily appreciated in the form of a river plot, as shown in Figure 1.19, which is a common way to view some of the more obvious trends. These systems and others joined a catalogue of

Table 1.1: Stellar, planetary and orbital parameters and their symbolic designations

	Symbol	Name	Source
		magnitude	
Stellar	$R_\star$	radius	evolutionary models
	$M_\star$	mass	radial velocity, asteroseismology
	log {\it g$_\star$}	surface gravity	asteroseismology
	$T_{\rm eff}$	temperature	spectroscopy
	l_1, l_2; u$_1$ and u$_2$	limb-darkening coefficients	transit light curve
Planetary			
	$R_p/R_\star$	radius	transit light curve
	$M_p \sin i$,M_p	mass	RV, TTV
	$T_{\rm eq}$	equilibrium temperature	transit spectroscopy, occulation photometry
	ρ_p	density	derived
Orbital			
	T_0	time of conjugation	transit light curve
	P	period	transit light curve, RV, TTV
	a	semi-major axis	transit light curve, microlensing, direct imaging
	e	eccentricity	transit light curve, TTV
	b	inclination	transit light curve
	b	impact parameter	transit light curve
	ν	true anomoly	RV, TTV
	μ	mean anomoly	RV, TTV
	ϵ	eccentric anomoly	RV, TTV
	ω	argument of periastron	RV, TTV
	Ω	longitude of ascending node	RV, TTV
	$\varpi = \omega$-Ω	longitude of periastron	RV, TTV
	$\theta = \nu$ - ϖ	true longitude	RV, TTV
	λ	mean longitude	TTV

Kepler systems showing TTVs being developed by Mazeh et al. (2013) and follow-up analysis was performed (Holczer et al., 2016).

When combined with RV measurements, TTVs can provide the absolute dimensions of a system Agol et al. (2005); Montet & Johnson (2012). The first system to be characterized by both methods was the three-planet Kepler-18 system, where TTVs were used to confirm the masses obtained by RV analysis and be validated as a method for finding mass (Cochran et al., 2011).

TTVs have also been used to confirm the presence of non-transiting companions

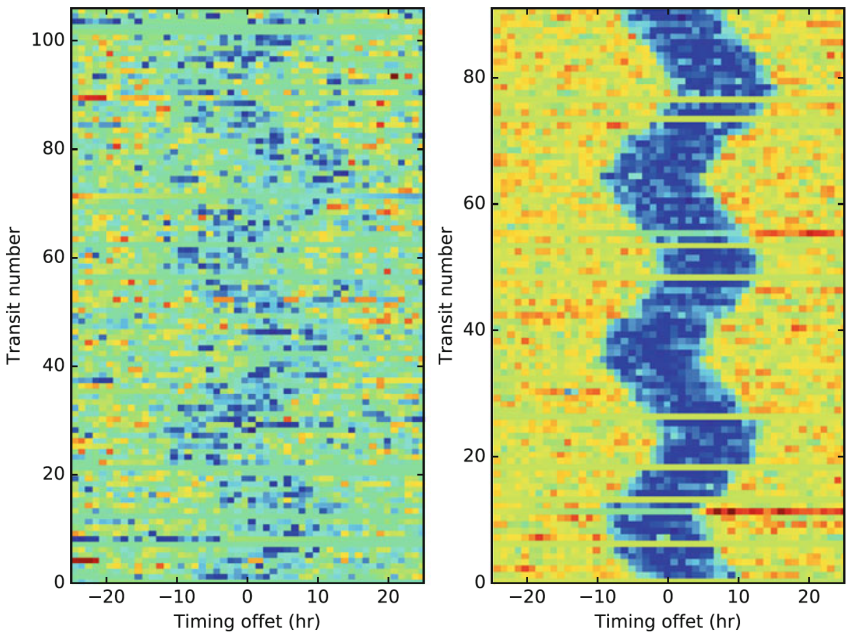


Figure 1.19: A River Plot showing 17 quarters of long-cadence Kepler data for Kepler-36 b and c, two planets displaying anticorrelated sinusoidal TTVs. It can be seen that planet b (on the left) is smaller and less massive than planet c, and thus has shallower transits more dominated by noise. As the smaller planet, the amplitude of its TTVs are correspondingly larger, since these are dependant on the mass of its companion. Altogether this riverplot represents several TTV superperiods, in which the planets make complete cycles through transiting earlier and then later than their average ephemerides.From Carter et al. (2012)

(Meschiari et al., 2009; Nesvorný & Vokrouhlický, 2014). The first of these was Kepler-19, for which Ballard et al. (2011) were able to tell that an unseen planetary companion was the only sensible cause of the TTV, and formed a limited set of planetary and orbital possibilities for this companion, but they were not able to break the degeneracy on specific parameters. Another famous example of this is Kepler 46c, a non-transiting Saturn-mass planet which was inferred from TTV analysis of its Jupiter-sized inner companion, and which is expected to transit in several decades when its orbit has precessed (Saad-Olivera et al., 2017). Since then, several non-transiting planets have been discovered through TTVs (Nesvorný et al., 2012). In the case where TTVs are not detected, or are small, they can still be used to place limits on the presence or absence of companions (Steffen & Agol, 2005; Steffen et al., 2012).

Beyond Kepler, the TRAPPIST-1 system mentioned previously, with its seven

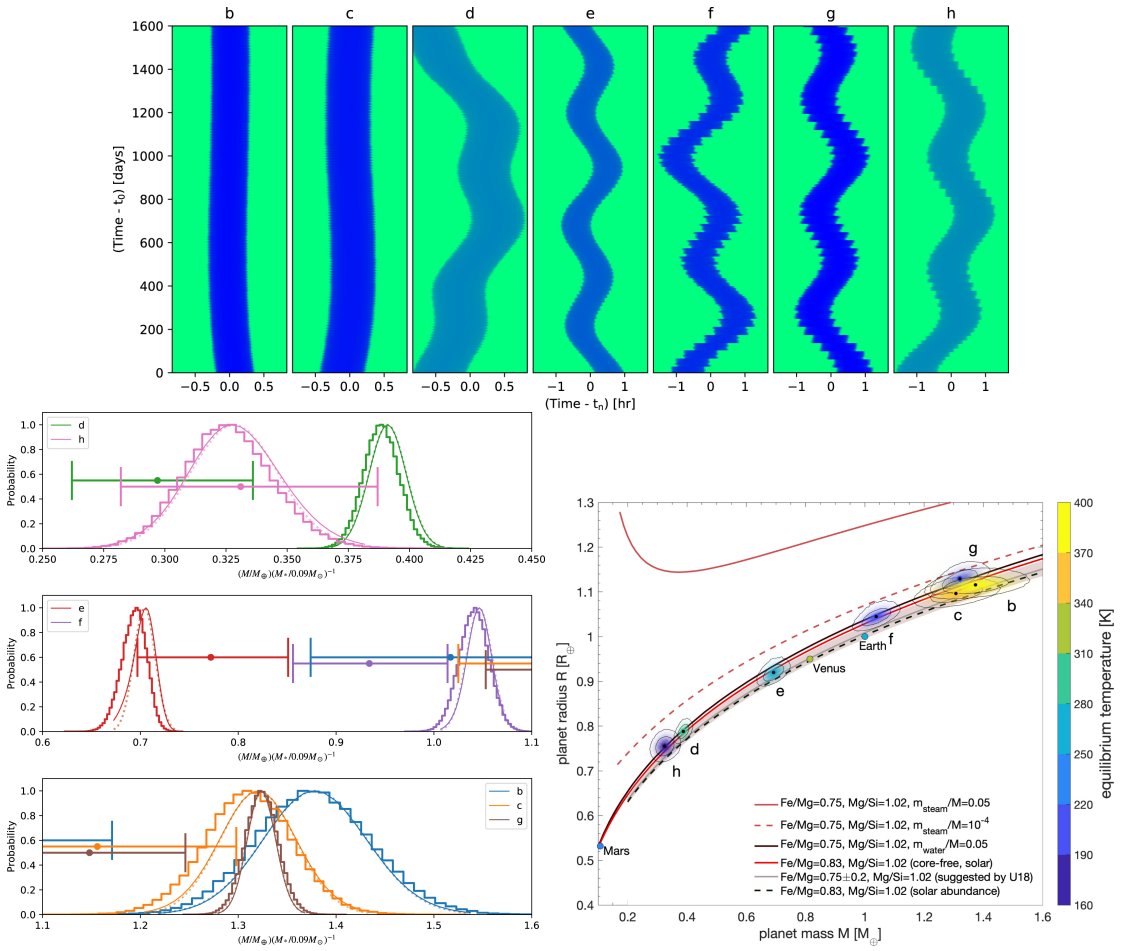


Figure 1.20: Figures from Agol et al. (2021), which used TTVs to derive masses for the 7 TRAPPIST-1 planets. The top plot (Agol Figure 7) gives the model river plot showing every transit over 1600 days for each planet. The bottom left plot (Agol Figure 6) gives the resulting probability distribution of the planet-to-star mass ratios from TTV fits, relative to previous mass estimates from RV data alone. The bottom right plot (Agol Figure 12) gives the resulting mass-radius relations from TTV and photodynamic analysis, colored by the equilibrium temperature. All in all, this study achieved a tremendous amount of mass precision and resulting insight into the planetary composition that was not possible with RV data alone.

Earth-sized planets, some in its M-dwarf host star's habitable zone, has garnered significant attention in recent years (Gillon et al., 2017; Grimm, Simon L. et al., 2018). TTV studies of the TRAPPIST-1 planets have revealed complex dynamical interactions, including resonant chain configurations (Agol et al., 2021; Bolmont et al., 2020). As can be seen in Figure 1.20, the analysis of Agol et al. (2021) of four years of precise transit timings has enabled mass measurements with TTVs two orders of magnitude more precise than current RV capabilities.

Compared to Kepler, TESS observes specific regions of the sky for shorter durations compared to Kepler, typically around 27 days. This shorter time span makes it more challenging to detect TTVs, especially for planets with longer orbital periods or for which the TTV signal is small. However, several 10s of systems have revealed TTVs in TESS data (Kane et al., 2019; Dawson et al., 2019), and as TESS enters its fifth year, and reobserves previous parts of the sky, the potential for TTV analysis of TESS systems continues to expand. Several cases of the utility of TESS for TTV followup are the topic of this thesis.

1.7 Atmosphere, composition and evolution

One of the most compelling reasons to obtain mass measurements for these planets is to enable studies into their bulk composition and formation. Follow-up spectroscopy can then reveal molecular abundances (Brown, 2001; Griffith, 2014; Deming et al., 2015), temperature profiles (Tinetti et al., 2007; Line & Parmentier, 2016), pressure gradients (Haynes, 2015), and cloud formation (Demory et al., 2013; Kreidberg et al., 2014a) within exoplanet atmospheres. These factors influence the overall structure and dynamics of the atmosphere, affecting its thermal properties and circulation patterns. By studying these atmospheric properties, we can gain insights into the climate, energy balance, and potential habitability of exoplanets.

Critically, with the starting point of mass and density, we can arrive at a planet's atmospheric scale height, $s = kT/mg$, where k is Boltzmann's Constant ($1.38x10^{-23}$ J/deg), T is the equilibrium temperature, m is the planetary mass, and g is the surface gravity. This quantity sets the strength of the molecular features in a planet's spectra (Batalha et al., 2018; Griffith, 2014).

If we have transit photometry and RV or TTV measurements, we are able to extract a full nine key parameters, namely, T_0 (or T_p), m_p, P, e, $\omega_\star$ (or ω), $r_\mathrm{p} = R_\mathrm{p}/R_\star$, $a/R_\star$, i and K. From these, among other things, we now easily get the planetary density as

$$\rho_{\rm p} = \frac{3m_{\rm p}}{4\pi R_{\rm p}^3} \tag{1.61}$$

As well as the planetary surface gravity

$$g_{\rm p} = \frac{{\rm G}m_{\rm p}}{R_{\rm p}^2}, \tag{1.62}$$

where $m_{\rm p}$ and $R_{\rm p}$ are the planet mass and radius, respectively, calculated assuming a given set of stellar parameters.

Uncovering and refining both the mass and radius and thereby arriving at a planetary density can give us valuable insights into the planet's composition and internal structure. This can be done by comparing the position of the planet on a mass-radius diagram with composition models (Kopparapu et al., 2014). For example, the inner Neptune-sized planet of Kepler-36, whose mass was arrived at through TTV analysis shows a density consistent with a rocky scaled-up version of Earth, while the outer planet (also Neptune-sized) requires a significant H/He envelope to explain its size (Carter et al., 2012).

Obtaining accurate masses and planetary compositions also gives us insight into models of evolution. In most evolutionary models, planets form from protoplanetary disks through a process known as *core accretion*, in which growing planetesimals gradually aggregate disk material in a young system (Mordasini et al., 2009). If some cores can acquire more mass than a critical value of several Earth masses during the persistence of the disk gas, they would be able to rapidly accrete gas and evolve into gas giant planets in a runaway process that is terminated when the residual gas is depleted either globally or locally in the form of a gap in the vicinity of their orbits (Baraffe et al., 2008). Since planets' masses are posited to grow rapidly from 10 to 100 $M_\oplus$, the gas giant planets rarely form with asymptotic masses in this intermediate range (Ida & Lin, 2004). This model proposed by Ida & Lin (2004) therefore predicts a paucity of extrasolar planets with mass in the range 10-100 $M_\oplus$ and semimajor axis less than 3 AU and suggests that a mass versus semimajor axes diagram can provide strong constraints on the dominant

formation processes of planets analogous to the implications of the color-magnitude diagram on the paths of stellar evolution.

On the other side of core-accretion is photoevaporation. Planets that orbit close to their host stars can receive incident high-energy irradiation in the first $\sim$100 Myr following formation that is an appreciable fraction of their gravitational binding energy (Lammer et al., 2003; Lecavelier Des Etangs, 2007). Thus planets with H/He-rich envelopes can be strongly evaporated by this irradiation (Yelle, 2004; Owen & Jackson, 2012). Combined, these effects should result in the radius valley discussed in Section 1.3.1 with a corresponding bifurcation of mass distribution into planets with either bare cores ($\sim 1.3\,R_\oplus$), or those with double the core's radius ($\sim 2.6\,R_\oplus$), observed in Kepler planets by Owen & Wu (2017). Further validation or challenges to these evolutionary models, and other effects such as planet-disk interactions (Kley & Nelson, 2012) will come from obtaining accurate planetary masses.

As discussed earlier, RV studies are the most common way to go about obtaining exoplanetary masses, but noise from instrumentation and stellar surface velocities from activity make it difficult to detect the signals of smaller planets (Zicher et al., 2022). Because TTVs can arise and be detected around a bright star with high precision and further because the gravitational effect of a small planet can be seen clearly in the deeper transits of its companion, TTVs enable us to probe and refine a smaller mass range than would be possible from RVs alone. This can be appreciated by Figure 1.21 which shows the population of exoplanets with known masses. Many of those with masses $< 10\,M_\oplus$ have had their masses measured or refined through TTVs.

Some studies have noted systematic discrepancies between TTV and RV analyses that find systematically lower masses for small planets ($<4\,M_\oplus$) through TTV analysis than through RV analysis (Weiss et al., 2013; Masuda et al., 2013). Malavolta et al. (2017) posited that such discrepancies could arise from other planets damping the observed effects. Mills & Mazeh (2017) show that these differences are present for planets with periods of greater than 11 days, while shorter period planets generally find good agreement. However, Borsato et al.

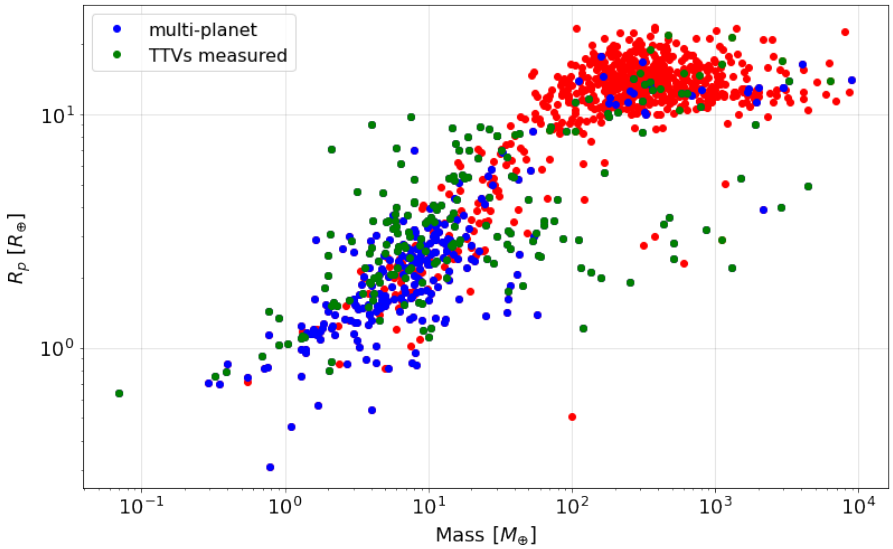


Figure 1.21: The distribution of discovered exoplanets as of June 2023 (Akeson et al., 2013)) with their masses and radii characterised. Red point represent single planet systems. Blue points represent known multi-planet systems. Green markers indicate that TTV measurements have been taken

(2019) suggests that with enough data points, TTV and RV approaches result in consistent masses, which they demonstrated to be the case for the Kepler-9 system, a two-planet near-resonant system with large TTVs. This thesis will explore a system in Chapter 2, TOI-270, in which both approaches are taken.

1.8 Summary and Outline of Thesis

Exoplanet astronomy has come a tremendous way in just a few decades. We've gone from early discoveries of zombie worlds orbiting to pulsars to radial velocity searches detecting flaming hot-Jupiters to large-scale transit searches unveiling thousands of new systems, a few systems of which host worlds perhaps not too dissimilar from our own. The coming decades will enable us to probe deeper into these systems revealing their companions, atmospheres, and histories.

Aiding in the mission to expand and better characterise this family of alien worlds, Transit Timing Variations form an increasingly interesting tool, especially as our baseline of transit monitoring increases through transit searches like TESS and the upcoming PLATO. By yielding valuable information about the masses, orbital

dynamics, and architectures of exoplanetary systems, TTVs have been instrumental in understanding the dynamical properties of multi-planet systems and exploring the complexities of planetary formation and evolution.

The rest of this thesis is centred on the application of TTVs to exoplanet characterisation and is structured as follows. Chapter 2 discusses TTVs in the TOI-270 system, a system of three planets in resonant orbits discovered by TESS and for which extensive ground-based follow-up has occurred. Chapter 3 presents a catalogue of systems discovered by Kepler and K2 that were re-observed with TESS. It presents updates to linear ephemerides as well as timing analysis of non-linear trends. Chapter 4 presents a dynamical analysis of selected systems of interest, including a return to TOI-270, as well as several Kepler and K2 systems discussed in Chapter 3. Appendix C discusses work on Kepler and TESS systems from earlier on in the DPhil. Chapter 5 concludes and provides a brief discussion of future transit searches and the role TTVs might play in the continuing search for other worlds.

Time is making fools of us again.

— Albus Dumbledore

CHAPTER 2

Transit Timing Variations in the 3-planet system TOI-270

Declaration: *The following chapter largely comprises the content of Kaye et al. (2022). As the first author on the paper, I received the raw light curves from collaborators and worked with them from that point on, performing all light curve fits, extracted transit times, assisted with the dynamical analysis, analysed the results and planetary profiles, and wrote the majority of the paper. Shreyas Vissapragada primarily ran the dynamical analysis with TTVFast and contributed to the writing of Section 2.4, and the Long-Term Stability Analysis was performed and its Section 2.4.2 was primarily written by Francisco Pozuelos and is expanded here.*

2.1 Introduction

Over the course of its two-year mission from 2018-2020, the Transiting Exoplanet Survey Satellite (*TESS*) was tasked with detecting small planets orbiting nearby bright stars so that detailed follow-up studies of their characteristics and atmospheres can be performed (Ricker et al., 2014). Among the *TESS* discoveries, systems containing multiple transiting planets are especially interesting, because they enable comparative planetology, enabling us to investigate the similarities and

differences in their geology, atmosphere, magnetic fields, and surface features. This helps in deciphering the underlying physical and chemical processes that guide planetary evolution.

Of the ∼30 multi-planet systems *TESS* has discovered so far, there are several that contain planets near mean-motion resonances and thus are expected to display TTVs. However, because *TESS* observes most target stars for relatively short time frames of about a month, these discoveries are relatively few, and to date, only 16 planets in 9 such systems have been reported (Demory et al., 2020; Kipping et al., 2019; Trifonov et al., 2021).

As discussed in Chapter 1, RV measurements form the bulk of higher-precision mass measurements for exoplanets, and are involved in confirmation of most planetary candidates. However, TTVs arising from dynamical interactions between planets, leading to deviations from their Keplerian orbits as predicted by Agol et al. (2005) and Holman & Murray (2005), can provide an alternate means for measuring exoplanetary masses and orbital parameters. In the uncommon case that these two approaches can be combined, they can be especially powerful. As was first demonstrated in the case of the Kepler-9 system in 2010 (Holman et al., 2010), TTVs can be sensitive to detecting, confirming and characterising planets. Since the discovery of TTVs in Kepler-9, TTVs have been found quite commonly in Kepler data, and several tens of systems with significant TTVs were predicted to be discovered in *TESS* light curves, as well (Kane et al., 2019; Dawson et al., 2019).

One such TESS system with exciting potential for precise mass characterization through TTV and RV analysis, is TOI- 270, a nearby, bright, M3V-type star with 3 confirmed transiting exoplanets discovered by Günther et al. (2020) (hereafter G20). The innermost planet, TOI- 270 b, is a 1.25 $R_\oplus$ super-Earth with a period of 3.36 days. The outer two planets are sub-Neptunes, with radii of 2.42 $R_\oplus$ and 2.13 $R_\oplus$ and periods of 5.66 days and 11.38 days (see Figure 2.1). TOI- 270 is one of the nearest and brightest M dwarf systems with transiting exoplanets, and is therefore a great candidate for follow-up atmospheric studies. G20 gives equilibrium temperatures of planets c and d of $424 \pm 20\,K$ and $340 \pm 14\,K$ respectively, making

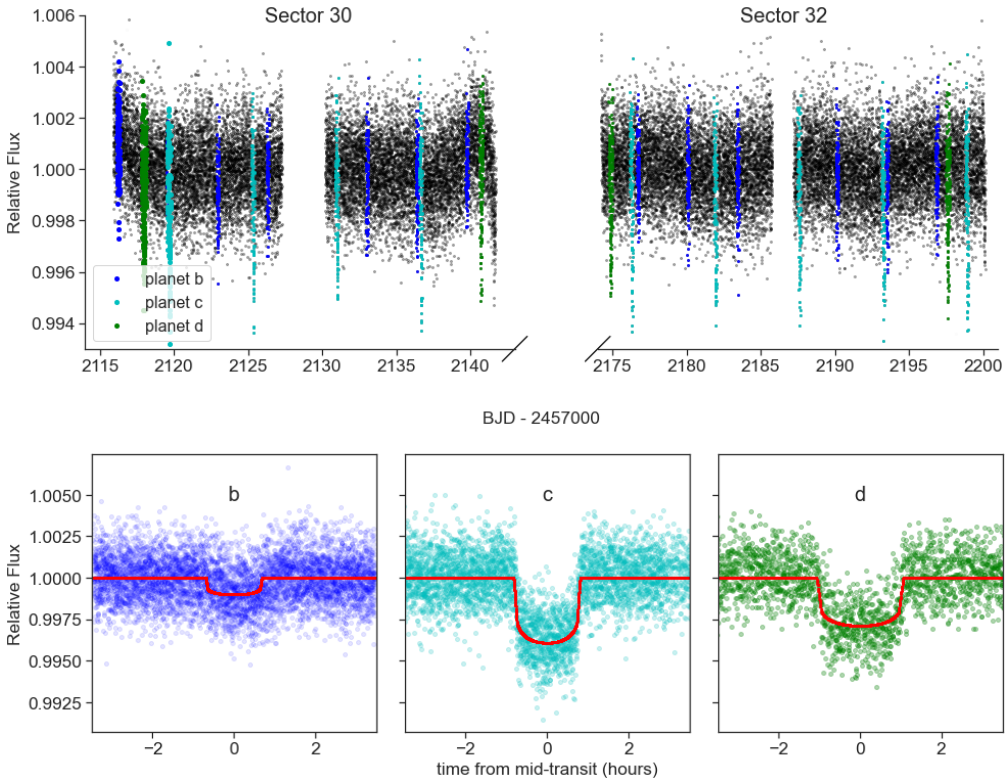


Figure 2.1: The top plot shows *TESS* sectors 30 and 32 in PDC-SAP flux, with transits highlighted for each planet. The bottom panels show phase folded transits for the respective planets, with the red showing the best-fit model.

them unique among planets of their size discovered in TESS and putting planet d within the survivable range of temperatures for extremophile organisms (Bolmont et al., 2015). Even though it might be itself a gaseous planet and therefor not host survivable oceans, or else be subject to runaway greenhouse or water loss, it could host rocky moons. G20 also noted that additional planetary companions beyond the orbit of TOI-270 d could fall within the terrestrial-like habitable zone, which for TOI-270 lies in the range of 0.10–0.28 AU (Kopparapu et al., 2014), without impacting the stability of the system.

The periods of planets d and c lie near the 2:1 mean motion resonance, and those of planets c and b near the 5:3 resonance. Consequently, the planets are expected to interact dynamically with each other, resulting in significant TTVs, in particular for planets c and d. However, as can be seen in Figure 2.2, the only ∼5 months time span of the *TESS* and ground-based observations included in G20 was

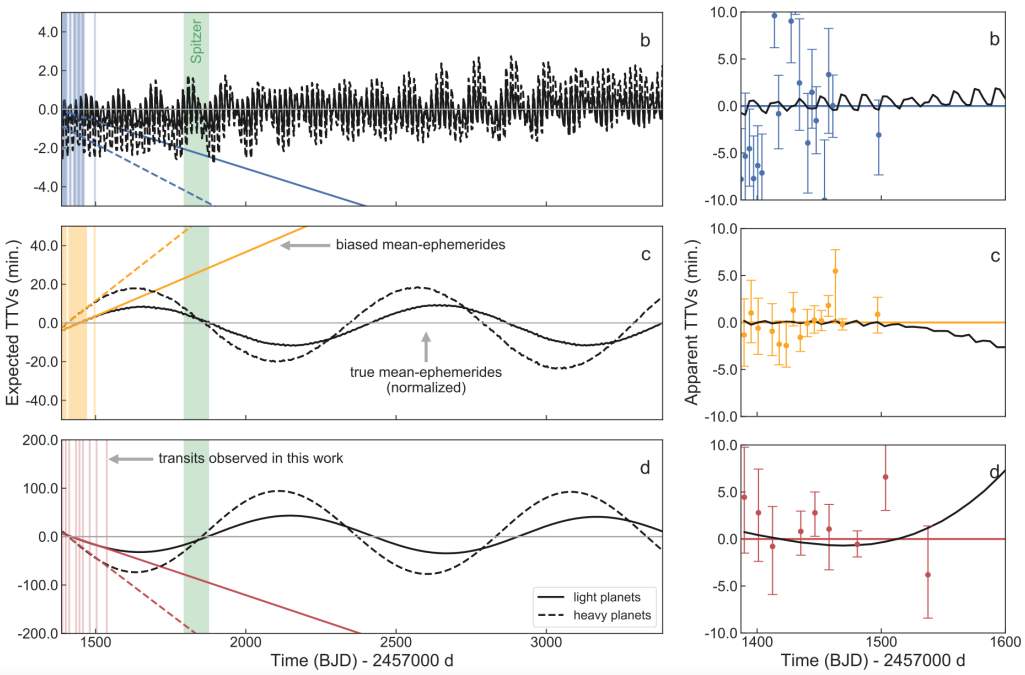


Figure 2.2: Expected and apparent transit timing variations (TTVs) of the TOI-270 system. The left panel shows the original expected TTVs from G20 using the mean-ephemerides known at the time of publication. Predictions are plotted across a range, with solid black lines depicting the expected TTVs of the assumption of 'light planets' or dashed lines for "heavy planets". Distinguishing between the two would have a significant impact on their probably composition. An observing window of Spitzer that had not yet transpired is shown in green. At the time of discovery, the combined TESS and follow-up ground-based observations showed no discernible TTVs

too small compared to the expected dominant timescale of the TTVs (∼3 years), to allow the TTVs to be detected. This is commonly the case when examining TTVs in TESS data, which, unless a target falls in the small fraction of sky that is in or near-to the continuous viewing zone (see Figure 1.7).

G20 discusses the amenability of this system for detailed characterization of the bulk density and atmospheric composition of its planets. This enables probing the formation history, molecular abundances, and potential signs of atmospheric or ocean loss with the James Webb Space Telescope (JWST) and the Extremely Large Telescopes (ELTs). Absorption features of TOI-270 planets c and d are expected to be readily detectable with SNR $>$ 40 and SNR $>$ 60, respectively, from just one transit with the JWST NIRISS instrument assuming cloud-free and

H2-dominated atmospheres (Rein & Liu, 2012a). A comparison of their atmospheric compositions and thickness would enable information and direct comparison of their formation histories, as well as the potential constraint of ocean loss, using red-sensitive JWST observations to probe O_3 abundance while deploying with ground-based, visible-spectrum observations from the Extremely Large Telescopes to probe O_2 abundances (Batalha et al., 2017; Kempton et al., 2018).

We have now achieved a clear detection of TTVs, by continuing to monitor the system from the ground and using *Spitzer*. *TESS* also re-observed the system in Cycle 3, and the observations to date now span a large enough portion of the TTV super-period to allow for a meaningful dynamical analysis of the system. However, TTV observations alone can be hard to interpret due to strong degeneracies between the orbital parameters. Relative uncertainties on pure-TTV mass determinations range from ∼5 to 100% depending on the number of planets in the system, their orbital configuration, as well as the number, precision, and time-span of the measured transit times (Agol & Fabrycky, 2018).

In the meantime, Van Eylen et al. (2021, hereafter VE21) also monitored the TOI- 270 system, using the Echelle Spectrograph for Rocky Exoplanet and Stable Spectroscopic Observations (ESPRESSO) to obtain RV measurements (Pepe et al., 2021b). VE21 reports masses of 1.58±0.26 $M_\oplus$, 6.14±0.38 $M_\oplus$, and 4.78±0.46 $M_\oplus$ for planets b, c, and d respectively, classifyng the inner planet as likely rocky, and the outer two as lower density sub-Neptunes. These results found no evidence of non-circular orbits and confirmed the status of planets c and d as outstanding targets for transmission spectroscopy and planet b as a good target for emission spectroscopy. The uncertainties on the masses reflect the small RV semi-amplitudes of the TOI- 270 planets (2, 5, and 3 m/s), and the limited number of RV measurements (∼80). This provides us with an opportunity both to compare the results of an independent analysis of our TTV measurements with those reported by VE21 based on RV observations, use the RV results as priors in our analysis of the TTVs, and obtain refined estimates of the planets' masses and orbital parameters.

The combination of TTV and RV observations was first demonstrated for the Kepler-9 system by Holman et al. (2010), and has since been reexamined for the system multiple times (Borsato et al., 2014; Dreizler & Ofir, 2014; Freudenthal et al., 2018; Borsato et al., 2019). Upon first re-examination with a combined RV-TTV analysis, Borsato et al. (2014) found much lower masses for the two Jupiter-sized planets than initially proposed in the discovery paper. However, several years of ground-based follow-up and further modelling by Freudenthal et al. (2018) and Borsato et al. (2019) has decreased this disparity and increased the precision of densities measured. The analysis of Freudenthal et al. (2018) reveals that Kepler-9 c is expected to stop transiting in the next 30 years due to strong dynamical interactions between Kepler-9 b and 9 c arising from their near 2:1 resonance, which will lead to a periodic change in inclination.

Other systems that have been analyzed jointly with RV and TTV data include K2-19 (Nespral et al., 2017), Kepler-19 (Malavolta et al., 2017), WASP-47 (Weiss et al., 2017), K2-24 (Petigura et al., 2018) and XO-6b (Garai et al., 2019). Like was the case with Kepler-9, some discrepancies have arisen between these two approaches (Weiss & Marcy, 2014; Mills & Mazeh, 2017), however, these seem to potentially be reconcilable with enough data points, as shown by Borsato et al. (2019). Nevertheless, these slight tensions highlight the importance of such joint studies for providing further elucidation on the biases and limits of these methods.

Precise planetary masses are essential for atmospheric characterization, particularly for resolving degeneracies in the interpretation of transmission spectra. Batalha et al. (2019) demonstrate that, for small planets, robust atmospheric retrievals are possible only if the planet mass is known to a precision of 50% or better, and that more precise mass estimates of 20% are required to exploit the full sensitivity of JWST, given the latter's expected noise floor. The mass estimates presented by VE21 and reported in this work will thus have a direct impact on atmospheric studies of the system, starting with the ongoing Hubble Space Telescope (HST) observations (HST, program id GO-15814, PI Mikal-Evans).

Our refined ephemeris and eccentricity constraints will also facilitate the scheduling of future transit and eclipse observations.

The rest of this chapter is structured as follows. Section 2.2 details the photometric observations we obtained using distinct ground- and space-based telescope facilities, including data reduction and basic light curve extraction. Section 2.3 describes the light curve analysis, which we took care to perform in a consistent manner across all telescopes and gives the resulting estimates of the bulk parameters and individual transit times for each planet. Section 2.4 presents the dynamic analysis of TTVs using Differential Evolution Markov Chain Monte Carlo (DEMCMC). In Section 2.5 we discuss our improved mass estimates, system stability, potential atmospheric composition and theories of planetary formation before concluding in Section 2.6.

2.2 Observations

This section details the observations and data reduction of each satellite and ground-based observatory. All observations are listed in Table 2.1.

Table 2.1: Observation Log

TOI- 270	Dates	Telescope	Filter	Exposure Time (sec)	No. of Exposures	Observation Dur (minutes)	Transit Coverage
TOI- 270 b-d							
	2018-2020	TESS	TESS	20-120	46874	-	-
TOI- 270 b							
	2018-12-18	PEST	Rc	120	189	449	full
	2019-01-14	LCO	i'	90	172	160	full
	2019-01-24	LCO	-	90	136	183	partial
	2019-01-27	LCO	-	90	119	219	full
	2019-09-03	NGTS	NGTS	10	8331	223	full
	2019-09-30	LCO	-	90	115	164	full
	2019-11-09	LCO	-	90	159	230	full
	2019-11-16	NGTS	-	12	6811	208	full
	2019-12-13	LCO	-	90	148	213	full
	2020-09-13	LCO	i'	90	128	198	full
	2020-10-23	LCO	i'	90	148	243	full
TOI- 270 c							
	2018-12-10	LCO	i'	132	86	187	full
	2019-01-07	LCO	i'	51	207	215	full
	2019-03-28	ASTEP	Rc	120	171	471	full
	2019-04-19	Spitzer	4.5	2	10045	345	full
	2019-07-30	TRAPPIST-South	z'	10	511	170	full
	2019-09-02	TRAPPIST-South	z'	10	667	209	full
	2019-09-08	TRAPPIST-South	z'	10	742	232	full
	2019-09-02	LCO	-	90	135	192	full
	2019-09-13	LCO	-	90	94	134	partial

2019-09-30	LCO	-	90	119	170	partial
2019-10-17	LCO	i'	90	132	189	full
2019-10-23	TRAPPIST-South	z'	15	544	171	full
2019-11-03	LCO	-	90	159	230	full
2019-11-09	TRAPPIST-South	z'	15	569	179	full
2019-11-09	LCO	-	90	160	229	full
2019-11-15	LCO	-	90	162	232	full
2019-11-26	PEST	Rc	130	91	210	partial
2019-12-02	LCO	-	90	162	232	full
2019-12-07	Spitzer	4.5	2	7643	263	full
2019-12-24	Spitzer	3.6	2	7510	262	full
2020-01-05	Spitzer	3.6	2	7380	258	full
2020-01-10	Spitzer	3.6	2	7462	260	full
2020-05-20	ASTEP	Rc	40	422	459	full
2020-05-25	ASTEP	Rc	40	345	373	full
2020-06-06	ASTEP	Rc	40	331	359	full
2020-10-25	LCO	i'	90	211	328	full
2021-01-01	LCO	i'	90			full
TOI- 270 d						
2019-01-19	LCO	i'	50	182	156	partial
2019-02-23	LCO	g'	96	123	192	partial
2019-06-16	Spitzer	4.5	2	10851	361	full
2019-08-24	TRAPPIST-South	z'	10	369	115	partial
2019-09-27	LCO	-	90	161	231	full
2019-09-27	NGTS	NGTS	10	5037	273	full
2019-10-08	LCO	-	90	132	192	full
2019-10-20	LCO	-	90	115	165	partial
2019-10-31	LCO	-	90	97	138	partial

2019-11-23	TRAPPIST-South	z'	10	630	197	full
2019-11-23	NGTS	NGTS	10	9167	328	full
2019-11-23	CHAT	-	-	-	-	partial
2019-12-04	Spitzer	4.5	2	7600	253	full
2020-01-07	Spitzer	4.5	2	7583	261	full
2020-07-19	LCO	i'	90	69	106	partial
2020-09-02	LCO	i'	90	124	190	partial

Many of the ground-based observations discussed below were coordinated through the *TESS* Follow-up Observing Program (TFOP)[1]. TFOP is an initiative that coordinates and facilitates the ground-based follow-up observations of TESS exoplanet candidates. It aims to confirm and characterize the exoplanets identified by the TESS space mission through a multi-wavelength and multi-telescope approach. We used the `TESS Transit Finder`, which is a customized version of the `Tapir` software package (Jensen, 2013), to schedule our transit observations. Unless otherwise noted, the photometric data were extracted using the `AstroImageJ` (`AIJ`) software package (Collins et al., 2017). Details of the facilities and instrumentation used are given in Table 2.2.

2.2.1 *TESS*

TESS first observed TOI- 270 in short cadence (2 minute) observing mode between 20-Sep-2018 and 17-Dec-2020 in 27 day increments in sectors 3-5. *TESS* then re-observed the target in sectors 30 and 32 in camera 3, with 20 second cadence data[2] (see Fig. 2.1). Data were reduced and light curves extracted using the Science Processing Operations Center (SPOC) pipeline (Jenkins, 2002; Jenkins et al., 2010; Smith et al., 2012; Stumpe et al., 2014; Jenkins et al., 2016; Jenkins, 2017). The SPOC pipeline consists of several steps that transform the raw pixel data into calibrated light curves, which are then searched for transit signals to identify potential exoplanet candidates. The pipeline begins by extracting Target Pixel Files (TPFs), which contain the raw pixel data for each observed target star. These files include information such as the position of the star on the detector, the aperture used for extraction, and the timestamp of each image. The raw pixel data then undergoes various pre-processing steps to correct for instrumental effects and remove systematics including the removal of instrumental artifacts, cosmic ray hits, and background noise (Jenkins et al., 2016).

[1] https://tess.mit.edu/followup

[2] thanks to the *TESS* GI programs G03196 (PI Günther), G03278 (PI Mayo), G03106 (PI Kane), and G03274 (PI Cloutier)

Aperture photometry is then performed to extract the flux measurements from the target star. A predefined aperture is used to sum the flux from the pixels surrounding the star. Background subtraction is also applied to account for the contribution from the nearby regions. The light curves obtained from the aperture photometry step are then corrected for systematic effects such as spacecraft jitter, instrumental drifts, and detector artifacts (Stumpe et al., 2014). Various algorithms and techniques are employed to model and remove these systematics, as will be discussed in 2.3.

Once the light curves are processed and systematics are corrected, the SPOC pipeline conducts a transit search to identify potential exoplanet candidates, and performs an initial validation, assessing SNR, transit shape, consistency across multiple transits, and statistical significance to determine the likelihood of a true exoplanet detection. Finally, the pipeline generates a catalog of exoplanet candidates, including their basic information such as period, depth, and duration of transit events. This catalog and all TESS SPOC data products are made publicly available to the scientific community for further analysis and follow-up observations on the Mikulski Archive for Space Telescopes (MAST).

2.2.2 *LCO*

TOI- 270 was observed by the Las Cumbres Observatory Global Telescope (LCOGT) (Brown et al., 2013) 1m telescope network as part of ground-based follow-up as reported in G20, through subsequent observations as part of the *TESS* Follow-up Observing Program (TFOP), and through an additional program with PI Parviainen over semesters 2019B, 2020B, and 2021A. The 4096×4096 LCOGT SINISTRO cameras have an image scale of 0.389" per pixel, resulting in a $26' \times 26'$ field of view.

The LCOGT observations led by Parviainen cover six full and one partial TOI-270c transits, and one full and two partial TOI-270d transits. The observations were carried out with SINISTRO cameras using the SDSS-ip filter with 60 s exposure times and slight defocussing to make sure neither the target star or any of the comparison stars saturate. All images were calibrated by the standard LCOGT `BANZAI` pipeline

(McCully et al., 2018). The pipeline begins by calibrating the raw images acquired by the telescopes, applying bias subtraction, dark current correction, and flat fielding to remove instrumental artifacts and variations. The photometry was done using a custom photometry pipeline developed for the MuSCAT2 instrument (Narita et al., 2019; Parviainen et al., 2019), and an initial transit modelling was carried out using the `PyTransit` package (Parviainen, 2015).

2.2.3 *TRAPPIST*-South

TRAPPIST-South at ESO-La Silla Observatory in Chile is a 60 cm Ritchey-Chretien telescope, which has a thermoelectrically cooled $2k \times 2k$ FLI Proline CCD camera with a field of view of $22' \times 22'$ and pixel-scale of 0.65 pixel^{-1} (Jehin et al., 2011; Gillon et al., 2013). We carried out a set of five full-transit observations of TOI-270 c, and one full and one partial transits for TOI-270 d.

2.2.4 *ASTEP*

ASTEP is 40 cm telescope installed at the Concordia Station, Dome C, Antarctica (Guillot et al., 2015). ASTEP is a Newtonian telescope equipped with a 5-lens Wynne coma corrector and a $4k \times 4k$ front-illuminated FLI Proline KAF 16810E CCD with a 16 bit dynamic. The camera has an image scale of 0.92" pixel^{-1} resulting in a $63' \times 63'$ corrected field of view (Abe et al., 2013).

Due to the extremely low data transmission rate at the Concordia Station, the data are processed on-site using an automated IDL-based pipeline producing data files which contain the star's flux computed through various fixed circular apertures radii, so that optimal lightcurves can be extracted (Mékarnia et al., 2016). TOI-270 was observed several times between March and April 2019 and between April and July 2020. For this study, we selected a set of four full-transit observations of TOI-270 c conducted under good weather conditions with temperatures ranging from $-70°$C to $-60°$C.

Table 2.2: Facilities used for ground-based follow-up observations

Observatory	Location	Aperture (m)	Pixel scale (arcsec)	FOV (arcmin)
Antarctic Search for Transiting ExoPlanets (ASTEP)	Concordia Station, Antarctica	0.4	0.93	63×63
Chilean-Hungarian Automated Telescope (CHAT)	Las Campanas Observatory, Chile	0.7	0.6	21×21
Las Cumbres Observatory Global Telescope (LCOGT)	Chile, South Africa, Australia	1.0	0.39	26×26
Next-Generation Transit Survey (NGTS)	Paranal, Chile	0.2	4.97	170×170
Perth Exoplanet Survey Telescope (PEST)	Perth, Australia	0.3	1.2	31×21
TRAPPIST-South	La Silla, Chile	0.6	0.64	22×22

2.2.5 *NGTS*

The Next Generation Transit Survey (NGTS) consists of twelve independently operated robotic telescopes, each with a 20 cm diameter and an 8 square-degree field-of-view, and is located at the ESO Paranal Observatory in Chile (Wheatley et al., 2018). The NGTS telescopes achieve sub-pixel level guiding through the use of the DONUTS auto-guiding algorithm (McCormac et al., 2013). Observing a single bright star simultaneously with multiple NGTS telescopes has been shown to significantly improve the photometric precision achieved (Smith et al., 2020; Bryant et al., 2020).

Two transits of TOI-270b were observed on 2019 Sep 03 and 2019 Nov 16 using eight and seven telescopes respectively. A total of 15142 images were obtained across the two nights. A further two transits of TOI-270d were observed on 2019 Sep 27 and 2019 Nov 23 using four and six telescopes. A total of 14204 images were taken across these two nights. All the NGTS observations of TOI-270 were performed using the custom NGTS filter (520 - 890 nm) and with an exposure time of 10 s.

A custom aperture photometry pipeline (Bryant et al., 2020) was used to reduce the images from all four nights of NGTS observations. This pipeline uses the `SEP` library (Bertin & Arnouts, 1996; Barbary, 2016) for source extraction and photometry. During the reduction comparison stars which are similar to TOI-270 in terms of brightness, colour, and CCD position are automatically identified using *Gaia* DR2 (Gaia Collaboration et al., 2016b, 2018).

2.2.6 *PEST*

A single transit of planet c was observed by the Perth Exoplanet Survey Telescope (PEST). PEST is a 12 Schmidt-Cassegrain telescope on a computer controlled, motorised fork mount that enables robotic pointing and tracking of a target. It uses a QHY183M CMOS camera cooled to -5 °C to reduce image noise – graininess or speckles. A computer controlled focuser enables auto focusing. A custom pipeline based on `C-Munipack`[3] was used to calibrate the images and extract the differential photometry.

[3]http://c-munipack.sourceforge.net

2.2.7 *Spitzer*

Soon after the TOI- 270 planet candidates were announced by the *TESS* project, we identified the system as an intriguing target for transit observations with the *Spitzer* Space Telescope. We observed five transits of TOI- 270 c and three transits of TOI- 270 d with *Spitzer*, four transits in each of two programs (GO-14084 and 14325) (Crossfield et al., 2018; Parmentier et al., 2019). Our *Spitzer* observations provided coverage of these planets' transits in each of the 3.6 and 4.5 channels of the IRAC instrument (Fazio et al., 2004). We planned our observations following standard practices for precise *Spitzer* transit photometry. In particular, an initial peak-up observation placed the target on the IRAC detector's "sweet spot" to minimize instrumental variations.

Because of the bright target star both channels of *Spitzer* photometry used subarray-mode observations, which consist of multiple sets of 64 quick subarray frames. All our *Spitzer* observations used 2 s subarray integrations, and raw and calibrated data products (processed with the standard *Spitzer* data calibration pipeline) are publicly available through the Spitzer Heritage Archive[4]. The pipeline, known as the Spitzer Science Center (SSC) Data Analysis Tool (DAT), performed various steps to calibrate and extract photometric measurements from the raw data. It first does a round of preprocessing in which it corrects the raw data for instrumental effects, removing known biases, dark current, and non-linearity corrections. Additionally, the data may undergo image persistence removal, which mitigates the impact of residual signals from previous exposures.

The DAT pipeline then performs Point Spread Function (PSF) fitting to accurately determine the centroid of the target source, which involves modeling the shape of the PSF and fitting it to the observed data. The PSF fitting helps to determine the precise location of the target and minimizes the impact of any pointing errors or image artifacts. Once the precise centroid of the target is determined, aperture photometry is performed to measure the flux of the target source. The

[4] https://sha.ipac.caltech.edu/applications/Spitzer/SHA/

background flux is estimated from a nearby annulus surrounding the target aperture, which is used to correct for the background contribution.

Spitzer's observations can be affected by variations in the pixel response function across the detector. To account for these variations, a pixel phase correction is applied to the photometric measurements. This corrects for the position-dependent flux variations caused by the changing sensitivity of individual pixels. Spitzer is also known to have a high degree of correlated "brown" noise in each pixel (Ingalls et al., 2012). We will talk about additional steps we took to remove this effect in Section 2.3.3.

2.3 Light curve analysis

Light curves contain not only the desired transit signal but also various sources of noise and systematic effects. These can include instrumental artifacts, stellar variability, and other astrophysical phenomena unrelated to the presence of an exoplanet. To extract the transit signal or to critically fit for an accurate transit time when analysing TTVs, detrending techniques are employed to remove the unwanted variations from the light curve (Hippke et al., 2019).

Detrending may involve correcting for instrumental effects, such as pixel-to-pixel sensitivity variations or telescope pointing errors. Instrumental trends are mitigated by a variety of methods, such as fitting and subtracting cotrending basis vectors (Thompson et al., 2016), decorrelating telescope pointing from photometric variation (Vanderburg & Johnson, 2014a; Lund et al., 2015; Aigrain et al., 2016a), or methods such as the trend filtering algorithm (TFA) (Kovács et al., 2005), or even using simultaneously observed stars to measure and remove systematic effects (Kim et al., 2009).

Detrending also needs to account for stellar variability caused by stellar activity, pulsations, or eclipsing binary companions (Hippke, 2015). While some of these cycles can be long, like that of our own sun at 11 years (Usoskin et al., 2009), younger stars can have short term, dramatic activity cycles on the scale of days or weeks (Cody & Hillenbrand, 2018). Additional variability-iducing features such as

star spots can add a layer of correlated noise, at the rate of stellar rotation, which in our sun's case is 27 days (Beck, 2000). Different techniques, such as polynomial fitting, wavelet analysis, or Gaussian processes, can be applied to estimate and subtract these systematic effects.

A common and classic technique, is using a sliding filter, such as the The Savitzky-Golay filter (Savitzky & Golay, 1964). A filter works by fitting a polynomial to a small window of data points and using this polynomial to estimate the value at the center point of the window. The window slides across the entire light curve, and at each position, a new polynomial is fitted and the estimated value is computed. The Savitzky-Golay filter differs from other smoothing techniques in that it performs a least-squares polynomial fit instead of using simple moving averages or low-pass filters. The key advantage of the Savitzky-Golay filter is that it can effectively suppress noise while preserving the important features of the signal, such as transits. The choice of the window size and polynomial order determines the trade-off between noise reduction and preserving signal details (Wheatley et al., 2010). A larger window and higher polynomial order provide more smoothing but may result in the loss of finer features.

On the other hand, polynomial or spline detrending methods work by fitting smooth, piecewise polynomial approximations to the data (Giles et al., 2018; Vanderburg et al., 2016). This is especially capable of capturing longer term trends and instrumental effects. The models employed for fitting can be based on simple mathematical functions or more complex algorithms, depending on the nature of the noise. Some methods such as LOWESS smoothing effectively combine the methods of sliding filters and polynomial detrending, fitting a locally-weighted polynomial regression to a specific window of the data (Cleveland, 1979).

Another technique is through use of a Gaussian process (GP) which is a non-parametric regression method, that establishs a probability distribution over functions, with the assumption that nearby observations are correlated. This method allows complex unknown detrending functions to be found for individual data-sets without having to guess the approximate form beforehand (Rasmussen C.,

2001). They are also incredibly useful in that they can be paired with transit light curve functions to simultaneously fit and detrend stellar activity (Foreman-Mackey et al., 2017). GPs are heavily used in this work, though one of the downsides is that they tend to be computationally intensive compared to other methods and therefore not as practical for large scale transit surveys.

When analysing the light curves from the different telescopes, our aim was to get as close as possible to a fully self-consistent analysis of all the available photometric data for each planet. However, this quickly results in an unfeasibly large number of data points and free parameters, as each transit has a specific mid-transit time, and each telescope a specific set of limb-darkening and noise model parameters, in addition to the bulk transit parameters which are common to all datasets. We therefore reached a compromise, whereby the light curve analysis was done sequentially, as follows.

We first fit the bulk parameters using the *TESS* cycle 1 data, ignoring the TTVs (which are negligible on this time scale). In the case of planets c and d, we then used the resulting linear ephemeris (period and time of conjugation) and bulk parameters as inputs to analyse the *Spitzer* data. This results in significantly tighter constraints on the bulk planet parameters. We then proceed to fit each transit from every instrument in turn, fixing the bulk parameters at the *Spitzer*-derived values, and varying only the parameters of the noise model, the mid-transit time, and the limb-darkening parameters. Early in the study, we tried allowing the bulk transit parameters to vary when fitting for the TTVs, using the *Spitzer* derived constraints as priors. This did not appreciably increase the uncertainties on the transit times, and resulted in much longer convergence times, given the larger number of parameters to fit, so we opted to fix the bulk parameters instead when fitting for the TTVs.

In the case of planet b, in the absence of *Spitzer* observations, we proceed in the same manner, but relied on the *TESS* cycle 1 and cycle 3 data to derive the bulk parameters and mean period used as priors in the individual fits.

This sequential, Bayesian approach enables us to keep the computational cost of each fit manageable, while ensuring the overall self-consistency of the results.

The final planetary parameters are reported in Table 2.3, and the mid-transit times for each transit (excluding those that were discarded because the fits were deemed unreliable, as discussed below) in Tables A.1, A.2 and A.3.

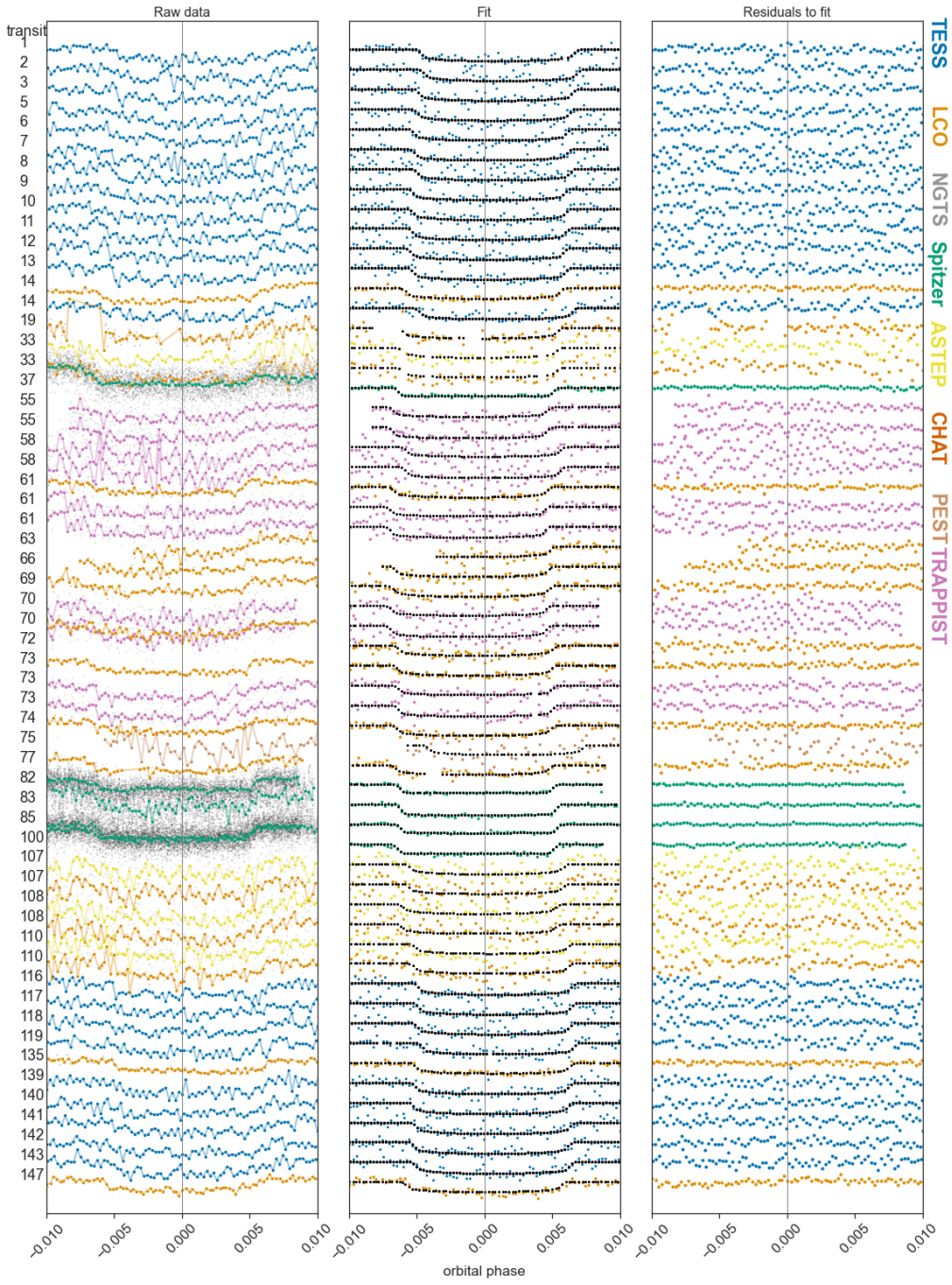


Figure 2.3: Planet c transits. The leftmost column shows unprocessed light curves with data binned to *TESS* 2 minute cadence for clarity. The middle column shows the fit by the GP plus the transit curve and the rightmost column gives the residuals to this fit. As can be seen in some cases, there were not enough data points to constrain the fitting. These observations were subsequently discarded before analysis.

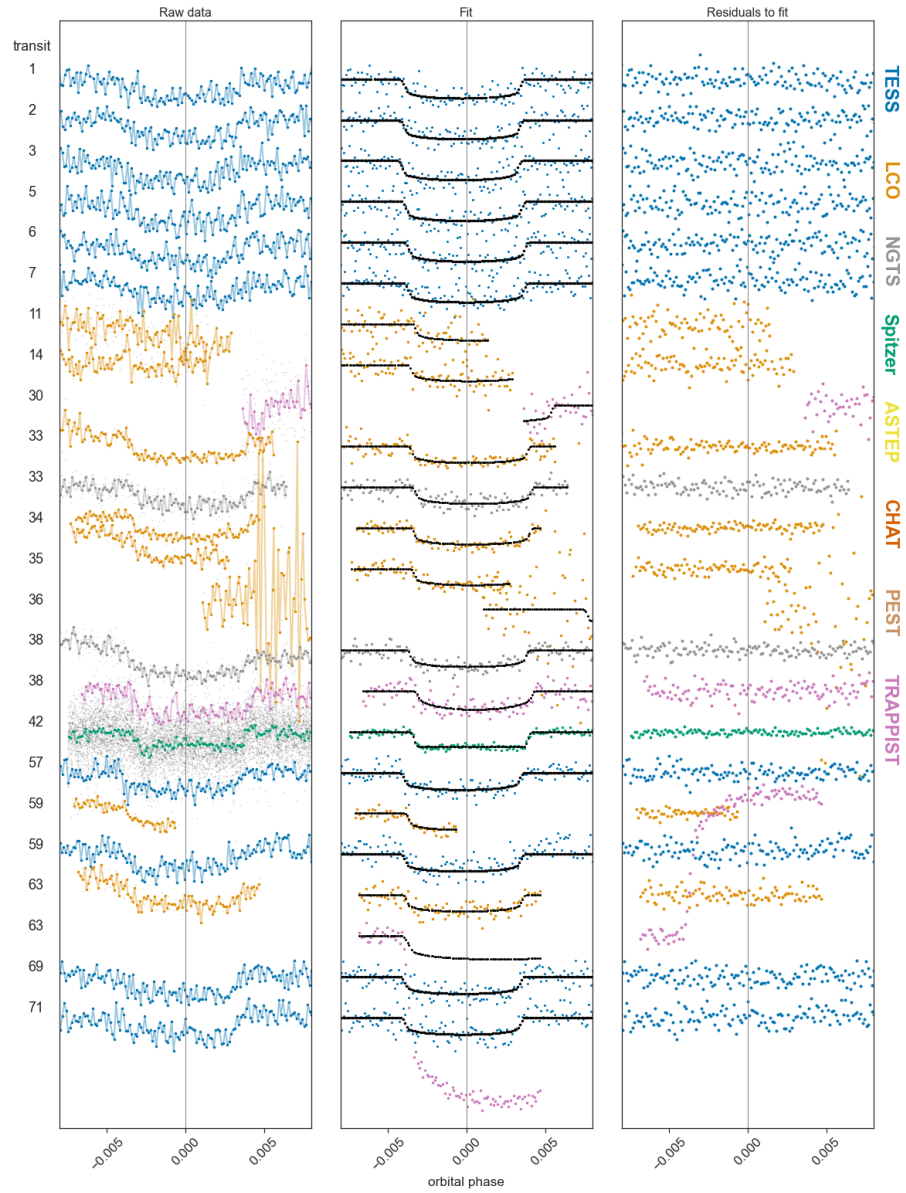


Figure 2.4: Planet d transits. Similar to fig 2.3, each color represents the respective telescope. Of note, several transits resulted in visibly incorrect fits, due to incomplete transit coverage or remnant correlated noise (most often due to high air mass). These transits were excluded from further analysis.

2.3.1 Model implementation

The light curve modelling was implemented in Python. All transit modelling was done using the Batman package (Kreidberg, 2015). The parameters of the transit model implemented in Batman are the orbital period P, the time of transit centre T_0, the planet-to-star radius ratio $R_p/R_\star$, the system scale $a/R_\star$ (where a is the

orbital semi-major axis), the orbital inclination i, the orbital eccentricity e and the longitude of periastron ω and the quadratic limb-darkening coefficients u_1 and u_2. In the present work, we fixed the eccentricity to zero, an assumption that is reasonable given the small eccentricity measured in RV by VE21 and is ultimately validated by our dynamical analysis of the TTVs (see Section 2.4). When fitting, we chose to fit for R_p, $R_\star$ and $M_\star$, which are then used to obtain $R_p/R_\star$ and $a/R_\star$ (through Kepler's 3rd Law). We used the Limb Darkening Toolkit (LDTk) of Parviainen & Aigrain (2015) to compute priors over the limb darkening coefficients u_1 and u_2, using the stellar parameters from G20 and the relevant instrument/filter throughput as inputs. We used uninformative, wide uniform priors over all the other parameters (except for inclination where we used a uniform prior in $\cos i$), except where explicitly stated otherwise below.

To account for correlated noise in the *TESS* and ground-based light curves, we used a Gaussian Process (GP) with a squared exponential covariance function:

$$k(t, t') = A \exp\left[-\frac{(t - t')^2}{2\tau}\right] \tag{2.1}$$

where A is the variance and τ the (squared) characteristic time-scale, or metric, of the GP. All GP calculations in this work were done using the GEORGE package (Ambikasaran et al., 2014). We used log uniform priors over the logarithm of the GP hyper-parameters A and τ.

When performing optimisation, we first used the MINIMIZE function of the SCIPY.OPTIMIZE module to determine initial input parameters, and explored the posterior distribution over the parameters of our models using Markov Chain Monte Carlo (MCMC) implemented with the EMCEE package (Foreman-Mackey et al., 2013a, 2019). We evolved chains of 40 walkers with a thinning factor of 15 with a conservative removal of the first 25% of steps as burn-in. Convergence was achieved when the estimated autocorrelation time $\tau_{autocor}$ (checked every 200 steps) was changed by less than 1% and the chain was longer than 200 times the autocorrelation time, resulting in chain lengths of about 100,000. Parameter values were taken to be the median of the posterior distribution, the with errors reported as the 68% confidence interval from the 16th to the 84th percentile.

2.3.2 *TESS*

Our starting point for the *TESS* data are the 2-minute cadence PDC-SAP light curves, in which most systematic effects have already been corrected (Stumpe et al., 2012; Smith et al., 2012; Stumpe et al., 2014). Nonetheless, we checked for any residual correlated noise using the out-of-transit data, in two distinct ways. First, we computed the Auto-Correlation Function (ACF) of the out-of-transit light curve and confirmed that it behaves as expected for white Gaussian noise, namely the ACF is within a standard deviation of zero for all non-zero lags. Second, we tried modelling the out-of-transit light curve using a GP, as described in Section 2.3.1, and found that this resulted in a very small best-fit value for A. In the remainder of our analysis of the *TESS* data, we do include a GP term, primarily for consistency with our later analysis of the ground-based data, but we fix the hyper-parameters at the best-fit values obtained on the out-of-transit cycle 1 (sectors 3–5) data. We note that essentially identical results would be obtained by either varying the hyper-parameters while fitting the transits, or not including a GP at all for the *TESS* data.

We then proceed to model the transits, initially in the cycle 1 data only, as the effects of the TTVs within the limited time-frame of those data is negligible, enabling a global analysis of the transits of each planet in turn, assuming a linear ephemeris. We start by extracting a segment of the light curve lasting 3 transit durations around the predicted centre of each transit, using the linear ephemeris from G20. We then fit the data in and around all the transits for each planet, keeping the GP hyper-parameters fixed, and varying the transit parameters only. The results of this analysis are shown in Table 2.3, and are in good agreement with the discovery paper, as expected.

Finally, to measure TTVs, we fix the planetary parameters to the values derived from the *Spitzer* data (for planets c and d, see Section 2.3.3 for details) and from *TESS* cycle 1 and 3 (for planet b), and fit each transit individually, varying only the time of the transit centre.

2.3.3 Spitzer

With its Infrared Array Camera (IRAC) in this warm viewing mode, which undersamples the PSF, *Spitzer* spacecraft wobble and jitter causes the PSF to move across pixels resulting in significant correlated noise (Ingalls et al., 2012). This is a well-characterised problem, and several methods have been used previously in order to remove these effects (Shporer et al., 2014; Lanotte et al., 2014). In this work, in order to reduce the level of systematic error seen in warm *Spitzer* data, we followed the process of Pixel Level Decorrelation (PLD) as described by Deming et al. (2015) with the new addition of Principal Component Analysis (PCA). In summary, PLD employs the relative of a 3x3 grid of pixels that captures the stellar image over a time series. Each pixel produces its own time series across the duration of the observation which accounts for any movement of the point spread function (PSF) of the star during that time (usually less than one pixel drift). The total light curve can then be expressed as a linear combination of a transit eclipse, the normalised pixel time series, and linear or higher order trends in time. If the light curve we are interested in is a function of these pixel time series, then PCA enables us to reduce the dimensionality of a data set by looking for uncorrelated components that contribute to the variance seen. In the end, this results in a function for the total light over time in the form:

$$\Delta S^t = \sum_{i=1}^{3} c_i \hat{C}_i^t + D_{transit}(t) + b_0 + b_1 t \tag{2.2}$$

Where ΔS^t is the brightness of the star over time, $c_i \hat{C}_i^t$ are the principal component time series regularized at each time point (and thus do not contain the transit information), $D_{transit}$ is the depth of the transit at any given time point (holding a value of 1 out of transit) and b_0 and b_1 are terms describing the constant and linear offsets. Higher order polynomial offsets were not found to impact the transit fit in the case of Deming et al. (2015), and we found that to be the case in our work as well.

We therefore proceeded as follows: For each transit, instead of using all 9 pixel time series, which are likely degenerate, we performed PCA and found that using 3

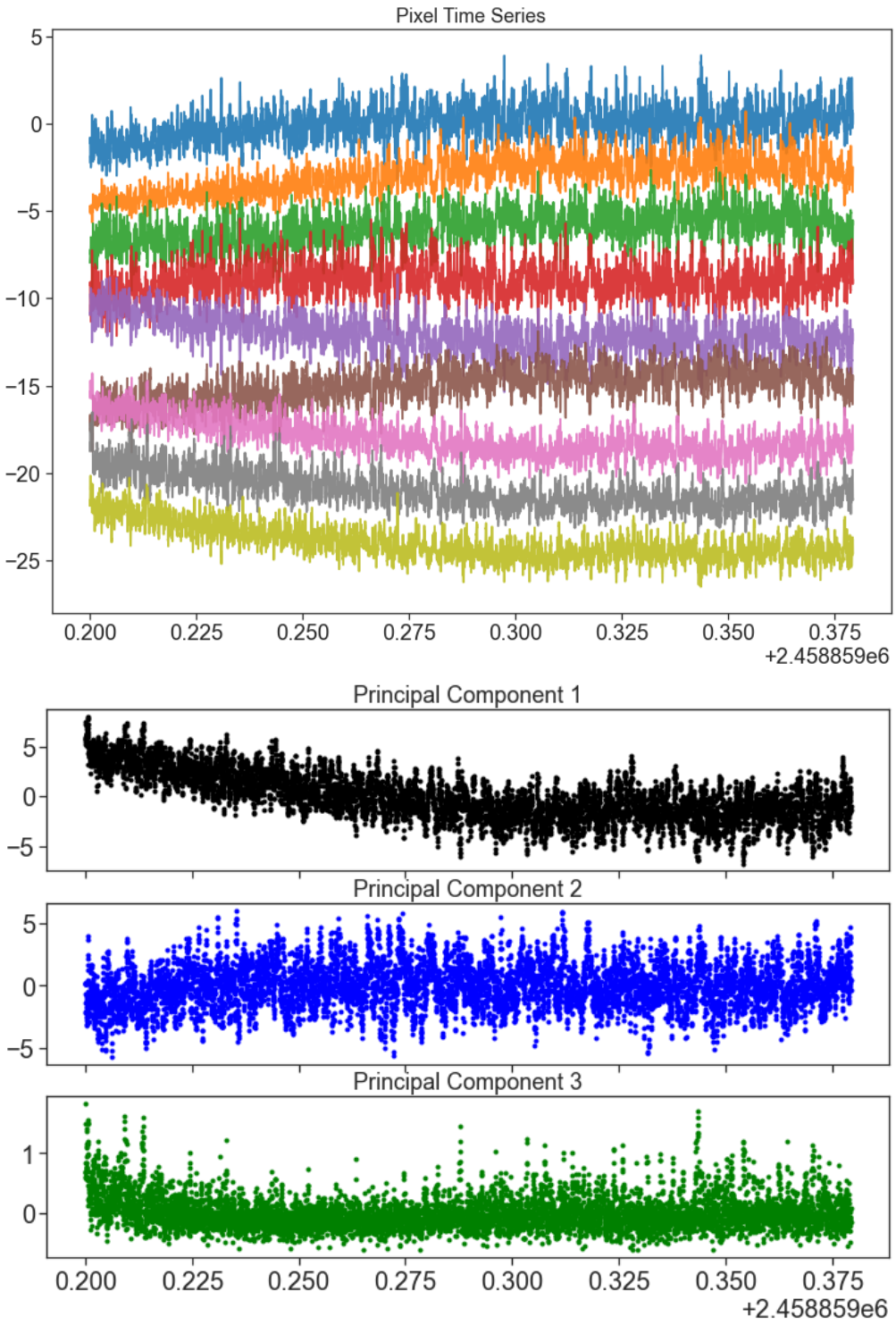


Figure 2.5: Pixel Level Decorrelation (PLD), which is used to remove correlated noise from *Spitzer* light curves (Deming et al., 2015) is shown here for a transit of planet c. In the top panel, the regularized pixel time series are shown, which come from a 3 x 3 grid of pixels. Because of the regularization at each time point, these time series do not show a transit. From these, we extract the three principal components shown in the bottom panel.

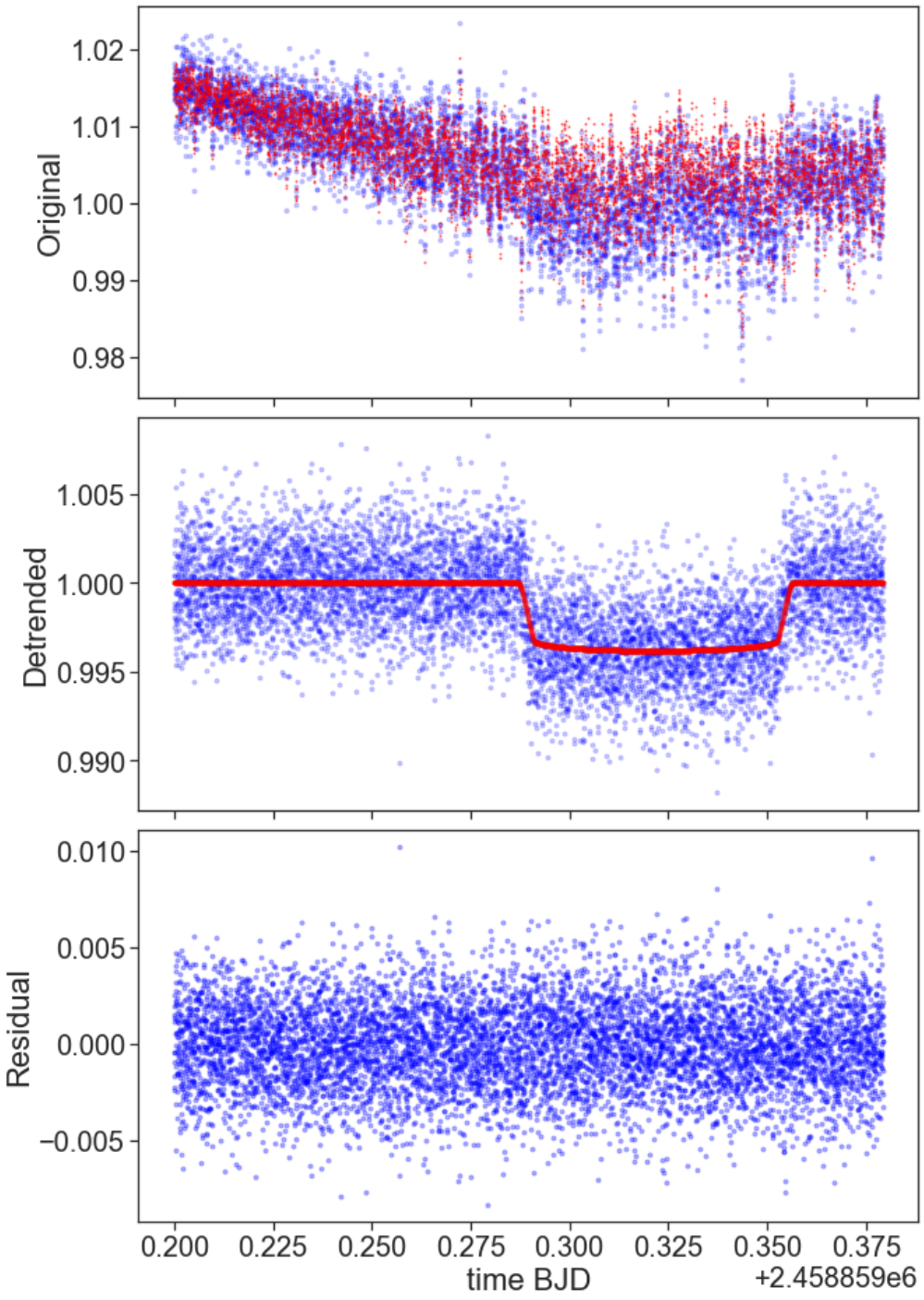


Figure 2.6: PLD Fitting Result: The top panel shows the original light curve. The primary principal component (shown in black in Figure 2.5 follows the most obvious trend of this lightcurve. Also shown in the top panel in red is the best-fit noise model and solution to Equation 2.2. In the middle panel, the noise is removed and the best-fit transit model is shown in red. The bottom panel shows the final residuals after fitting.

components explained $> 95\%$ of the variance. Reducing this to two components resulted in a slight worsening of the eventual transit fit, and adding a fourth component did not produce a measurable change. We then constructed a model using the equation above with the 3 principal components of the pixel series, a BATMAN light curve as described in Section 2.3.1, and a linear and constant offset. This resulted in a fit that is exemplified in Figures 2.5 and 2.6. We then optimised for c_i b_0 b_1 and all planetary parameters described above using wide, uniform priors. This conferred a slight improvement on the bulk planetary parameters derived from *TESS* as shown in Table 2.3. We adopted these as the fixed planetary parameters for the remainder of the ground-based fitting described below for planets c and d (no *Spitzer* observations were taken of planet b). We further returned to *TESS* data for planet c and d and fixed the bulk planetary parameters to *Spitzer*-derived values, while fitting for transit time, GP hyper parameters, and limb darkening.

2.3.4 Ground based observatories

LCO observations were next fit in an identical manner to *TESS* using GP normalisation simultaneously with an MCMC. First, to test whether ground-based observations could further constrain the bulk planetary parameters achieved by *Spitzer*, each transit was individually fit for all planetary parameters including mid-transit time using posterior distributions from the *Spitzer* fitting as priors. However, such fits for planetary parameters proved to be significantly less constraining than the *Spitzer* fit, therefore, in a second step, the bulk planetary parameters were held fixed at *Spitzer* fit values (or *TESS* fit parameters for planet b), and fitting was performed only for mid-transit time and GP hyperparameters, using wide uninformative uniform priors, and for limb darkening parameters using LDTk. At first, this resulted in GP over-fitting, with a very small GP timescale tau, as well as likelihood splitting around two values of tau (a high and a low, with the low being associated with over-fitting), and thus two local likelihood maxima. This was resolved by running a "burn-in" phase of 600 steps, and then selecting the

highest likelihood walker value to initialize the subsequent run to convergence, which invariably resulted in the higher value of tau being selected.

Other ground-based observatory data including NGTS, TRAPPIST, PEST, and CHAT were carried out in an identical manner, with limb darkening coefficients fit using LDTk with each filter's respective transmission functions used as input. In all cases, for ground-based observatories, *Spitzer* data fitting resulted in more constrained planetary parameters, so these were again held fixed, and only the timing offsets, limb darkening, and GP hyperparameters were fit.

If, upon visual inspection, the fit resulted in an obviously incorrect transit center or clear residuals showing correlated noise, the transit was discarded. In all cases, this was due to either too few data points, or to significant residual correlated noise (often attributable to air mass). A clear anticorrelated trend of TTVs is shown between the two outer planets in Figure 2.7 with an amplitude of around 10 minutes, which is on the lower end of the range of the predictions made by G20. We perform dynamical analysis on these timing offsets in further detail in the following section.

2.4 Dynamical Analysis

2.4.1 TTV Retrieval

Our long-term followup campaign revealed a near-linear ephemeris for TOI-270 b and substantial, anti-correlated deviations from linear ephemerides for TOI-270 c and d. We modeled the transit timing data for all three planets using the `ttvfast` code (Deck et al., 2014a). Given the planetary and stellar masses along with the osculating planetary orbital elements (using the orbital periods instead of the semi-major axes) at the beginning of the integration, `ttvfast` rapidly forward-models the transit timings, which can then be compared to observations. Rather than fitting directly in these parameters, we chose a basis that allows us to speed up computations and avoid bias. First, rather than fitting for the eccentricity e and argument of periastron ω separately, we fit in the $(\sqrt{e}\cos\omega, \sqrt{e}\sin\omega)$ basis. This avoids the pitfalls of fitting for periodic parameters while naturally admitting a uniform prior on e and ω due to the constant Jacobian (Eastman et al., 2013).

Table 2.3: Planetary Parameters

Parameter	Source		
Planet b	**G20**	**Spitzer**	**TESS**
T_0	$1461.01464^{+0.00084}_{-0.00093}$		$1461.01556^{+0.0005859}_{-0.0005894}$
Period (days)	3.36008 ± 0.00007		3.36016 ± 0.000004
R_p/R_*	$0.0300^{+0.0015}_{-0.0011}$		$0.0307^{+0.0012}_{-0.00091}$
$\cos i$	$0.024^{+0.024}_{-0.015}$		$0.0267^{+0.0256}_{-0.0184}$
a/R_*	$17.48251^{+3.97329}_{-1.37537}$		$17.10761^{+3.52558}_{-1.85761}$
Planet c			
T_0	1463.08481 ± 0.00025	$1463.08056^{+0.00039}_{-0.00040}$	
Period (days)	5.66017 ± 0.00004	5.66057 ± 0.00001	5.66057 ± 0.00001
R_p/R_*	$0.05825^{+0.00079}_{-0.00058}$	0.05595 ± 0.00171	$0.05781^{+0.00067}_{-0.00058}$
$\cos i$	$0.0083^{+0.0073}_{-0.0051}$	$0.01393^{+0.00230}_{-0.00282}$	$0.00698^{+0.00657}_{-0.00476}$
a/R_*	$27.005^{+1.677}_{-0.591}$	25.5690 ± 0.3062	$27.443^{+0.512}_{-1.253}$
Planet d			
T_0	$1469.33834^{+0.00052}_{-0.00046}$	1469.33823 ± 0.00032	
Period (days)	$11.38014^{+0.00011}_{-0.00010}$	11.37948 ± 0.00002	11.37958 ± 0.00003
R_p/R_*	0.05143 ± 0.00074	0.04914 ± 0.00158	$0.05181^{+0.00048}_{-0.00078}$
$\cos i$	$0.0054^{+0.0021}_{-0.0027}$	$0.0062^{+0.0019}_{-0.0026}$	$0.0062^{+0.0028}_{-0.0043}$
a/R_*	$41.5627^{+0.864}_{-0.691}$	41.7437 ± 0.5274	$41.776^{+1.353}_{-0.359}$

Stellar parameters and planetary priors are drawn from G20 and are shown in the first column. T_0 is reported in days $(\mathrm{BJD}_{TDB}) - 2,457,000$. The middle column shows planetary parameters from fitting *Spitzer* transits as described above. The third column shows *TESS* fits incorporating all available data to date from sectors 3-5, 30 and 32. Limb darkening coefficients are not shown, as they were fit using LDTk (Parviainen & Aigrain, 2015) for each individual observatory and filter used. Timing fits were performed by fixing planetary parameters to the *Spitzer*-derived values for planet c, and for *TESS* all-sector values for planets b and d.

Second, we used the time of first transit as a convenient reparameterization of the mean anomaly [e.g.] (Jontof-Hutter et al., 2016; Libby-Roberts et al., 2020). Fourth, for the purposes of the dynamical modeling we fixed the inclinations and longitudes of ascending node to 90° and 0°, respectively. This is commonly done to reduce dimensionality in TTV modeling, as the signal has only a higher-order dependence on the mutual inclinations (e.g. Lithwick et al., 2012; Nesvorný & Vokrouhlický, 2014) which are known to be small for multi-planet systems in general (Fabrycky et al., 2014; Gilbert & Fabrycky, 2020) and for the multi-transiting TOI- 270 specifically (G20). All in all, we fit five parameters ($M_\mathrm{p}/M_\star$, P, $\sqrt{e}\cos\omega$,

$\sqrt{e}\sin\omega$, and T_0) for each of the three planets, giving a total of 15 fit parameters. Orbital elements were osculating and defined at the simulation start time BJD = 2458381 using Jacobi coordinates.

With our forward model defined, we proceeded to find the model parameters with Differential Evolution Markov Chain Monte Carlo (DEMCMC), implemented in the v3.0 of the `emcee` package (Foreman-Mackey et al., 2013a, 2019). We used Gaussian priors on the planet mass ratios from VE21, wide uniform priors on all other parameters, and these priors are noted in Table 2.4, labeled as "TTV+RV". We also ran a dynamical retrieval with wide uniform priors on the planet mass ratios to assess the degree to which the TTVs alone could constrain the system dynamics; those priors are noted in Table 2.4 as well and labeled "TTV-only". In this fit we used only linear ephemerides for planet b, fixing the eccentricity to 0 and the mass to the value from VE21, to isolate the dominant impact of the 2:1 resonance for planets c and d and improve convergence. When computing the likelihood, we assumed the data were drawn from a Student-t distribution with 2 degrees of freedom (DOF) rather than a Gaussian. Previous studies of *Kepler* TTV data found this distribution tends to better fit the timing residuals than a Gaussian (Jontof-Hutter et al., 2016; MacDonald et al., 2016), and the Student-t distribution can also help retrievals on large, heterogeneous datasets remain resilient to outliers (Agol et al., 2020). While Agol et al. (2020) use a Student-t distribution with 4 DOF for analysing TTVs in the TRAPPIST-1 system, we choose to adopt 2 DOF following Jontof-Hutter et al. (2016), whose Kepler residual histogram with more data points displays a higher signal to noise. We verified that these choices did not skew our results by first fitting the TTVs of the well-characterized three-planet system Kepler-51; we used the same fitting basis as Libby-Roberts et al. (2020) and reproduced their posteriors to well within 1σ on each of the model parameters.

We first optimized the model using the Powell minimizer implemented in `scipy.optimize.minimize`, and then initialized 48 walkers for our DEMCMC in a Gaussian ball around this starting point. We ran each chain for 5×10^6 steps to burn-in the sampler, and then proceeded to run for 2×10^7 steps. This rather

long chain length was required to capture more than 50 autocorrelation lengths in the $(\sqrt{e}\cos\omega, \sqrt{e}\sin\omega)$ parameters, whereas the other parameters converged comparatively rapidly. The posterior distributions for our model parameters are summarized in Table 2.4 and visualized for the TTV + RV fit in Figure A.2. For ease of comparison to VE21, we transformed the planet-to-star mass ratios back to the planetary masses in this Figure and Table.

The results of our TTV-only retrieval agree reasonably well with the analysis of VE21. The mass of planet c is concordant to within 1σ considering the uncertainty on both measurements, but there is a slight tension at the 1.5σ level between the results for planet d, with TTVs suggesting a slightly lower mass. However, the TTV-only masses are less precise than the RV masses. Still, the reasonable agreement between independently-derived masses suggests that both experiments have good control over systematic effects, and that the masses are realistic. Additionally, from our TTV-only posteriors we obtain a mass ratio of $M_{\rm d}/M_{\rm c} = 0.80^{+0.17}_{-0.14}$, in excellent agreement with VE21 who measured $M_{\rm d}/M_{\rm c} = 0.78 \pm 0.09$.

To get the full benefit of both datasets, we adopt our TTV+RV dynamical solution in Table 2.5, which is shown with the TTV data in Figure 2.7. The precision of the mass constraints are modestly increased for planets b and c, and are greatly improved for planet d. This is because the TTVs place strong constraints on the covariance between $M_{\rm c}$ and $M_{\rm d}$, so prior information on one or both of these masses results in a very precise posterior. We are further able to constrain the eccentricities and arguments of periastron for all three planets. The TTV data suggest that the eccentricities of the TOI-270 planets are quite low, with $e_{\rm b} < 0.024$ (95th-percentile), $e_{\rm c} = 0.00619^{+0.00092}_{-0.00088}$, and $e_{\rm d} < 0.011$ (95th-percentile). While we can only place an upper limit on the inner and outer planets' eccentricities, the eccentricity of TOI-270 c is detected. Moreover, the eccentricity constraints are not too affected by the choice of mass prior: for the uniform prior retrieval, we obtained $e_{\rm c} = 0.00575^{+0.00097}_{-0.00093}$, and $e_{\rm d} < 0.015$ (95th-percentile). More precise constraints on the masses and eccentricities will await further sampling of the TTV curve by *TESS* and other instruments.

2.4.2 Long-term Stability

Using these dynamical constraints, we performed a suite of tests aimed at characterizing the longer-term behavior of the system. To start, we loaded 100 random samples from our posterior into the `rebound` n-body integrator (Rein & Liu, 2012b; Rein & Spiegel, 2015). First, we integrated each sample for 100 yr, tracking the resonant arguments $2\lambda_d - \lambda_c - \varpi_c$ and $2\lambda_d - \lambda_c - \varpi_d$. We found that both arguments circulate rather than librate, suggesting that this system is only near and not in resonance despite the small resonant proximity $\Delta = \frac{P_d}{2P_c} - 1 = 5 \times 10^{-3}$. We then integrated ten samples for 1 Myr, finding them to be stable on these timescales. Longer integrations were prohibitively expensive as the timestep must be small enough to sample the 3.36 day orbit of the inner planet. We also integrated 1000 random samples for 10 kyr, and calculated the distribution for the Mean Exponential Growth of Neighboring Orbits (MEGNO) parameter (Cincotta & Simó, 2000; Rein & Tamayo, 2016). We found the entire sample was tightly clustered around a MEGNO of 2, indicating the system is not rapidly chaotic. Together, these tests suggest the stability and dynamical regularity of the system.

We then performed a longer time scale analysis of stability, making use of the Stability Orbital Configuration Klassifier (SPOCK) (Tamayo et al., 2020), a machine-learning model capable of classifying the stability of compact 3+ planetary systems with period ratios of adjacent planets $\lesssim$2 over 10^9 orbits of the innermost planet, which for our case is $\sim 10^7$ yr. First, we computed the stability of the system by considering the nominal values of the planet parameters derived from our TTV analysis combined with the results of the RV follow-up made by VE21. We used the two models provided by SPOCK: the original machine-learning model `FeatureClassier`, and `DeepRegressor`, a Bayesian neural network model (Cranmer et al., 2021). Using these models we found that the system has a stability probability of 92% and 97%, respectively. Then, once it was established that the system is highly stable in its nominal configuration, we explored the masses and eccentricities of the planets, i.e., the parameters which have the most dramatic effect on the orbital dynamics, by building stability maps of adjacent planets. This was

motivated by the fact that perturbation effects among planets fall exponentially with their separation; therefore, non-adjacent interactions can be neglected (Cranmer et al., 2021; Petit et al., 2020; Quillen, 2011). The map building entailed exploring the parameter space M_b–M_c and e_b–e_c for the inner planets b and c, and M_c–M_d and e_c–e_d for planets c and d. In each case, we explored each parameter within its uncertainty up to 5σ. In our sets of simulations, we took 10 values from each range, meaning that the size of the stability maps were 10×10 pixels. We made use of the two algorithms `FeatureClassier` and `DeepRegressor`. In the case of `FeatureClassier`, for each scenario we set 20 different random initial conditions by varying the longitude of the ascending node and mean anomaly in the range 0–360 deg. We then averaged these 20 initial conditions to obtain the averaged probability. On the other hand, in the case of `DeepRegressor`, due to its higher computational cost we only set 5 different random initial conditions. Hence, for each stability map, we ran 2000 simulations with `FeatureClassier` and 500 with `DeepRegressor`. For each stability map, using `FeatureClassier` and `DeepRegressor` respectively, we found the following stability probabilities: (1) for the M_b–M_c map, values of $\gtrsim$92% and $\gtrsim$97%; (2) for the e_b–e_c map we found $\gtrsim$70% and $\gtrsim$97%; (3) for the M_c–M_d map we found $\gtrsim$83% and $\gtrsim$97%; and (4) for the e_c–e_d map we found $\gtrsim$86% and $\gtrsim$97%. These results hint that the system is very stable in the 5σ range of masses and eccentricities.

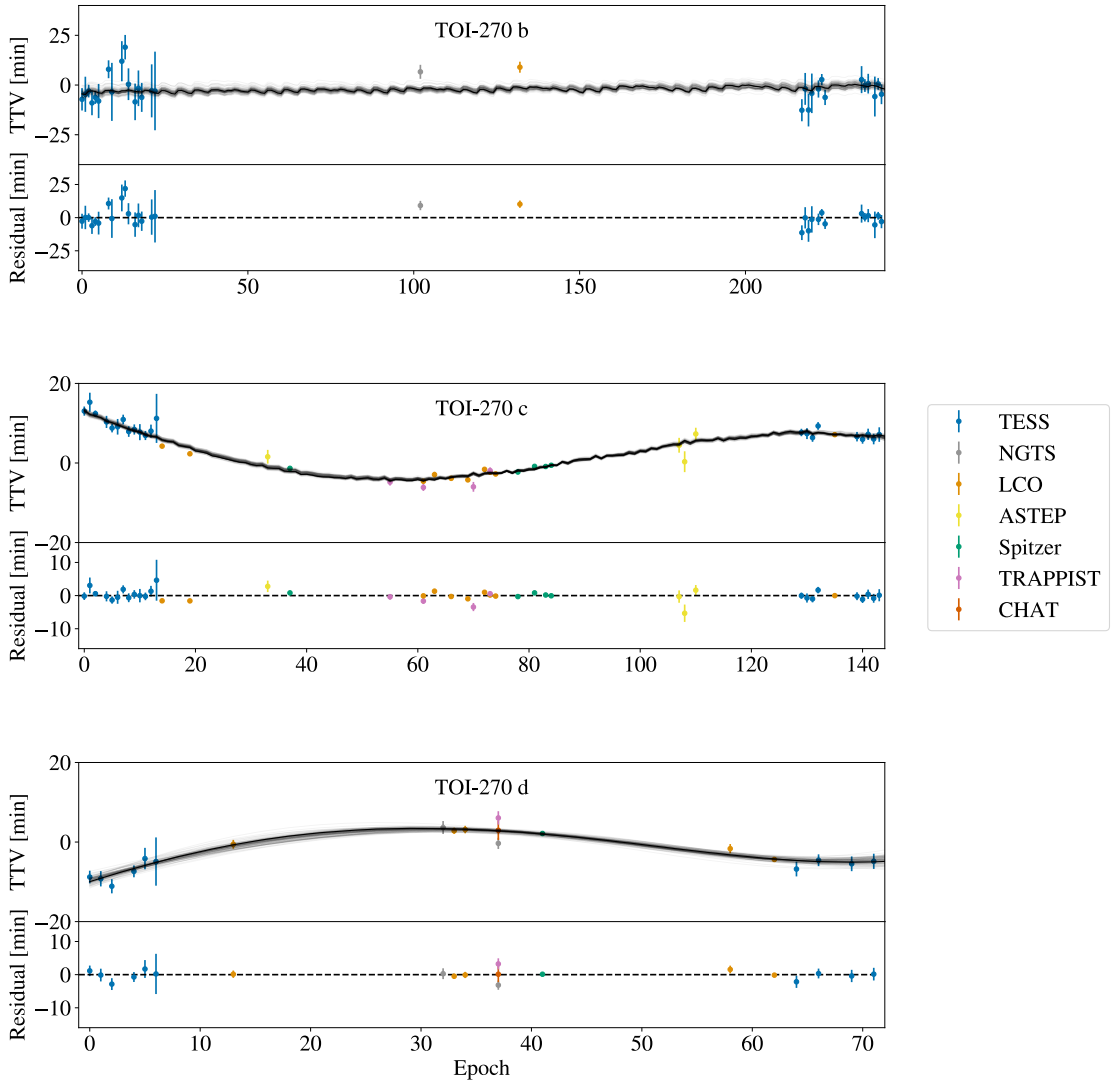


Figure 2.7: Results of the TTV analysis. In the top panels, the timing data are shown with a linear ephemeris (determined via least-squares) removed. We show the MAP model with dark blue curves, and 100 random samples from the posterior are plotted in light blue to give a sense for the uncertainty. In the bottom panels, the residuals from the MAP model are given, with the black dashed line indicating a perfect fit.

Table 2.4: Orbital and planetary parameters fit for.

Parameter	Prior (TTV+RV)	Posterior 1 (TTV+RV; adopted)	Prior 2 (TTV-only)	Posterior 2 (TTV-only)	Units
M_b	$\mathcal{N}(1.58, 0.26)$	$1.48^{+0.19}_{-0.18}$	1.58 (fixed)	–	$M_\oplus$
P_b	$\mathcal{U}(3.35, 3.37)$	$3.35992^{+0.00005}_{-0.00004}$	$\mathcal{U}(3.35, 3.37)$	$3.35999^{+0.00005}_{-0.00007}$	days
$\sqrt{e_\mathrm{b}}\cos\omega_\mathrm{b}$	$\mathcal{U}(-0.7, 0.7)$	$0.007^{+0.085}_{-0.067}$	0 (fixed)	–	–
$\sqrt{e_\mathrm{b}}\sin\omega_\mathrm{b}$	$\mathcal{U}(-0.7, 0.7)$	$-0.005^{+0.061}_{-0.059}$	0 (fixed)	–	–
$T_{0,\mathrm{b}}$	$\mathcal{U}(2.65, 2.81)$	$2.72985^{+0.00111}_{-0.00129}$	$\mathcal{U}(2.65, 2.81)$	$2.7301^{+0.0012}_{-0.0013}$	days
M_c	$\mathcal{N}(6.14, 0.38)$	$6.20^{+0.31}_{-0.30}$	$\mathcal{U}(0, 50)$	$4.5^{+1.7}_{-1.2}$	$M_\oplus$
P_c	$\mathcal{U}(5.65, 5.67)$	5.66051 ± 0.00004	$\mathcal{U}(5.65, 5.67)$	5.66052 ± 0.00005	days
$\sqrt{e_\mathrm{c}}\cos\omega_\mathrm{c}$	$\mathcal{U}(-0.7, 0.7)$	$0.008^{+0.019}_{-0.017}$	$\mathcal{U}(-0.7, 0.7)$	$-0.025^{+0.014}_{-0.015}$	–
$\sqrt{e_\mathrm{c}}\sin\omega_\mathrm{c}$	$\mathcal{U}(-0.7, 0.7)$	$0.077^{+0.006}_{-0.007}$	$\mathcal{U}(-0.7, 0.7)$	$0.0700^{+0.0058}_{-0.0055}$	–
$T_{0,\mathrm{c}}$	$\mathcal{U}(2.82, 2.86)$	2.8417 ± 0.0003	$\mathcal{U}(2.82, 2.86)$	$2.84157^{+0.00029}_{-0.00029}$	days
M_d	$\mathcal{N}(4.78, 0.46)$	4.20 ± 0.16	$\mathcal{U}(0, 50)$	$3.62^{+0.47}_{-0.47}$	$M_\oplus$
P_d	$\mathcal{U}(11.36, 11.4)$	11.38194 ± 0.00010	$\mathcal{U}(11.36, 11.4)$	$11.38165^{+0.00045}_{-0.00033}$	days
$\sqrt{e_\mathrm{d}}\cos\omega_\mathrm{d}$	$\mathcal{U}(-0.7, 0.7)$	$-0.021^{+0.071}_{-0.041}$	$\mathcal{U}(-0.7, 0.7)$	$-0.090^{+0.021}_{-0.017}$	–
$\sqrt{e_\mathrm{d}}\sin\omega_\mathrm{d}$	$\mathcal{U}(-0.7, 0.7)$	$0.047^{+0.024}_{-0.036}$	$\mathcal{U}(-0.7, 0.7)$	$0.016^{+0.026}_{-0.021}$	–
$T_{0,\mathrm{d}}$	$\mathcal{U}(8.66, 8.70)$	8.68021 ± 0.00052	$\mathcal{U}(8.66, 8.70)$	$8.67964^{+0.00071}_{-0.00073}$	days

Table 2.4: Orbital elements are osculating and defined using Jacobi coordinates at the simulation start time BJD = 2458381.

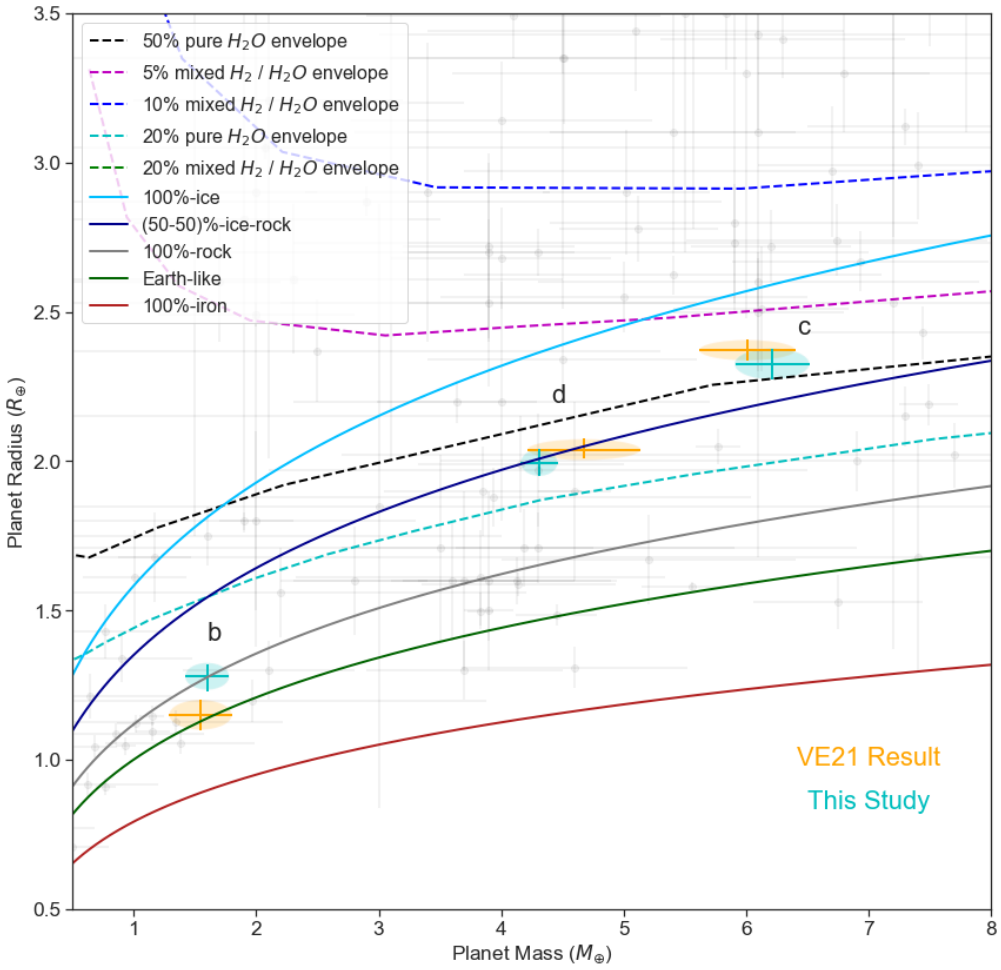


Figure 2.8: Mass fits shown against a population of small mass and radius known exoplanets obtained from the NASA Exoplanet Archive (in grey). The orange points represents the RV mass priors from VE21, which are consistent with the posterior to two sigma level, and the teal points show the results of our TTV fit. Because our TTV fitting does not incorporate planetary radius, these two parameters are not correlated in our study. The dotted lines describe gas envelopes of varying composition. All composition profiles are from Kopparapu et al. (2014) (water/ice: H_2O; rock: Mg_2SiO4; iron: Fe; Earth-like: 67% rock / 33% iron)

.

Parameter	**Value**			**Source**
Star	**TOI- 270**, TIC 259377017, L231-32			
Right ascension, Declination (J2000)	04h33m39.72s, -51°57022.44"			
Longitude, Latitude (ecl. J2000)	02h52m35.24s, -71°53049.29"			
Magnitudes	V = 12.62, TESS = 10.416, J = 9.099 ± 0.032, Gaia = 11.63			
	H = 8.531 ± 0.073, K = 8.251 ± 0.029			
Distance, d_* (parsec)	22.453 ± 0.021			
Mass, M_* ($M_\odot$)	0.386 ± 0.008			fit
Radius, R_* ($R_\odot$)	0.380 ± 0.008			fit
Density, g/cm^3	10.63 ± 0.74			derived
Effective temperature, T_e (K)	3506 ± 70			
Surface gravity $\log(g)$ (cgs)	4.872 ± 0.026			
Parameter	**b**	**c**	**d**	**Source**
$T_0 - 2,457,000$ (BJD)	$1461.01464^{+0.00084}_{-0.00093}$	1463.08056±0.00040	1469.33823±0.00032	fit
Period (days)	3.35992±0.00005	5.66051 ± 0.00004	11.38194±0.00011	fit
R_p/R_*	$0.0307^{+0.0012}_{-0.0009}$	0.0560 ±0.0017	0.0491±0.0016	derived
$\cos i$	$0.0267^{+0.0256}_{-0.0184}$	$0.01393^{+0.00230}_{-0.00282}$	$0.0062^{+0.0019}_{-0.0026}$	fit
a/R_*	$17.108^{+3.526}_{-1.858}$	25.569±0.306	41.744±0.527	derived
mass $M_\oplus$	1.48±0.18	6.20 ± 0.31	4.20±0.16	fit
radius $R_\oplus$	$1.28\ ^{+0.05}_{-0.04}$	2.33±.01	2.00±.05	fit
eccentricity e	$0.0167^{+0.0084}_{-0.0089}$	$0.0044^{+0.0005}_{-0.0006}$	0.0066±0.0020	fit
impact parameter b	0.48 ± 0.46	0.35 ± 0.06	0.23 ± 0.08	derived
transit dur (hours)	1.294±0.026	1.682±0.019	2.117±0.018	derived
density ρ_p (g/cm^3)	3.89±0.66	2.70±0.14	2.90±0.24	derived
T_{eq} (albedo = 0.3)	548±15	448±10	351±8	derived
T_{eq} (albedo = 0)	600±16	489±11	383±9	derived
surface gravity $\log_{10}(g)$ (cgs)	2.95±0.43	3.05±0.15	3.01±0.19	derived

Table 2.5: Stellar and Planetary Parameters Stellar parameters are drawn from VE21 and G20. Both fit and derived planetary parameters from this study are shown. Timing fits were performed by fixing planetary parameters to the *Spitzer*-derived values for planet c, and for *TESS* all-sector values for planets b and d.

2.5 Results and Discussion

By combining our transit timing results with RV follow-up from VE21, we arrive at precise masses of 1.48±0.18 $M_\oplus$ for planet b, 6.20±0.31 $M_\oplus$ for planet c, and 4.20±0.16 $M_\oplus$ for planet d. We also detect eccentricities for all three planets of $e_\mathrm{b} = 0.0167^{+0.0084}_{-0.0089}$, $e_\mathrm{c} = 0.0044^{+0.0005}_{-0.0006}$ and $e_\mathrm{d}0.0066 \pm 0.0020$.

For the star, we find a density of 10.63 ± 0.74 g/cm^3, in agreement with previous studies. No notable correlation was observed in the stellar parameters being fit, nor was any found in the RV analysis performed by VE21. The final results, including the adopted stellar parameters for all three planets are summarized in Table 2.5. We are thus also able to further refine the system's ephemerides, which will be crucial for accurate planning of future transit observations and spectral studies.

2.5.1 Combined TTV and RV Analysis

There are only a small handful of exoplanetary systems (about a dozen) for which TTVs and RV data have been analysed both together and separately. In the case of the previously mentioned Kepler 9 system discovered by Holman et al. (2010), which was the first system characterized by TTVs, a series of follow-up studies (Borsato et al., 2014; Borsato et al., 2019) used high precision RVs in combination with TTVs to better determine the system's masses. While the initial studies reported discrepant masses, with the TTV analysis giving significantly lower masses than those produced by the RV analysis, the 2019 reanalysis with further *Kepler* transits and followup with HARPS-North revealed agreement between mass estimates with the two methods (Borsato et al., 2019).

K2-19 is another 3-planet, jointly analysed system which is comprised of a Neptune sized inner planet and a Saturn sized planet in a 2:1 mean motion resonance, as well as a close-in Earth sized planet found in K2 data (Armstrong et al., 2015; Nespral et al., 2017). In a similar manner to this study, RV and TTV follow-up of K2-19 by Nespral et al. (2017) demonstrated either approach's ability to constrain planetary masses, and further refine them through joint analysis. WASP 47 is a system with four known planets: a hot Jupiter, two sub-Neptunes, and an eccentric,

long period giant planet (Becker et al., 2015). Combining RV data with several years of TTV data allowed for more accurate masses to be obtained for the three inner planets, enabling a clearer picture of these planet's likely 2-part evolutionary history to be formed (Weiss et al., 2017).

Nonetheless, several recent studies have noted systematic discrepancies between TTV and RV analyses (Weiss et al., 2013; Masuda et al., 2013). Weiss & Marcy (2014) noted that for small planets ($<4\,M_{\oplus}$) TTV studies found systematically lower masses than did RV analyses of the same systems, with Malavolta et al. (2017) positing that such discrepancies could arise from other planets damping the observed effects. Mills & Mazeh (2017) show that these differences are present for planets with periods of greater than 11 days, while shorter period planets generally find good agreement. Our study points to the compatibility of these two approaches, but more systems with masses analysed jointly by both TTVs and RVs could further illuminate the source of these systematic tensions.

2.5.2 Evolution and Additional Planets

Systems exhibiting mean-motion resonance can be powerful indicators of evolution. Current models of planetary formation allow for planets to form at any distance, and it is thought that mean motion resonance develops later on due to dissipative forces, rather than as a direct result of planetary formation. For example, in the two planet, 2:1 MMR system K2-24, the magnitude of the observed TTVs indicates that disk migration alone could not produce its current configuration, pointing to the role of disk eccentricity damping and excitation, as well as the possible presence of a third planet (Teyssandier & Libert, 2020). Mills et al. (2016b) demonstrate through the example of the resonant chain in the 4-planet Kepler 223 system, that migration resulting in often-temporary resonances is likely responsible for the orbits of many close-in sub-Neptune planets.

TTV measurements can also provide significant evidence of further non-transiting planetary companions whose orbits are distributed across inclinations (Brakensiek & Ragozzine, 2016). While our results do not cover enough of a superperiod to

provide direct evidence, they leave open the possibility of an additional planet TOI-270 e either within the orbit of planet b or outside the orbit of planet d. As can be seen in the top panel of Figure 2.7, planet b contains several points that are outliers to the main trend line. Individual planet b transits proved difficult to fit and were typically not discernible by eye, so it is likely these are genuine outliers where the fit was sensitive to air mass and correlated noise. However it is possible that these points should not be treated as outliers and that further follow-up will reveal a longer superperiod trend for this planet, which could be further indication of a non-transiting companion. With continued monitoring of this system, we can place further constraints on any possible undiscovered companions.

2.5.3 Atmospheric and Composition

Our analysis produces densities for the TOI-270 planets of $3.89 \pm 0.66 g/\mathrm{cm}^3$, $2.70 \pm 0.14 g/\mathrm{cm}^3$ and $2.90 \pm 0.24 g/\mathrm{cm}^3$ for planets b, c, and d respectively. Their mass-radius relation places them in the region of super-Earth and sub-Neptunes, as seen in Figure 2.8. The inner-most planet has a significantly higher density making its composition likely rocky and Earth-like. To date, TOI-270 b is one of the smallest planets to be characterised with joint TTV and RV analysis, the others consisting of members of the TRAPPIST-1 system (Agol et al., 2021). TOI-270 c and TOI-270 d have lower densities, which suggests similarly rocky core composition with the addition of a more substantial H/He atmosphere. Compared to VE21, our adopted radii change the densities for planet c and d slightly. As seen in Figure 2.8, this does not alter the bulk planetary characteristics significantly, but shifts the atmospheric composition, increasing the ratio of H_2 to H_2O.

2.5.4 Potential for Atmospheric Characterization

Planets between the size of Earth and Neptune are very common results of planet formation, and it appears that approximately half of Sun-like stars have at least one sub-Neptune in an orbit closer than that of Mercury (Petigura et al., 2013). However, no such planets exist in our solar system and our understanding of their

evolution and atmospheres remain limited. One of the best studied sub-Neptunes to date is GJ 1214 b which has a very flat transmission spectrum, most likely because of a high altitude haze formed through methane photochemistry (Kreidberg et al., 2014a; White et al., 2021).

Cool sub-Neptunes in particular are useful probes of planet formation. Because they have not been exposed to such extreme photoevaporation as their more heavily irradiated counterparts, they retain more of their initial atmospheres. In the case where the planet is relatively free from clouds or haze, this can be paired with spectroscopic observations to provide excellent evidence for different models of planet formation. Even with haze present, as is the case for GJ 1214 b, and simulated analogues, Hood et al. (2021) demonstrates that with high resolution infrared transmission spectra, numerous molecular features (such as for H_2O, CO, and CO_2) can be detected in hazy sub-Neptune spectra that otherwise appear "featureless", with even more promise at higher resolution with upcoming ELT instruments. White et al. (2021) further demonstrate the potential of JWST to penetrate through hazy layers and detect features of CO_2 and CH_4 for GJ 1214 b,.

We calculated the transmission spectra metric (TSM) for the planets of TOI- 270 as described by Kempton et al. (2018), which is meant to identify top *TESS* targets for atmospheric characterization defining an expected signal-to-noise for a given planet's transmission and emission spectroscopy, and which enables us to compare the amenability to atmospheric follow-up of our system with that of others. All three targets fall well above the suggested cutoff for follow-up and amongst the highest (most promising) for small-sized targets below 600K. Planet b, which is classed by Kempton et al. (2018) as terrestrial, has a TSM of 102.1, above the a suggested TSM cutoff of 12. Planets c and d, which are classed as small sub-Neptunes, have TSMs of 125.8 and 124.0 respectively, above the suggested cutoff of 92.

2.6 Conclusion and Future Work

This chapter reports on two years of follow-up transit observations of the three TOI- 270 planets, detecting significant TTVs which enable us to refine planetary

parameters, masses, and eccentricities.

This work demonstrates the potential of TTV and joint TTV-RV analyses to refine the orbital parameters and masses of small near-resonant planets to within 5-10%. Systems that have been jointly analysed by these approaches are limited, and as *TESS* re-observes targets from previous cycles in the coming years, further such studies could serve to emphasize the strengths of this combination as well as help elucidate potential discrepancies and systematic biases.

Our work in this chapter took a self-consistent approach to light curve analysis between eight different observatories, including reanalysing *TESS* data with the inclusion of new observations from Cycle 3, finding largely consistent refinements to planetary parameters and orbital ephemerides found by G20 and VE21, and producing a picture of a dynamically stable system of super-Earth/sub-Neptune planets which show significant promise for future comparative planetology through atmospheric studies. TOI-270 continued to be observed through 2021 with transit studies done with *LCO* (program id *LCO* 2021A, PI Parviainen), *ASTEP*, *NGTS*, and *TRAPPIST*.

Ongoing observations of TOI-270 with *HST* (program id GO-15814, PI Mikal-Evans) should provide a valuable glimpse into the system's chemical abundances, as well as a unique opportunity for comparison between the two outer planets, whose similar size and density lends itself extremely well to comparative planetology. Of particular interest is the methane content of each planet, which is expected to be measured to high sensitivity, as is the presence or absence of photochemical haze on either or both of the planets, which would allow for a direct comparison of the effect of temperature and irradiation on haze production.

Obtaining accurate masses is critical to the interpretation of follow-up atmospheric studies and evolutionary models, and provides further insight into the benefits of joint TTV and RV analyses. Follow-up observations from NGTS, ASTEP and TESS have provided more data points that did not fall in the timeframe of Kaye et al. (2022), and which have been analysed independently. These will be discussed in Chapter 4 in Section 4.4.

Where there is an observatory and a telescope, we expect that any eyes will see new worlds at once.

— Henry David Thoreau

CHAPTER 3

Transit Timing Variations from Kepler and K2 to TESS

3.1 Introduction

Both the original Kepler mission, and the later K2 mission were highly prolific, discovering over half of the approximately 5,000 validated exoplanets to date (Borucki et al., 2010; Howell et al., 2014). While the success of these missions is undeniable, accurate and up-to-date ephemerides are critical in order for meaningful follow-up to take place. As the primary successor to Kepler in space-based exoplanet-hunting missions (*TESS*) is a natural tool to turn to when it comes to re-examining these earlier discoveries. However, unlike the Kepler mission, which continuously looked at one small patch of sky for several years, or K2, which searched equatorially for several months at a time, TESS examines large swaths or sectors in 27 day increments. To date, TESS has reexamined most of the Kepler and K2 fields anywhere from once to three or more times between 2019 and 2022, as can be seen in Figure 3.1. This provides the unique opportunity to take a long look at Kepler and K2 systems over a period spanning nearly a decade.

A notable benefit of taking such a long look is the ability to search for long-term trends in transit timings. A scoping search for TTVs in the Kepler and K2 field

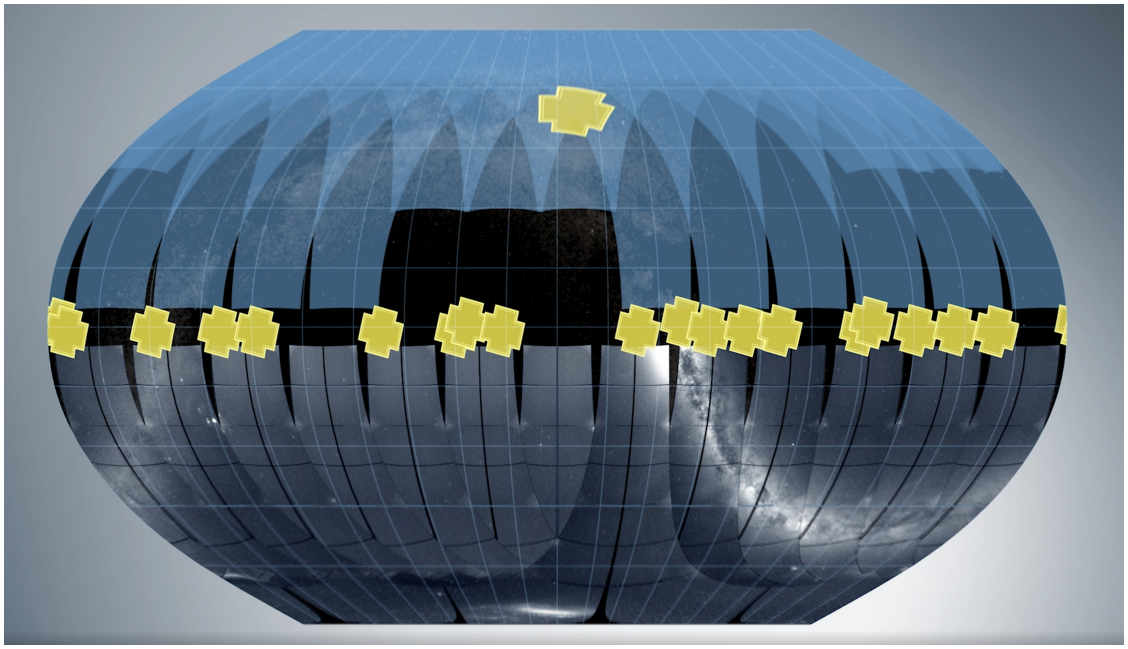


Figure 3.1: The central yellow field raised from the ecliptic depicts the original Kepler field, while the equatorially spread fields are the various sectors of the K2, which relied on minimizing solar pressure during pointing with only two remaining reaction wheels. Overlying these are the TESS sectors 1-40. These fields are further highlighted in Figure 3.2

was initially performed by Mazeh et al. (2013), who found 130 systems amongst 721 Kepler Objects of Interest (KOIs) that showed evidence of either periodic TTVs or shorter time-scale modulations with small amplitudes. This enabled the creation of a public catalogue of transit timing and transit durations for the Kepler mission by Holczer et al. (2016). In this later, more complete study, transit times were extracted from a total of 2599 KOIs in the Kepler long-cadence data set, with 260 of these showing significant long-term TTVs. An analysis of planetary masses and eccentricities from these results was performed by Hadden & Lithwick (2016), enabling robust mass calculations for half of the systems.

As seen in the previous chapter with the example of TOI-270, TTV analysis enables us to refine planetary mass estimates and orbital eccentricities, and provide insight into composition critical for atmospheric follow-up (Fabrycky et al., 2014; Nespral et al., 2017), provide evidence of further non-transiting planets (Ballard et al., 2011; Nesvorný & Vokrouhlický, 2014), or indicate other effects such as orbital evolution from disk friction or tidal orbital decay (Christ et al., 2019; Birkby et al.,

2014). However, because the length of a TTV dynamic cycle, or superperiod, can span many years, it is very possible that long term trends exist that were not spotted in the time frame of a planet's Kepler or especially the shorter K2 observing sector.

Several Kepler systems have been followed up more recently by Battley et al. (2021); Demory et al. (2020); Ikwut-Ukwa et al. (2020), which re-examined systems with known TTVs or with known planets near to orbital resonance. Battley et al. (2021) examined 22 Kepler systems in total, providing significant improvements to the linear ephemerides of 4 systems. Ikwut-Ukwa et al. (2020) similarly examines a total of 4 systems discovered by K2, chosen for their observability by TESS. These studies highlight the utility of reexamining Kepler targets for more in depth system parameterisation and to obtain updated ephemerides critical for follow-up.

In this chapter we expand on these previous follow-ups by re-examining over one hundred Kepler and K2 systems systems that were re-observed with TESS with high signal to noise, and take a more systematic approach to their analysis. We also include TESS data up to and including Cycle 4. We seek to refine linear ephemerides, which help with future observation scheduling and atmospheric studies, as well as to follow-up on systems with known TTVs. We further hope to identify planets for which there is evidence of long-term variation that was not previously observed. The rest of this chapter is structured as follows. Section 3.2 details the methods of target selection and inclusion in this study, Section 3.3 discusses the observations from Kepler, K2, and TESS before discussing light curve fitting and analysis in Section 3.4. We present our results in Section 3.6 before discussing the implications of our findings in Section 3.7.

3.2 Target Selection

Most Kepler systems are too faint for detailed follow-up with RV analysis or ground-based telescopes (Ricker et al., 2014). However TESS has reobserved much of the Kepler and K2 field, sometimes multiple times, in its four year mission. A study by Christ et al. (2019) calculated that TESS should detect 260 Kepler planets in one sector and 120 planets in two or more sectors, not including K2 planets being

reobserved by TESS. While Christ et al. (2019) points out that hot Jupiters will be the easiest planets to reobserve and detect in TESS, it should be possible to detect a handful of smaller Neptune-sized, or even rocky planets.

For this study, targets were initially selected based on whether they appeared in either Kepler or K2, including KOIs, and were reobserved in at least one TESS sector. A signal to noise (SNR) per transit estimation was made for each target as follows

$$\mathrm{SNR} = \frac{\delta}{\sigma_T} \times \sqrt{t_{\mathrm{dur}} \times \Delta t} \tag{3.1}$$

Where δ is the transit depth σ_T is the expected noise level of TESS observations (calculated per target using ticgen (Jaffe, 2017), and $t_{\mathrm{dur}} \times \Delta t$ gives the number of data points per transit, where Δt is the time interval between consecutive data points. In the TTV catalog of KOIs produced by Mazeh et al. (2013) and Holczer et al. (2016), target selection and refinement was grouped into three categories on the basis of SNR.

For our study, we we initially restricted ourselves to Kepler and K2 TOIs for which the estimated SNR per transit 2.5, following (Mazeh et al., 2013), who used this cutoff for Kepler planets, but eventually extended this down to an SNR of 2. To arrive at this value, we explored the detectability of individual TESS transits at each level of SNR, as well as the transit timing uncertainty, with the aim of developing an SNR cutoff around which TESS transits were either not detectable (as described below) or could offer no improvement on the linear ephemeris of Kepler or K2 data alone. Transit detection was determined through cross correlation as described below in Section 3.4.4. If a transit was not detected, it was discarded from further analysis, and if more than half of a system's TESS transits were not detected, the system was fully excluded from further analysis for being too faint to offer an accurate or helpful improvement on linear ephemeris or evidence of TTVs.

Although 293 targets of SNR > 2 fall into the coverage of at least one TESS sector, TESS light curves were only produced for 196 of these. For several long period planets, no transits aligned within the time frame of the sector being observed,

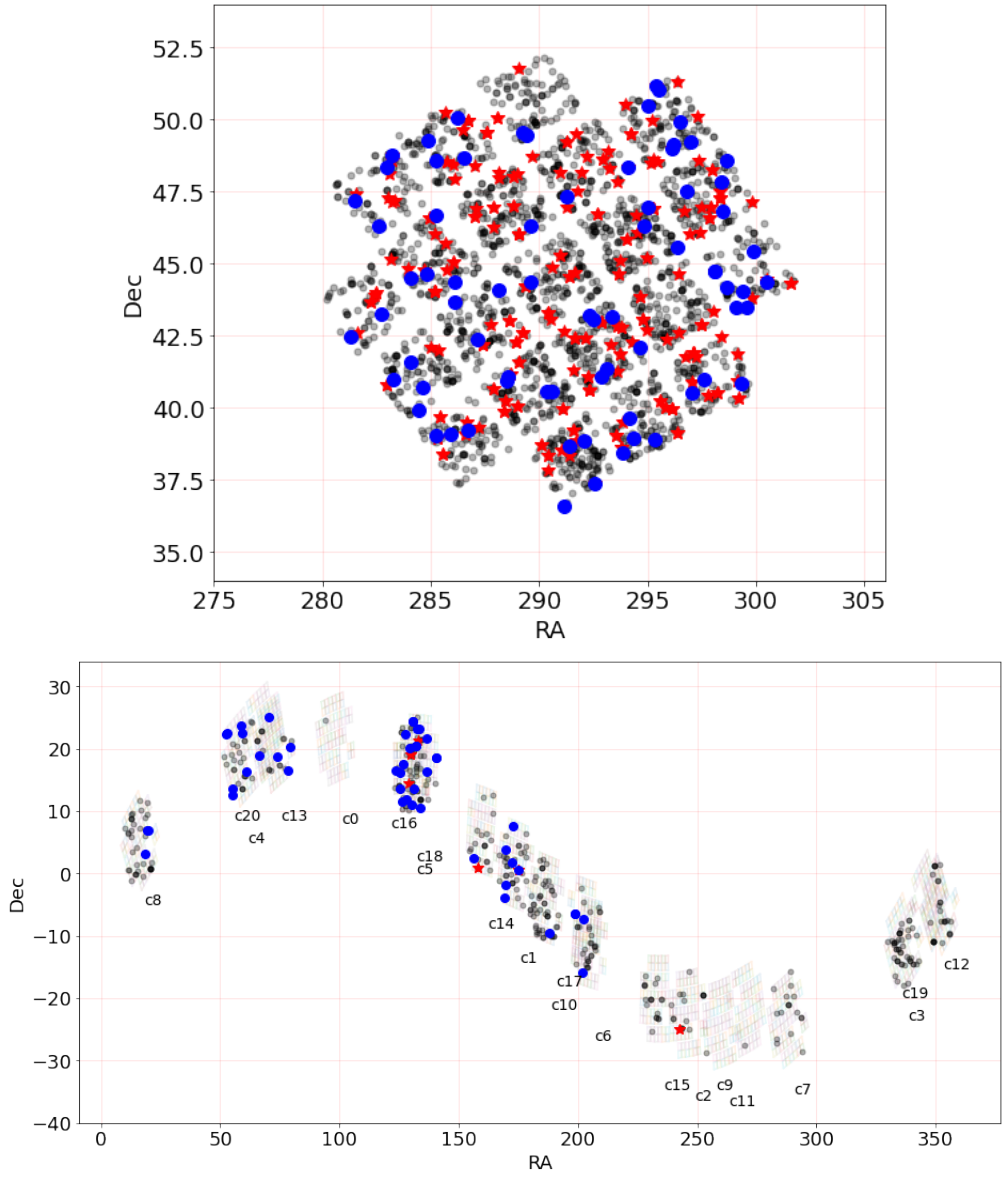


Figure 3.2: The top panel shows the original Kepler field and the bottom panel shows the K2 fields. Red star markers indicate systems with TTVs known prior to the study. Green circles indicate multi-planet systems. Blue markers show the systems selected for this study reobserved with adequate SNR in at least one sector of TESS.

leaving 150 planets with at least one full transit covered by TESS. These planets can be seen in blue in Figure 3.2.

The majority (114) of Kepler and K2 targets in this group were only observed in one TESS sector, though 36 were observed in 2 sectors. This contrasts with the proportion predicted by Christ et al. (2019) where they found that TESS should detect 260 Kepler planets in one sector and 120 planets in two or more

sectors, though their detections relied on stacking transits, which enables fainter detections than individual transit fits.

While higher SNR systems tend to favour planets with large radii, our population represents a wide range with several dozen super earths and sub-Neptunes. 17 systems have periods greater than 30 days, and one planet (Kepler-51 d) has a period of 130 days, with a transit that happened to align with TESS sector 41. A period-radius distribution of the final population along with timing trends uncovered in this analysis is presented in Figure 3.10.

3.3 Observations

This section details the observations and data reduction of each mission, which follow a similar pattern to the data reduction performed for TOI-270 in the previous chapter.

3.3.1 Kepler

Kepler's primary mission, which ran nearly continuously for 4 years between 2009 and 2013 until the failure of its second reaction wheel, is responsible for the discovery of thousands of planets in the constellations of Cygnus and Lyra, including several earthlike planets in the habitable zone of their stars (Borucki et al., 2010). It observed most of its targets in 30 minute cadence mode, with the exception of 512 pre-selected targets for which it observed with 1 minute cadence (Thompson et al., 2016).

Publicly available transit light curves for a pre-selected list of targets were taken from the Mikulski Archive for Space Telescopes (MAST). We utilized the PDC-SAP light curves extracted by the Kepler science processing pipeline (Jenkins et al., 2010). This flux employs an aperture mask made of a subset of pixels that capture the highest SNR of flux from a target. It then detrends the data, removing instrumental and spacecraft anomalies as well as data artifacts. Further detrending was performed as described in Section 3.4.

3.3.2 K2

We can recall from the introduction, the K2 mission was an extension of the original Kepler mission that was put into place when two of the original reactor wheels failed for Kepler. By observing along the ecliptic, and rotating its field of view every three months to continue pointing away from the sun, the effects of solar radiation pressure were minimized, allowing the spacecraft to maintain stability (Howell et al., 2014). In the years from 2014-2018, it added significantly to the growing population of confirmed Kepler exoplanets, contributing a couple hundred planets and many more planet candidates.

Each target was observed once for a period of 80 days in one of 20 sectors located along the ecliptic, some of which overlap as can be seen in the lower half of Figure 3.2. K2 observed targets in either long cadence (30 minute images) or short cadence (1 minute images) mode: both are used for various targets in this study. Several data pipelines are available to correct for K2s pointing accuracy and systematic noise. For this study, we chose to use the EPIC Variability Extraction and Removal for Exoplanet Science Targets pipeline EVEREST which employs pixel-level correlation as described in Deming et al. (2015) to remove systematics and achieve a comparable precision to the original Kepler mission (Luger et al., 2018) (Luger et al., 2016). While other pipelines such as K2SFF (Vanderburg & Johnson, 2014b), K2S (Aigrain et al., 2016b) are also effective at correcting for K2 systematics, EVEREST has been shown to be marginally better at reducing K2 systematics across both long and short cadence data (Hirano et al., 2018).

3.3.3 *TESS*

The entire Kepler field was re-observed by TESS from 2019-2020, primarily in Sector 14, with 962 stars pre-selected to receive 2minute cadence data. Parts of it were also observed in sectors 15, and 26. It was then more recently observed in 2021 in Sector's 40 and 41, and again in sectors 53-55 in 2022. Because the K2 fields lie along the ecliptic, many stars will never be observed by TESS, which avoids the ecliptic, however, because these fields are more numerous, enough overlap

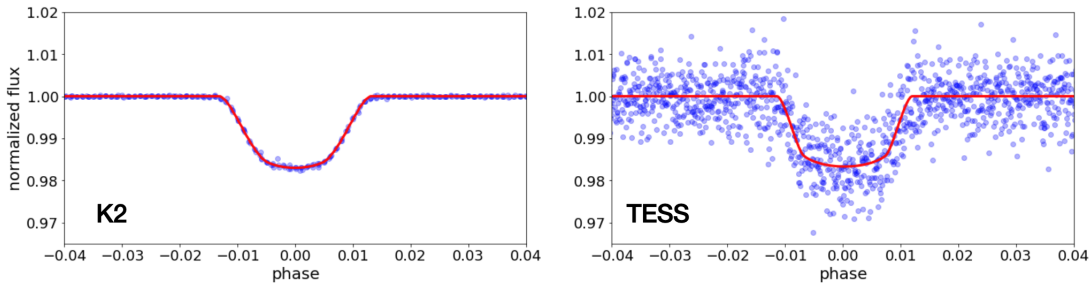


Figure 3.3: K2-30 b is a warm Jupiter with an orbital period of 11.6 days. Transit data are phase folded around the best-fit period, totalling 17 transits in K2 and 5 transits in TESS. With a SNR of 29, while its transits are quite clear in both K2 and TESS data, there is a pronounced difference in the two data sets which will limit the precision of transit time measurements for the latter.

occurs to make this interesting. We used data from Cycles 1-4 in this work, which concluded with sector 55 in September 2022.

The data were reduced and light curves extracted using the Science Processing Operations Center (SPOC) pipeline (Jenkins, 2002; Jenkins et al., 2010; Smith et al., 2012; Stumpe et al., 2014; Jenkins et al., 2016; Jenkins, 2017). We extracted the 2-minute cadence PDC-SAP light curves, in which most systematic effects have already been corrected (Stumpe et al., 2012; Smith et al., 2012; Stumpe et al., 2014), which became the starting point for our further detrending and analysis.

3.4 Light curve analysis

When analysing the photometric data across two different missions, our aim was to be as self-consistent as possible between Kepler and TESS while acknowledging the limits of these two different datasets, namely TESS's higher scatter, as can be appreciated in Figure 3.3 and more limited observing windows, as well as differences in limb darkening.

3.4.1 Overview

An overview of the fitting and analysis process for each planet is as follows and is then described in greater detail in the following sections: For every target for which

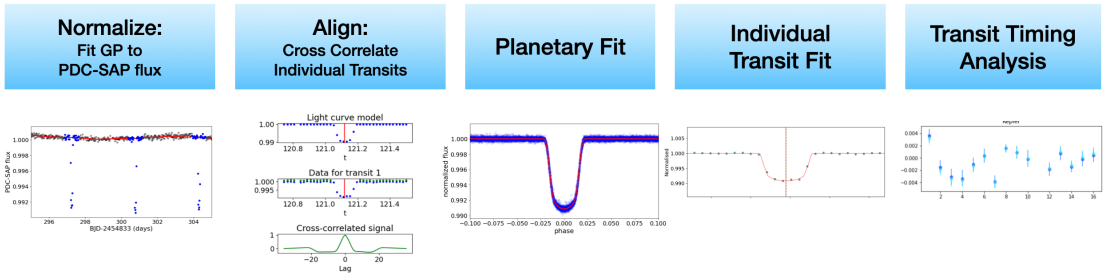


Figure 3.4: An overview of the process for fitting each planet and its transits. These steps are described in Section 3.4.1 and shown for a Hot Jupiter and sub-Neptune respectively in Figures 3.5 and 3.7.

both Kepler or K2, and TESS data were available, we started with each target's higher signal to noise Kepler or K2 data and proceeded with the PDC-SAP flux. After a normalization step, cross-correlation was performed on individual transits in order to correct for large timing differences. After applying these corrections to individual transits to achieve a phase folded transit that corrected any major timing offsets, a fit was then performed for global planet and system parameters. These parameters were then held fixed as individual transit times were fit. A similar procedure was then carried out for TESS transits. Finally linear ephemerides were fit and tests of timing variability were performed to the $O - C$ residuals. A summary of this process is shown in Figure 3.4 and shown in further detail for a hot Jupiter and a sub-Neptune in Figures 3.5 and 3.7 respectively. Each of these steps will be described in detail below.

3.4.2 Normalization

First, a simple normalization was performed, dividing by the average flux. Then, to account for correlated noise, a GP was fit to the out-of-transit light-curve. In most cases, a 1.5 transit-duration window around the archival time of conjugation achieved a masking of these transits. However, for a few cases of systems with large TTVs of magnitudes greater than their transit duration, different individualized windows were adopted.

All GP calculations in this work were done using the GEORGE package Ambikasaran et al. (2014) with a squared exponential covariance function:

$$k(t, t') = A \exp\left[-\frac{(t - t')^2}{2\tau}\right] \tag{3.2}$$

where A is the variance and τ the (squared) characteristic time-scale, or metric, of the GP. We used log uniform priors over the logarithm of the GP hyper-parameters A and τ.

When performing optimisation, we first used the MINIMIZE function of the SCIPY.OPTIMIZE module to determine initial input parameters, and explored the posterior distribution over the parameters of our models using Markov Chain Monte Carlo (MCMC) implemented with the EMCEE package (Foreman-Mackey et al., 2013a, 2019). We evolved chains of 40 walkers with a thinning factor of 15 with a burn-in of 1000 steps and conservative removal of the first 25% of steps of the production chain. Convergence was achieved when the estimated autocorrelation time $\tau_{autocor}$ (checked every 200 steps) was changed by less than 1% and the chain was longer than 200 times the autocorrelation time, resulting in chain lengths of about 10,000-20,000. Parameter values were taken to be the median of the posterior distribution, the with errors reported as the 68% confidence interval from the 16th to the 84th percentile. We then checked for any residual correlated noise using the out-of-transit data, by examining autocorrelation. In most cases none was observed, and where it was, transits were discarded.

3.4.3 Cross Correlation

After using the out-of-transit GP to normalize the light curve, cross-correlation was then performed on the transit in windows of 4 transit durations (or 5 transit durations in exceptional cases with large TTVs), using a template transit model drawn from archival transit parameters.

Light curve modelling was implemented in PYTHON using the BATMAN package (Kreidberg, 2015), which was found to better fit the Kepler limb-darkening coefficients than PYTRANSIT, which was intitially tried, similar to TOI-270. The

Figure 3.5: Fitting Process for Hot Jupiter Kepler-8 b

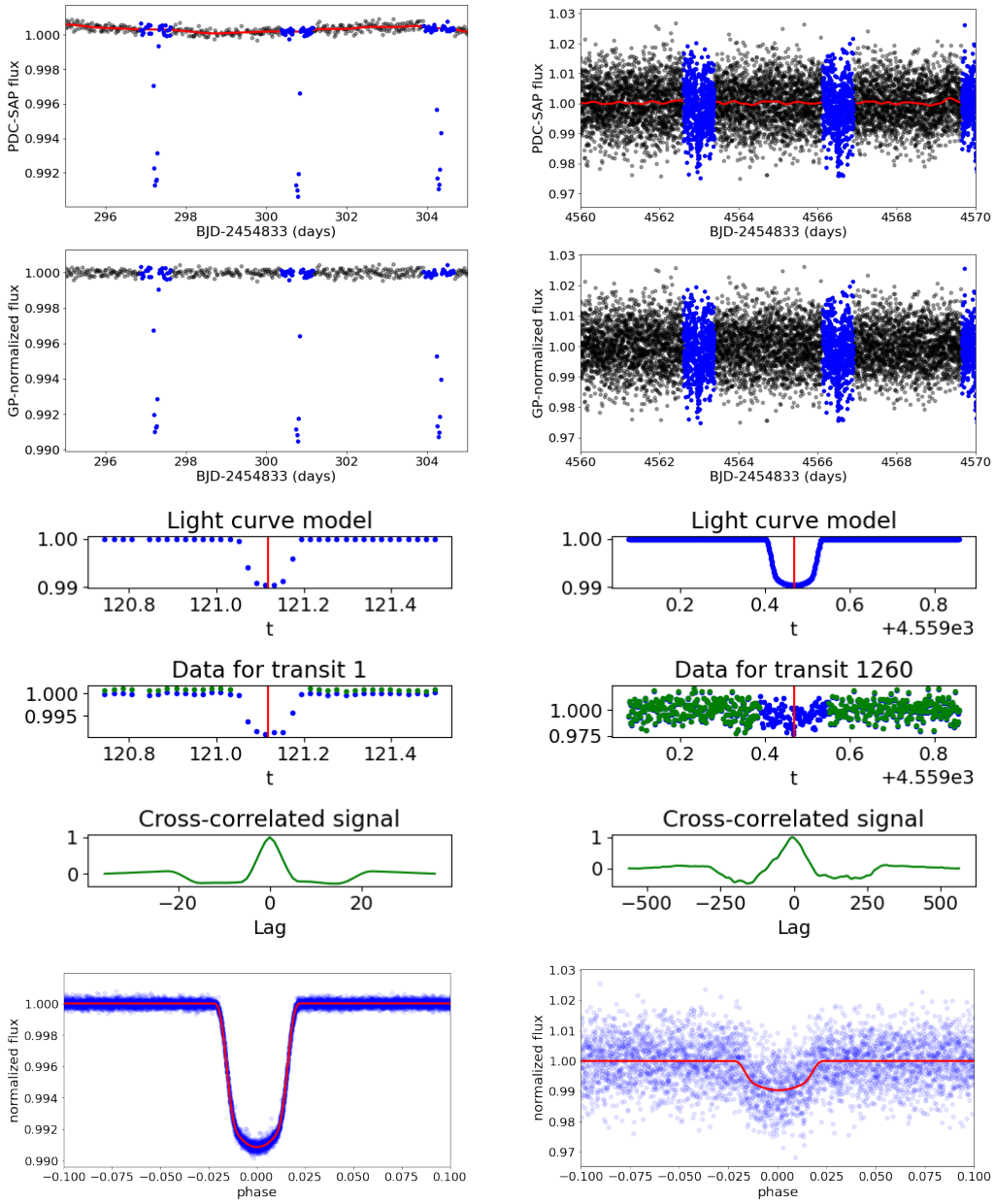


Figure 3.6: As described by Section 3.4.2, a) and b) show the GP fit to the PDC-SAP flux of Kepler and TESS respectively for the Hot Jupiter Kepler-8 b. This GP fit to the out-of-transit data is then used to normalize the flux as seen in c) and d). Cross correlation is then performed on each transit as shown in e) and f), using archival parameters to correct any significant transit offsets to facilitate with the global planetary parameter fit shown in g) and h).

Figure 3.7: Fitting Process for sub Neptune K2-133 b

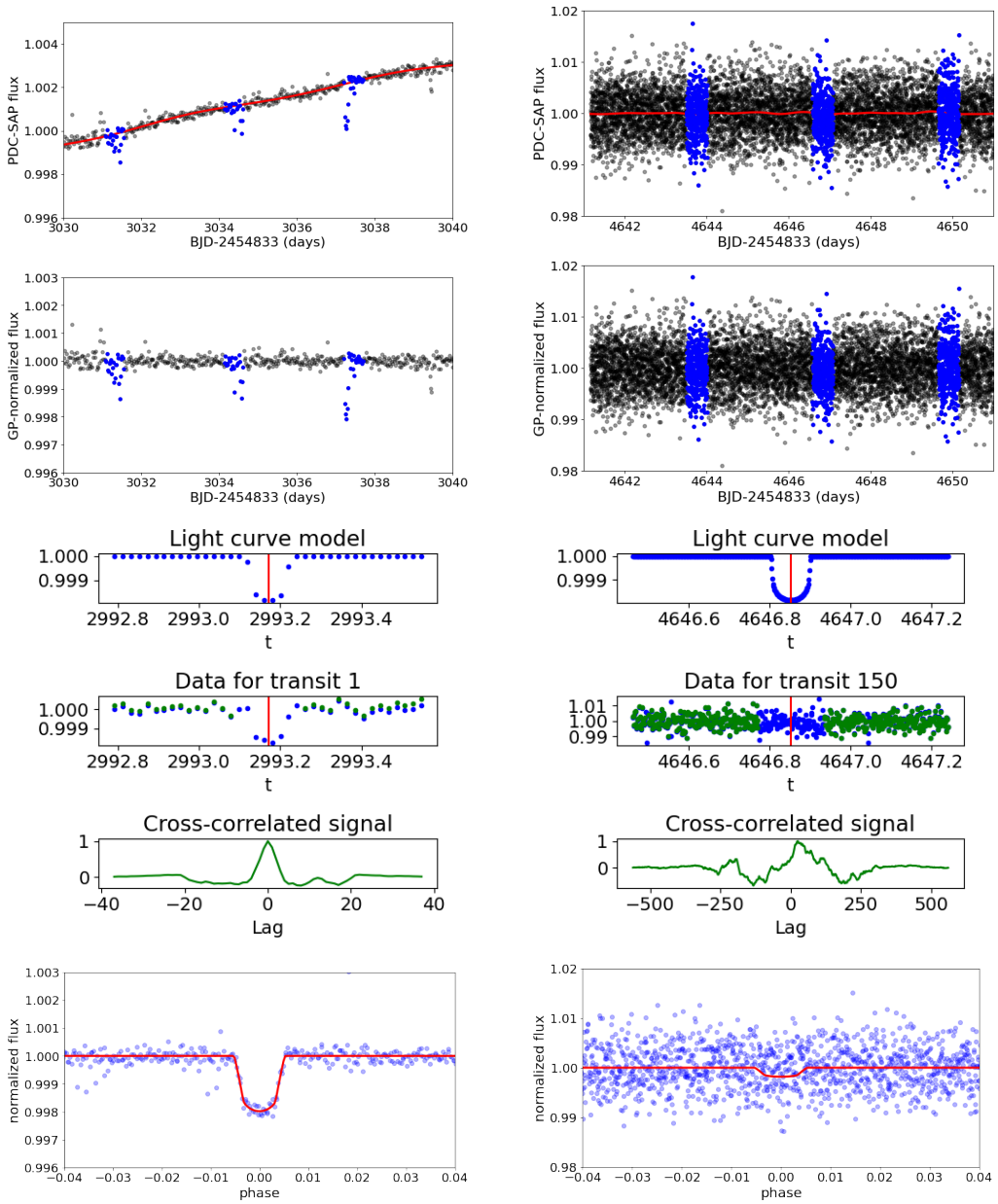


Figure 3.8: Same as previous figure but for the lower signal-to-noise sub Neptune K2-133.

parameters of the transit model implemented are the orbital period P, the time of transit centre T_0, the planet-to-star radius ratio $R_p/R_\star$, the system scale $a/R_\star$ (where a is the orbital semi-major axis), the orbital inclination i, the orbital eccentricity e and the longitude of periastron ω and the quadratic limb-darkening coefficients u_1 and u_2. We chose to reparameterize $R_p/R_\star$ and $a/R_\star$ to R_p, $R_\star$ and $M_\star$, using Kepler's third law, and used cos_i since this makes convergence quicker. Starting parameters were taken from the exoplanet archive, with references given in Table B.1.

We used the Limb Darkening Toolkit (LDTk) of Parviainen & Aigrain (2015) to compute priors over the limb darkening coefficients u_1 and u_2, using the stellar parameters from the NASA Exoplanet Archive and the relevant instrument/filter throughput as inputs.

An individual transit was determined to be detected if the peak cross correlation value was > 3 standard deviations above the out-of-transit mean, calculated by taking the cross correlation values between 1 and 2 transit durations on either side of the linear prediction of mid-transit time. For systems with very large TTVs, this window was expanded, and for systems with other nearby transits, these were masked in durations of 1.2 times the duration of the companion's transit. If the transit was not detected, the transit was discarded from further planetary parameter fitting and timing analysis. At this point, transits that overlapped with the transits of companions were also discarded. If more than half of a planet's TESS transits were not detected, the planet was excluded from any further analysis.

3.4.4 Planetary Parameter Fits

We started our data analysis with the greater SNR Kepler and K2 light curves, which were treated identically to one another beyond data extraction as described above.

Global planetary parameters were fit to Kepler or K2 data using an MCMC to the phase folded light curve with any significant timing offsets corrected for by cross correlation lags of individual transits. We used uninformative, wide uniform priors over all parameters apart from limb darkening, for which we used LDTK to calculate priors over the limb darkening coefficients u_1 and u_2. Any

non-zero lag in maximum cross correlation signal was applied as an initial timing offset to align transits for a global fit of the planetary parameters. While this process could be repeated recursively, the initial correction resulted in an fit for planetary parameters that was typically consistent with and matched or exceeded the precision of archival parameters.

For TESS, we used the planetary parameters derived from the Kepler fit as Gaussain priors for TESS planetary fitting, and used the TESS response function to generate priors on the limb darkening coefficients from LDTK and again fit using MCMC. However, we found that this method rarely resulted in an improvement to the precision of Kepler fitting alone, even at higher SNR, so planetary parameters derived from the Kepler fit were adopted and fixed and the MCMC was rerun to fit TESS limb darkening coefficients alone.

3.4.5 Timing Fits

Finally, we fit for individual transit times using a flux window of 3 transit durations around the initial transit midpoint (or 5 if a system was known to have large TTVs). Planetary parameters derived in the previous step of fitting were kept fixed. A second order polynomial was used to account for any long-term trend not corrected for by the GP in the first step and the only other parameter allowed to vary was δt, the correction to a linear ephemeris. All parameters were fit using MCMC as described above and residuals were checked to ensure they were Gaussian. Where they were not (sometimes in the case of starspots or very active stars), the transit was discarded.

Of the more than 20,000 transits fit, several hundred were deemed as outliers and thus discarded by one of the following criteria:

1. Divergence from typical scatter: If the $O-C$ deviation of a given transit was more than 3 sigma away from the median $O-C$ plus the median error or if their error was more than 3 sigma larger than the median error.

2. Overlapping transits: For systems containing multiple companions, an overlapping transit was considered a transit for which a window of $1.2 \times t_{dur}$ centred on each transit overlapped. These were removed from further analysis.

3. Partial transits: partial transits of approximately 70% or less were found to be unconstraining to system parameters and TTV trends. If a window of $1.2 \times t_{dur}$ contained fewer data points than $0.8/cadence$, it was discarded as a likely partial transit.

4. No transit detected: for each transit we examined the cross correlation of the flux (normalized by out-of-transit fit with a GP) with a transit model based on archival parameters. If the peak in correlation was less than 3 times greater than the standard deviation of out of transit correlation lag, the transit was discarded. This was most often the case for TESS transits of smaller planets, lower SNR planets, or transits for which the data were flawed or missing.

5. Visual Inspection: Every transit was visually inspected, along with its cross-correlation signal, with close attention to those whose timings visually diverged from a clear trend. In some cases, a fit was clearly incorrect. This was typically due either to features in the transit, such as star spots, or erroneous/outlier points in the processed light curves. Rarely, it was a case of a failure of fit of the GP or individual transit polynomial, in which a fit was reattempted placing realistic constraints, such as in very active stars with large trends.

These transits were not used in fitting for planetary parameters, ephemeris updates or in TTV analysis.

3.5 Transit Timing Analysis

In order to identify systems with significant TTVs we performed a series of statistical tests to characterize the scatter of timing residuals. First all transit times were fit to a linear ephemeris using SCIPY.OPTIMIZE. Because of the significantly more numerous points and smaller errors arising from Kepler and K2 datasets compared to those of TESS, Kepler points tended to dominate the trend. With the $O - C$ residuals to this best-fit linear ephemeris, we then identified three major types of variation: clear periodic trends, significant scatter, or higher order trends.

1. Periodic trends: TTVs in systems of planets near j:j-1 orbital resonance are characterized by a sinusoidal trend with a superperiod relating to the ratio of periods as

$$P_{\rm TTV} = \left| \frac{j-1}{P_{\rm inner}} - \frac{j}{P_{\rm outer}} \right|^{-1} \tag{3.3}$$

We looked for periodic trends in the O-C residuals to linear fit using a Lomb-Scargle (LS) periodogram. We examined peak power of the LS, which corresponds to a False Alarm Probability (FAP) of the periodicity. For systems with previously known TTVs, the LS Power and period are recorded in Table 3.1. For systems without previously known TTVs, a FAP of 0.05 or lower was taken to indicate significant periodicity.

2. Significant scatter: Even if a long-term periodic trend is not obvious, systems might display more scatter in their transit times than could be expected in a purely linear, non-interacting case. These could be the chopping effects of planets close to resonance but whose superperiods still exceed the span of data collection as to appear linear on average (Deck & Agol, 2014). This can be quantified in terms of comparison between the median scatter of the $O-C$ timing residuals s_{O-C}, and the median error of these residuals σ_{O-C}. Mazeh et al. (2013) defines a median absolute deviation (MAD) statistic for the $O-C$ series and a corresponding alarm score, defined as $\sigma_{res}/\sigma_{O-C}$ where $\sigma_{res} = 1.483 \times s_{O-C}$. A significant scatter is defined as an alarm score greater than 15 (Tamuz et al., 2006). Alarm scores were calculated for all datapoints together as well as for Kepler/K2 and TESS separately.

3. Long term TTVs: For longer term trends for which a full period is not yet captured in the available data, a fit to a second or third order polynomial is still indicative of timing trends. For linear, second and third order fits to the residuals to $O-C$, we calculated the Akaike information criterion (AIC) to determine how well each model accounted for the data. Given the heavy dominance of Kepler data on model fitting due to its significantly lower timing error, we calculated AICs for each fit type for all datapoints as well as for

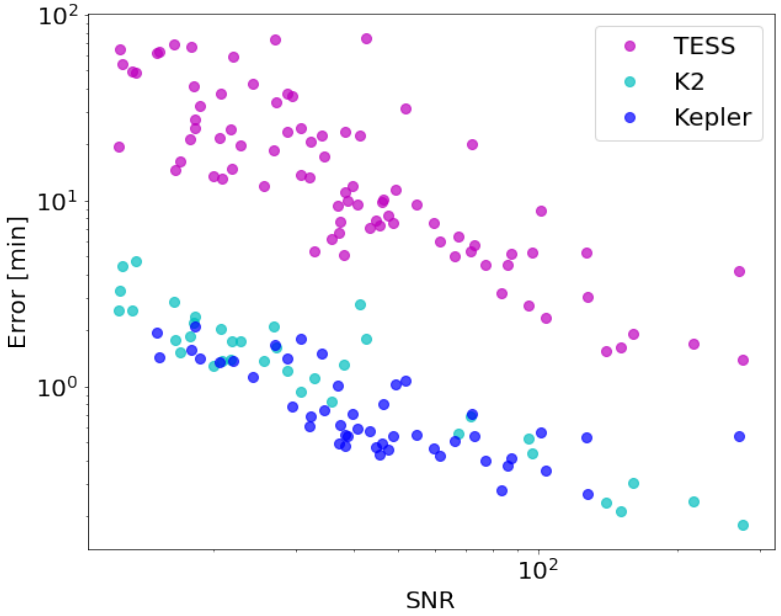


Figure 3.9: The median error on timing residuals of individual transits is plotted verses Signal to Noise Ratio (SNR) for each observing program, following the expected trend. TESS has a significantly higher timing error than Kepler.

TESS datapoints only given fits to all datapoints. For a difference in AIC $>$ 1, a system was considered to exhibit significant high order timing variation.

4. No evidence of variation: If a system did not exhibit any of the above behaviors, it was deemed to show no variance. For these systems we updated their linear ephemeris in the context of further TESS datapoints.

3.6 Results

Of the 293 total systems with an SNR $>$ 2, and 150 with TESS transits, 117 had detectable transits in both Kepler/K2 and TESS fields that were not considered outliers. Errors on transit times scaled with SNR as can be seen in Figure 3.9, with the timing errors of TESS points consistently being significantly larger than those of Kepler as expected. In a large fraction of systems, we were able to use TESS data to refine the ephemerides by a factor of 2 to 10. Summaries of the improvement factors can be seen in Figure 3.16.

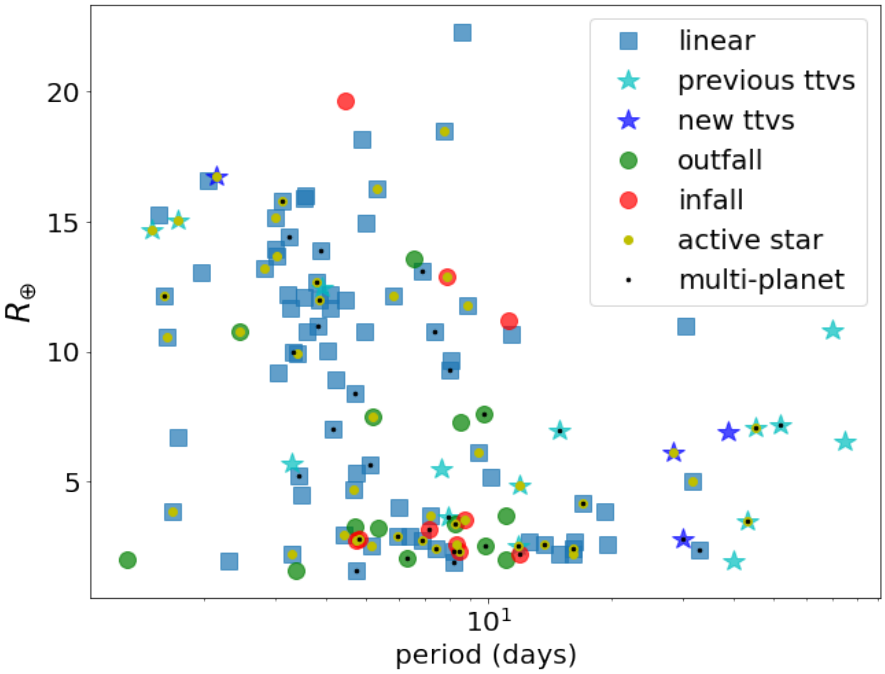


Figure 3.10: The population of Kepler and K2 planets whose timings were updated in this work. Systems with periodic timing trends either previously known, or newly identified in this study are marked with stars. Non-periodic second order trends are marked as either outfall (if their period increased from Kepler/K2 to TESS) or infall (if their period decreased from Kepler/K2 to TESS. Active stars and multi-planet systems are also designated.

In almost all cases, using Kepler transit times alone resulted in comparable or improved errors on archival values, which in part validates our detrending and fitting methods. For planets where our analysis of Kepler data alone resulted in significantly greater errors on the linear ephemeris than previously reported values, these were typically systems surrounding highly active stars, as can be seen in Figure 3.16. Because we performed no special individualised analysis beyond what is described above for such systems, it is quite possible that our analysis is not sufficient to handle significant variability, starspots, etc. However, in several systems for which our reported error on the ephemeris for Kepler data was comparable to or better than archival values, the addition of TESS data made the error on transit times less certain than analysis of Kepler transit times alone. This hints at the possibility of non-linear timing trends that were not captured by our analysis. Examples of the changes to linear ephemerides achieved by this work can be seem in Figure 3.11

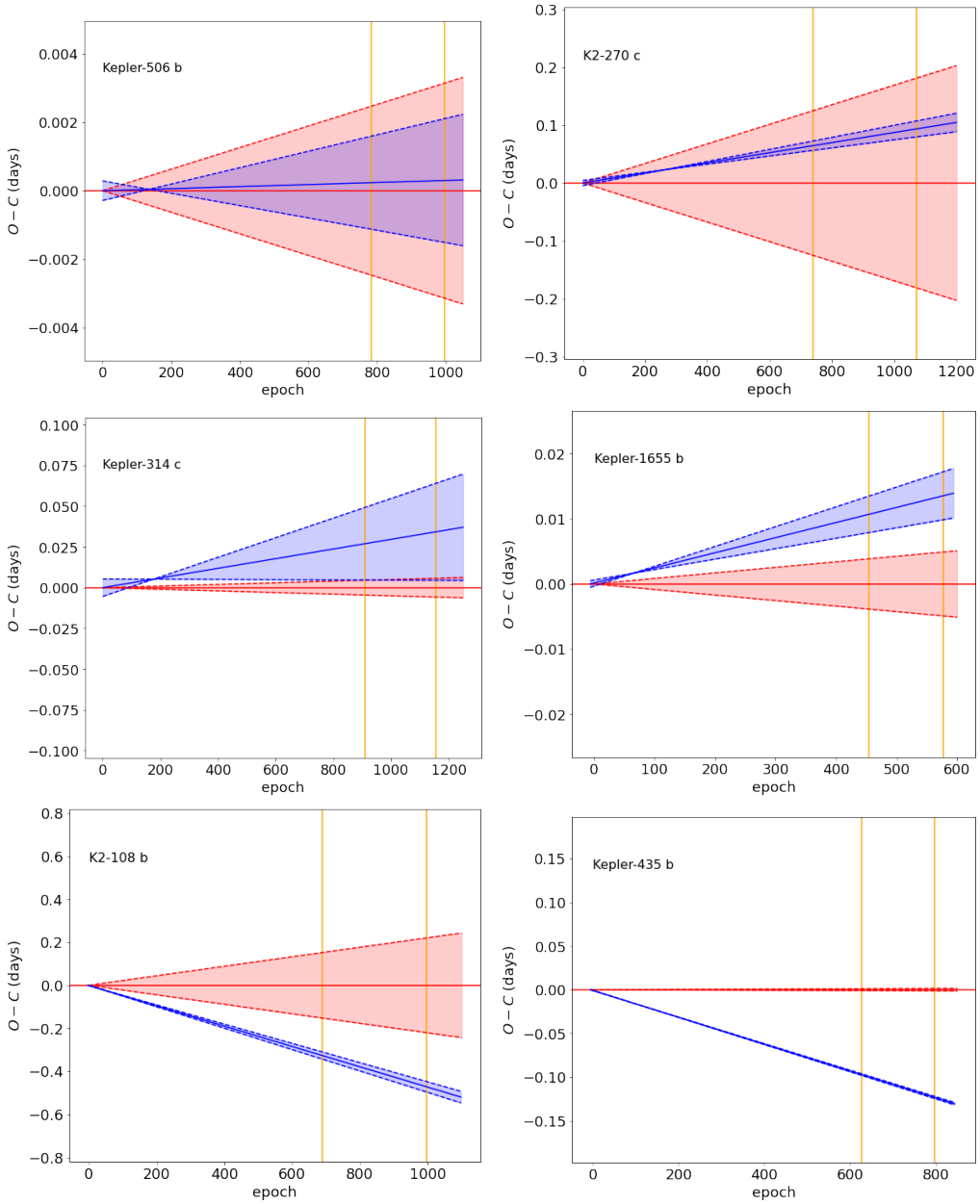


Figure 3.11: Representations of a few of the updated ephemerides for the systems in this work. The red shaded region represents the archival uncertainty on the linear ephemeris and the blue shaded region shows the resulting ephemeris of this study. Epoch 0 begins at T_0, which is typically near to the start of the Kepler mission. The first yellow vertical line represents observations in April 2024, and the second vertical line represents April of 2028. Most systems show modest to significant improvement on the timing uncertainty, and several show significant offsets from archival parameters that would be expected to impact observations. In some cases, such as for Kepler-314 c, we are not able to refine the ephemerides as much as in archival values. In the case of Kepler-314 c, second order timing trends are found (see Section 3.6.3), which might explain the increase in uncertainty, whereas other systems with larger errors on their updated ephemerides have high levels of stellar activity that are not adequately corrected for by the methods in this study.

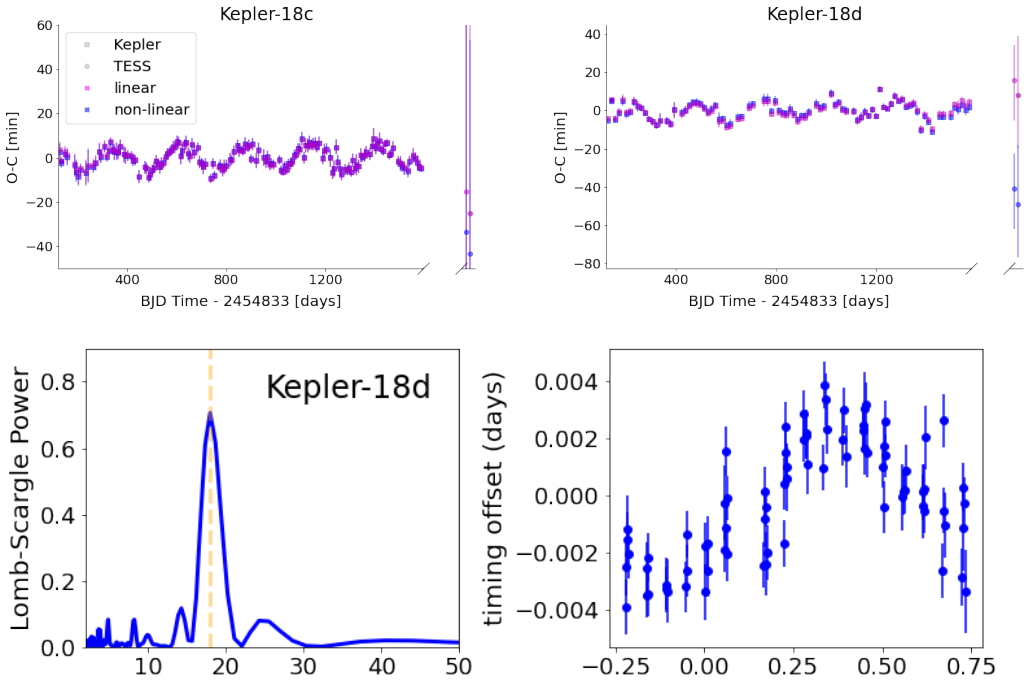


Figure 3.12: Kepler-18 c and d are previously known to have TTVs. The top panel shows $O - C$ timing residuals from Kepler and TESS, with pink points denoting residuals to a linear trend, and blue showing residuals to a second order trend. The bottom left panel shows the LS periodogram for planet d's Kepler data and the bottom right panel shows the timing residuals phase-folded around the peak power LS period. The large errors on individual TESS transit times make it unlikely that any further refinement is possible for for this system. Plots of residuals and LS periodograms can be seen for all systems with previously known TTVs in Figure B.3.

3.6.1 Systems with Previous TTVs

Of these, 19 planets across 16 systems had been flagged previously as displaying TTVs. These are presented in Table 3.1 and shown in Figure B.3. In most cases, these timing trends are also apparent in our data, such as the clear periodicity of the Kepler-18 system, shown in Figure 3.12. This three-planet system comprised of a an inner super Earth and two outer Neptune sized planets in near 2:1 orbital resonance has been well characterized and its TTVs used to measure masses (Cochran et al., 2011; Hadden & Lithwick, 2016). However, as can be seen for Kepler-18 c, some TESS transits, while detected, are not very constraining.

Table 3.1: Previously Known TTVs

Name	Period	Mass if Known (M_J)	Known Companions	LS Period (epochs)	LS Period (days)	LS FAP
Kepler-114 d	11.77591	0.01	2	6.27	73.78	0.22
Kepler-1524 b	70.96693		none	9.00	638.70	0.41
Kepler-1624 b	3.29031		none	7.09	23.33	0.09
Kepler-17 b	1.48571	2.45	none	8.07	11.99	0.006
Kepler-18 c	7.64157	0.05	2	34.11	260.63	5.31E-45
Kepler-18 d	14.85892	0.05	2	17.96	266.91	1.61E-08
Kepler-210 c	7.97252		1	91.00	725.50	7.47E-05
Kepler-297 c	74.92816		1	10.63	796.11	0.04
Kepler-37 d	39.79220	0.04	3	5.29	210.66	0.44
Kepler-396 b	42.99282	0.24	1	18.33	788.20	0.91
Kepler-412 b	1.72086	0.94	none	7.81	13.45	1
Kepler-419 b	69.72857	2.50	1	5.28	368.01	0.85
Kepler-51 b	45.15530	0.01	2	16.67	752.59	0.0008
Kepler-51 d	130.17719	0.02	2	6.67	867.85	0.32
Kepler-79 d	52.09086	0.02	3	16.88	879.03	0.012
Kepler-9 b	19.23555	0.14	2	45.00	-	-
KOI-217 b	3.90508		none	8.98	35.07	5.96E-10
K2-19 b	7.92005		2	-	-	-
K2-19 c	11.90549		2	-	-	-

There are also cases for which periodic trends were not recaptured to statistical significance, as can be seen in Figure B.3 and Table 3.1. Several high amplitude TTV systems, such as Kepler-9 b and c as well as K2-19 b and c were excluded due to the difficulty of disentangling their overlapping or highly displaced transits. Such a system would require a more individualised approach than is possible through the methods in this study. In some cases with previously known TTVs, the TESS data exhibit a faint second order trend to the linear average of a system's periodic behavior (for example, KOI-217 b as seen in Figure B.3), and in several cases, the addition of TESS data in one or more sectors will enable a reanalysis of the planetary masses. However, in other systems, the TESS data is not very constraining. In most cases, even if it does not constrain TTV amplitudes, TESS data does make a slight improvement on the average linear ephemeris, as can be seen in Figure 3.16.

3.6.2 New Periodic TTVs

Several systems that were not previously noted to have TTVs show variation from linear ephemeris via one of the methods described in Section 3.3. In total, we identified 18 systems with notable periodicity that were previously unknown to have TTVs, of which 5 are believed to have long-term periodicity arising from possible TTVs (shown in Figure B.4 and described in Table 3.2). A LS FAP (false alarm probability) of < 0.05 supplied strong evidence of periodicity, which is the case for 9 such systems. We then examined up to a FAP of 0.71, following-up cases where small numbers of data-points combined with outliers might contribute to a diminished signal.

For the initial 15 systems that met this criteria, in order to ensure that this observed periodicity was independent from stellar activity we examined the following: We first plotted the out of transit average stellar flux over a window of two transit durations against the timing offset and ensured that there was no correlation. We then did the same comparing the first and second coefficients of the polynomial fit to the out-of-transit flux against the timing offset, to further check for effects of slope or curvature of the time series impacting the timing fit and falsely appearing as timing

periodicity. Where these tests showed no correlation, the periodicity was believed. Kepler-531 has timing variations on the order of ∼30 minutes, however is also noted to be quite active and likely has starspots, as seen in Figure 3.14. A sample fit of a transit that was excluded is shown in that same figure. Although K2-121 b is an active star, timing trends did not appear to correlate to any periodicity in the stellar signal.

In several cases (Kepler-45 b, Kepler-102 e , Kepler-96 b, and Kepler-314 c), periodicity indeed lined up obviously with stellar activity periods or low-order multiples thereof, as noted in Table 3.3, so these are suspected as not having "true" TTVs. Kepler-12 b showed a small amplitude signal corresponding to the first order coefficient of polynomials fitting the out-of-transit flux, so it too is discounted from having true timing variations.

Name	Period	LS Period (epochs)	LS Period (days)	FAP	Stellar Activity Period (days)
Kepler-531 b	2.99E+01	36.923	1,103.44	3.3E-05	35.053
Kepler-522 b	38.58497185	17.333	668.81	3.1E-04	4.919
Kepler-450 b	28.45494453	38.462	1,094.42	6.4E-04	20.796
K2-108 b	4.733526568	11.538	54.62	0.64	
K2-105 b	8.266995036	6.000	49.60	0.71	

Table 3.2: New Periodic TTVs . The first three systems appearing on this list show clear periodicity and have FAP $\ll 1\%$. The two K2 systems appear periodic and both have second order offsets in their timing

Name	Period	LS Period (epochs)	LS Period (days)	FAP	Stellar Activity Period (days)
Kepler-12 b	4.44E+00	5.282	23.44	4.8E-10	
Kepler-422 b	7.89E+00	4.987	39.35	3.2E-05	
Kepler-45 b	2.46E+00	6.383	15.67	6.7E-03	15.805
Kepler-102 e	1.61E+01	6.569	106.07	0.01	26.572
Kepler-856 b	8.03E+00	4.888	39.24	0.03	
Kepler-96 b	1.62E+01	6.154	99.93	0.06	14.922
Kepler-5 b	3.55E+00	15.468	54.89	0.15	
Kepler-447 b	7.79E+00	24.416	190.30	0.25	6.459
K2-121 b	5.19E+00	5.200	26.97	0.29	

Table 3.3: Periodicity without clear TTVs . These planets were flagged for showing periodicity in their timing trends, though this periodicity is low amplitude, high frequency and in several planets corresponds to a fraction or multiple of their host's stellar activity cycle. We note these here but do not trust these to be TTVs caused by dynamical interactions.

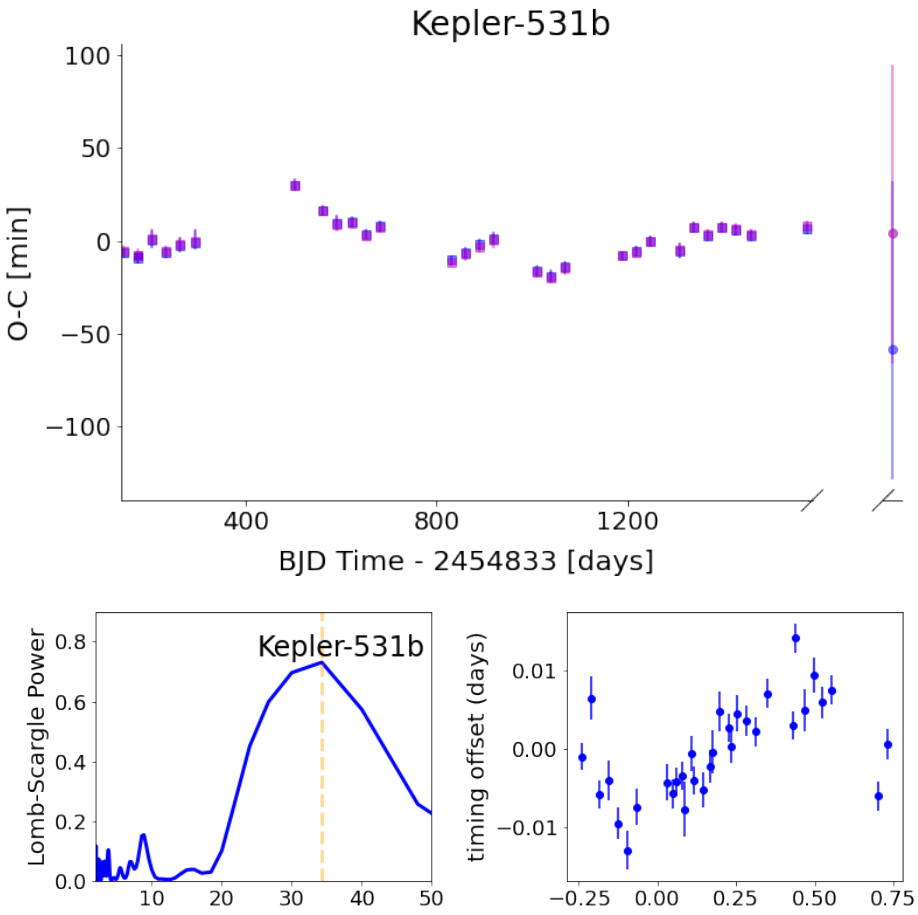


Figure 3.13: Kepler-531 b shows significant periodic behaviour with an amplitude of 20 minutes and a superperiod of about 37 epochs or 1100 days, as seen in the top panel. However, its TESS datapoint is minimally constraining and it is an active star as seen in Figure 3.14.

In total, the five systems identified as having potentially new dynamically induced periodic TTVs are Kepler-531 b , Kepler-522 b, Kepler-450, K2-108 b and K2-105 b, which can be seen in Figure B.4. For one of these, Kepler-522 b we proceed to dynamically model and fit its transit times to extract a possible companion planet in Chapter 4. For the remaining 10 systems, we make note of them as systems of interest in Table 3.3. One such system, K2-121 b shows some amount of periodicity (FAP = 0.29) but is limited by few K2 data points, from which the LS distribution is drawn. However, its TESS datapoints are offset from a linear ephemeris, which potentially increases the likelihood of dynamical

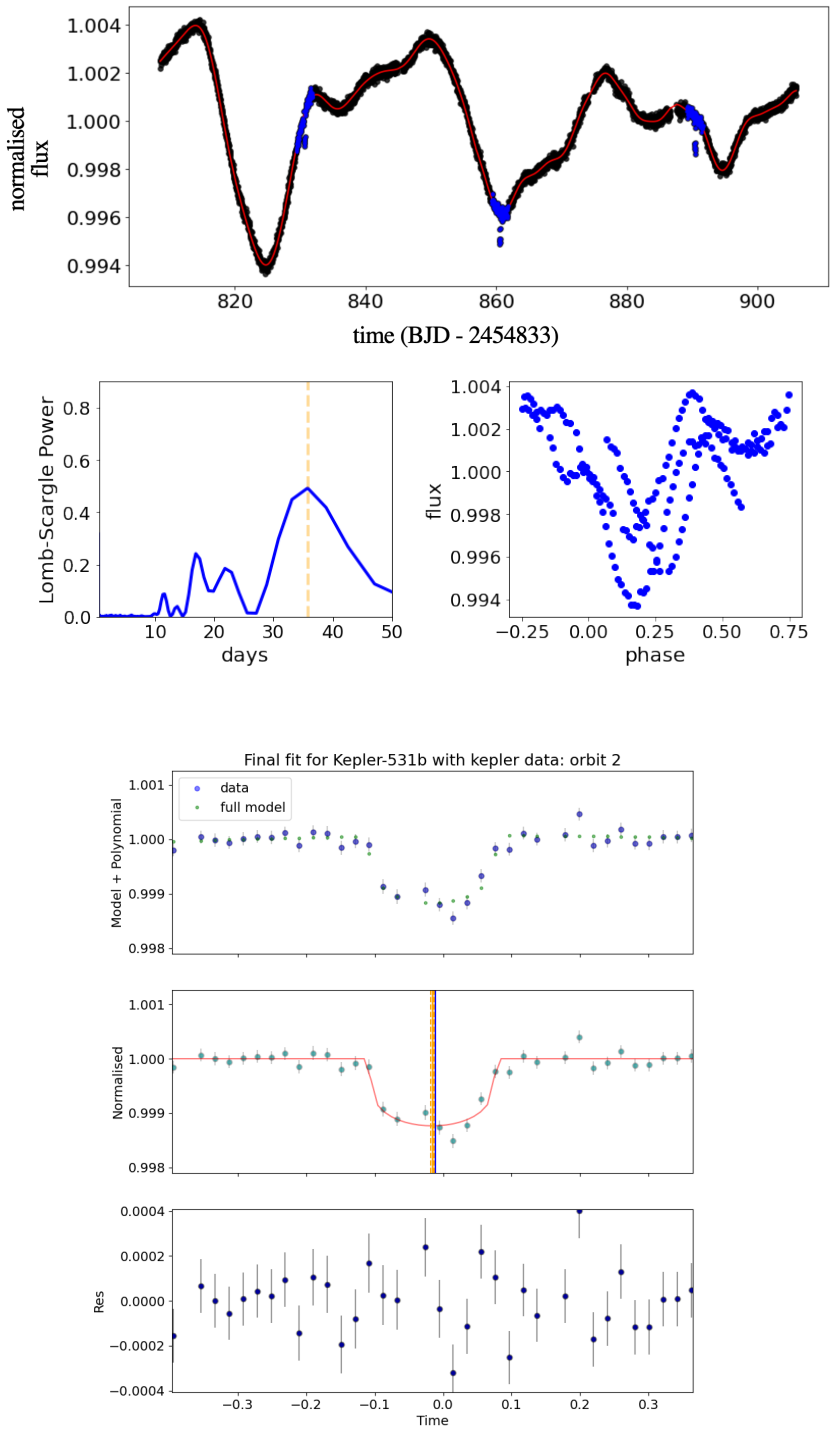


Figure 3.14: Although Kepler-531 b shows significant periodic behaviour as seen in the previous Figure 3.13 and in the top panel here, which shows the GP fit in red over the PDC-SAP flux. It also has a clear stellar activity cycle lasting 35.053 days (from McQuillan et al. (2013)) that was replicated by our own periodicity indicator shown in the middle panel. Significant short term variation and outlying data points, possibly from star spots led to the exclusion of several transits, including the transit shown above in the bottom panel.

interactions in the system contributing to these timing trends. Another is Kepler-422 b, which is has a very strong low amplitude periodicity with a FAP=0.00003, also has a second order offset in TESS transit times, and it is therefore included in both categories and appears in Figure B.5.

3.6.3 Systems with Second Order Trends

Of our systems analysed, 17 show a significant deviation from a linear ephemeris in the form of non-periodic second order trends as determined through AIC comparison to a linear ephemeris. Of these, 8 planets show a decreasing period or "infall" over the observing window and 9 show an increasing period or "outfall". These systems are shown in Figure B.5 and summarized in Table 3.4. One of these systems, a sub-Neptune K2-182 b with a 4.7 day period is shown in Figure 3.15 to have a longer period in TESS data than it had in K2, with scatter and slight periodicity in the K2 datapoints potentially pointing to evidence of short-term "chopping" in the context of a longer-term periodic timing trend. This also results in a significantly different refit linear ephemeris, as can be appreciated in the river diagram. Another such system is K2-117 b, a super-earth on a tight 1.3 day orbit which shows some level of scatter in Kepler data that could be interpreted as "chopping" on top of a clear second order trend (see Figure B.5).

3.6.4 Large Corrections to Ephemerides

In several cases, quite significant changes were made to previous ephemerides. These are often longer period systems that had very few transits in Kepler or K2. While the uncertainty on the period would sometimes increase in these situations, it likely demonstrates an underestimation of the original uncertainty due to the small number of samples.

Within those analyzed, a further 9 systems show statistically significant timing variation or fits to non-linear trends according to our criteria, but have fewer than 5 points in their Kepler or K2 datasets, so while our analysis provides a valuable updates to their ephemerides, further observation is likely needed in order

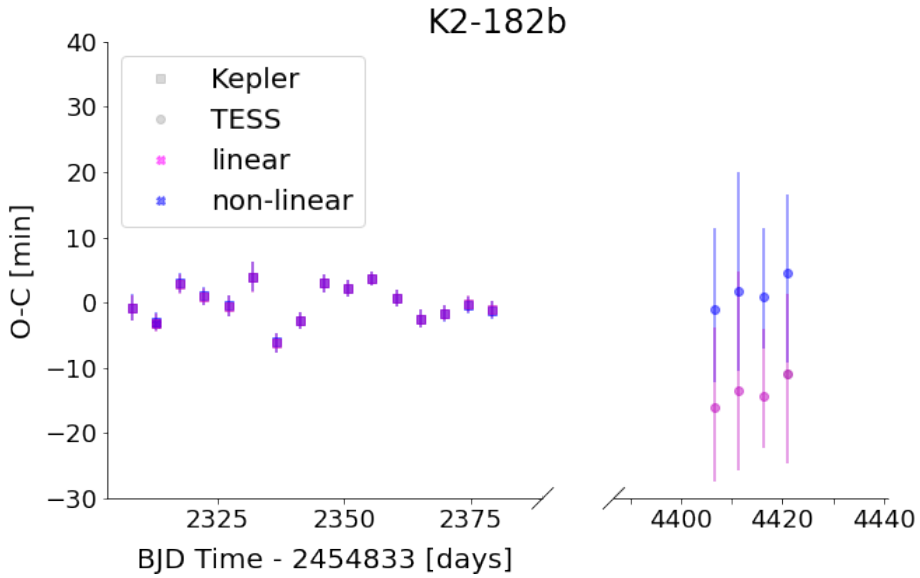


Figure 3.15: K2-182 b is warm sub-Neptune with an 4.7 day period that shows potential short term variability and exhibits a clear second-order trend in its timings (the blue points indicate residuals to a second-order and the black to a first-order ephemeris). Other systems that show such timing trends can be seen in Figure B.5

Name	Type	Period	Radius (Earth)	Known Companions
K2-232 b	Infall	11.16844	11.21	none
K2-178 b	Infall	8.74794	3.56	none
K2-284 b	Infall	4.79491	2.78	none
Kepler-422 b	Infall	7.8914483	12.89	none
K2-182 b	Infall	4.74	2.76	none
K2-197 b	Infall	8.357881	2.56	none
Kepler-1655 b	Infall	11.87	2.21	none
K2-187 d	Infall	7.14921	3.17	3
K2-277 b	Outfall	6.32674	2.07	none
K2-133 d	Outfall	11.02478	2.00	3
K2-140 b	Outfall	6.56920	13.56	none
K2-87 b	Outfall	9.72657	7.60	none
K2-348 b	Outfall	4.68861	3.26	1
K2-121 b	Outfall	5.19	7.50	none
K2-105 b	Outfall	8.27	3.37	none
K2-117 b	Outfall	1.2916	2.03	1
K2-344 b	Outfall	3.35585	1.59	none

Table 3.4: Systems with Second Order Trends . These systems show significant evidence of deviations from a linear ephemeris through their AICs to second order polynomials as described in Section 3.5. This list includes planets with previously identified TTVs or periodic TTVs identified in this study. The updated times of conjugation and average periods for all systems are given in Table B.1

to analyse the significance of any non-linear timing trend. These systems are given a 3* flag in Table B.1 but not included in our count of systems that show more definitive timing trends.

3.7 Discussion

Up-to-date linear ephemerides are critical to future observations of planetary systems. Overall, we are able to update the linear ephemerides of 121 Kepler and K2 systems and identify robust timing trends for 24 systems. This approximately matches the incidence of significant timing trends recorded by Mazeh et al. (2013) in the Kepler population. A summary of our improvements to linear ephemerides as well as systems with timing trends can be seen in Figure 3.16 and in Table B.1. While mild to moderate improvements to precision are made for most of the planets in our study, there are a few for which we don't achieve the same level or worse precision than archival parameters. This falls slightly short of the predictions made by Batalha et al. (2019) and Christ et al. (2019) but is similar to the findings of Battley et al. (2021), though our study looks at somewhat higher SNR planets as well as K2 planets and with more TESS sectors available. A potential approach to further improvement to these less precise ephemerides would be to fit an average time for phase folded TESS transits, and use it as a single data point of comparison to Kepler ephemerides.

Several systems examined in this study have been recently reexamined by others with TESS data. For example, Goldberg et al. (2019) highlights two systems, Kepler-396 and Kepler-89, as a priority for seeing improvements in ephemerides or further evidence of non-transiting perturbers with more TESS data points. We are indeed able to update and improve the precision of the ephemerides of Kepler-396 b by a modest factor of two with a single TESS data point, which also serves to expand its pattern of TTVs, which had cycled through slightly less than a full superperiod in the course of its Kepler observations. In Kepler-51b, another system showing clear periodic TTVs in Kepler data, we improved the precision of its average period by an order of magnitude, though the TESS data points are not as constraining to its pattern of TTVs as the original Kepler points had been.

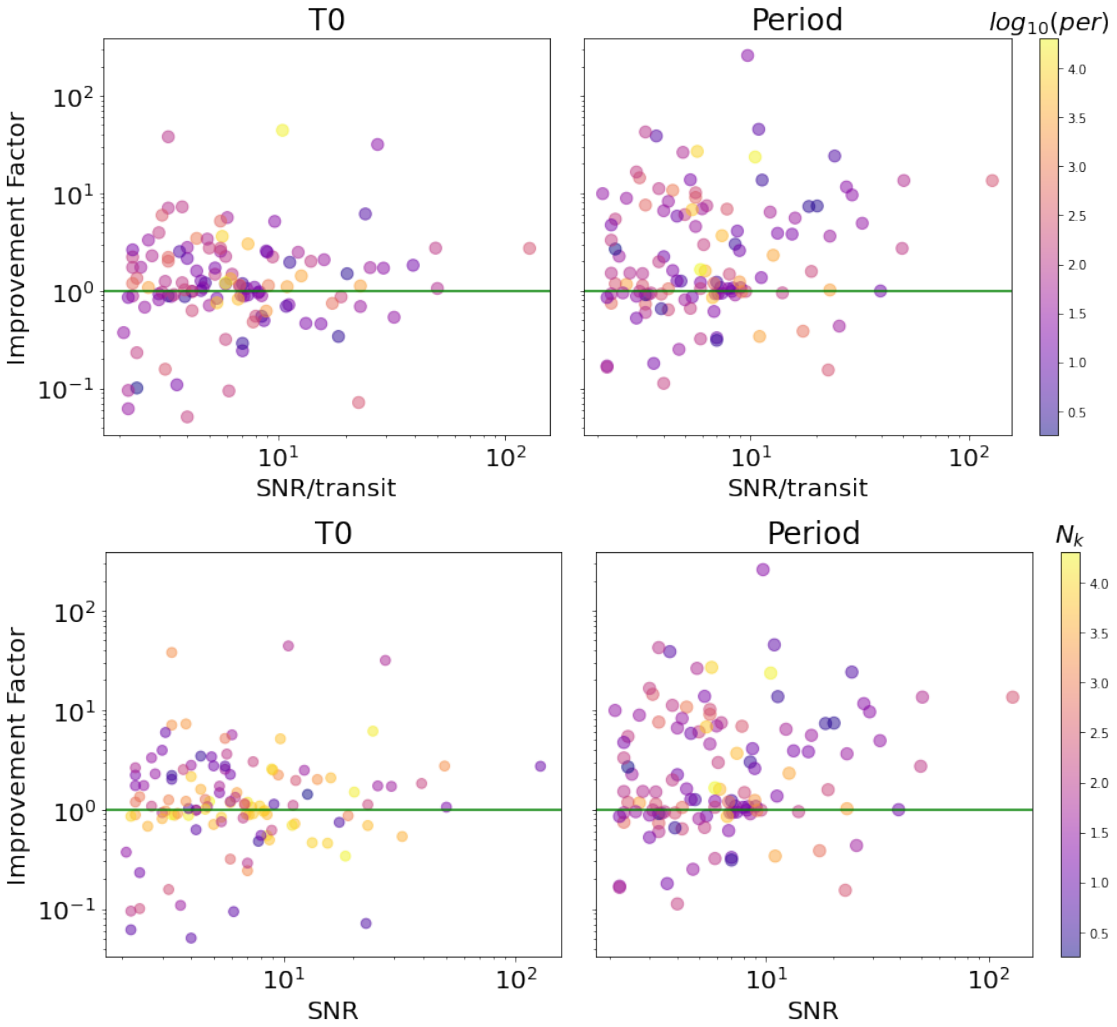


Figure 3.16: Plotted is the factor of precision for T_0 and period achieved in this study compared to archival values. In the top panels, this is shown in relation to the periods with a very slight effect of longer period planets to exhibit a refinement of parameters. In the bottom panels, this is shown in relation to the number of transits initially captured by Kepler or K2.

This is similar to the results found by Battley et al. (2021), who looked at these two systems as well, further validating this approach. Ikwut-Ukwa et al. (2020) identified several K2 systems that would be among the first observed with TESS with a promising potential for follow-up. Of these, we observe K2-114 b, which only transited three times in its K2 sector observing runs. We now have two additional TESS transits which enable us to update the ephemerides in a much more accurate way should follow-up observations be performed.

One of the most interesting results of this reexamination of the Kepler and

K2 fields with TESS is the uncovering of long-term second order trends. Battley et al. (2021) found in their study of 22 Kepler planets that one of these, Kepler-2b/HAT-P-7b showed a similar second order trend that resulted in a TESS offset of several minutes from the Kepler linear trend. Our findings of similar trends in other systems over a larger sample point to the increased possibility of this being a real evolution of the period, rather than a fitting error. However, erroneous fitting should not be discounted as a possibility, especially in cases where there are fewer transit point and fits are increasingly sensitive to even small outliers.

While the $O - C$ residuals for the 17 systems we have identified do not yet appear periodic in the time frame of this study, several factors could account for this period evolution, if it is believed to be real. One possibility is the presence of long super-period TTVs due to the presence of further planets. For example, one of the planets with $O - C$ residuals that are best fit to a second order polynomial is the Neptune-sized K2-348 b with a period of 4.6 days, which can be seen in Figure B.5. It displays short-term variability in its K2 data that shows moderate signs of short-term variability that could be attributed to TTV "chopping". It has one known companion K2-348 c, another sub-Neptune with 12.55 day period, whose timing residuals also display some evidence of second order trends, though there are not enough data-points for us to reliably conclude that this is the case. Taken together, it seems quite possible that the timing trends in this system correspond to one another. Follow-up of this system is recommended to better understand if the trends observed are due to dynamic interaction between these two or a third unobserved inner or outer planet, as well as continue to provide accurate ephemerides.

It is worth noting that these second order trends that are also not periodic appear predominantly in K2 systems. There might be several reasons for this. One possibility is an overfit of relatively few transits. Most K2 targets were only observed in one ∼80 day time frame, so those with medium length to long periods, only had a handful of captured transits. Because K2 data are still much more precise than TESS transits, these points dominate the linear fit, but because they represent a small baseline, 'overfitting' these K2 transits would result in a

magnified offset from linear ephemeris by the TESS observation timeline. In this case, TESS observations offer an important correction to the initial overfit, and more observations in future TESS or PLATO viewing fields will continue to correct the ephemeris, resulting in an eventual linear ephemeris.

The other possibility for the frequency of K2 systems in the subset of systems showing second order trends accounts for the case that these are dynamically induced TTVs that do not yet cover a full superperiod. Because K2 is both more recent, and again, did not observe for as long a baseline as Kepler, it is more likely that systems with longer super periods were "missed" and appeared approximately linear in the K2 time frame alone. For either scenario, further observations will elucidate the nature of the timing trends and continue correcting the linear ephemeris.

Even where timing trends are not observed, the TESS points included in our study can place limits on the presence or masses and eccentricities of known companions or of non-transiting or not-yet transiting companions. Goldberg et al. (2019) predicted that updated mass estimates would be possible for 12-25 Kepler systems with TESS's extended mission. It is also worth noting that of the 5 systems with new periodic trends observed, only one of them (Kepler-450 b) has known companions. While further observation of all of these systems will be important for verifying the definitive periodicity of these apparent TTVs, each could indicate significant evidence of non-transiting perturbers.

For systems with non-periodic, but non-linear timing trends another possibility is orbital or tidal evolution (Christ et al., 2019). The rate of orbital decay depends on several factors, including the exoplanet's mass, the star's mass, and the exoplanet's orbital separation. Close-in exoplanets are more prone to tidal effects due to their proximity to the star, wherein tidal interactions can cause an exoplanet to spiral inward over time, potentially leading to its eventual destruction or engulfment by the star. Tidal forces can also decrease a planet's eccentricity, circularising the orbits of close in planets (Ragozzine & Wolf, 2009). The interplay between tidal dissipation and infall have important implications for the exoplanet's long-term stability. In some cases, tidal forces can dampen the eccentricity and circularize

the orbit, while in other cases, interactions with planetary companions can create changes in inclination that drive the eccentricity to higher values.

While larger timing offsets from Kepler to TESS of several minutes to tens of minutes in some systems are likely more indicative of long-superperiod TTVs, smaller offsets in shorter period hot planets might indeed be evidence of orbital evolution. In this study, such systems were unlikely to be found statistically significant for timing trends through our methods of analysis, but appear to have small visible effects. For example, our study examined Kepler-1658, a hot Jupiter which was recently studied by Vissapragada et al. (2022), who showed evidence for tidal infall using data from TESS and Palomar. We also find similar timing trends, where TESS data points appear to come ∼10-20 minutes earlier than predicted by the average linear ephemeris. This can be seen in Figure 4.12 and will be discuss in greater detail in Chapter 4 Section 4.5.1. In this chapter we adopt the approach of stacking TESS transits for several hot Jupiters to achieve an average timing offset corresponding to period evolution in the four-ten intervening years between sets of observations, and compute tidal quantities predicted for each system.

We also plot the spin:orbit commensurability for systems with published rotation periods in Figure 3.17. For planets orbiting faster than their star, we would expect the tidal bulge raised on the star, as well as dissipate forces in the planet to cause energy loss or slowing and therefore infall. In the case where a planet orbits slower, we'd expect the opposite to be true. However, this effect is most pronounced for close-in and tidally locked planets, whereas Figure 3.17 suggests that trends do not necessarily correlate to this commensurability for the planets on closer orbits. Further, though not appreciated in this figure, the amplitude of timing offset, which in some cases is several tens of minutes, is likely too high to be due to tidal effects alone (Ragozzine & Wolf, 2009).

Overall, our findings speak to the incredible quality of Kepler data and the instrument's ability to achieve highly precise transit timings. However, while TESS is only able to achieve a fraction of the precision, its follow-up of Kepler targets is

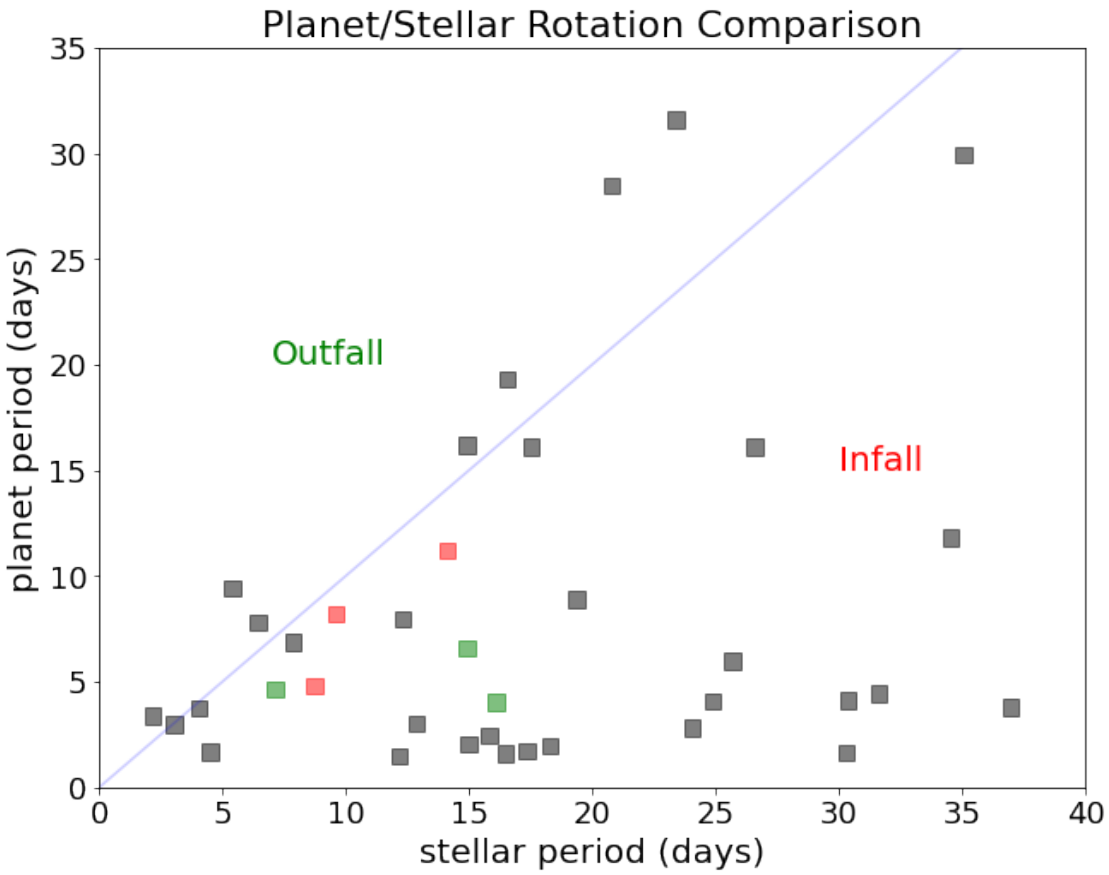


Figure 3.17: Stellar rotation verses planetary period is plotted. While Ragozzine & Wolf (2009) predicts that tidal interactions with a host star can cause the evolution of planetary orbits, this is much more likely for large, close-in companions. In this case, the lack of such a trend indicates that these larger offsets on the order of tens of minutes to hours are more likely to be due to other dynamical effects, such as the presence of planetary companions.

capable of providing useful updates to ephemerides as well as uncovering previously unknown trends in transit timings.

3.8 Conclusion

This study clearly demonstrates the utility of reexamining Kepler and K2 targets for more in depth system parameterization and to obtain updated ephemerides which would help in follow-up studies. While TESS provides one tool for doing so, the majority of systems examined in this work saw small to modest improvements to their linear ephemerides. However, several systems saw significant updates, or evidence of previously unseen timing trends that will be very important for follow-up

observations and have potentially interesting implications for the dynamics and evolution of those systems. In the coming years, programs like the James Webb Space Telescope (JWST) and the Extremely Large Telescopes (ELT) will enable detailed follow-up and characterization of exoplanet atmospheres and composition (Gardner et al., 2006). Given the busy observing schedules and value of telescope time, achieving precise ephemerides is critical for these studies.

This study has several limitations in that it did not look beyond a TESS SNR, which was in turn an estimate. Other studies have detected transits for Kepler and K2 targets with SNR below our cutoff. Deeper looks into the Kepler and K2 catalogue could be possible, especially by stacking or phase-folding TESS transits. Furthermore, transits were readily discarded from analysis as were full systems if they did not fall within our capacity to fit transits and timing trends in a relatively uncomplicated reproducable, semi-automated manner. This excludes systems with higher stellar activity, starspots, or many companions, as well as longer period planets for which there are large data gaps or insufficient transits to do a meaningful analysis. However, these methods could further refine planetary parameters and ephemerides for these systems as TESS continues to reexamine the Kepler and K2 fields. This approach could also be taken for other survey programs, prompting longer looks at known systems. Such studies open doors to more in-depth characterisation, as we will explore in the next chapter.

Be ready for highs, be ready for lows
A dream is a dream, until you go
Through the mistakes, you'll find who you are
Don't reach for the moon, you're going to Mars — *Judah and the Lion*

CHAPTER 4

Transit Timing Analysis and Prediction of Selected Systems

4.1 Introduction

While programs of follow-up on systems for the specific purpose of identifying and analysing TTVs build rich pictures of system dynamics and planetary parameters, TTVs are also useful in more limited senses as a temperature check on parameters and system architectures determined through other means. By simulating the expected TTV signals based on theoretical models, we can compare them with the observed TTV data to gain insights into the underlying system dynamics and explore different scenarios.

One of the key benefits of forward modeling TTVs is the ability to test and refine planetary mass and orbital parameters where actual transit times are more limited. By varying the parameters in the model, such as the masses, eccentricities, and orbital inclinations of the planets, we can generate a suite of TTV curves that represent different possible configurations. Comparing these simulated TTVs with the observed TTV data allows us to identify the parameter combinations that best reproduce the observed variations, helping us constrain the masses and orbital properties of the planets more accurately.

Forward modeling also aids in understanding the stability and long-term evolution of exoplanetary systems. By incorporating additional physical effects, such as gravitational interactions with other planets or tidal forces, into the model, we can simulate the long-term behavior of the TTVs over extended periods. This allows us to investigate the stability of the system and assess the potential presence of unseen planets that might induce detectable TTV signals.

Furthermore, forward modeling can be used to make predictions for future observations. By extrapolating the TTV signals into the future based on the modeled system dynamics, we can anticipate the timing and magnitude of future TTV events. This information is invaluable for planning and optimizing future observations, as it helps determine the optimal times and configurations to detect and characterize additional transits. It also aids in identifying potential opportunities for follow-up studies, such as spectroscopic observations or atmospheric characterization during specific transit events.

This chapter will explore several examples of forward modelling for systems with limited transit times, before taking a deeper look at TTV analysis of systems for which we have more data. First, we will examine two newly discovered planets in the young star, AU Mic, for which we use a small self-contained TTV analysis to do a sensibility check of planetary masses determined via RVs. We then turn to another two-planet system discovered by PlanetHunters TESS, HD 152843, where TTVs similarly help us understand and constrain possible planetary masses and eccentricity as well as provide a guideline for future observation. We then circle back around to TOI-270, where we show the results of ongoing transit follow-up and TTV "maintenance" before examining several of the systems identified in Chapter 3 that show interesting timing trends.

4.2 AU Mic

Declaration: *The following segment describes the AU Mic system from the two papers Zicher et al. (2022) and Wittrock et al. (2022) on which I am a co-author. As co-author I contributed the transit timing analysis and TTV predictions described*

in further detail below, and wrote the corresponding section in Zicher et al. (2022), and performed forward modelling, as well as advice and feedback on the fitting for Wittrock et al. (2022).

AU Mic is a nearby M-type star, located approximately 32 light-years away in the constellation Microscopium (Torres et al., 2006). It is relatively young, with an estimated age of only 20-30 million years, which makes it an important target for studying the early evolution of planetary systems, and it hosts an edge on debris disk (Kalas et al., 2004). Due to the rapid rotation and enhanced magnetic activity of young host stars, it is often quite difficult to detect planetary transits and perform RV follow-up. However, using TESS data in 2018, Plavchan et al. (2020) discovered two Neptune-sized exoplanets orbiting AU Mic. The discovery of young planets is rare and provides the unique opportunity to probe the amount of primordial gas accreted from the stellar disk before it is dispersed as a star ages. Answering questions about the composition of these planets also lends critical insight to the uncertain origins of close-in planets (Bean et al., 2021).

AU Mic b, has a radius of $R_{\rm b} = 4.2 \pm 0.2\,R_{\oplus}$ and orbits the star every 8.46 days at a distance of about 0.07 AU. AU Mic c has a radius of $R_{\rm c} = 3.24 \pm 0.16\,R_{\oplus}$ and orbits the star every 18.859 days at a distance of about 0.19 AU (Martioli et al., 2021). The proximity to 2:1 orbital resonance between these planets make them good candidates for potential TTV follow-up.

AU Mic was observed intensively for 10 months with HARPS in high-cadence mode by Zicher et al. (2022) in order to better constrain the masses and other orbital parameters of the two planets, totaling 91 observations. In order to model the significant stellar activity, a multi-dimensional Gaussian Process framework was used to simultaneously model the stellar and planetary contribution to RV signals. This resulted in RV signals for both planets, corresponding to a mass of $11.7 \pm 5.0\ M_{\odot}$ for planet b, and a mass of $22.2 \pm 6.7\ M_{\odot}$ for planet c. However, these masses suggest that planet b might be less dense, and planet c considerably

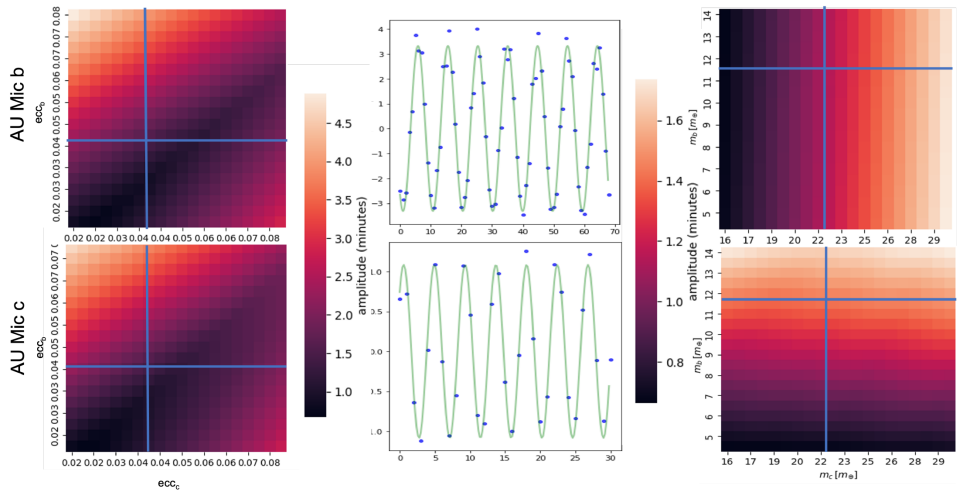


Figure 4.1: Expected TTV amplitudes for the AU Mic system. In the left panel, we vary the eccentricities, while keeping the masses fixed. In the right panel, we keep the eccentricities fixed but vary the masses. In both panels, the vertical and horizontal solid lines indicate the maximum a posteriori values from our modeling of the RVs. The explored range of eccentricities and masses extend slightly beyond the 1f confidence limit in each direction. In the middle panel, the blue dots show the expected TTVs (time of transit centre relative to a linear ephemeris) when the planet parameters are set to their maximum a posteriori values. The x-axis corresponds to transit number. The green lines show a sinusoidal fit to those TTVs.

denser, than previously thought, and present values in tension with the current standard models of core-accretion which suggest that density decreases with orbital radius (Lee & Chiang, 2015).

As was demonstrated in the case of TOI-270, RV and TTV observations combined have the potential to complement one another and deliver more information on a system than either approach alone. In this case, because the transit time points are so limited, fitting is unlikely to be feasible, however, forward modelling of transit times based on planetary and orbital parameters can confirm the agreement of observations to predictions.

As AU Mic b and c are close to a 2:1 mean-motion resonance, it is indeed possible that TTVs can be used to constrain their masses and eccentricities. Mid transit times for these planets from multiple observing programs appear as in Figure 4.2. Because they show divergence/residuals from a linear ephemeris these were then analysed for consistency with masses derived from the above RV/GP methods with

HARPS observations. Szabó et al. (2021) and Gilbert et al. (2022) report tentative TTVs for AU Mic b at the level of 3–4 min and 80 s, respectively, using TESS and CHEOPS observations. Although the measurement of transit times is somewhat difficult because of AU Mic's frequent flaring, these results indicate that strong TTVs, with amplitudes in excess of $\sim$10 min, are not present in the system. This can be used to provide a sanity check on the mass and eccentricity estimates derived in this work and in previous RV analyses, and to motivate future TTV follow-up.

Using the `TTVFast` package (Deck & Agol, 2014) we forward modelled the TTVs expected from a two-planet configuration as observed in the system. TTV amplitudes are most sensitive to planetary mass and eccentricity, so we varied those on a grid over a plausible range for these parameters, noting the amplitude of the TTV signal in each case. Our predictions are summarised in Figure 4.1. Even for the most extreme mass ratio and eccentricities compatible with the results of our RV analysis, the maximum amplitude of the TTVs never exceeds a few minutes, with a super-period of 80 days. We therefore concluded in this study that the mass estimates derived from RV analysis are consistent with existing transit observations.

Alongside the forward TTV modelling presented in Zicher et al. (2022), AU Mic b was independently followed up by Wittrock et al. (2022), which introduced additional transits from Gilbert et al. (2022) including three Spitzer (4.5 µm) transits, five TESS transits, 11 LCO transits, one PEST transit, one Brierfield transit, and two transit timing measurements from Rossiter-McLaughlin observations for AU Mic b, and three TESS transits for AU Mic c, shown in Figure 4.2.

Mid-transit times were extracted by a member of the research team using the EXOFASTv2 package (Eastman et al., 2019), which estimates the posterior probabilities through MCMC to both determine the statistical significance of our ground-based Spitzer detections and the confidence in the time of conjunction measurements to assess for the presence of detectable TTVs. Expected midpoint times were calculated using AU Mic b's period and T_0 from Gilbert et al. (2022). TTV analysis was then carried out using the Exo-Striker package (Trifonov, 2019). Exo-Striker utilizes MCMC to assess the statistical significance of the measured

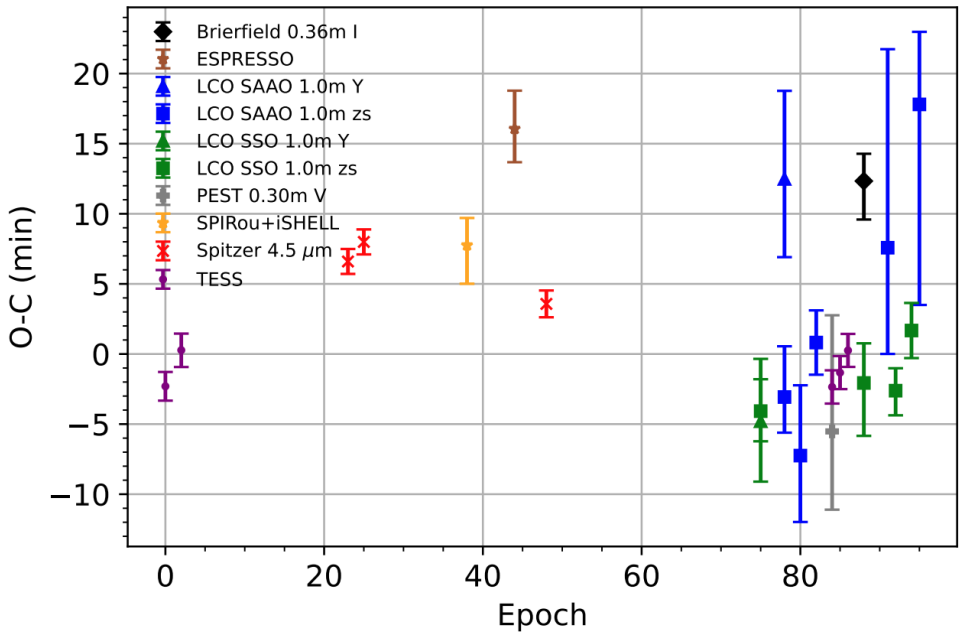


Figure 4.2: $O - C$ residuals from 8 observing campaigns for AU Mic b by Wittrock et al. (2022). With a $^2 \gg 1$ it is clear that the precise Spitzer transit times (which are corrected for relative light-time travel delay between Spitzer and the Solar System barycenter) are significantly offset from the linear ephemeris predicted by TESS transit times alone. The ground-based R-M transit midpoints are similarly late and consistent with the Spitzer transit times. As expected, other ground-based photometric transits show large scatter and correspondingly larger timing uncertainties relative to the space-based transit midpoint times.

TTVs and the confidence in the dynamical model posteriors that can be inferred from the data-points. Two scenarios were modelled: a two-planet system, and a three-planet system. The results of each of these fits is shown in Figure 4.3.

Overall, this TTV analysis yielded a mass of $10.8^{+2.3}_{-2.2}\,M_{\odot}$ for planet c, making it close to the mass of Neptune. Because TTVs observed in one planet constrain the mass of its companion, limited transit time points from planet c made it unfeasible to obtain a mass for planet b. However, as can be appreciated in Figure 4.3, a two-planet fit does not do an adequate job at accounting for the extracted TTVs. Further, this mass for planet c is not consistent with the RV data of Zicher et al. (2022), which is significantly lower.

This leaves us with several possible explanations for the timing residuals, which are on the order of ∼10 minutes. The first is that the impact of the rotational

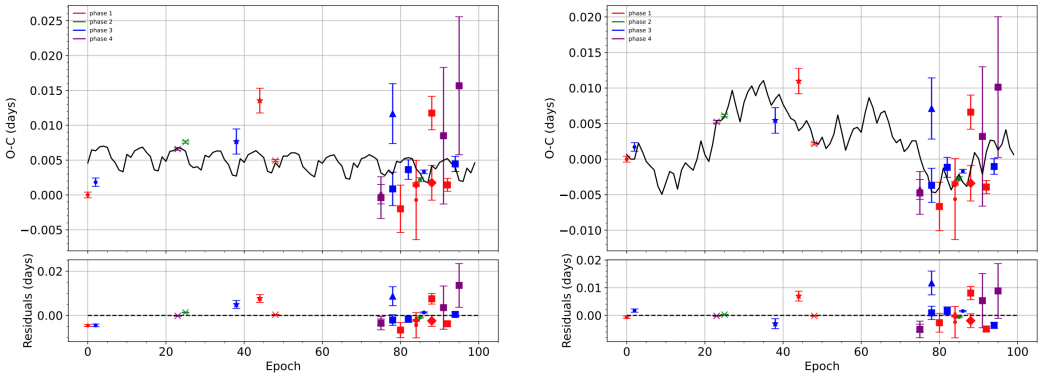


Figure 4.3: The black line shows the best fit Exo-Striker 2-planet model (left) and Exo-Striker 3-planet model (right) from Wittrock et al. (2022).

modulation of star spots is not being adequately accounted for in transit or photodynamical modeling, we are over or underestimating the impact on the TTVs. Stellar spots can significantly impact the recovered stellar and planetary model parameters (Pont et al., 2007; Désert et al., 2011) and can produce TTV-like signals that potentially lead to false-positive detection of non-transiting planets (Alonso et al., 2008; Sanchis-Ojeda & Winn, 2011). For AU Mic, it is estimated that with a spot fraction $> 3\%$, this could account for timing offsets of up to 7 minutes. Although the rotational period of the star (spin-orbit ratio of 7:4), producing a presumably repeating pattern of starspots does not align directly with the directional time offsets for all of the transits, it is possible that this could account for some of the scatter seen in the data.

Second, as a young active star, AU Mic flares frequently, which could also have a significant impact on transit times, depending on the specific modelling used to account for it. This study found that that the derived transit times are sensitive to the methods employed for accounting for the stellar flares. However, the analysis done by Gilbert et al. (2022), showed no dependence of transit timing on activity after marginalizing over models for the flares and spot modulation, and the TESS transit times of AU Mic b are fairly constant to within 4 minutes. Therefore, this effect could perhaps account for some, but not all of the timing offsets observed in this system.

Finally, considering the three-planet fit produced by ExoStriker, it is a possibility that a third planet is contributing to the small but seemingly significant timing

residuals seen in these data. While such a candidate must be too small or inclined to be thus far detected in either transit or RVs, Cale et al. (2021) explored additional candidate RV planet signals when modeling the RVs of the AU Mic system. One candidate period that was explored in particular proposed the presence of a planet in-between b and c, a "middle d" non-transiting planet with a period of 12.742 days. Such a planet would establish the AU Mic system in a 4:6:9 orbital resonance and result in significant TTVs. Confirmation of such a planet would rely on a wider baseline of transit timing and RV data.

While it is possible that a middle or outer "planet d" could lead to the observed timing residuals, because the transit times themselves are so limited in number and time-span, future RV and TTV observations of AU Mic b and c are needed to further constrain the masses and confirm the existence of possible additional planets. Further, it is important to reexamine the modelling of each transit in the context of spots and flaring in this young and active system. However, the work that has been done thus far in the discovery and characterisation of these planets is significant because it provides new insights into the formation and evolution of planetary systems around young stars. The system is still intriquing in that the planets' inferred masses from RV measurements, which have implications for the bulk and atmospheric compositions, highlight a discrepancy between the observed density of AU Mic c, and that inferred from core-accretion models. Overall, the AU Mic two-planet system is a unique and important target for further study in order to better understand the early evolution of planetary systems around young and active stars, as well as develop the tools needed to do so.

4.3 Discovery and Analysis of the HD 152843 system

Declaration: *The following segment describes the HD 152843 system, a discovery by Planet Hunters TESS, from the two papers Eisner et al. (2021) and Nicholson et al. (in prep) on which I am a co-author. As co-author I contributed the transit timing analysis and TTV predictions described in further detail below, and wrote*

the corresponding sections in the respective papers.

Planet Hunters TESS is a citizen science project that aims to discover exoplanets using transit data from TESS. While TESS pipelines do the mammoth share of discovery, the data produced by TESS is vast and running the majority through a single pipeline leads to some transits being missed. Specifically, detecting transiting systems with longer-period planets is challenging due to the reduced transit probability of those planets appearing, as well as the difficulty associated with detecting planets showing single transits using automated detection algorithms that rely on folding and stacking data. Therefore other approaches are used to identify longer period, single transit candidates, such as machine learning (Pearson et al., 2017; Zucker & Giryes, 2018), or visual vetting with the help of citizen science (Eisner et al., 2020; Fischer et al., 2011). Planet Hunters TESS recruits members of the public to help search for exoplanets by analyzing TESS data through a user-friendly online platform. Users examine light curves, searching for dips in brightness that occur at regular intervals, and can also flag any other interesting features in the light curves that may warrant further investigation.

One of the systems discovered through this mechanism with the help of 25 citizen scientists is a two-planet system around a bright (V = 8.85 mag) early G dwarf, HD 152843 or TOI 2319. Three transit events from two planets were first detected in TESS sector 25, revealing a period of $11.6264^{+0.0022}_{-0.0025}$ days and radius of $3.41^{+0.14}_{-0.12} R_\oplus$ for the inner planet, and a period in the range 19.26–35 days and a radius $5.83^{+0.14}_{-0.14} R_\oplus$ for the outer planet, which was only seen to transit once (see Figure 4.4). Follow-up RV observations were performed with HARPS-N, which confirmed the detection of planet b, giving it an approximate mass of $11.56^{+6.58}_{-6.14} M_\oplus$ and placing an upper limit on the mass of planet c of 27.5 $M_\oplus$.

Because the planets in the HD 152843 system are potentially near orbital resonance, it might be possible to measure TTVs in future observations of the system. With RV measurements on hand to perform a joint analysis, further refinement of planetary mass and orbital parameters are possible, critical for interpreting

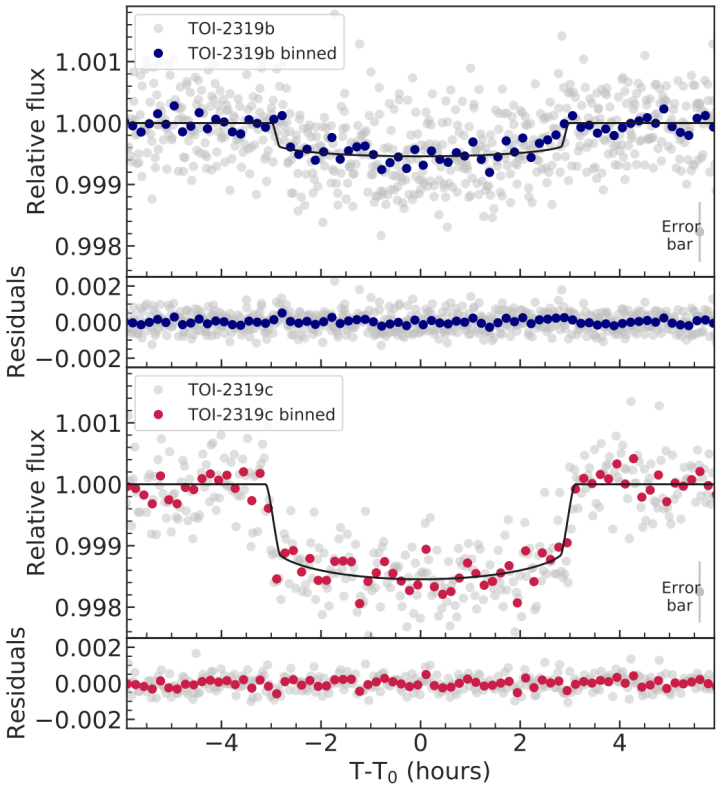


Figure 4.4: Phase-folded transits of HD 152843 in TESS from Eisner et al. (2021). Nominal TESS data are shown in light gray together with 10-min binned data in solid colour. The inferred transit model for each planet is over-plotted with a solid black line

atmospheric transmission spectra in smaller planets (Batalha et al., 2019). TTVs can also enable the detection of inclined non-transiting planets and can therefore lend insight into system demographics and architectures (Brakensiek & Ragozzine, 2016).

TTVs were assessed for this system using the best-fit planetary parameters across a range of mass, period, and eccentricity solutions using the `TTVFast` framework of n-body simulations (Deck & Agol, 2014). Maximum likelihood solutions for the periods of planets b and c indicate a possible 2:1 resonance, which would result in TTVs with an amplitude ranging from 5-40 minutes, and a super period of approximately 2-3 years, allowing for follow-up observations to detect discernible TTVs on the scale of about a year. This amplitude would be greatly increased for non-zero eccentricities. In the window of possible period solutions for planet c, one configuration involves a 5:3 commensurability; however, significant TTVs would not be observed away from resonance. At the time of discovery, followup studies of this system would

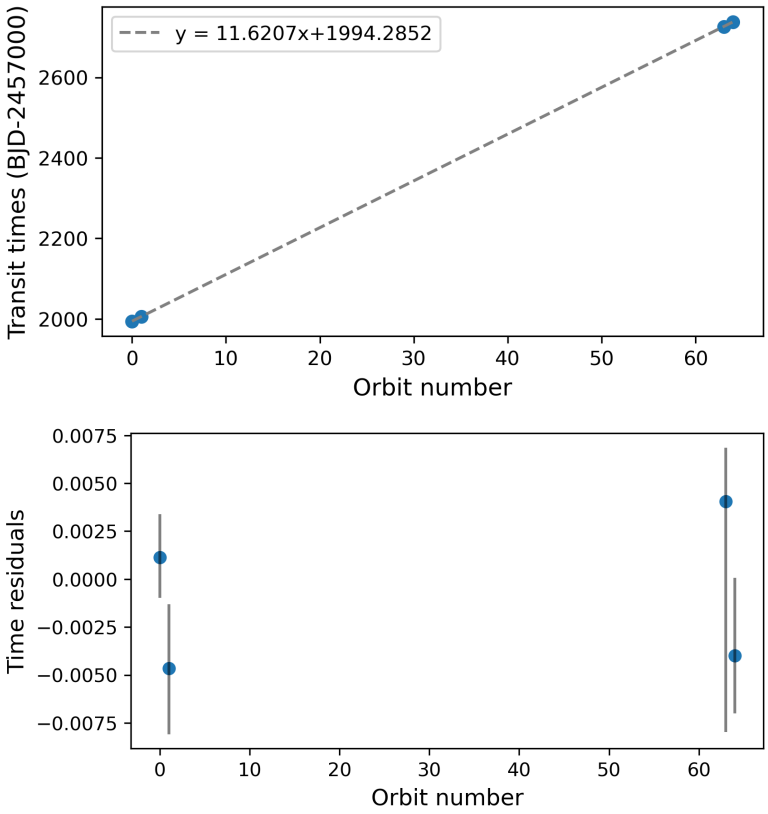


Figure 4.5: Transit times and $O-C$ residuals of HD 152843 b in TESS sector 25 and 52

be necessary to significantly constrain planetary masses, eccentricities, and other orbital parameters, given both the presence or absence of significant TTVs.

A paper in prep by Nicholson et al. presents two more transits for planet b combined as well as one of planet c when HD 152843 was reobserved in Sector 52 of TESS's extended mission. We additionally acquired high-resolution ($R \approx 115\,000$) spectra with the High Accuracy Radial velocity Planet Searcher in the Northern hemisphere (HARPS-N) obtaining a total of 172 spectra between spectra between September 2020 and October 2022. Joint RV and transit analysis yields a period of $11.62071^{+9.6e-05}_{-0.000106}$ days and a mass of $9.82^{+1.71}_{-1.61}\,M_\oplus$ for planet b and a period of $19.502104^{+7.4e-05}_{-8.5e-05}$ days and a mass of $9.67^{+1.97}_{-1.92}\,M_\oplus$ for planet c. This combination of a second transit of planet c plus the RV monitoring critically enabled us to narrow down from a range of potential periods for planet c to this one, which as it

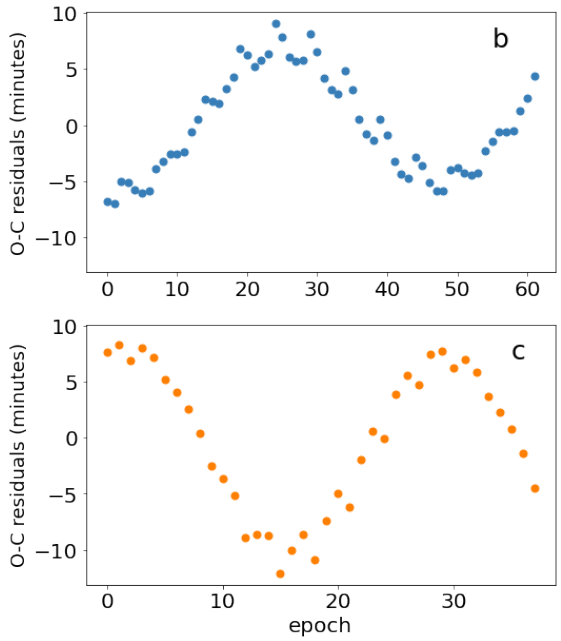


Figure 4.6: The expected Observed minus Calculated (O-C) residuals for planet b (top) and c (bottom) for planetary parameters obtained in this study, which show periodic TTVs with detectable amplitudes. Significant scatter or "chopping" on the order of minutes can be seen in the timings of both planets.

turns out is the shortest period allowed by the TESS data. This therefore places planet b and c very close to 5:3 orbital resonance.

We thereby checked for any tentative evidence of TTVs in the 4 transits observed so far for planet b, as follows. We fit each transit individually, keeping all the parameters fixed to the values, and varying only the time of transit centre (T_0). The transit time residuals from this linear ephemeris are shown in the bottom panel of Figure 4.5. There are no TTVs obviously present in this data, however, given the scatter and uncertainties of each time point, TTVs are not ruled out.

As we now have periods and masses for both planets from the joint analysis of light curves and RVs, we can check if the observed transit timing residuals are consistent with what we would expect. We simulated the expected TTV signal given the planetary system parameters obtained above using the `TTVFast` package (Deck et al., 2014a). Because of the proximity of the planets' periods to MMR, a periodic signal is expected to be observed with an amplitude of 15-20 minutes, as seen in Figure 4.6, which shows the simulated residuals to a linear ephemeris of each planet

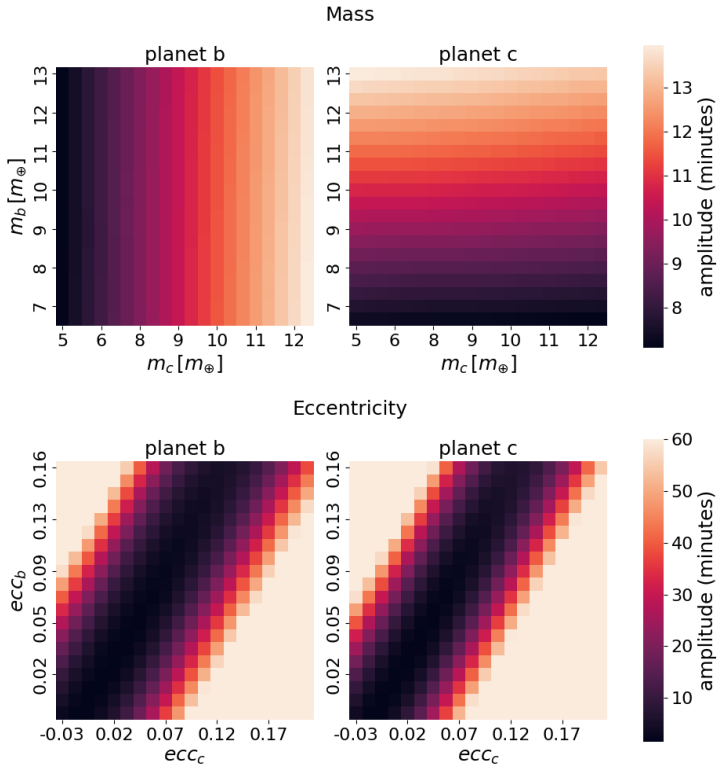


Figure 4.7: Heatmaps show expected amplitudes of TTVs (O-C offsets) for a range of parameters across our uncertainty distribution. The effect of varying the mass of each planet to two sigma plus or minus is shown in the top panel, and the effect of varying eccentricities is shown in the bottom panel. For most combinations, TTVs remain detectable at amplitudes of 10 minutes or more. In each case, the parameter in question is varied while all other parameters are fixed at their median value.

over a superperiod. While uncertainties exist on each of the input parameters, Figure 4.7 shows a range of TTV amplitudes across a two sigma distribution of input parameters, with the most significant influence coming from planetary masses and eccentricities. As expected, the signal is most sensitive to eccentricity, with higher eccentricities leading to larger TTVs. However, a wide range of masses and eccentricities in the two planets should still allow for TTVs to be detectable, given the precision of individual transit times for each planet on the order of 4 minutes and 2 minutes for planets b and c respectively.

As mentioned earlier, the superperiod of two interacting planets in j:j-i orbital resonance is given by $P_{TTV} = \left|\frac{j-i}{P_{inner}} - \frac{j}{P_{outer}}\right|^{-1}$. For HD 152843 this gives rise to a superperiod of approximately 560 days, which for planet b is on the order of 50 epochs. While the spread in transit times covers this superperiod, several

more intermediate transits would be necessary to confirm the non-linearity of residuals. However, the scatter currently observed in the four transits of planet b is consistent with chopping effects, the short timescale offsets associated with the planet's synodic period evolution (Deck & Agol, 2014).

Further observations of HD 152843 will confirm the presence of any TTVs and enable us to better constrain planetary masses and orbital properties. Due to the brightness of the host star and the strong likelihood of an extended H/He atmosphere on both planets, this system makes for an interesting prospect for follow-up. The combination of a bright host star and two Neptune-mass planets makes it an ideal target for atmospheric studies and comparative planetology.

4.4 Further Work on TOI-270

Following the work of Kaye et al. (2022) presented in Chapter 3, TOI-270 has continued to be monitored from the ground and from space throughout 2022. A total of 16 new observations were made between the end of 2020 and and 2022, comprised of 3 observations for planet b, 8 observations for planet c, and 5 observations for planet d. New observations are listed in Tables B.3 and B.4 to round out those presented in Table 2.1. We hereby present an updated analysis of these added data, which demonstrate good agreement with the work performed earlier, giving us a small adjustment to the masses and eccentricities of planets c and d, and a small correction to the predicted ephemerides.

4.4.1 Transit and TTV Analysis

In addition to the observations discussed in Chapter 2, TOI-270 was observed from January 2020 to August 2022 with ASTEP and NGTS. Transit fits were performed as described in Section 2.3. Fits are shown for one transit of each TOI-270 c and TOI-270 d in Figure 4.9

As in Kaye et al. (2022), I proceeded to perform TTV analysis using the `TTVFast` package to model and fit our transit times. `TTVFast` utilises a numerical integration approach (symplectic integrator with a Keplerian interpolator) to simulate the

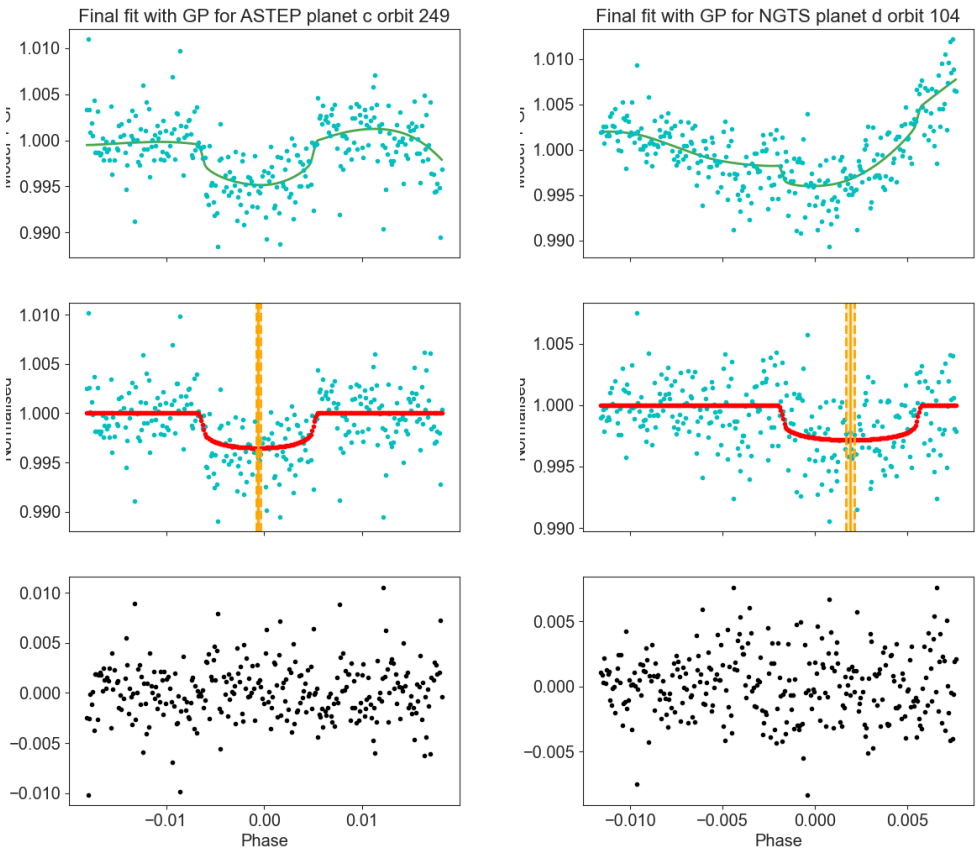


Figure 4.8: Fits of planet c and planet d with ASTEP and NGTS respectively.

dynamical interactions between planets and accurately calculate the resulting transit timing variations. With this package, I constructed a dynamical model of the TOI-270 system by defining the initial orbital parameters and masses of the planets from the values in Kaye et al. (2022). I fit for five orbital parameters for each planet, $M_{\rm p}/M_\star$, P, $e\cos\omega$, $e\sin\omega$, and T_0, for an initial total of 15 parameters. However, we experimented with fixing the transits of planet b to that of a linear ephemeris and found that it greatly improved our convergence time without impacting fit values, reducing our paramter array to 12.

For fitting, we used MCMC instead of the DEMCMC used in Chapter 2. DEMCMC incorporates the principles of Differential Evolution (DE), a stochastic optimization method. In DEMCMC, multiple chains are evolved simultaneously

using a combination of MCMC steps and DE steps, which involve generating trial parameter vectors by combining and perturbing existing parameter vectors. These trial vectors are then evaluated using the likelihood function, and a selection process determines whether they are accepted or rejected. The DE steps introduce additional exploration and exploitation capabilities compared to traditional MCMC.

However, MCMC methods are often computationally more efficient than DEMCMC, as DEMCMC involves additional steps of generating trial parameter vectors and evaluating them, which can be computationally demanding, particularly in high-dimensional problems. Further, MCMC methods are known to have good convergence properties when properly implemented and tuned. The Markov chain constructed by MCMC tends to converge to the target distribution, ensuring that the samples generated provide reliable estimates of the posterior distribution. In contrast, DEMCMC may have more complex convergence properties and may require careful tuning of its parameters to achieve desirable convergence, which proved time consuming and finicky in the the previous analysis.

In this round of fitting, orbital elements were osculating and defined at the simulation start time BJD = 2458380 using Jacobi coordinates. As before, we used the time of first transit of planet b as a convenient reparameterisation of the mean anomaly [e.g.] (Jontof-Hutter et al., 2016; Libby-Roberts et al., 2020) and fixed the inclinations and longitudes of ascending node to 90° and 0°, respectively. We employed the same priors as in Kaye et al. (2022) for an RV-informed analysis and computed an MCMC to compute the posterior distributions. After 10,000 burn-in steps with 40 walkers, chain lengths of around 300,000 steps were required to achieve convergence. We then adopted 68.300% confidence intervals for estimating one-σ posterior uncertainties, which are reported in Table 4.1.

4.4.2 Results and Discussion

In total, the newer observations added two years to our baseline and reached another half of the TTV superperiod. As can be seen in Figure 4.9 the newer transits of planet c are constraining and quite consistent with the pattern set up by the earlier

fits (pictured in red). The transits of planet d, as would be expected with its smaller radius and thus shallower transits, have greater uncertainty on their times. No updates were made to the mass of planet b. Overall, we arrive at masses in this study of $M_c = 6.174^{+0.19}_{-0.16}\,M$ and $M_d = 4.18 \pm 0.12\,M$, the latter of which is very slightly lower but consistent with the masses obtained in Kaye et al. (2022). Notably, the error on the mass of planet c has been further halved by the addition of these data, making it one of the planets with the best constrained mass. We now arrive at an eccentricities for planet c of 0.0085 ± 0.0007, and for planet d of 0.0111 ± 0.001, which for both planets are significantly greater than the value measured previously, and might speak to power of having the definitive completion of one superperiod cycle and commencement of the next. Updated parameters are summarised in Table 4.1 and fits for planet c and d and can seen in Figure 4.9.

Table 4.1: Orbital and planetary parameters fit for TOI-270.

Parameter	Prior	Posterior	Units
$M_{\rm b}$	$\mathcal{N}(1.58, 0.26)$	$1.38^{+0.19}_{-0.21}$	M
$P_{\rm b}$	$\mathcal{U}(3.35, 3.37)$	$3.35992^{+0.00005}_{-0.00004}$	days
$e_{\rm b}\cos\omega_{\rm b}$	$\mathcal{U}(-0.7, 0.7)$	$0.007^{+0.085}_{-0.067}$	–
$e_{\rm b}\sin\omega_{\rm b}$	$\mathcal{U}(-0.7, 0.7)$	$-0.005^{+0.061}_{-0.059}$	–
$T_{0,\rm b}$	$\mathcal{U}(5.61, 5.81)$	$5.7155^{+0.0012}_{-0.0014}$	days
$M_{\rm c}$	$\mathcal{N}(6.14, 0.38)$	$6.174^{+0.19}_{-0.16}$	M
$P_{\rm c}$	$\mathcal{U}(5.65, 5.67)$	5.66051 ± 0.00004	days
$e_{\rm c}\cos\omega_{\rm c}$	$\mathcal{U}(-0.7, 0.7)$	$0.0036^{+0.0009}_{-0.0009}$	–
$e_{\rm c}\sin\omega_{\rm c}$	$\mathcal{U}(-0.7, 0.7)$	0.0077 ± 0.0008	–
$T_{0,\rm c}$	$\mathcal{U}(6.5, 6.8)$	6.6834 ± 0.0002	days
$M_{\rm d}$	$\mathcal{N}(4.78, 0.46)$	4.20 ± 0.16	$\mathcal{U}(0, 50)$
4.184 ± 0.12	M		
$P_{\rm d}$	$\mathcal{U}(11.36, 11.4)$	11.38194 ± 0.00010	days
$e_{\rm d}\cos\omega_{\rm d}$	$\mathcal{U}(-0.7, 0.7)$	$0.0081^{+0.0028}_{-0.0025}$	–
$e_{\rm d}\sin\omega_{\rm d}$	$\mathcal{U}(-0.7, 0.7)$	0.0075 ± 0.0024	–
$T_{0,\rm d}$	$\mathcal{U}(6.8, 7.1)$	6.9757 ± 0.0006	days

Table 4.1: Orbital elements are osculating and defined using Jacobi coordinates at the simulation start time BJD = 2458380.

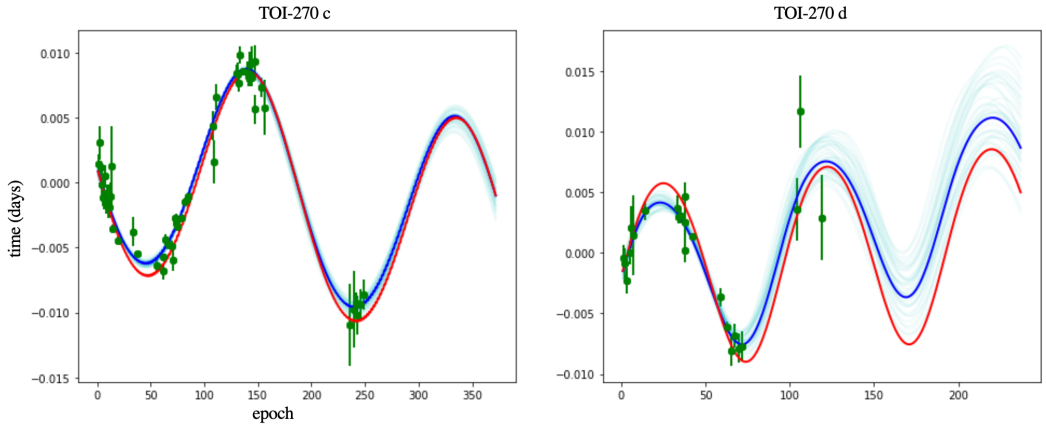


Figure 4.9: The final fits for planets c and d are plotted. The updated best-fit fit is plotted in dark blue with samples from the posterior in light blue whereas the original best-fit from Kaye et al. (2022) is plotted in red. While this yields quite similar results for planet c, there is a more pronounced difference for planet d.

Overall, the increased temporal coverage of TOI-270 resulted in an updated analysis that revealed slight adjustments to the mass and especially eccentricity estimates for the two outer planets. The increased temporal coverage allowed for a more precise determination of the transit timing variations, which in turn provided more stringent constraints on the planetary mass of planet c. This also results in up to ∼20 minutes of adjustment to the predicted ephemerides of planet d in particular looking towards 2030, which will be a valuable update when planning precisely timed transit spectroscopy studies with JWST and other upcoming space missions. Telescope time is costly and accurate allocation of observing time is important to make the strongest science case for follow-up.

Follow-up spectroscopy for TOI-270 is ongoing. One transit of planet c was obtained with IGRINS high-res spectrograph, but no signals were extracted. A current JWST proposal (GO 4098, PI Bjorn Benneke) will be observing TOI-270 in the coming year. The observing programme is aiming to conduct a targeted search for a class of planets known as "water worlds", whose existence would have implications for theories of planet formation, and with compositions dominated by volatiles other than H/He, they represent a new regime of atmospheric chemistry that has until now remained uncharted by observations.

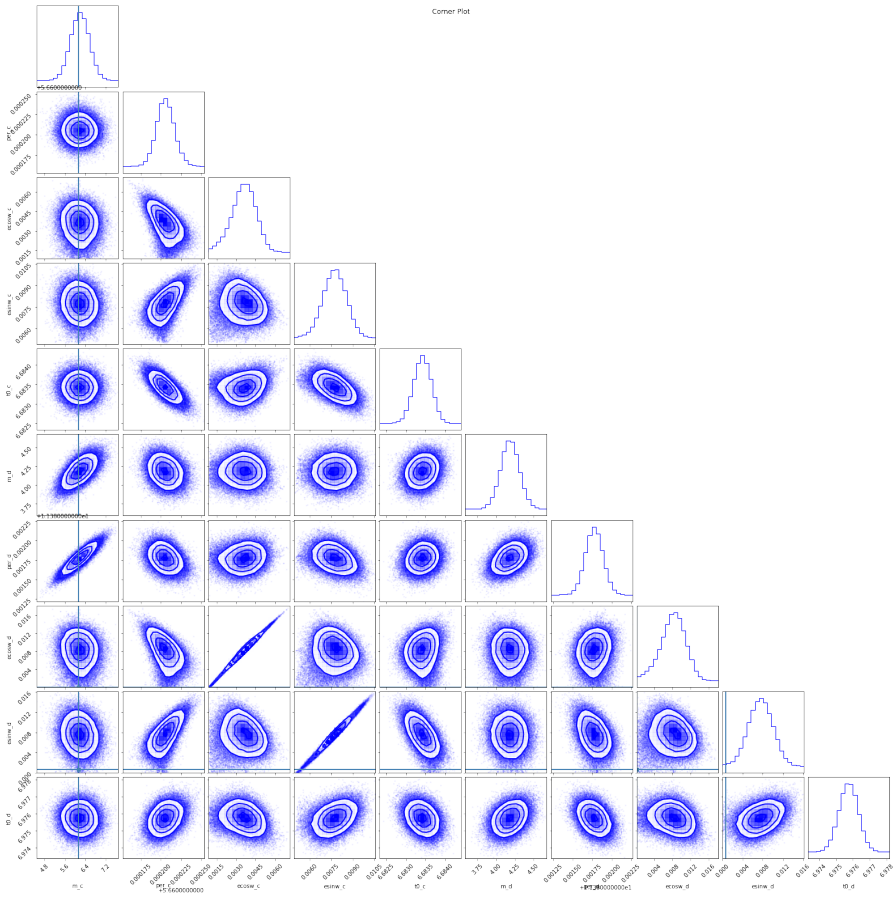


Figure 4.10: Corner plot showing the posterior distribution for planets c and d (planet b was fit for a linear ephemeris).

Due to its large aperture, broad infrared wavelength coverage, and ultra-stable space-based platform, JWST provides the first opportunity to unambiguously identify water worlds and characterize their atmospheric compositions. They will measure atmospheric transmission spectra using JWST's NIRISS SOSS to observe 0.8-2.8um and NIRSpec G395H NIRISS/SOSS will be used to observe 2.9-5µm.

TOI- 270's transit times will continue to be monitored by TESS and other ground-based facilities. Even with some of the best characterised TTVs in a TESS system, obtaining more years of observations of any exoplanet system with TTVs is crucial for accurately characterizing the planetary system's architecture, understanding the dynamical interactions within the system, and confirming the long-term stability of the system. Longer observation periods enable more precise determination of planetary masses, orbital parameters, and the presence of additional

bodies, providing a deeper understanding of the underlying physics and dynamics of these systems.

4.5 Systems from Catalogue paper

4.5.1 Hot Jupiters

Some of the planets discovered by Kepler, K2, and TESS are considered "hot Jupiters", with roughly Jovian masses and orbiting their host stars with semi-major axes less than 0.1 AU. However, the presence of such planets so close into their host star does not match the most classically accepted giant planet formation models, core accretion and gravitational instability, which would occur further out in a system's protoplanetary disk (Papaloizou & Terquem, 2005). Initial migration happens to some extent in the formation process itself, with protoplanets interacting with other forming planets and material in the disk (Papaloizou et al., 2006). After the disk has dissipated after a few Myr, most significant migrations likely arise from interactions with the newly formed planets, with planets collided with and ejecting one another until only a few remain with dynamic stabilities of $> 10^8$ yr (Chatterjee et al., 2008; Ford & Rasio, 2008). In this stage of evolution, interactions and collisions can induce significant changes to the eccentricities and inclinations of the remaining planets (Jurić & Tremaine, 2008). Other mechanisms that produce temporary changes in eccentricity and induce orbital migration are the Kozai mechanism mentioned in Section 1.6.2, which occurs when a companion star or second high mass planet can periodically induce large changes in eccentricity (Wu & Murray, 2003). Then, when the planet reaches is periapse with a significantly reduced pericentre, it is then subject to greater tidal dissipation and a gradual inwards migration.

In turn, tidal dissipation or tidal friction, refers to the conversion of mechanical energy into heat due to internal friction within the planet. This dissipation occurs as the planet experiences tidal deformations caused by the star's gravitational pull. Tidal dissipation acts as a damping mechanism, causing the planet's orbit to gradually decay over time, and continue a hot Jupiter's inward migration. Tidal interactions with the host star cause other effects such as tidal locking, in which

one side of the planet faces the star, as well as evolution of the spin-orbit angle, between the angular momentum vectors of a star's rotation and a planet's orbit.

The efficiency of tidal dissipation in a body is often parameterised by a dimensionless quality factor Q, which reflects the fact the body undergoes a forced oscillation and dissipates a small fraction of the associated energy during each oscillation period. This is analogous to the quality factor in a forced, damped harmonic oscillator and can be described (as in Murray & Dermott (1999)) as

$$Q = 2\pi E_0 \left(\oint -E \mathrm{dt} \right)^{-1} \tag{4.1}$$

where E_0 is the maximum energy stored in an oscillation, or in this case an orbit, and the integral represents the energy dissipated over one cycle. Q is also related to the time lag τ in the response of the body to tidal forcing of frequency $\hat{\omega}$ by $Q^{-1} = \hat{\omega}\tau$ for $Q \gg 1$. We can then further define $Q' = \frac{3Q}{2k}$ where k is the second–order potential Love number of the body, a dimensionless parameter that quantifies the degree to which the body's shape is deformed under the influence of tidal gravitational forces. Its value depends on various factors, including the body's mass distribution, elastic properties, and internal structure, but it is often estimated from theoretical models, numerical simulations, or observational data. For stars, Q' is typically set to $\sim 10^6$, and for hot Jupiters, similar values are applied, ranging from 6×10^4 - 2×10^6 (Yoder & Peale, 1981). In order to determine the extent of tidal dissipation in a system and therefore be able to quantify the evolution of the system, we need to calculate Q' for each body. This manifests as a gradually decaying period, where the energy from the system if lost at a rate (from Millholland & Laughlin (2018)) of

$$\frac{dE}{dt} = \frac{(GM_\star)^{3/2} M_P}{6\pi} a^{-5/2} \dot{P} \tag{4.2}$$

Which in turn relates to the stellar and planetary tidal factors, $Q_\star$ and Q_P as

$$Q'_\star = \left(\frac{M_p}{M_\star} \right) \left(\frac{R_\star}{a} \right)^5 \frac{27\pi}{\dot{P}} \left(\frac{\omega_\star}{n} - 1 \right) \tag{4.3}$$

for inspiral that is dominated by tidal dissipation in the star and

$$Q'_P = -\frac{3}{2}\left(\frac{M_\star}{M_p}\right)\left(\frac{R_P}{a}\right)^5 \frac{171\pi e^2}{\dot{P}} \tag{4.4}$$

for inspiral that is dominated by tidal dissipation in the planet, where e is the eccentricity.

Kepler systems reobserved with TESS make good candidates for observing this late stage of orbital evolution (Christ et al., 2019). Vissapragada et al. (2022) recently presented some evidence of a tidally-driven inspiral in the Kepler-1658 system, which consists of a hot Jupiter(1.1 R_J, 5.9M_J). They used transit timings from Kepler, Palomar/WIRC, and TESS, to show a decrease in orbital period period of 131^{+22}_{-20} for Kepler-1658 b, corresponding to an infall timescale of 2.5 Myr. Rosário et al. (2022) similarly examines several WASP systems that were re-observed with TESS data, finding small changes in periods, though not enough evidence to align with tidal decay models.

Here we present several of the hot Jupiters examined in Chapter 3 and discuss the possibility of observing orbital evolution using TESS data. While we do not delve deeply into the mechanisms of potential orbital evolution at play in the system, we demonstrate the potential utility of TESS to calculate and find two planets, K2-34 b and Kepler-426 b, for which a significant $\dot{P}$ is measured.

We started by selecting 11 systems with $a < 0.1$ AU, with $M_p > 0.6\,M_J$, and with $\mathrm{SNR}_{\mathrm{TESS}} > 6$, listed in Table 4.2. A population plot appears in Figure 4.11 and residuals plots can be seen in Figure B.7.

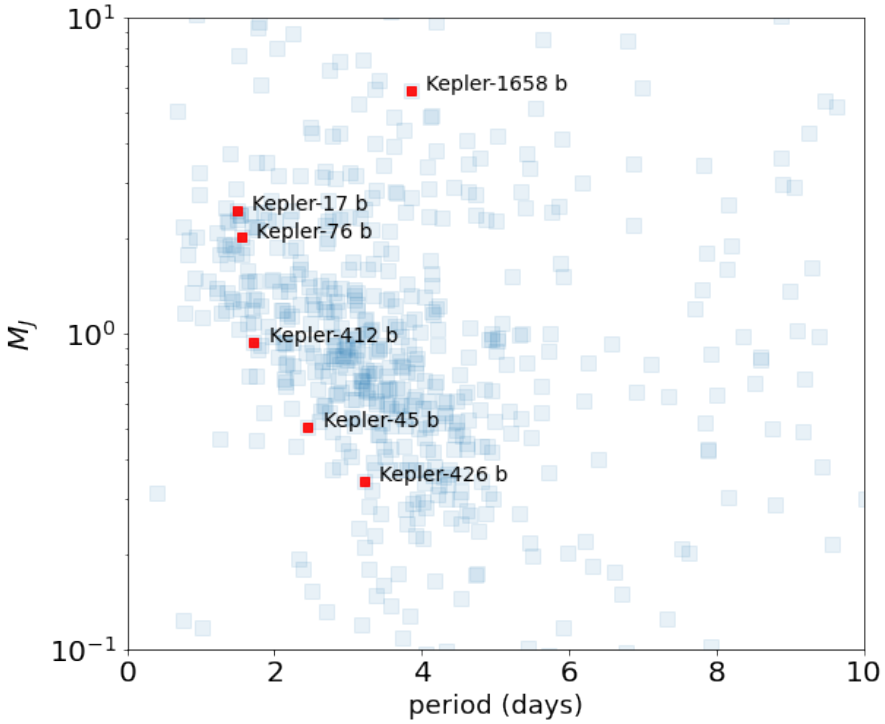


Figure 4.11: The population of selected hot Jupiters with well-characterised masses. In transparent black are known transiting exoplanets.

Table 4.2: hot Jupiter Systems from Kepler/K2 to TESS.

Planet	radius (R_J)	mass (M_J)	a (AU)	Source	Kepler T_0	Kepler P	TESS ΔP	SNR
K2-34 b*	1.44	1.77	0.0426	4	231.1347 $\pm 5.5e^{-05}$	2.9956361 $\pm 1.60e^{-07}$	0.000140 $\pm$0.000130	39.4
K2-45 b	0.60		0.0224	5	170.8218 $\pm 3.4e^{-05}$	1.72925968 $\pm 6.40e^{-06}$	-0.000017 $\pm$0.000100	11.3
Kepler-1658 b**	1.07	5.88	0.0544	7	172.9245 $\pm 1.55e^{-04}$	3.849373 $\pm 1.47e^{-06}$	0.0011 $\pm$ 0.0006	6.8
Kepler-17 b	1.31	2.45	0.02591	1	352.6787 $\pm 1.5e^{-05}$	1.48571096 $\pm 3.20e^{-08}$	0.000032 $\pm$0.000068	20.2
Kepler-412 b	1.34	0.94	0.02897	2	133.0210 $\pm 3.1e^{-05}$	1.72086125 $\pm 6.40e^{-08}$	0.000002 $\pm$0.000008	8.5
Kepler-426 b*	1.09	0.34	0.0414	3	133.6320 $\pm 4.7e^{-05}$	3.2175187 $\pm 2.00e^{-07}$	0.000025 $\pm$0.000024	7.4
Kepler-45 b	0.96	0.51	0.03	3	197.6526 $\pm 1.7e^{-05}$	2.45524035 $\pm 1.00e^{-08}$	0.000017 $\pm$0.000100	10.9
Kepler-485 b	1.29			6	133.6690 $\pm 4.8e^{-05}$	3.243259 $\pm 1.90e^{-07}$	0.000025 $\pm$0.000130	7.9
Kepler-488 b	1.41			6	139.4662 $\pm 4.1e^{-05}$	3.12082928 $\pm 1.00e^{-07}$	-0.000006 $\pm$0.000014	8.9
Kepler-76 b	1.36	2.01	0.0274	2	133.5487 $\pm 3.4e^{-05}$	1.5449289 $\pm 6.00e^{-08}$	0.000014 $\pm$0.000061	18.5
Kepler-785 b	1.16			6	178.6893 $\pm 3.4e^{-05}$	1.9737609 $\pm 8.70e^{-08}$	-0.000005 $\pm$0.000090	7

Table 4.2: Systems from Chapter 4. Kepler-1658 b shows a detection of an evolving period. K2-34 b and Kepler 426 (starred) show very tentative constraints on their ΔP from their Kepler/K2 to their TESS fits. Sources listed are [1] Désert et al. (2011), [2] Esteves et al. (2013), [3] Bonomo et al. (2017), [4] Hirano et al. (2016), [5] Crossfield et al. (2016), [6] Morton et al. (2016), [7] Chontos et al. (2019)

Name	$Q'_\star$	Q'_P	$\dot{P}$
Kepler-17 b	$2.9 \pm 0.7 \times 10^5$	430 ±220	26±7
Kepler-412 b	$1.8 \pm 0.9 \times 10^5$	-	36±19
Kepler-426 b	$1.8 \pm 1.1 \times 10^3$	$3.3 \pm 1.1 \times 10^4$	22.5±4.8
Kepler-45 b	630±230	$4.4 \pm 0.9 \times 10^3$	77.3±19
Kepler-76 b	$7.1 \pm 0.7 \times 10^5$	-	29±18
Kepler-1658 b	$2.2 \pm 0.8 \times 10^4$	10±3.2	180±62

Table 4.3: Timing Characteristics Calculations of lower limits of $Q'_\star$ and Q'_P and minimum $\dot{P}$ for which we could expect to see infall given our timing error. Not all planets have reported masses, and not all stars have reported rotational periods. $\dot{P}$ is presented in milliseconds per year.

In the previous chapter, when extracting transit times for individual transits, we performed a global planetary parameter fit using the data from Kepler or K2 for respective systems and then fixed the majority of these planetary parameters, while fitting only for T_0 and limb darkening parameters in TESS. Here, we look at higher SNR planets, and therefore fit TESS data as one phase-folded light curve for T_0, p, $cosi$, and limb darkening, while keeping the values of R_p and $R_\star$ fixed to the values obtained from the Kepler/K2 fit. Fits were otherwise performed as described in Section 3.3. No differences in $\cos i$ are found to be statistically constraining in TESS data.

We then compared the error on the period offsets and T_0 timing precision to the quantities $Q'_\star$, Q'_P, and $\dot{P}$ calculated for each target, presented in Table 4.3. In order to achieve this, as can be seen in equations 4.3 and 4.4, information is needed on each planet and star's mass, and on the stellar rotation period. As a rough estimate, for our predictions, we use $Q'_\star = 10^5$ and $Q'_P = 2 \times 10^4$. The expression $\left(\frac{\omega_\star}{n} - 1\right)$ in equation 4.3 is akin to the ratio of solar and planetary spin:orbital commensurability. We are left with 6 planets for which some of these calculation are achievable. $\dot{P}$ (typically presented in millisecond yr^{-1}) relates to the total time offset between observations as

$$t\,(N) = t_0 + NP + \frac{1}{2}\dot{P}N^2 \tag{4.5}$$

From our fitting of T_0 and P, we find no strong evidence of tidal infall for the majority of these systems, with a $T_{0\mathrm{TESS}} - T_{0\mathrm{Kepler}}$ consistent with zero. However, through our simple fitting, we find moderate evidence for infall in Kepler-1658 b and tentative evidence in K2-34 b and Kepler-426 b.

Kepler-1658 is a hot Jupiter (Mp $= 5.88\,M_J$; Rp $= 1.07\,R_J$,P $= 3.85$ days), recently characterised and confirmed by Chontos et al. (2019) through RV measurements and astroseismology. These authors searched but did not find any evidence for tidal infall on the 4 year timescale of the original Kepler mission. Howeever, Vissapragada et al. (2022) recently reexamined it with data from TESS and Palomar, finding evidence for evolution with a $\dot{P} = 131^{+20}_{-22}\,ms\,yr1$ and a $Q_\star$ of $2.5^{+0.85}_{-0.62} \times 10^4$.

While lacking the Palomar data points in our analysis, we find a clear divergence from a linear ephemeris (see Figure 4.12) with several minutes of residuals in TESS. Through fitting the TESS alone, similar evidence of tidal evolution with a total change in T_0 of $-14.62^{+3.3}_{-4.8}$ minutes compared to TESS data. We calculated a $Q_\star = 2.2 \pm 0.8x10^4$, consistent with their results, as well as a $\dot{P} = 180 \pm 62$ ms yr1 consistent both with their measurements and our own, though our error is considerably larger ($\dot{P}_{\mathrm{measured}} = 205 \pm 150$ ms yr1). While we perform this analysis as a rough assessment of the potential of our systematic transit fitting, and leave detailed analyses to future studies, these results showcase the potential for exciting follow-up with TESS and other transit programs as we continue to expand the observing baseline out from Kepler.

While most other systems had an error on their Kepler to TESS $\dot{P}$ too great to constrain it in any way, two other planets, K2-34 b and Kepler-426 b that are somewhat better constrained show very tentative evidence of evolution, with the $1-\sigma$ error on their $\dot{P}$ not quite consistent with zero in a way that could lend itself to infall. K2-34 is a metal-rich F-type star with a hot Jupiter planet K2-34 b first discovered in K2 Cycle 5 by Hirano et al. (2016). K2-34 b has a radius of 1.44 R_J, a period of 2.996 days ($a = 0.0426$) and RV measurements give a mass of $1.773 \pm 0.086 M_J$. A detection of the Rossiter-McLaughlin effect demonstrate spin-orbit alignment of $\lambda = -1^{+10}_{-9}$ degrees. It showed no evidence of long term periodic

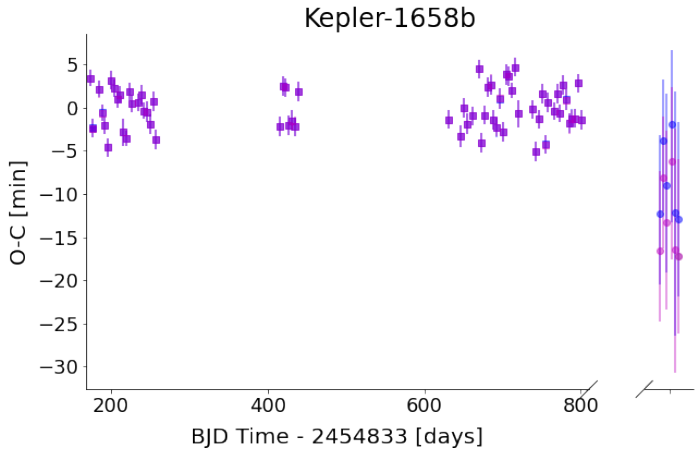


Figure 4.12: Kepler-1658. Pink points show residuals to a linear ephemeris and blue show those of a second order trend. While both trend lines are dominated by the precise Kepler points and neither fits the TESS data, it is clear that transits are earlier in TESS than predicted by initial Kepler linear ephemerides.

timing behaviour in either our study or that of Mazeh et al. (2013), and is an evolved, slow rotating star (McQuillan et al., 2013; Lillo-Box et al., 2016). Kepler-426 b has a mass is 0.34 $\pm 0.08 M_J$ a period of 3.2 days and an $a = 0.0414 AU$ (Hébrard et al., 2014). With a lower mass than the typical hot Jupiter, it can be considered more of a "Hot Saturn". We find a δP for K2-34 b of 0.000140 $\pm$0.000130 days and for Kepler-426 of 0.000025 $\pm$0.000024 days, which again, lie at the $1-\sigma$ level of a possible effect of interest, should further follow-up be performed.

K2-34 b is considered inflated, with a radius considerably larger than its mass would suggest. Stellar irradiation can play a role in the inflation of the close-in Jupiter planets with radii up to $\sim 1.2\ R_J$ (Showman & Guillot, 2002). However, since this alone cannot account for even larger radii, it is likely that other mechanisms must contribute, such as tidal heating and planetary dissipation. This is especially interesting since many gas giants orbiting evolved stars appear to be inflated or reinflated, which requires the deposition of additional energy beyond the incident stellar radiation (Grunblatt et al., 2017). Further, since the host star is very bright (V = 11.5) and the planet's atmosphere is likely quite extended, K2-34 b makes a good candidate for continued transit monitoring and atmospheric follow-up either from the ground or from space.

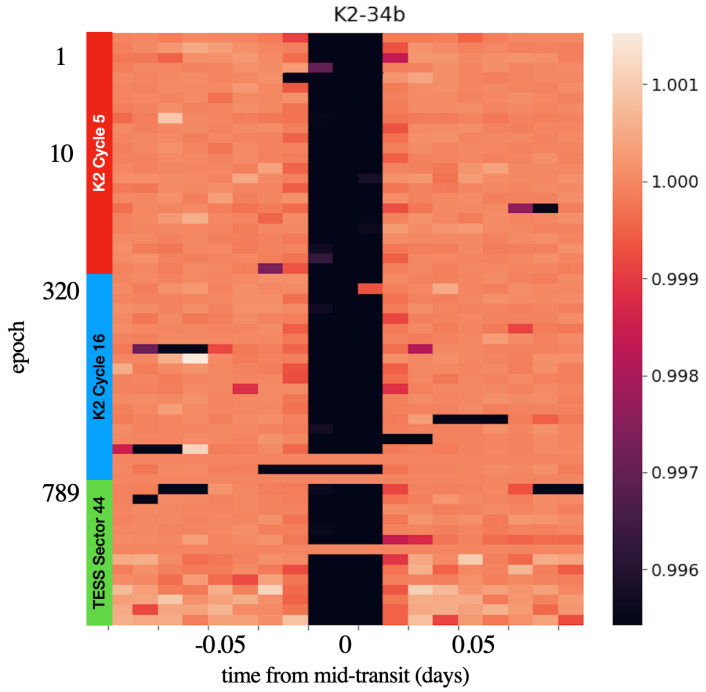


Figure 4.13: K2-34 was observed in two K2 sectors and one TESS sector, giving a wide spread of time and period sampling, and giving us three natural points at which to "sample" the period evolution. With its high $\mathrm{SNR}_{\mathrm{TESS}} \sim 40$, the TESS transit times are some of the best constrained for all Kepler/K2 targets re-observed by TESS.

While the work of this study is quite limited in scope, we found a significant change in the period of one system consistent with previous studies, point to two planets that show very tentative signs of orbital evolution, and guidance on the limits for calculating such effects on several other systems. This demonstrates the significant potential of TESS to provide insight into Kepler and K2 hot Jupiters and suggests that future transit searches like PLATO and ARIEL will have even more success at identifying such trends, especially at ever greater elapsed time points (Rauer et al., 2014; Tinetti et al., 2021). Continued transit observations of Kepler-1658, K2-34 and Kepler-426 are especially encouraged to further constrain and achieve calculations of other tidal quantities.

4.5.2 Analysis of Kepler-522 b

Three systems were found in Chapter 3 to show periodic TTVs, which have not been identified previously in the literature, most notably Kepler-522 b, Kepler-531 b and

Kepler-450 b, which all show a clear sinusoidal variation in their timing residuals through the better part of what could be described as a super-period. Kepler-450 b (periodic FAP = 0.0006) is a Neptune-sized planet with a radius of 6.02 $R_{\oplus}$, a mass of $19.4^{+11.1}_{-6.8}$ $M_{\oplus}$, and a period of 28.455 days. The amplitude of its $O-C$ timing differences is ∼7 minutes and occurs on a superperiod of approximately 45 transits of planet b or 1280 days. Kepler-450 is an F-type star known to host a total of 3 transiting exoplanets (Van Eylen & Albrecht, 2015). Kepler-450 c is a super earth (radius of ∼2.5 $R_{\oplus}$ and mass of $12.5^{+3.2}_{-2.6}$ $M_{\oplus}$ (Yoffe et al., 2021) lies inside the orbit of planet_ with a period of 15.413 days, giving it a period ratio of 1:1.85 with planet c. This proximity to the 1:2 resonance might account for these small amplitude TTVs seen in Keler-450 b.

Planet d is further nested inside the orbit of planet c and is an earth-sized planet with a radius estimated by different studies to be 0.83 or 0.995 $R_{\oplus}$ (Yoffe et al. (2021) and Berger et al. (2018) respectively) and a period of 7.515 days. It's mass, from a radial velocity follow-up by Yoffe et al. (2021) is $17.6^{+9.5}_{-6.7}$ $M_{\oplus}$, which gives it a rather high density even at the lowest end of the its uncertainty range.

On the other hand, Kepler-531 b and Kepler-522 b do not yet have any known companions, yet they show significant periodic timing residuals. Nesvorný et al. (2012) detected a non-transiting planet KOI-142c (Kepler-88c) from its gravitational perturbations on the transiting planet KOI-142b (Kepler-88b). In this case, they were able to compute the mass of KOI-142c with a 5% precision and that of KOI-142b with a 25% precision. Here we present the further analysis of Kepler-522, chosen of these three systems for having the highest amplitude trend, and for the consistency of its residuals which appeared in the work of Holczer et al. (2016) but were not followed up upon. We examine potential sources of this variation and suggest that this could be very well due to an additional planetary companion, though we are unable to constrain specific parameters.

We detected a periodic signal in the transit times of Kepler-522 b (FAP = 0.0003). The signal has an amplitude of approximately 11 minutes and indicates a superperiodicity on a time scale of ∼25 transits of planet b or close to 960 days.

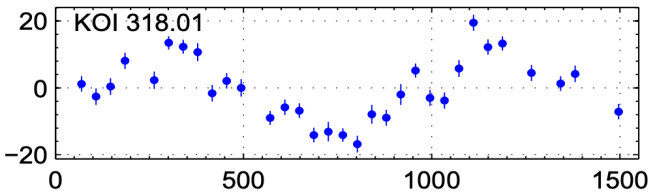


Figure 4.14: Kepler-522 d was identified in Holczer et al. (2016) as showing periodic signals, consistent with the transit timing residuals $O-C$ that we recover, which are can be seen in Figure B.4.

Kepler-522 is G star observed in Kepler's short cadence mode (Morton et al., 2016). It was reobserved by TESS in sector 40 from June to July of 2021. With a TESS SNR of 6.2, Kepler-522 has readily apparent TESS transits, though with $\sim$20 minute timing uncertainties, which make it difficult to detect periodicity in the TESS data themselves. However, these transits are significantly offset from average linear trend seen in the Kepler data. It is not flagged in the NASA Exoplanet Archive as showing signs of TTVs, however Holczer et al. (2016) identifies it as showing periodicity identical to our study (see Figure 4.14, citing a superperiodicity of 880 days and an amplitude of 11.9 minutes. Hadden & Lithwick (2016) performed mass follow-up on this initial set of Kepler systems, however, they limited their selection to multiplanet systems hosting at least one planet pair with a period ratio smaller than $P_2/P_1 < 2.2$. With new TESS time points indicating a significant offset from linear ephemeris on top of clear periodicity in the Kepler data, we therefore chose to attempt a TTV fit to a hypothetical companion.

Global planetary parameters and transit times were fit as described in Chapter 3 Section 3.3, with small timing differences corrected for prior to fitting of the planetary parameters through cross correlation, though in this case, offsets were not large enough to need realignment a the stage of planetary parameter fitting. The results of this planetary fit are summarised in Table 4.4 and shown in Figure 4.15. While periodicity is difficult to make out by appearance on a river plot (also in Figure 4.15), a noticeable offset in TESS transits from the average linear ephemeris of Kepler data points is readily apparent, consistent with longer term

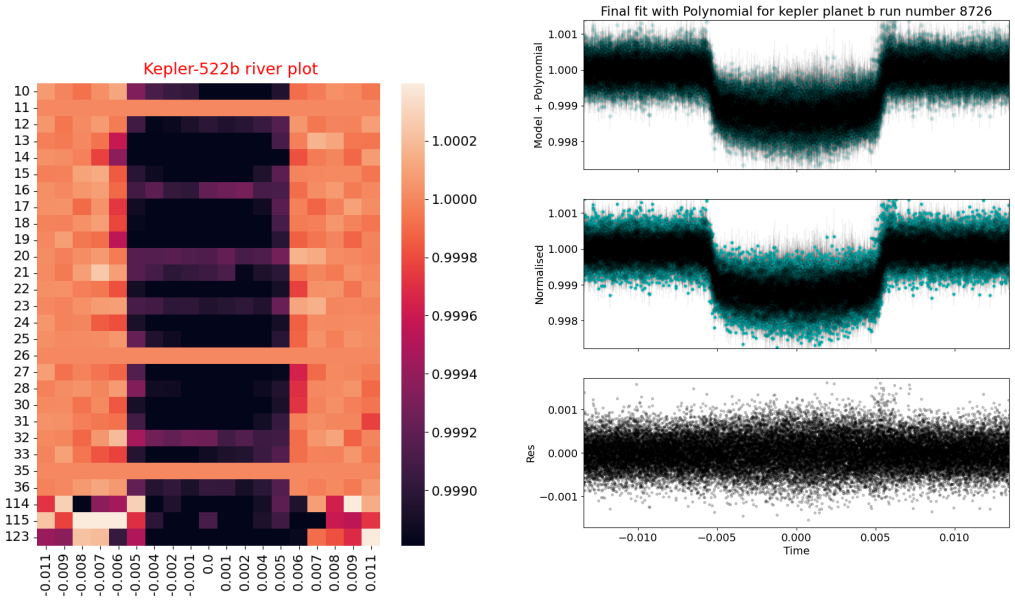


Figure 4.15: A river plot is shown for Kelper-522 b on the left. While not obvious, signs of periodic variation are possible to make out, and notably, the TESS datapoints shown at the bottom show a distinct departure from the average linear ephemeris of Kepler data alone. On the right is shown the fit for planetary parameters.

Parameter	Fit Value	Archival Value	Units
T_0	$174.8232^{+0.0009}_{-0.0009}$	174.8334 ± 0.0009	days
P	$38.58470^{+0.000040}_{-0.000038}$	38.58423 ± 0.00005	days
R_p	$8.15^{+0.10}_{-0.19}$	$7.52^{+0.37}_{-0.61}$	$M_\oplus$
$R_\star$	$2.20^{+0.025}_{-0.044}$	$1.98^{+0.431}_{-0.346}$	$R_\odot$
$M_\star$	$1.13^{+0.086}_{-0.042}$	$1.54^{+0.141}_{-0.109}$	$M_\odot$
$\cos i$	$0.03^{+0.001}_{-0.002}$		-
ld_1	$0.40^{+0.005}_{-0.003}$		-
ld_2	$0.11^{+0.012}_{-0.006}$		-

Table 4.4: Planetary parameters fit for Kepler-522 b from Kepler data. T_0 is expressed in $BJD - 2454833$. Reference values are from Morton et al. (2016).

period evolution of such a dynamically interacting system. Planetary parameters from our fit are in good agreement with archival values and have comparable errors.

When examining the cause of TTVs, we consider several possibilities. The first is the possibility that the signal is due to stellar activity. The most plausible candidate for dynamical interaction with the star causing the TTV signal is the Applegate effect first noted in eclipsing binaries (Applegate, 1992), and applied to exoplanets by Watson & Marsh (2010). The effect suggests that the presence of an exoplanet

in a close orbit around a star can induce changes in the star's magnetic activity, which in turn affects the star's luminosity. In essence, the gravitational interaction between the planet and the star can cause variations in the star's internal rotation and magnetic field. These variations can lead to changes in the star's magnetic activity cycle, influencing the amount of sunspots and flares the star has.

In turn, as the star undergoes a magnetic cycle, the gravitational pull of its rotational bulge on the planet has the potential to slightly vary the planet's orbital period. This effect has not been definitively observed in any exoplanet-star systems to date. In the case of Kepler-522, the star has rotational period measured by McQuillan et al. (2013) of 4.914 days and is magnetically active. However, Watson & Marsh (2010) demonstrate that this effect is much more pronounced for planets in tight orbits (<0.01 AU), whereas above this point, TTVs from an external planet are more likely to cause significant timing perturbations (see Watson & Marsh (2010)), while the Applegate mechanism would cause timing changes totaling less than a minute in the ∼900 year superperiod observed here. At an orbital radius of $a = 0.255\,\mathrm{AU}$, this effect is much less pronounced. While we do not perform an in-depth mathematical treatment of this scenario, we consider this a possible but unlikely explanation for the ∼20 minute total deviation in transit times observed for Kepler-522 b.

Another source of the TTVs could be from star spots (Rabus et al., 2009) but, in our case, even with excellent Kepler photometry, no spots are detected, either from out-of-transit stellar modulation or in excess residuals during transit due to spot crossings. We therefore explore the possibility that this periodic signal is due to a companion outer planet.

We start by assuming the existence of a planet c outside of the orbit of planet b, as an outer companion would be fittingly less likely to have been observed to date in Kepler or TESS transit curves. Using the same `TTVFast` forward model (Deck & Agol, 2014) as with the follow-up observations for TOI- 270 we proceed by fitting for five orbital parameters for each planet, $M_\mathrm{p}/M_\star$, P, $e\cos\omega$, $e\sin\omega$, and T_0, for a total of 10 fit parameters. Orbital elements were osculating and defined at the simulation

start time BJD = 2454833 using Jacobi coordinates. As before, we used the time of first transit of planet b as a convenient reparameterization of the mean anomaly [e.g.] (Jontof-Hutter et al., 2016; Libby-Roberts et al., 2020) and fixed the inclinations and longitudes of ascending node to 90° and 0°, respectively, as the signal has only a higher-order dependence on the mutual inclinations which are known to be small for multi-planet systems (Fabrycky et al., 2014; Gilbert & Fabrycky, 2020).

We proceeded to find the model parameters with MCMC, implemented in the v3.0 of the `emcee` package (Foreman-Mackey et al., 2013a, 2019). When modelling `TTVFast`, Monte Carlo methods tend not to converge unless a "good guess" is made, which is more difficult in the case of an unknown planetary companion. Starting with the known parameters of Kepler-522 b, we constructed a planet c that would give rise to the $O - C$ residuals obtained in our study. We explored the possibility of two resonances for an outer planet, one with a 2:1 resonance and another with 3:2 resonance. Other solutions are possible but n:n+1 resonance gives rise to greater magnitude TTVs, so we chose to start with these two for simplicity. We then iteratively ran short chains of 2000 steps to find "good enough" guesses at initial masses and period. We employed a wide grid of starting masses, periods and eccentricities and found that even in these short runs, walkers quickly settled into a set of parameters that was chosen as the start for our starting optimization using the Powell minimiser implemented in `scipy.optimize.minimize`

We then set up our full run using Gaussian priors on the period of planet b from our own planetary fitting, and wide uniform priors on all other parameters, listed in Table 4.5. A chain of 40 walkers in a Gaussian ball was initialised around this starting point, with a burn-in of 40,000 steps, followed by a run of 200,000 steps, to achieve convergence across parameters. The posterior distributions for our model parameters for both period ratios are also summarized in Table 4.5 and visualized for the TTV two-planet fit in Figure B.8.

We found that in the case of 3:2 resonance, convergence was achieved at a fairly low mass ($M_c = 1.60^{+0.47}_{-0.23}$) M companion with a period of $P_c = 59.2530^{+0.0697}_{-0.0666}$ days, as compared to a $3.23^{+1.14}_{-0.56}$ M companion in the case of a period ratio of $\sim 2:1$.

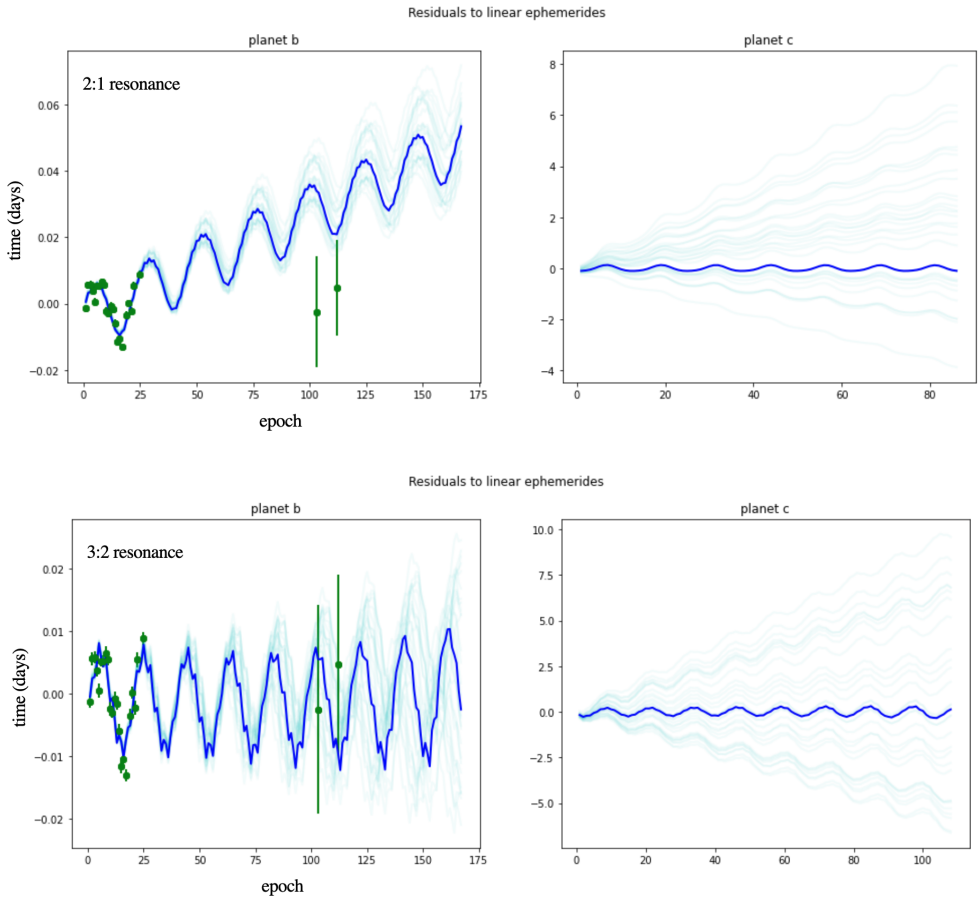


Figure 4.16: The final dynamical fits for a 2:1 resonance and 3:2 resonance are shown in the top and bottom panels respectively, demonstrating a lower AIC and more believable fit for a 3:2 resonance scenario. The hypothetical planet c does not have any transit times.

In both cases, the mass of hypothetical planet c is better constrained than that of planet b, as expected, since the amplitude of TTVs is related to the ratio of the perturbing planet's mass to the stellar mass. X^2 residuals favour a 3:2 resonance, which can be appreciated in Figure 4.16. A 2:1 resonance scenario does not appear to easily incorporate the two TESS transits, whereas a 3:2 resonance predicts these and maps on to an apparent chopping signal present in the Kepler data set.

Altogether, this examination is quite limited in scope and represents a basic temperature check indicating the possibility of a planetary companion that would explain the periodic residuals to a linear ephemeris and non-linear offset of TESS transit times. The next steps for pursuing this system and eventually confirming the existence of a companion planet would be to rigorously assess various alternative

explanations that could rise to this system's apparent TTVs, as well as other orbital architectures, such as an inner companion, or higher orders of resonance. Under the assumption of a planetary companion, we'd first question whether said planet would transit itself, with a mutual inclination that would have made it visible in Kepler or TESS light curves. We'd then check that the solution for such a planet who meets the above two criteria is evolutionarily stable. Finally, likely follow-up would include a reexamination of transit curves in the case of a far-out smaller companion that might have been missed by pipelines, or in the case of a larger or closer in companion that is inclined enough to be non-transiting, an RV follow-up study to search for a corresponding planetary signal.

Table 4.5: Orbital and planetary parameters fit for Kepler-522 b.

Parameter	Prior (2:1 res)	Posterior (2:1 res)	Prior (3:2 res)	Posterior (3:2 res)	Units
$M_{\rm b}$	$\mathcal{U}(10, 40)$	$38.42^{+1.15}_{-1.45}$	$\mathcal{U}(10, 40)$	$38.79^{+0.70}_{-1.06}$	M
$P_{\rm b}$	$\mathcal{N}(38.5847, 0.0005)$	$38.5839^{+0.0004}_{-0.0009}$	$\mathcal{N}(38.5847, 0.0005)$	38.5869 ± 0.0002	days
$e_{\rm b} \cos \omega_{\rm b}$	$\mathcal{U}(-0.7, 0.7)$	$-0.032^{+0.008}_{-0.007}$	$\mathcal{U}(-0.7, 0.7)$	$-0.006^{+0.022}_{-0.024}$	-
$e_{\rm b} \sin \omega_{\rm b}$	$\mathcal{U}(-0.7, 0.7)$	$0.011^{+0.011}_{-0.008}$	$\mathcal{U}(-0.7, 0.7)$	$0.016^{+0.012}_{-0.011}$	-
$T_{0,\rm b}$	$\mathcal{U}(16.59, 16.79)$	$16.6955^{+0.0005}_{-0.0006}$	$\mathcal{U}(16.59, 16.79)$	$16.6945^{+0.0007}_{-0.0006}$	days
$M_{\rm c}$	$\mathcal{U}(.5, 40)$	$3.23^{+1.14}_{-0.56}$	$\mathcal{U}(.5, 40)$	$1.60^{+0.47}_{-0.23}$	M
$P_{\rm c}$	$\mathcal{U}(74.0, 74.4)$	$74.1118^{+0.0553}_{-0.0244}$	$\mathcal{U}(59.0, 59.4)$	$59.2530^{+0.0697}_{-0.0666}$	days
$e_{\rm c} \cos \omega_{\rm c}$	$\mathcal{U}(-0.7, 0.7)$	$-0.022^{+0.008}_{-0.008}$	$\mathcal{U}(-0.7, 0.7)$	$0.001^{+0.019}_{-0.019}$	-
$e_{\rm c} \sin \omega_{\rm c}$	$\mathcal{U}(-0.7, 0.7)$	$-0.041^{+0.007}_{-0.004}$	$\mathcal{U}(-0.7, 0.7)$	$-0.038^{+0.008}_{-0.007}$	-
$T_{0,\rm c}$	$\mathcal{U}(90.58, 90.78)$	$90.7081^{+0.0629}_{-0.0768}$	$\mathcal{U}(90.58, 90.78)$	$90.6799^{+0.0712}_{-0.0675}$	days

Table 4.5: Fit priors and posteriors are given for two scenarios: one with 2:1 orbital resonance between planet b a presumed companion, and one with 3:2 resonance. Orbital elements are osculating and defined using Jacobi coordinates at the simulation start time BJD = 2454833.

4.5.3 Concluding Remarks

In this chapter, we presented a series of systems entailing studies of limited scope that employed transit timing information to follow-up and answer specific questions. For the systems AU Mic and HD 152843, we demonstrated the utility of forward-modelling of TTVs to validate mass, period, and system architectures obtained through transit photometry and RV analysis as well as provide guidance for future observations. For TOI- 270, we showed the power of continuing observations to further refine the mass and provide updates to predicted ephemerides that will be critical for accurate observation planning of this interesting system.

In the hot Jupiter systems K2-34 b and Kepler-426 b, we provided tentative evidence for orbital evolution and tidal infall that present promising opportunities for follow-up, and demonstrated the utility of TESS for uncovering such evolution in systems with high enough SNR. Finally, we followed up on the evidently periodic timing residuals in the Kepler-522 system identified in Chapter 4.

To further validate the results of all of these studies, further observations from space and ground-based facilities is highly recommended. For Kepler-522, we propose a comprehensive follow-up campaign utilising high-precision radial velocity measurements and photometric observations to provide independent constraints on the masses, orbits, and densities of potential companions. Overall, this chapter showcases the power of TTV analysis as a tool in exoplanet discovery and characterisation.

Now that she's back in the atmosphere
With drops of Jupiter in her hair.

— Train *Drops of Jupiter*

CHAPTER 5

Conclusion

5.1 Concluding Remarks

This thesis explored multiple applications of transit timing variations to exoplanet characterisation and discovery from Kepler up through TESS. After introducing the current state of the field, including tools of discovery and analysis, we build a physical basis for the observations of TTVs in particular. We then started in Chapter 2 by exploring the three-planet system, TOI- 270, which was discovered in TESS sectors 30 and 32. Containing one super earth and two sub-Neptunes in approximate 5:3 and 2:1 mean-motion resonance TOI- 270 is a prime candidate for TTV mass characterisation, but the data from its first two sectors did not cover a significant enough fraction of its super period to see timing variations. We therefore conducted an extensive observing campaign using eight different space-based and ground-based observatories between 2018 and 2020.

Our first aim was to reduce and fit the transit times in a manner that was self-consistent across all eight telescopes. Research team members performed the first steps of data reduction to produce transit light curves. I then used a GP on out of transit flux to normalise before using the maximally constraining TESS data to fit bulk planetary parameters. For Spitzer light curves we obtained of planets c and d

in particular, we implemented a strategy of Pixel Level Decorrelation combined with Principal Component Analysis to remove the significant correlated noise generated from the spacecraft's jitter and under-sampling of the PSF in its warm viewing mode. With three principal components, we found that this was quite effective at normalising and fitting. We also found that we could use the high SNR light curve to further refine the parameters obtained by TESS, so we adopted these parameters for the remainder of our fitting, keeping them fixed and varying only the mid-transit time and limb-darkening coefficients for each transit on each respective telescope.

With the transit times extracted, we saw a clear sinusoidal timing trend that appeared to cover a full superperiod for planets c and d. We then proceeded with the TTV analysis using the code `TTVFast` (Deck et al., 2014b) which, given the dynamical state of the system at a reference time along with planetary masses relative to the mass of a star, integrates the full Newtonian equations of motion for interacting point masses. It then rapidly forward models the system's evolution and generates expected transit times. For fitting we used `TTVFast` with DEMCMC to obtain posterior distributions on five parameters for each planet. TTV analysis can be combined with RV data to build a more complete and constraining picture of a system, and TOI-270 is one of the few systems that gives us the unique opportunity to do both. We therefore performed one of our fits using RV data on TOI-270 from Van Eylen, and another fit with wide uniform priors. When fitting with RV data, we achieved mass estimates that further refined those made previously. For the fit with uniform priors, the shallow transits and larger timing errors of planet b proved not to be very constraining. With degeneracies between mass and eccentricity, and a full 15 parameters, we were unable to get the DEMCMC chains to converge. However, by fitting for a linear ephemeris in planet b, we are able to achieve convergence and informative posterior distributions for planets c and d in good agreement with the RV results.

Overall, our analysis produced robust mass estimates and non-zero eccentricities for all three planets. Dynamical modeling of the TTVs alone puts strong constraints on the mass ratio of planets c and d and on their eccentricities. When fitting for

all three planets and including the RV data from Van Eylen, we obtain masses of $M_b = 1.48 \pm 0.18\,M$, $M_c = 6.20 \pm 0.31\,M$ and $M_d = 4.20 \pm 0.16\,M$ for planets b, c and d, respectively, as well as small, but significant eccentricities of $e_b = 0.0167 \pm 0.0084$, $e_c = 0.0044 \pm 0.0006$ and $e_d = 0.0066 \pm 0.0020$. There are very few systems for which both RV and TTV data are available, so this provided a unique opportunity to both better constrain the planetary masses and orbital parameters and to compare the results of the two approaches independently. TOI-270 is now one of the best-constrained systems of small transiting planets.

We then obtained planetary densities and compared them to known profiles. Our findings imply an Earth-like rocky composition for the inner planet, and Earth-like cores with an additional He/H_2O atmosphere for the outer two. We calculated the transmission spectra metric (TSM) for each planet, and found that all three targets fall well above the suggested cutoff for follow-up and amongst the highest (most promising) for small-sized targets below 600K. In total we managed to capture a time frame of several years, enabling us to capture clear periodic deviations in transit times with an amplitude of 10 minutes for planets c and d, and obtain precise masses and eccentricities for all three planets. With a systematic approach to analysing the data from 8 space-based and ground based facilities, this study further showed the power of combining RV data with TTVs, and served to validate the results of RV methods.

This work, which resulted in the paper Kaye et al. (2022) also represented a huge multinational cooperation that took place through the COVID-19 pandemic. With co-authors on all 7 continents, it was in interesting challenge to communicate, write observing proposals, plan observations, and conduct analysis. TTV fits alone took several months to accomplish as methodologies were tested between myself and Shreyas Vissapragada (then at Caltech). Collaboration with many of the co-authors to follow-up with this interesting system is still ongoing.

We then made an ambitious attempt in Chapter 3 to catalogue all Kepler and K2 planets observable with TESS. Up until this point, all Kepler systems had had their transit times catalogued by Mazeh et al. (2013) and Holczer et al. (2016). Beyond

that, several individual Kepler or K2 systems have been selected for re-examination with TESS. However no study to date has done a broad examination of all targets in order to identify those with high enough SNR transits, and update the linear ephemerides of such systems. We therefore chose to take this on, in order to provide critical updates to ephemerides, identify potentially interesting timing behaviour between the two missions and provide a framework for carrying out similar work as we continue to re-observe previously discovered exoplanets with future missions.

Similar to TOI- 270, we attempted to create a systematic and semi-automated approach to fitting and analysing transit times for all targets. After selecting targets with high enough SNR to likely be detected by TESS, we extracted all transit light curves available from MAST. In the first step, we normalised all out-of-transit flux with a GP. We then proceeded with cross correlation to adjust for any significant timing offsets before fitting the bulk planetary parameters to the more constraining Kepler or K2 data. We had examined whether the addition of TESS data would further constrain any of these parameters and found that not to be the case, therefore that step was omitted, and we chose to only fit for the TESS-specific limb darkening coefficients for each system. In the next step we extracted transit times by using MCMC to fit each individual transit with all other planetary parameters held fixed. Finally, we performed a linear fit that incorporated both Kepler/K2 and TESS points in order to update each system's linear ephemeris and assess any non-linear transit timing trends through three main metrics: using AIC to assess for the goodness of a second or higher order fit, an alarm score to identify significant scatter, and Lomb-Scargle periodograms to search for periodic behaviour.

As a result, we provided updated ephemerides for over 100 systems, and searched for long term timing trends not captured by the original Kepler and K2 missions. We identified over 20 systems of particular interest, which either displayed new documented periodic TTVs, or else non-linear higher order trends. For such "second order systems", our findings could indicate TTVs on a superperiod that exceeds the total observing time, or else they could be a function of fairly few but quite constraining Kepler or K2 data points (often fewer than 5 previously observed

transits) where linear estimates are subject to overfitting the small n. In either case, the newly widened baseline and updated ephemerides will be critical for continuing to observe these systems, and future observations are encouraged to distinguish between these two effects. The work from this chapter forms a nearly-complete paper, which will be soon be submitted for publication with myself and Suzanne Aigrain as co-authors.

Finally, in Chapter 4, we presented several systems in which transit timing analysis can lend an important hand in better understanding the utility of in-depth transit timing analysis in all stages of exoplanet exploration. We started by modeling the TTVs of the two-planet AU-Mic system, a young and active system that provides us with an exciting chance to peer into the early stages of planetary formation. In this section which follows the work of Zicher et al. (2022), on which I am a co-author, I forward-modelled TTVs given masses measured by members of the research team from RV data and found them to be consistent so far with the limited transit data points we have. I then looked at a TTV fit to a combination of ground and space-based observations of planet b that was presented in a second co-authored paper, Wittrock et al. (2022). However, this second approach did not render masses consistent with RV analysis, and instead found a mass for planet c from TTV analysis alone that was much lower than expected. Further studies suggest a potential third planet in the system and stellar activity makes it difficult to fit for accurate and precise transit times, so in this case, more observations are needed to better understand the precise pattern of potential TTVs and continue characterising the system.

In the two-planet system HD 152843, I forward-modelled TTVs over a range of masses and eccentricities to provide supporting evidence for RV-derived mass measurements and guide future observing focuses, contributing as co-author to two papers. In the discovery paper Eisner et al. (2021), which included two transits of planet b and only one of planet c, we noted that a possible period configuration would place these two planets in 5:3 orbital resonance. We then added another year of data in a paper by Nicholson et al (in prep), including a second sector of TESS

data capturing another an additional transit of planet c as well as RV data, that in combination, enabled us to fully constrain the period of planet c, also confirming that it lies close to 5:3 orbital resonance with planet b, making it a prime candidate for the detection of TTVs. I then modelled the expected TTVs across the range of mass and eccentricity uncertainties, finding that TTVs should be observable on a time frame of 2-3 years with an amplitude in the range of 15-20 minutes.

Following the analysis of HD 152843, we revisited the TOI- 270 system, adding a further 2 years of data with ground-based observatories, which completes a significant part of another TTV superperiod. We fit these new times with a modified `TTVFast` and compared the predicted times from the updated fit, to that of the one achieved in our earlier study. We find consistent masses, but now find slightly larger eccentricities for planets c and d. We also further half the mass error of planet c, making it one of the most precisely constrained small planets to date.

We finished by revisiting several of the Kepler and K2 systems first examined in Chapter 3, to take a closer look at their timing trends. We first identified 10 hot Jupiter systems observed in both K2 and TESS with high SNR. We fit for T_0 and P separately for Kepler/K2 and TESS transits to assess whether any change in period had occurred in the intervening years between observations. While no statistically significant differences were found, a slight detection of a shorter period in two systems, K2-34 and Kepler-426 points to the possibility of infall and makes the prospect of continuing to revisit these systems more enticing. Finally, we used `TTVFast` to fit for potential TTVs for the planet Kepler-522 b, fitting over a range of planetary masses and eccentricities and exploring two outer-planet resonances, 2:1 and 3:2. We found that a 3:2 resonance produced a better fit, matching a predicted short-term chopping signal as well as longer term periodicity, and resulted in a super-earth massed companion with a period of 59 days. While our exploration of scenarios is limited given that only one planet is known to transit, this study points to the potential presence of an additional planet and emphasises the need to reexamine such systems.

5.2 Future Work

The research presented in Chapter 2 and in Chapter 4 Section 4.4 on the TOI-270 system has provided valuable insights into the dynamics and composition of the three transiting planets. The detection of strong TTVs for planets c and d, along with the refined estimates of their radii and mean orbital periods, opens up several intriguing avenues for future research. One important direction for further investigation is the characterization of the TTVs in more detail. Analyzing the TTV signals with higher precision and modeling, searching for effects of chopping, and completing out more superperiods can provide additional constraints on the masses, eccentricities, and orbital architectures of the planets. This can be achieved by incorporating more observational data, including continued monitoring of the system using both ground-based and space-based observatories. Additionally, refining the dynamical modeling of the TTVs by considering additional physical effects such as gravitational interactions with further non-transiting planets can enhance our understanding of the underlying dynamics of the system.

The study's findings also highlight the potential for atmospheric characterization of the TOI-270 planets. The Earth-like rocky composition inferred for the inner planet and the Earth-like cores with additional He/H2O atmospheres for the outer two planets present an exciting opportunity to study their atmospheres in more detail. Future research can focus on conducting transmission spectroscopy observations during the planetary transits, aiming to detect and analyze the spectral signatures of the planetary atmospheres. This can provide insights into the atmospheric compositions, temperature profiles, and potential presence of key molecules, allowing for comparisons with theoretical models. Observational follow-up of this interesting system is ongoing, with transit monitoring through ASTEP and NGTS of all three planets, and an atmospheric study of planet d planned for JWST's Cycle 2 (GO 4098, PIs Bjorn Benneke and Thomas Mikal-Evans).

Moreover, the TOI-270 system can serve as a benchmark for comparative studies of small transiting planets. Further investigations can involve comparing the TOI-270 system with other similar systems to identify common trends and understand

the diversity of small exoplanets. Overall, the work in this thesis on the TOI-270 system opens up exciting possibilities for future investigations. The continued exploration of the TOI- 270 system can contribute significantly to our knowledge of exoplanetary systems and provide valuable insights into the formation, dynamics, and composition of small planets.

To follow up on the work done in Chapter 3, there are several promising directions to explore. Firstly, further investigation into the exoplanetary systems that were previously known to exhibit TTVs is warranted. Full dynamical fits can be performed to see what, if any improvements TESS datapoints have to offer on previous fits. However, in many cases, these system's masses are already quite well constrained by their Kepler or K2 points, and the addition of a few TESS datapoints with larger errors is unlikely to improve the fits. By contrast, for the systems where evidence of timing residuals or non-linear trends in the ephemerides was detected for the first time, follow-up studies are crucial. By combining data from new TESS sectors, ground-based observatories for brighter targets, and upcoming missions such as PLATO and ARIEL, we can significantly increase the number of systems with extensive TTV data. Then characterizing the nature and origin of these variations could involve exploring potential causes such as additional, unseen planets in the system, stellar activity, or else simply confirm linear ephemerides that provide significant updates to archival ones based on small numbers of data points. In-depth analyses, including dynamical simulations and statistical modeling, can help determine the most likely explanations for the observed timing trends and provide insights into the system's long-term stability.

This work also showcased the importance of updating and maintaining accurate linear ephemerides, as most known exoplanets have not been re-observed, until recently by TESS. As was seen in our study, it is likely that many of the known planet ephemerides are, or will be stale, limiting our ability to conduct detailed follow-up. The ephemerides of exoplanets discovered with TESS will also quickly degrade, since most will only be discovered with a ~ 27 day baseline of observations. Future work should use the method presented here to reanalyze all known exoplanets

observed by TESS, providing the community with a larger pool of targets on which to perform detailed characterization in the era of JWST. My supervisor will be offering MPhys projects in the coming year to monitor these timing trends as new TESS data comes in, using the code I developed.

Overall, this study serves as a stepping stone for further investigations in long-term timing follow-ups. Future research efforts should focus on determining the presence and prevalence of TTVs in known exoplanetary systems, exploring systems with newly seen timing residuals or trends, and expanding the observational sample to build a more comprehensive picture of TTVs in exoplanetary systems.

In the case of the systems we analysed independently, we often brushed the surface, using TTVs as one of many tools to provide details or guidance on future observations for a system. A lot more work remains to be done to follow up on each individually.

With AU-Mic, achieving further transit observations of both planets as well as any possible companions will be critical for dynamical follow-up. Further observations will better confirm the presence of as well as amplitude, period, and shape of the variations- it is possible that variations observed to this point are part of a chopping signal or are influenced by the activity of the star. More detailed analyses of their TTV signals could involve incorporating additional physical effects, such as stellar activity, or gravitational interactions with additional planets into the modeling framework to better constrain the system parameters and orbital architectures. The TTV analysis in our study was only performed with two planets- including a third planet in our models along with the addition of further transits could paint a more complete picture of this system's configuration. AU-Mic is a fascinating system and follow-up is currently ongoing with CHEOPS and NGTS, though the star's frequent flaring continues to present a challenge to this work.

In the case of HD 152843, the combination of a bright host star and two Neptune-mass transiting planets makes the system an ideal target for future atmospheric studies and comparative planetology. Planet c in particular is an outstanding target for transmission spectroscopy owing to its extremely low density. Near-infrared

observations using JWST's NIRISS/SOSS would give access to a number of water bands, though the presence of a haze could impact their detectability. On the other hand, observing at redder wavelengths with the NIRSPEC G395H grism would give access to H_2O, CO_2 and CH_4 features simultaneously, and would be relativley insensitive to the presence of a haze. By measuring the transmission spectra of both planets over an appropriate wavelength range, one could constrain the metallicities and C/O rations of their atmospheres, and this would help to resolve some of the degeneracies between the possible formation and evolution scenarios for the system.

Next, for the hot Jupiters we examined from Kepler and K2, after obtaining several years of baseline transit observations and fitting updated periods, there are several follow-up avenues to explore in order to assess the tidal decay of these exoplanets. Importantly, continued monitoring the systems over an extended period of time to gather additional transit data will provide a more comprehensive dataset for detecting any potential changes in transit timings or duration. In many cases, these systems will be re-examined by TESS in future sectors as well as potentially by PLATO. Aside from further observations, we can also more deeply employ theoretical models and simulations to better explore the potential tidal decay of these planets. The lack of significant decay can also place constraints on the masses and tidal quality factors of these stars and planets.

For Kepler-522 b, the next steps of analysis would could involve a more complete examination of all possible explanations of timing variability. While it is unlikely that general relativistic effects or tides could explain $\sim$20 minute variations, a more in depth treatment could rule these possibilities out for sure. Beyond that, further period resonances could be explored with `TTVFast`, and in general, more data points are needed to narrow down between these possibilities. This star is moderately bright (Vmag = 12.2), and future TESS sectors as well as PLATO fields might be able to revisit it in a way that will provide useful constraints to several of these scenarios. However, it is potentially not so bright for a radial velocity follow-up to be able to detect a low mass companion, though a more rigorous assessment is needed to explore this option. Finally, by testing the long-term orbital

stability of various configurations we might be able to narrow down these choices further and also guide future observations.

Overall, in this work we have covered a lot of ground in terms of depth and scope of some our explorations into TTV characterisation, and we have in turn pointed towards a good deal of promising future investigation.

5.3 The Direction of Future Exoplanet Searches

Looking ahead, the future of exoplanet astronomy holds great promise for advancing our understanding of TTVs, and in turn TTVs will help uncover hidden details of orbital configurations, masses and new planets. With continuous improvements in observational capabilities including the recent launch of telescopes like JWST, and with upcoming space missions like PLATO (Rauer et al., 2014) and ARIEL (Tinetti et al., 2021), we can expect to detect TTVs in even more exoplanetary systems as well as put what we uncover to good use. These missions will provide high-quality, precise data that will rely on accurate ephemerides and system characteristics in order to capture and analyse, and enable further tracking or discovery of timing trends.

In the coming years, JWST holds great promise for studying exoplanet atmospheres and advancing our understanding of these distant worlds. With its advanced suite of instruments, including the Near Infrared Spectrograph (NIRSpec) and the Mid-Infrared Instrument (MIRI) that analyse reflected or transmitted light, the JWST is already enabling detailed observations of exoplanet atmospheres that have not been achievable before, providing valuable insights into their composition, temperature structure, and physical processes. Its high spectral resolution and sensitivity in the infrared range will enable the characterization of exoplanet temperature profiles, cloud formations, and the potential presence of hazes or aerosols.

Beyond the JWST, PLATO (Planetary Transits and Oscillations of Stars), a mission led by the European Space Agency (ESA), is designed to detect and characterize transiting exoplanets (Rauer et al., 2014). Proposed to launch in 2026, it will follow in the footsteps of Kepler and TESS, observing a large sample of stars with high precision photometry over an extended period of time and searching up to

1,000,000 stars for the slight dimming caused by exoplanet transits. PLATO aims to identify and study a diverse range of exoplanets, from small rocky worlds to gas giants, including those in the habitable zone of their host stars. The mission will provide valuable data for statistical studies of exoplanet populations, investigating their occurrence rates, sizes, orbital properties, and potential habitability.

PLATO will use 24 x 20cm telescopes optimized for a single 450-1000 nm band pass, which will have a total viewing area of a very large $49°x49°$ (about 5% of the whole sky), with the stars in the centre of the viewing field being monitored with a much higher photometric precision than the peripheral ones (Nascimbeni et al., 2022). Although its search strategies are not yet set, its baseline scenario includes two pointings that are to be monitored during the Long-duration Observation Phase (LOP fields) of two years each, complemented by shorter pointings during the "Step and stare" Observation Phase (SOP fields), which can expand the total areas surveyed by PLATO to 40% of the sky. Altogether, this gives PLATO an interesting combination of scope and depth in its search, that will likely cover many of the targets discussed in this thesis.

ARIEL, on the other hand, is a mission led by ESA that will focus on the study of exoplanet atmospheres (Tinetti et al., 2021). It is proposed to launch in 2029 will perform spectroscopic observations in the infrared range, enabling the analysis of exoplanet atmospheres to determine their composition, temperature, and other key properties. ARIEL will study a broad range of exoplanets, from hot Jupiters to smaller rocky worlds, providing insights into their atmospheric chemistry and physical processes. By examining the chemical signatures present in exoplanet atmospheres, ARIEL aims to advance our understanding of planetary formation, evolution, and the potential for habitability.

Importantly, these missions are designed to complement and synergize with other ground-based and space-based observatories, to maximize scientific returns and enable comprehensive studies of exoplanets. The combination of TTV analysis with other observational techniques, such as radial velocity measurements, direct imaging, and spectroscopy, will further enhance our understanding of exoplanets. By

integrating multiple datasets and employing sophisticated data analysis techniques, we can gain a comprehensive picture of exoplanetary systems, including their masses, compositions, atmospheres, and orbital dynamics.

Overall, TTVs provide a rich source of information for advancing our knowledge of exoplanet astrophysics. The future holds exciting prospects for uncovering the mysteries of exoplanetary systems through the continued study of TTVs, paving the way for a deeper understanding of planetary formation, evolution, and the potential for habitability beyond our own solar system.

APPENDIX A

TOI-270

Supplementary material for Chapter 2 on Transit Timing Variations in the three planet system TOI-270

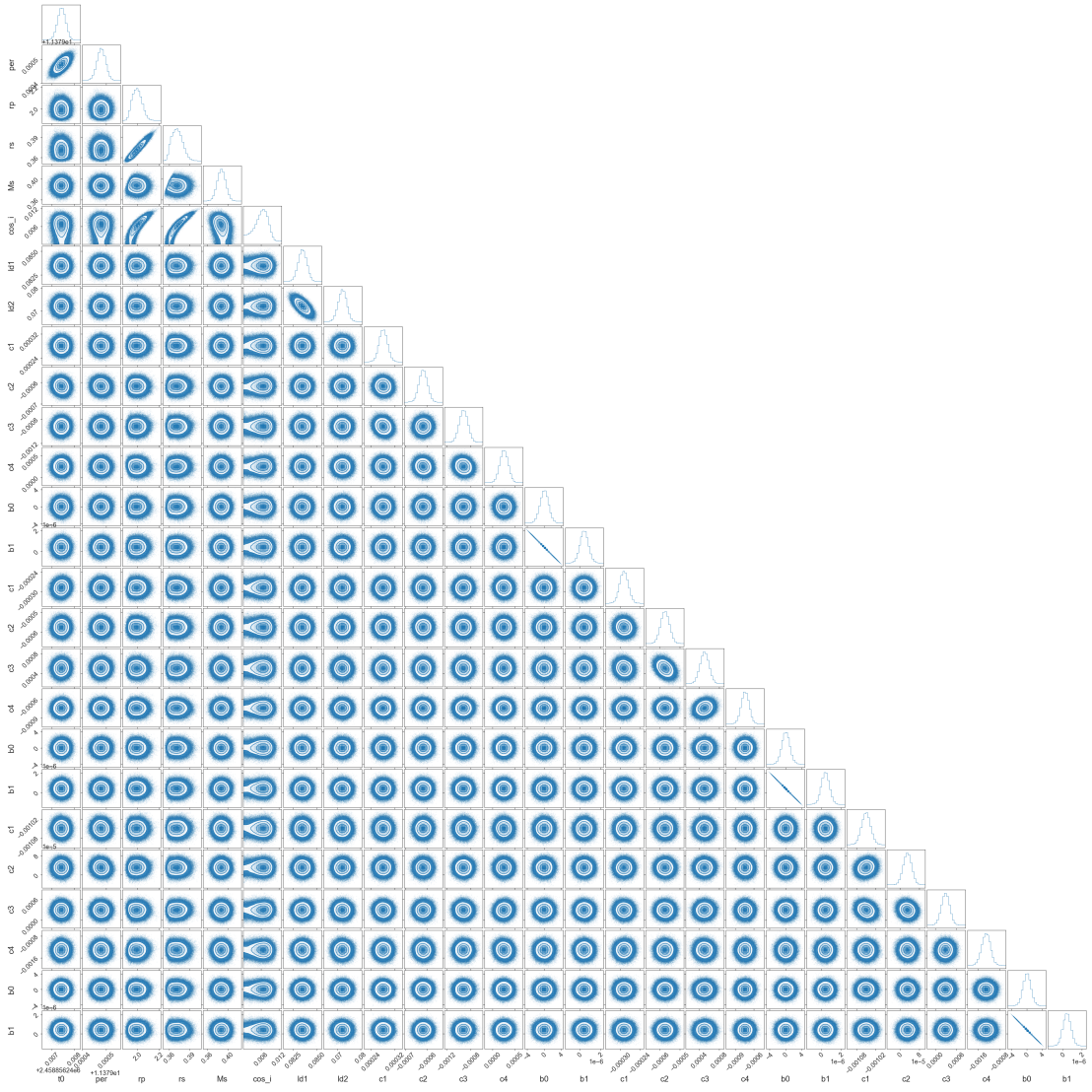


Figure A.1: Corner plot showing the posterior distribution of the simultaneous Spitzer transit fit for planet d, incorporating three transits. The fit uses Pixel Level Decorrelation (PLD), as described by Section 2.3.3.

Table A.1: Transit Timing Variations Planet b

Transit Number	Telescope	Mid-Transit Time (BJD	Timing Offset (days)	Error
b				
1	TESS	2458387.09027	-0.00261	$^{+0.02110}_{-0.00899}$
2	TESS	2458390.45207	-0.00089	$^{+0.00378}_{-0.00719}$
3	TESS	2458393.81351	0.00047	$^{+0.01845}_{-0.01340}$
4	TESS	2458397.16906	-0.00406	$^{+0.02853}_{-0.01907}$
5	TESS	2458400.53171	-0.00149	$^{+0.01164}_{-0.00563}$
6	TESS	2458403.89026	-0.00302	$^{+0.00561}_{-0.00158}$
9	TESS	2458413.98191	0.00839	$^{+0.00724}_{-0.00195}$
10	TESS	2458417.33404	0.00044	$^{+0.00937}_{-0.00525}$
13	TESS	2458427.42528	0.01144	$^{+0.00135}_{-0.01211}$
15	TESS	2458434.13850	0.00450	$^{+0.00714}_{-0.00048}$
17	TESS	2458440.85173	-0.00243	$^{+0.02183}_{-0.00992}$
18	TESS	2458444.21671	0.00247	$^{+0.00253}_{-0.00687}$
19	TESS	2458447.57362	-0.00070	$^{+0.00130}_{-0.00304}$
22	TESS	2458457.65648	0.00192	$^{+0.00920}_{-0.00671}$
23	TESS	2458461.01628	0.00164	$^{+0.01262}_{-0.00072}$
34	LCO	2458497.97113	-0.00439	$^{+0.01585}_{-0.00122}$
37	LCO	2458508.05202	-0.00374	$^{+0.01428}_{-0.01056}$
38	LCO	2458511.41210	-0.00374	$^{+0.00679}_{-0.00338}$
103	NGTS	2458729.82844	0.00740	$^{+0.00311}_{-0.01621}$
133	LCO	2458830.63207	0.00863	$^{+0.01162}_{-0.01385}$
215	LCO	2459106.16860	0.01860	$^{+0.00022}_{-0.00555}$
218	TESS	2459116.23825	0.00801	$^{+0.01181}_{-0.00759}$
219	TESS	2459119.60599	0.01567	$^{+0.00526}_{-0.00555}$
220	TESS	2459122.95868	0.00828	$^{+0.01197}_{-0.01316}$

221	TESS	2459126.32468	0.01420	$^{+0.00414}_{-0.00683}$
223	TESS	2459133.04645	0.01581	$^{+0.01880}_{-0.02103}$
224	TESS	2459136.40990	0.01918	$^{+0.01333}_{-0.03099}$
225	TESS	2459139.76388	0.01308	$^{+0.01296}_{-0.02113}$
227	LCO	2459146.48644	0.01548	$^{+0.00794}_{-0.01916}$
236	TESS	2459176.73154	0.01986	$^{+0.00112}_{-0.00293}$
237	TESS	2459180.08965	0.01789	$^{+0.00268}_{-0.00114}$
238	TESS	2459183.45059	0.01875	$^{+0.00004}_{-0.00585}$
240	TESS	2459190.16616	0.01416	$^{+0.00736}_{-0.00111}$
241	TESS	2459193.53089	0.01881	$^{+0.01788}_{-0.02524}$
242	TESS	2459196.88738	0.01522	$^{+0.00599}_{-0.00208}$

Table A.1: Mid-Transit times for planet b. The Timing Offset is reported in relation to the initial G20 *TESS* linear ephemerides

Table A.2: Transit Timing Variations Planet c

Transit Number	Telescope	Mid-Transit Time (BJD	Timing Offset (days)	Error
c				
0	TESS	2458383.84177	0.00376	$^{+0.00086}_{-0.00093}$
1	TESS	2458389.50354	0.00503	$^{+0.00098}_{-0.00141}$
2	TESS	2458395.16239	0.00340	$^{+0.00064}_{-0.00060}$
4	TESS	2458406.48248	0.00249	$^{+0.00106}_{-0.00134}$
5	TESS	2458412.14178	0.00131	$^{+0.00073}_{-0.00091}$
6	TESS	2458417.80261	0.00164	$^{+0.00145}_{-0.00126}$
7	TESS	2458423.46444	0.00298	$^{+0.00084}_{-0.00081}$
8	TESS	2458429.12270	0.00075	$^{+0.00103}_{-0.00098}$
9	TESS	2458434.78365	0.00120	$^{+0.00101}_{-0.00097}$
10	TESS	2458440.44412	0.00118	$^{+0.00127}_{-0.00155}$
11	TESS	2458446.10403	0.00060	$^{+0.00087}_{-0.00094}$
12	TESS	2458451.76531	0.00138	$^{+0.00128}_{-0.00114}$
13	TESS	2458457.42794	0.00352	$^{+0.00394}_{-0.00205}$
14	LCO	2458463.08389	-0.00103	$^{+0.00032}_{-0.00033}$
19	LCO	2458491.38544	-0.00193	$^{+0.00037}_{-0.00043}$
33	ASTEP	2458570.63326	-0.00102	$^{+0.00149}_{-0.00134}$
37	spitzer	2458593.27348	-0.00277	$^{+0.00018}_{-0.00018}$
55	TRAPPIST	2458695.16181	-0.00332	$^{+0.00061}_{-0.00085}$
61	TRAPPIST	2458729.12413	-0.00395	$^{+0.00067}_{-0.00066}$
61	LCO	2458729.12540	-0.00268	$^{+0.00036}_{-0.00036}$
63	LCO	2458740.44769	-0.00138	$^{+0.00056}_{-0.00053}$
66	LCO	2458757.42889	-0.00166	$^{+0.00031}_{-0.00031}$
69	LCO	2458774.41028	-0.00175	$^{+0.00040}_{-0.00038}$
70	TRAPPIST	2458780.06961	-0.00291	$^{+0.00080}_{-0.00096}$

72	LCO	2458791.39388	0.00037	$^{+0.00033}_{-0.00032}$
73	LCO	2458797.05387	-0.00013	$^{+0.00034}_{-0.00035}$
73	TRAPPIST	2458797.05430	0.00030	$^{+0.00066}_{-0.00067}$
74	LCO	2458802.71417	-0.00032	$^{+0.00034}_{-0.00036}$
77	LCO	2458819.69528	-0.00069	$^{+0.00128}_{-0.00100}$
78	spitzer	2458825.35745	0.00098	$^{+0.00019}_{-0.00018}$
81	spitzer	2458842.33935	0.00141	$^{+0.00014}_{-0.00014}$
83	spitzer	2458853.66120	0.00228	$^{+0.00015}_{-0.00015}$
84	spitzer	2458859.32203	0.00261	$^{+0.00013}_{-0.00012}$
107	ASTEP	2458989.51812	0.00736	$^{+0.00106}_{-0.00113}$
108	ASTEP	2458995.17581	0.00455	$^{+0.00200}_{-0.00195}$
110	ASTEP	2459006.50192	0.00968	$^{+0.00105}_{-0.00106}$
129	TESS	2459114.05383	0.01222	$^{+0.00070}_{-0.00072}$
130	TESS	2459119.71415	0.01205	$^{+0.00099}_{-0.00100}$
131	TESS	2459125.37407	0.01147	$^{+0.00076}_{-0.00076}$
132	TESS	2459131.03666	0.01358	$^{+0.00069}_{-0.00071}$
135	LCO	2459148.01698	0.01241	$^{+0.00027}_{-0.00029}$
139	TESS	2459170.65889	0.01235	$^{+0.00086}_{-0.00090}$
140	TESS	2459176.31907	0.01204	$^{+0.00081}_{-0.00079}$
141	TESS	2459181.98058	0.01305	$^{+0.00100}_{-0.00101}$
142	TESS	2459187.64029	0.01228	$^{+0.00092}_{-0.00088}$
143	TESS	2459193.30171	0.01320	$^{+0.00129}_{-0.00124}$
147	LCO	2459215.94006	0.00958	$^{+0.00112}_{-0.00111}$

Table A.2: Mid-Transit times for planet c. The Timing Offset is reported in relation to the initial G20 *TESS* linear ephemerides

Table A.3: Transit Timing Variations Planet d

Transit Number	Telescope	Mid-Transit Time (BJD	Timing Offset (days)	Error
d				
1	TESS	2458389.67893	-0.00320	$^{+0.00118}_{-0.00097}$
2	TESS	2458401.05791	-0.00370	$^{+0.00118}_{-0.00158}$
3	TESS	2458412.43573	-0.00536	$^{+0.00614}_{-0.00128}$
5	TESS	2458435.19786	-0.00219	$^{+0.00087}_{-0.00098}$
6	TESS	2458446.57953	0.00000	$^{+0.00203}_{-0.00164}$
7	TESS	2458457.95868	-0.00033	$^{+0.00449}_{-0.00243}$
14	LCO	2458537.61795	0.00259	$^{+0.00067}_{-0.00075}$
24	spitzer	2458651.41688	0.00672	$^{+0.00025}_{-0.00024}$
33	LCO	2458753.83030	0.00484	$^{+0.00033}_{-0.00033}$
33	NGTS	2458753.83266	0.00720	$^{+0.00108}_{-0.00125}$
34	LCO	2458765.21150	0.00656	$^{+0.00046}_{-0.00047}$
35	LCO	2458776.59113	0.00671	$^{+0.00071}_{-0.00069}$
38	NGTS	2458810.72707	0.00421	$^{+0.00079}_{-0.00083}$
38	TRAPPIST	2458810.73193	0.00908	$^{+0.00142}_{-0.00116}$
39	spitzer	2458822.10886	0.00652	$^{+0.00023}_{-0.00022}$
42	spitzer	2458856.24751	0.00674	$^{+0.00024}_{-0.00023}$
59	LCO	2459049.69684	0.00492	$^{+0.00070}_{-0.00070}$
63	LCO	2459095.21369	0.00386	$^{+0.00043}_{-0.00037}$
65	TESS	2459117.97101	0.00221	$^{+0.00094}_{-0.00107}$
67	TESS	2459140.73102	0.00327	$^{+0.00118}_{-0.00128}$
70	TESS	2459174.86949	0.00331	$^{+0.00136}_{-0.00119}$
72	TESS	2459197.62899	0.00385	$^{+0.00123}_{-0.00106}$

Table A.3: Mid-Transit times for planet d. The Timing Offset is reported in relation to the initial G20 *TESS* linear ephemerides

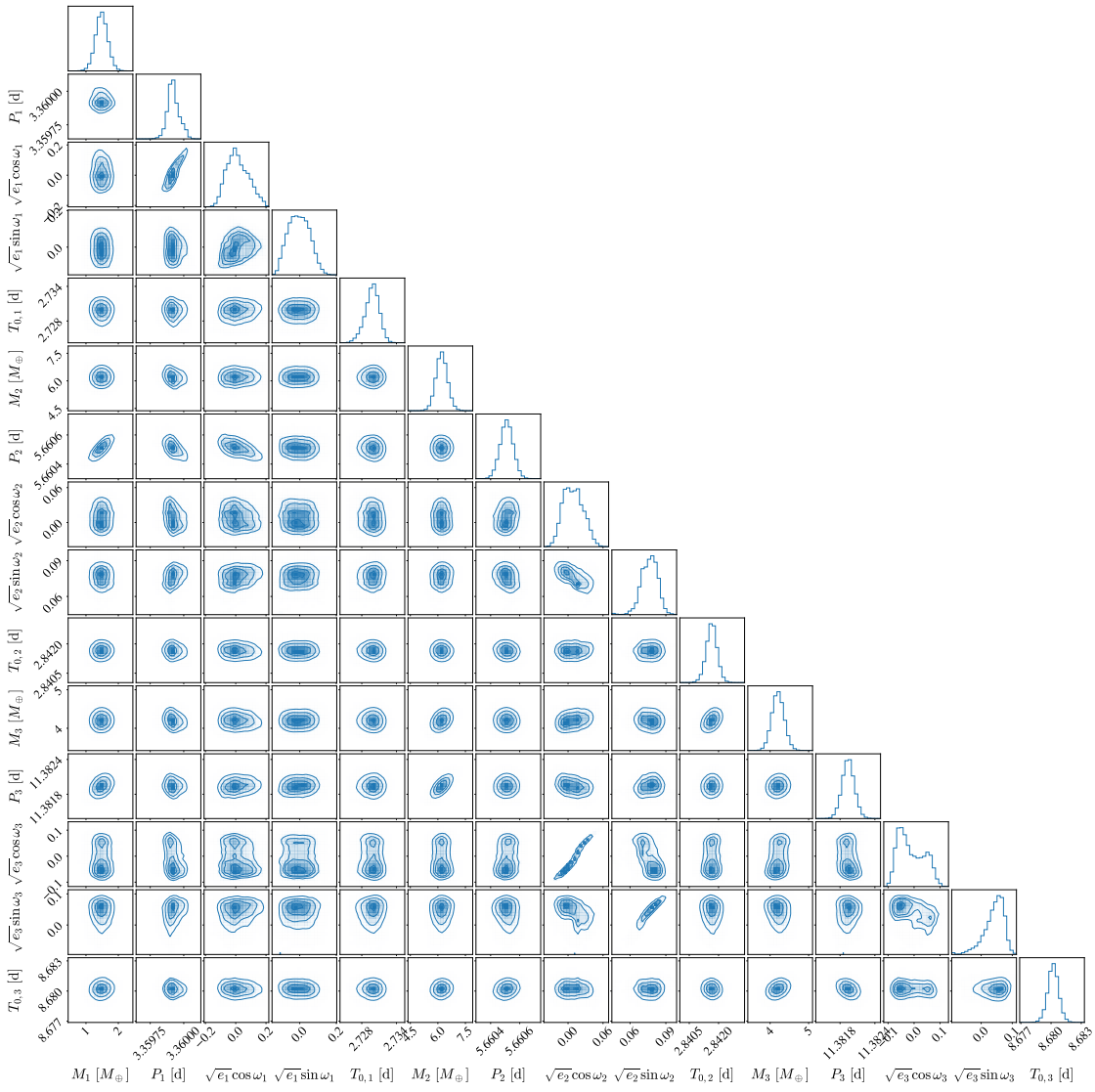


Figure A.2: Posterior distributions on the parameters in our dynamical analysis combining our TTVs with the RVs from VE21. 1σ, 2σ, and 3σ contours are shown. Planets b, c, and d are indexed as 1, 2, and 3, respectively.

APPENDIX B

Appendix: TTV Catalogue

Supplementary material for Chapter 3 on Transit Timing Variations from Kepler and K2 to TESS

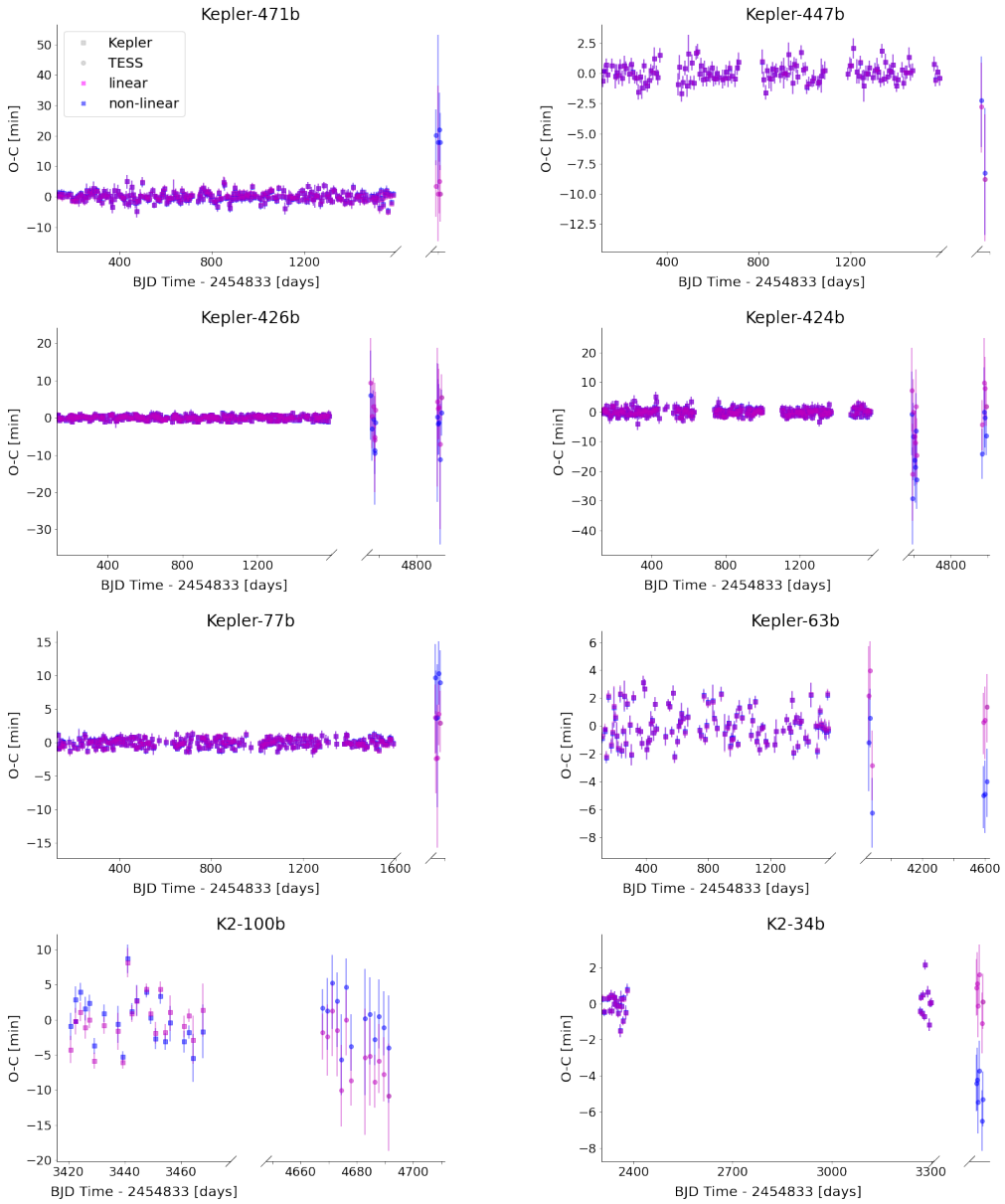


Figure B.1: Residuals to linear ephemerides. O-C plots for Kepler and K2 systems after fitting for a linear ephemeris. These are systems for which no timing trends were detected. In some cases, timing trends look to be visible by eye, but were either not determined to be statistically significant, or there were too few data-points to conclude the presence of a trend without further follow-up

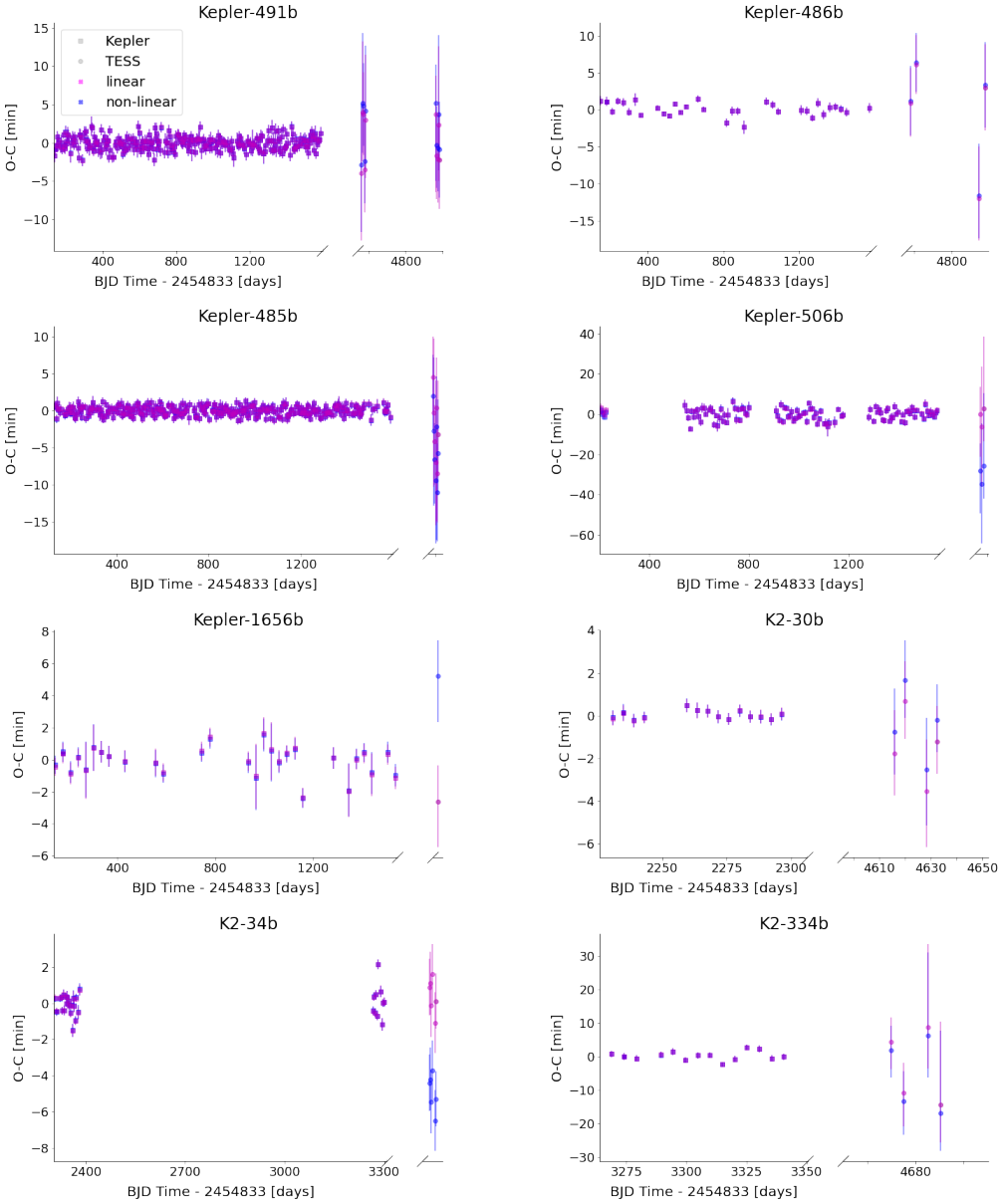


Figure B.2: Continued linear ephemerides

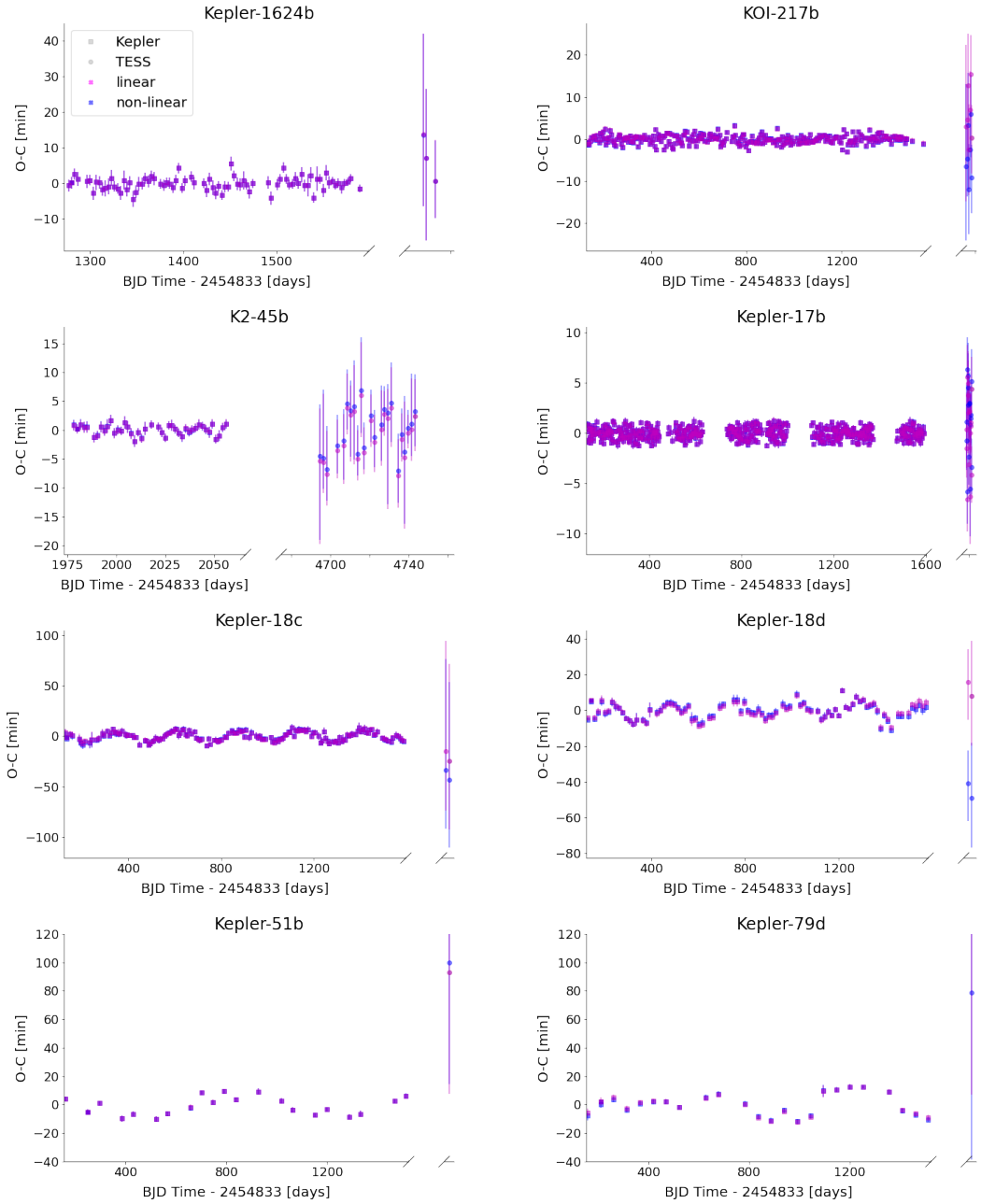


Figure B.3: Systems with previously identified TTVs . These systems were previously identified to display TTVs through periodic variability or significant scatter. In some cases, error bars on TESS transit times are too large to be considered in any way constraining.

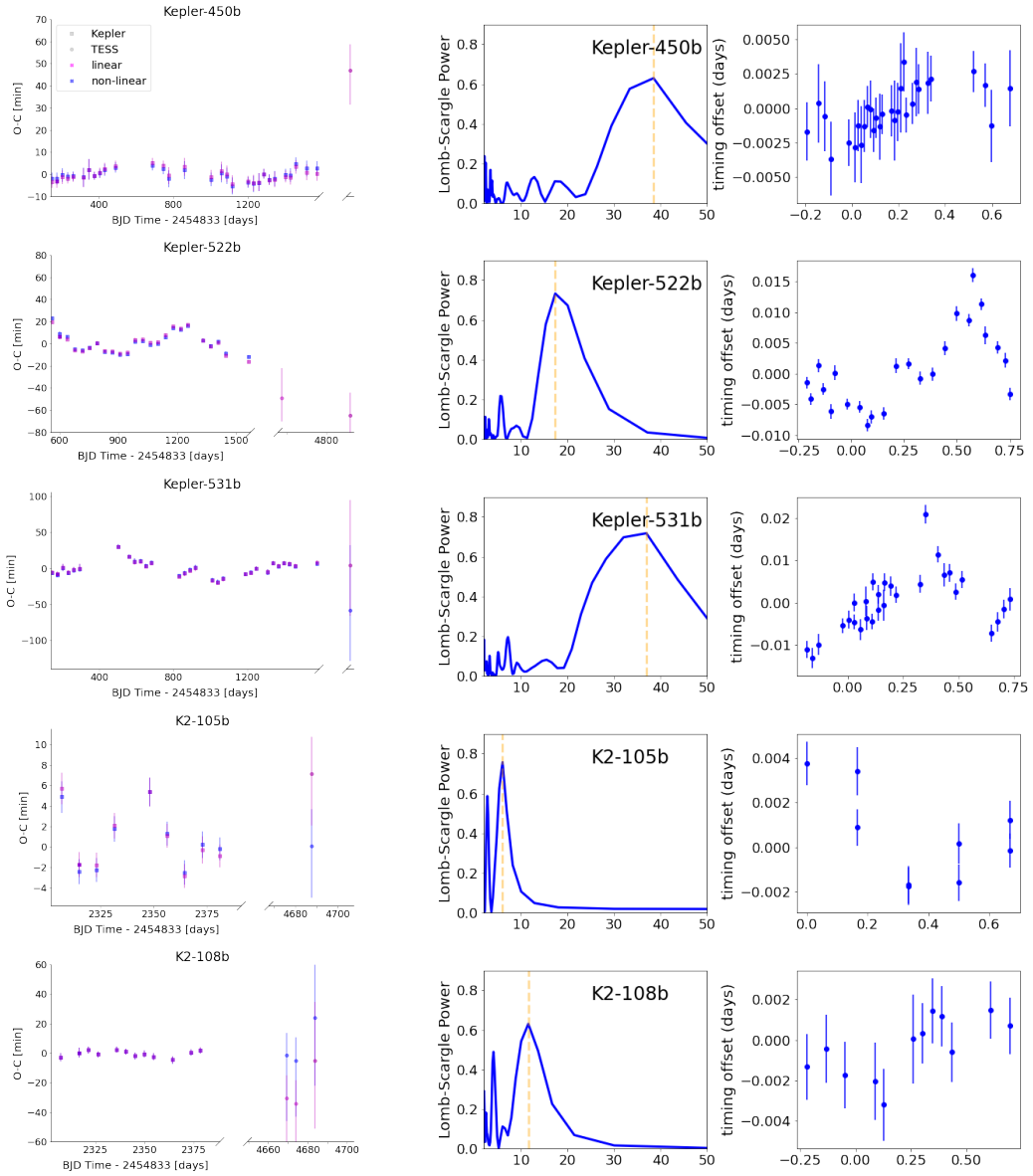


Figure B.4: Newly identified TTVs . Kepler and K2 systems that show periodic trends but not previously identified as having TTVs. In the leftmost column are the O-C residuals to linear ephemerides. In the middle column are the Lomb-Scargle (LS) periodograms that show significant periodicity in the residuals, and in the right-most column are the timing residuals of Kepler/K2 transits phase-folded around the best-fit superperiod.

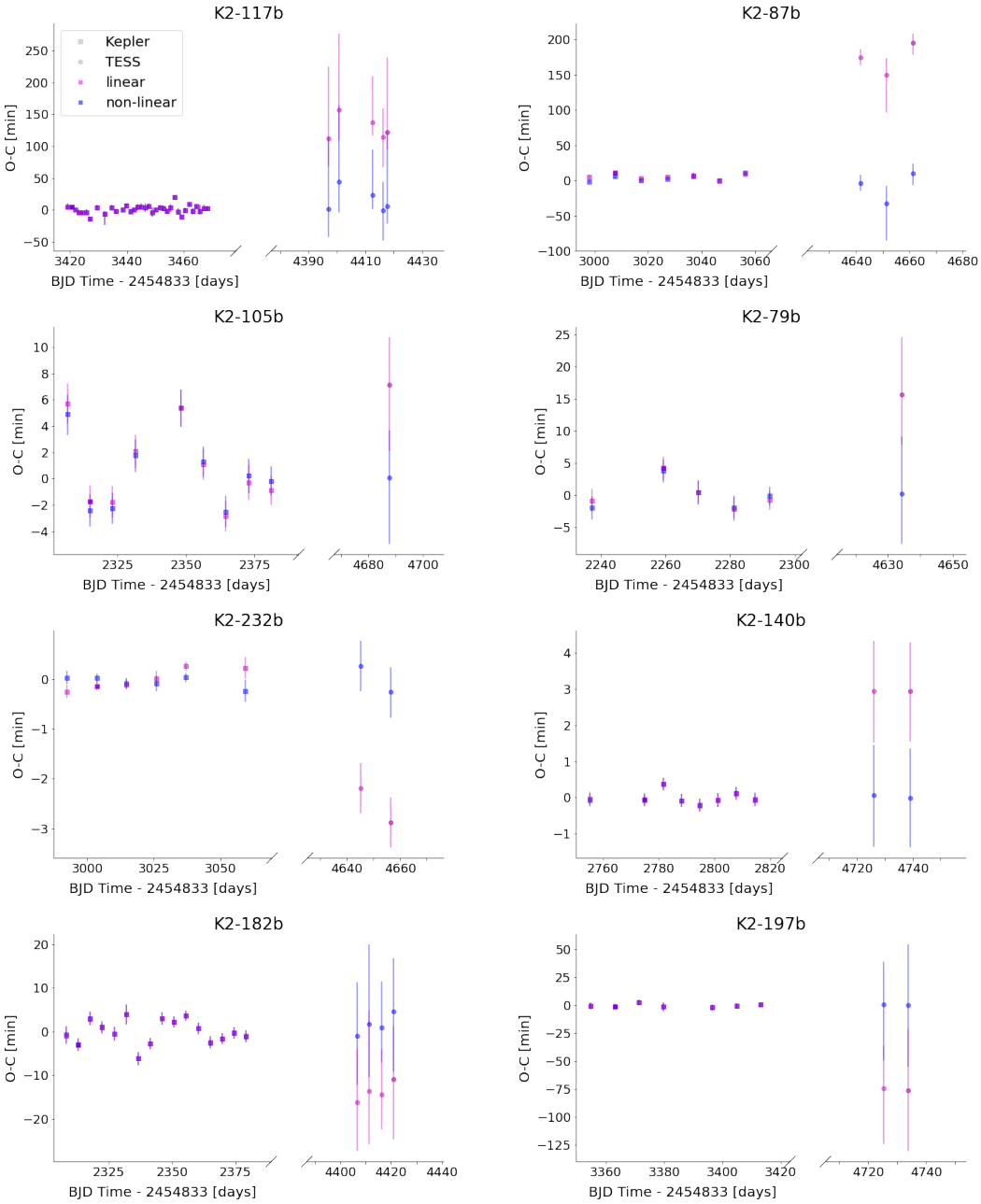


Figure B.5: Systems with non-linear timing trends. These systems display significant deviations from a linear ephemeris, however, they do not yet show enough evidence of periodicity to determine the cause of their offset.

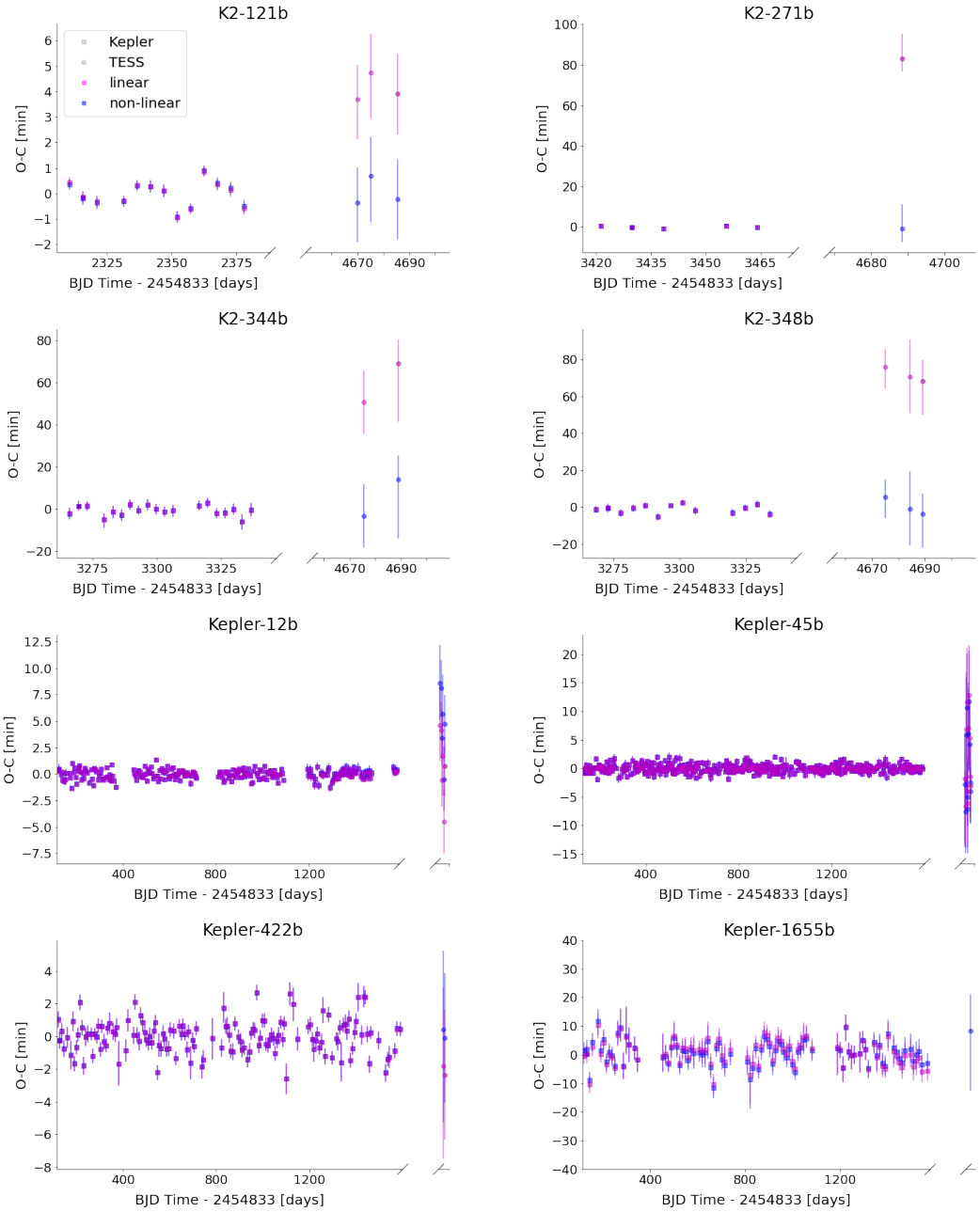


Figure B.6: Systems with non-linear timing trends continued

pl_name	Archival T_0 (BJD-2454833)	Archival Period	Reference	Updated T_0	Updated Period
K2-10 b	1986.5814 $\pm 2.10e^{-03}$	19.304400 $\pm 1.20e^{-03}$	Van Eylen et al. (2016)	1986.5838 $\pm 6.09e^{-04}$	19.303515 $\pm 1.12e^{-04}$
K2-100 b	2307.7194 $\pm 2.70e^{-04}$	1.673904 $\pm 4.00e^{-07}$	Barragán et al. (2019)	2307.7200 $\pm 9.33e^{-04}$	1.673903 $\pm 1.29e^{-06}$
K2-105 b	2314.9895 $\pm 4.44e^{-04}$	8.266993 $\pm 7.00e^{-06}$	Castro-González et al. (2022)	2314.9902 $\pm 3.01e^{-04}$	8.266995 $\pm 1.06e^{-05}$
K2-108 b	2312.0960 $\pm 1.72e^{-03}$	4.733999 $\pm 2.21e^{-04}$	Livingston et al. (2018)	2312.0999 $\pm 5.20e^{-04}$	4.733527 $\pm 2.49e^{-05}$
K2-113 b	2565.7043 $\pm 3.00e^{-04}$	5.817685 $\pm 4.10e^{-05}$	Livingston et al. (2018)	2565.7045 $\pm 1.21e^{-04}$	5.817594 $\pm 6.39e^{-06}$
K2-114 b	2831.3068 $\pm 1.60e^{-04}$	11.390931 $\pm 3.40e^{-06}$	Ikwut-Ukwa et al. (2020)	2831.3070 $\pm 4.96e^{-05}$	11.390941 $\pm 2.21e^{-06}$
K2-117 b	2309.7745 $\pm 1.62e^{-03}$	1.291600 $\pm 4.90e^{-05}$		2309.7968 $\pm 1.61e^{-02}$	1.291582 $\pm 1.83e^{-05}$
K2-121 b	2310.5605 $\pm 7.80e^{-05}$	5.185754 $\pm 6.00e^{-07}$	Castro-González et al. (2022)	2310.5606 $\pm 4.51e^{-05}$	5.185752 $\pm 1.38e^{-06}$
K2-124 b	2309.1810 $\pm 1.05e^{-03}$	6.413651 $\pm 3.60e^{-05}$		2309.1871 $\pm 4.60e^{-04}$	6.413625 $\pm 2.37e^{-05}$
K2-133 d	2993.1709 $\pm 1.20e^{-03}$	11.024540 $\pm 3.60e^{-04}$	Wells et al. (2019)	2993.1707 $\pm 6.90e^{-04}$	11.024777 $\pm 1.03e^{-04}$
K2-140 b	2755.2850 $\pm 5.00e^{-05}$	6.569188 $\pm 3.10e^{-05}$	Korth et al. (2019)	2755.2851 $\pm 4.73e^{-05}$	6.569201 $\pm 2.29e^{-06}$
K2-174 b	2250.7791 $\pm 9.50e^{-04}$	19.562307 $\pm 7.80e^{-05}$	Livingston et al. (2018)	2250.7755 $\pm 8.40e^{-04}$	19.562568 $\pm 7.97e^{-05}$
K2-178 b	2237.3365 $\pm 1.47e^{-03}$	8.747818 $\pm 3.63e^{-04}$	Mayo et al. (2018)	2237.3366 $\pm 5.37e^{-04}$	8.747985 $\pm 6.00e^{-05}$
K2-179 b	2233.5803 $\pm 1.37e^{-03}$	5.172191 $\pm 2.01e^{-04}$	Mayo et al. (2018)	2233.5778 $\pm 7.88e^{-04}$	5.172441 $\pm 8.88e^{-05}$
K2-18 b	2431.3914 $\pm 6.50e^{-04}$	32.939623 $\pm 9.50e^{-05}$	Sarkis et al. (2018)	2431.3922 $\pm 4.57e^{-04}$	32.940019 $\pm 4.10e^{-05}$
K2-182 b	2886.1151 $\pm 2.80e^{-04}$	4.736968 $\pm 2.30e^{-06}$	Akana Murphy et al. (2021)	2886.1154 $\pm 2.62e^{-04}$	4.736970 $\pm 9.18e^{-06}$
K2-187 d	2370.5208 $\pm 1.90e^{-03}$	7.149584 $\pm 1.20e^{-04}$		2370.5234 $\pm 1.09e^{-03}$	7.149065 $\pm 7.91e^{-05}$
K2-19 c	2020.0007 $\pm 4.00e^{-04}$	11.899300 $\pm 8.00e^{-04}$	Petigura et al. (2020)	2019.9983 $\pm 8.36e^{-04}$	11.906617 $\pm 1.16e^{-04}$
K2-197 b	2385.1824 $\pm 3.64e^{-03}$	8.357881 $\pm 7.10e^{-04}$	Livingston et al. (2018)	2385.1651 $\pm 1.57e^{-02}$	8.357986 $\pm 1.31e^{-04}$
K2-198 b	2371.5687 $\pm 1.40e^{-04}$	17.042868 $\pm 7.10e^{-06}$	Hedges et al. (2019)	2371.5695 $\pm 1.88e^{-04}$	17.042934 $\pm 1.84e^{-05}$
K2-198 d	2380.5759 $\pm 1.00e^{-03}$	7.450018 $\pm 5.20e^{-06}$	Hedges et al. (2019)	2380.5763 $\pm 4.45e^{-04}$	7.450027 $\pm 1.62e^{-05}$
K2-212 b	2566.6410 $\pm 3.90e^{-04}$	9.795647 $\pm 2.10e^{-05}$	Duck et al. (2021)	2566.6380 $\pm 6.23e^{-04}$	9.795671 $\pm 3.29e^{-05}$
K2-232 b	2992.3497 $\pm 9.30e^{-05}$	11.168454 $\pm 2.30e^{-05}$	Brahm et al. (2018)	2992.3516 $\pm 3.41e^{-05}$	11.168436 $\pm 1.71e^{-06}$
K2-270 c	2309.9751 $\pm 1.66e^{-03}$	4.400028 $\pm 1.69e^{-04}$		2309.8976 $\pm 4.46e^{-03}$	4.400115 $\pm 1.70e^{-05}$
K2-271 b	2316.7127 $\pm 5.30e^{-04}$	8.562421 $\pm 1.27e^{-04}$	Livingston et al. (2018)	2316.7009 $\pm 5.64e^{-03}$	8.562418 $\pm 4.27e^{-05}$

K2-275 b	2309.1339 $\pm 3.37e^{-04}$	3.280963 $\pm 1.60e^{-06}$	Castro-González et al. (2022)	2309.1351 $\pm 3.10e^{-03}$	3.280958 $\pm 8.89e^{-06}$
K2-275 c	2309.4867 $\pm 4.58e^{-04}$	8.438839 $\pm 7.50e^{-06}$	Castro-González et al. (2022)	2309.4797 $\pm 9.00e^{-03}$	8.438887 $\pm 6.68e^{-05}$
K2-277 b	2388.2295 $\pm 2.21e^{-03}$	6.326763 $\pm 3.55e^{-04}$	Livingston et al. (2018)	2388.2295 $\pm 6.52e^{-04}$	6.326747 $\pm 1.35e^{-05}$
K2-284 b	3026.1131 $\pm 4.30e^{-04}$	4.795069 $\pm 8.60e^{-05}$	David et al. (2018)	3026.1119 $\pm 4.36e^{-04}$	4.794867 $\pm 1.04e^{-05}$
K2-295 b	2562.4140 $\pm 1.20e^{-03}$	4.024867 $\pm 1.50e^{-05}$	Smith et al. (2019)	2562.4138 $\pm 3.79e^{-05}$	4.024892 $\pm 1.29e^{-06}$
K2-30 b	2230.8071 $\pm 1.00e^{-04}$	4.098503 $\pm 1.10e^{-05}$	Johnson et al. (2016)	2230.8072 $\pm 5.85e^{-05}$	4.098476 $\pm 1.15e^{-06}$
K2-308 b	2990.2233 $\pm 6.00e^{-04}$	3.386280 $\pm 2.00e^{-05}$	Rampalli et al. (2019)	2990.2242 $\pm 6.45e^{-04}$	3.386333 $\pm 3.81e^{-05}$
K2-321 b	3076.1700 $\pm 1.42e^{-03}$	2.298000 $\pm 1.00e^{-03}$	Castro González et al. (2020)	3076.1727 $\pm 5.64e^{-04}$	2.297934 $\pm 2.58e^{-05}$
K2-334 b	3263.8102 $\pm 5.50e^{-04}$	5.113981 $\pm 6.10e^{-05}$	de Leon et al. (2021)	3263.8112 $\pm 2.17e^{-04}$	5.113862 $\pm 1.34e^{-05}$
K2-34 b	2308.3514 $\pm 6.90e^{-05}$	2.995635 $\pm 2.00e^{-07}$	Castro-González et al. (2022)	2308.3511 $\pm 3.78e^{-05}$	2.995636 $\pm 2.01e^{-07}$
K2-344 b	3262.7477 $\pm 1.27e^{-03}$	3.35585 $\pm 9.10e^{-05}$		3262.7488 $\pm 4.82e^{-04}$	3.355734 $\pm 1.92e^{-05}$
K2-348 b	3263.7167 $\pm 9.95e^{-04}$	4.688418 $\pm 1.19e^{-04}$	de Leon et al. (2021)	3263.7148 $\pm 3.57e^{-04}$	4.688620 $\pm 1.80e^{-05}$
K2-348 c	3271.4356 $\pm 3.15e^{-03}$	12.550171 $\pm 1.02e^{-03}$	de Leon et al. (2021)	3271.4366 $\pm 5.29e^{-04}$	12.550204 $\pm 7.07e^{-05}$
K2-352 c	3265.7169 $\pm 2.71e^{-03}$	8.234885 $\pm 5.08e^{-04}$		3265.7159 $\pm 1.22e^{-03}$	8.235395 $\pm 1.54e^{-04}$
K2-352 d	3270.6228 $\pm 2.28e^{-03}$	14.871387 $\pm 9.16e^{-04}$	de Leon et al. (2021)	3270.6226 $\pm 1.03e^{-03}$	14.871385 $\pm 1.21e^{-04}$
K2-36 c	1979.8394 $\pm 1.19e^{-03}$	5.341051 $\pm 2.57e^{-05}$		1979.8406 $\pm 2.11e^{-04}$	5.340828 $\pm 3.71e^{-06}$
K2-43 b	1976.8843 $\pm 7.10e^{-04}$	3.471149 $\pm 1.04e^{-04}$	Hedges et al. (2019)	1976.8834 $\pm 4.14e^{-04}$	3.471240 $\pm 7.56e^{-06}$

Table B.1: Observation Log . Updates to linear ephemerides for all the planets and planet candidates examined in this work. Most planets see a modest improvement in ephemerides of a factor of 2-10. Some see noticeably worse linear ephemerides which in several cases is due to the finding of significant variation between Kepler and TESS datapoints.

Table B.2: Timing Characteristics

Name	SNR	**Timing Trend**	n TESS Sector	Stellar Activity
K2-10 b	4.4	3*	1	N
K2-100 b	7		1	Y
K2-105 b	5.3	2,3	1	Y
K2-108 b	2.7	2,3	1	N
K2-113 b	12.3		1	Y
K2-114 b	22.7		2	N
K2-117 b	2.4	3	1	N
K2-121 b	25.5	2*	1	Y
K2-124 b	2.8		1	N
K2-133 d	0	3	1	N
K2-140 b	50.4	3	1	N
K2-174 b	9.1	3*	1	N
K2-178 b	5	3	1	Y
K2-179 b	2.5		1	Y
K2-18 b	12.7	3*	1	N
K2-182 b	4.7	3	1	Y
K2-187 d	2.3	3	1	N
K2-19 c	7.8	1	1	Y
K2-197 b	2.4	3	1	Y
K2-198 b	17.4	3*	1	Y
K2-198 d	5.9		1	Y
K2-212 b	4.2	3	1	N
K2-232 b	128.2	3	1	N
K2-270 c	2.1		1	Y
K2-271 b	6.1	3	1	N
K2-275 b	3.6		1	Y
K2-275 c	4	3	1	Y
K2-277 b	4.9	3	1	N
K2-284 b	4.2	3	1	Y
K2-295 b	27.5		1	N
K2-30 b	29.2		1	N
K2-308 b	3		1	Y
K2-321 b	3.7		1	N
K2-334 b	5.6		1	N
K2-34 b	39.4		1	N
K2-344 b	2.3	3	1	N
K2-348 b	4	3	1	N
K2-348 c	3.1		1	N
K2-352 c	2.3		1	N
K2-352 d	3.3	3*	1	N
K2-36 c	6	3	1	N
K2-43 b	5.3		1	N

K2-45 b	11.3		2	N
K2-77 b	3		1	N
K2-79 b	3.9	3	1	N
K2-87 b	8	3	1	N
K2-90 b	3.3	3*	1	Y
K2-98 b	5.6		1	N
Kepler-102 e	4.2	2*	1	Y
Kepler-114 d	3.2	1	1	Y
Kepler-12 b	32.5	2*	1	N
Kepler-131 b	2.3		1	Y
Kepler-15 b	16		2	N
Kepler-1624 b	4.6	1	1	N
Kepler-1627 b	3.3		1	Y
Kepler-1655 b	2.4	3	1	N
Kepler-1656 b	11		1	Y
Kepler-1658 b	6.8		1	Y
Kepler-17 b	20.2	1	1	Y
Kepler-18 c	3.8	1	1	N
Kepler-18 d	5.6	1	1	N
Kepler-210 c	3.8	1	1	N
Kepler-297 c	5.9	1	1	N
Kepler-314 c	2.2		1	Y
Kepler-318 b	2.2		2	Y
Kepler-37 d	7.4	1	2	N
Kepler-396 b	6.7	1	1	Y
Kepler-40 b	3.3		2	N
Kepler-412 b	8.5	1	2	Y
Kepler-419 b	10.5	1	1	N
Kepler-422 b	14	2*,3	1	Y
Kepler-424 b	9		2	N
Kepler-425 b	8.2		1	N
Kepler-426 b	7.4		2	N
Kepler-428 b	8.3		1	N
Kepler-43 b	8.7		1	Y
Kepler-433 b	5		1	Y
Kepler-435 b	9.5		1	N
Kepler-447 b	49.5	2*	1	Y
Kepler-45 b	10.9	2*	1	Y
Kepler-450 b	8.9	2	1	Y
Kepler-471 b	8.5		1	N
Kepler-485 b	7.9		1	N
Kepler-486 b	23.1		2	N
Kepler-488 b	8.9		1	Y
Kepler-490 b	5.4		2	N
Kepler-491 b	6.9		2	N

Kepler-493 b	4		1	Y
Kepler-495 b	2.2		1	N
Kepler-5 b	15.5	2*	1	N
Kepler-506 b	3.2		1	Y
Kepler-51 b	5.4	1	1	Y
Kepler-522 b	6.2	2	2	N
Kepler-531 b	2.7	2	1	N
Kepler-546 b	3		1	N
Kepler-547 b	2.3		1	N
Kepler-548 b	7.3		1	N
Kepler-63 b	19		2	Y
Kepler-670 b	7		1	Y
Kepler-685 b	3.3		1	Y
Kepler-686 b	3.9		1	Y
Kepler-695 b	4.6		1	N
Kepler-7 b	23.1		2	N
Kepler-714 b	3.5		1	N
Kepler-718 b	4.8		1	N
Kepler-720 b	3.4		1	N
Kepler-723 b	7.1		2	N
Kepler-731 b	5.9		1	N
Kepler-74 b	6.3		1	N
Kepler-75 b	5.9		1	Y
Kepler-76 b	18.5		1	N
Kepler-762 b	4.4		1	Y
Kepler-77 b	11.2		1	N
Kepler-785 b	7		1	N
Kepler-79 d	5.7	1	1	N
Kepler-8 b	13.3		1	N
Kepler-854 b	24.3	2*	1	Y
Kepler-856 b	3.1	2*	1	N
Kepler-93 b	2.6		2	N
Kepler-96 b	6.8	2*	1	N
KOI-217 b	9.7	1	1	N

Table B.2: Timing trend indicators and stellar activity. A timing trend indicator of 1 indicates TTVs were previously found in the system. A Flag of 2 indicates new periodic TTVs found in this work; a flag of 2* indicates planets for which periodicity was found, but it either corresponded to stellar activity timescales, or was low amplitude and high frequency (less than 10 epochs), thus more follow-up should be performed to verify if these findings are significant. A Flag of 3 indicates a non-periodic second order trend and a flag of 3* indicates that data better fit a second order trend, but there were fewer than 5 Kepler or K2 transits, and thus overfitting is likely.

Supplementary material for Chapter 4 on TTV Analysis of Selected Systems

Transit Number	Telescope	Mid-Transit Time (BJD	Timing Offset (days)	Error
c				
147	NGTS	2459215.94374	0.01326	$^{+0.00144}_{-0.00094}$
153	NGTS	2459249.90476	0.01132	$^{+0.00072}_{-0.00077}$
156	NGTS	2459266.88472	0.00980	$^{+0.00268}_{-0.00158}$
236	ASTEP	2459719.70836	-0.00600	$^{+0.00337}_{-0.00297}$
240	ASTEP	2459742.35156	-0.00477	$^{+0.00308}_{-0.00275}$
242	ASTEP	2459753.67307	-0.00425	$^{+0.00073}_{-0.00082}$
243	ASTEP	2459759.33262	-0.00519	$^{+0.00180}_{-0.00111}$
246	ASTEP	2459776.31499	-0.00430	$^{+0.00111}_{-0.00123}$
249	ASTEP	2459793.29721	-0.00355	$^{+0.00127}_{-0.00102}$

Table B.3: Transit Timing Variations Planet c Newer mid-Transit times for planet c. The timing offset is reported in relation to the initial G20 *TESS* linear ephemerides

Transit Number	Telescope	Mid-Transit Time (BJD	Timing Offset (days)	Error
d				
104	NGTS	2459561.79020	0.02173	$^{+0.00243}_{-0.00269}$
106	NGTS	2459584.55766	0.03023	$^{+0.00374}_{-0.00228}$
119	ASTEP	2459732.48484	0.02419	$^{+0.00398}_{-0.00302}$

Table B.4: Transit Timing Variations Planet d Newer mid-Transit times for planet d. The timing offset is reported in relation to the initial G20 *TESS* linear ephemerides

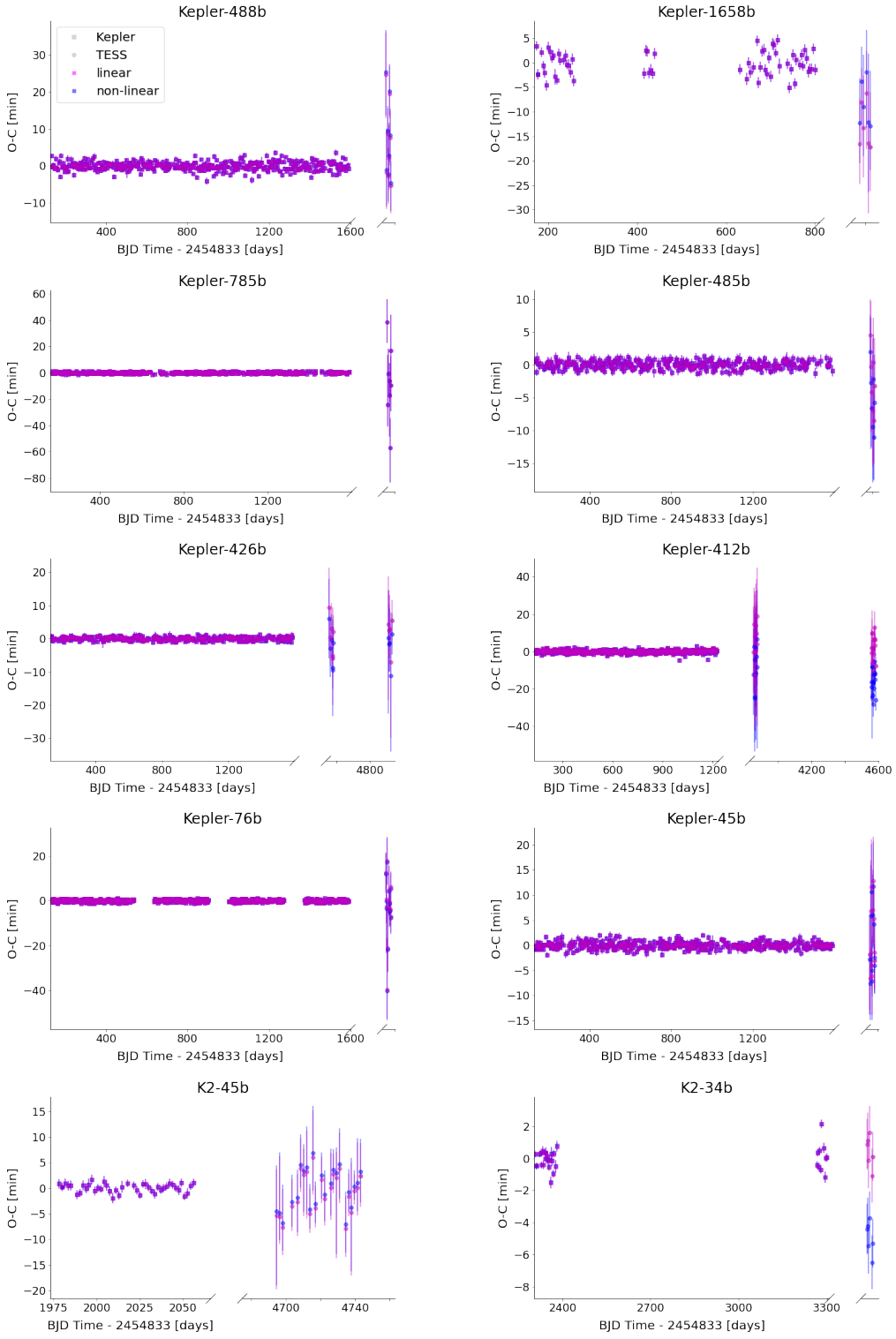


Figure B.7: Residuals to linear ephemerides. O-C plots for Kepler and K2 systems after fitting for a linear ephemeris. These are systems for which no timing trends were detected. In some cases, timing trends look to be visible by eye, but were either not determined to be statistically significant, or there were too few data-points to conclude the presence of a trend without further follow-up

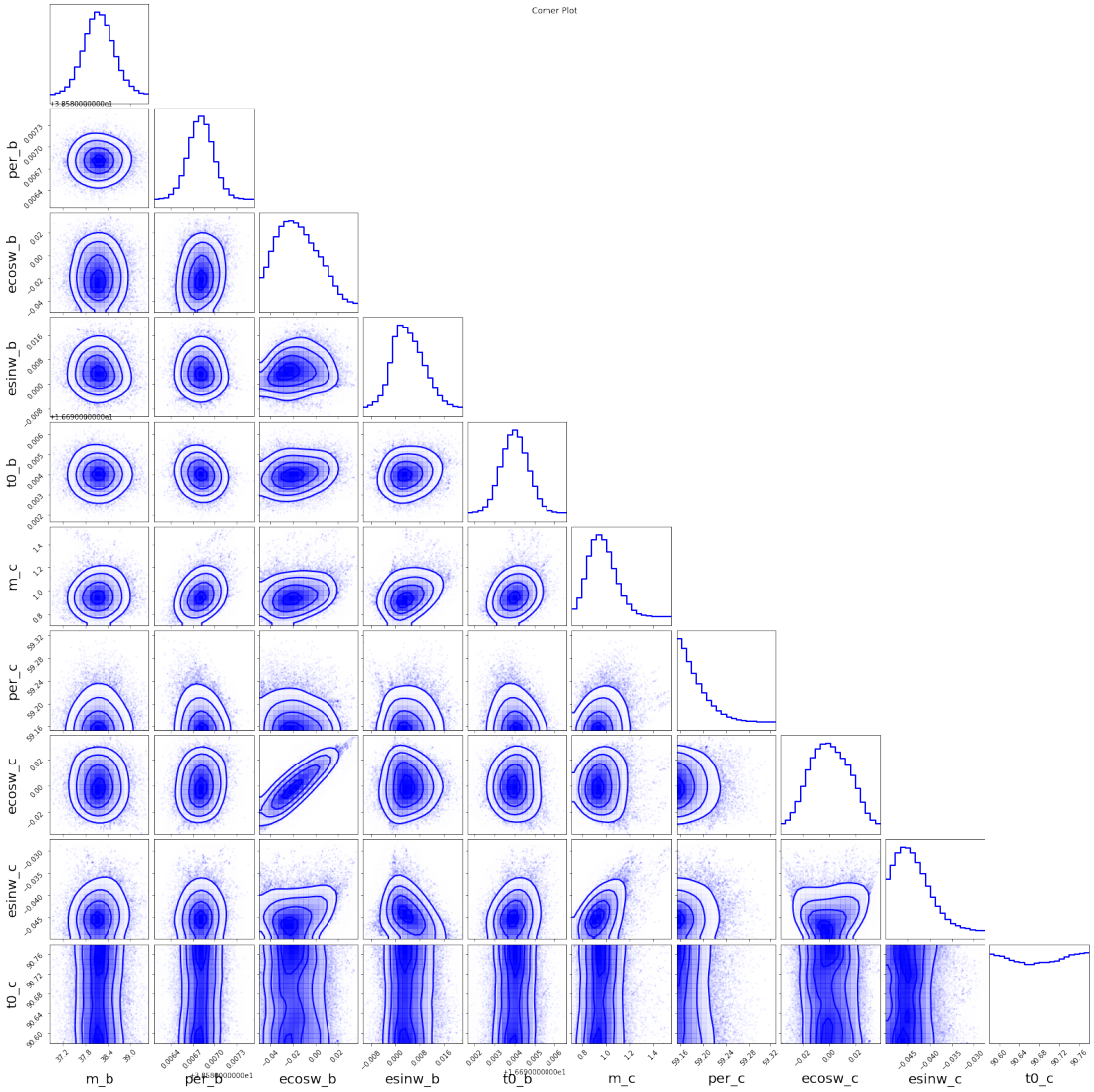


Figure B.8: Corner plot showing the posterior distribution of the 2:3 resonance fit for Kepler-522 b

.

APPENDIX C

Appendix: Further Work

This appendix covers two parts of my early DPhil work that did not end up falling into the TTV-focus of the majority of my thesis. The first section of this Appendix looks at medium resolution spectroscopy for the interesting "dipper" object, GY326. The second section explores the possibility of discovering signs of asymmetric cloud distribution in the transit curves of large close-in exoplanets.

C.1 Follow-up Spectroscopy of GY326

The K2 mission, beyond identifying several dozen more exoplanets beyond the thousands discovered by Kepler, observed several other systems of interest. Among these is a somewhat peculiar light curve, shown in Figure C.1 belonging to the object GY326, a young (1 Myr) T-Tauri star in the Ophiuchus cluster, which displays quasi-periodic eclipses that differ in depth and duration and a period of approximately 4.3 days. Such behaviour is not characteristic of a classic exoplanet and could be indicative of multiple system geometries. Therefore, follow-up spectra in the visible and near-infrared (NIR) were obtained by a previous graduate student using the XSHOOTER echelle spectrograph on the Very Large Telescope (VLT).

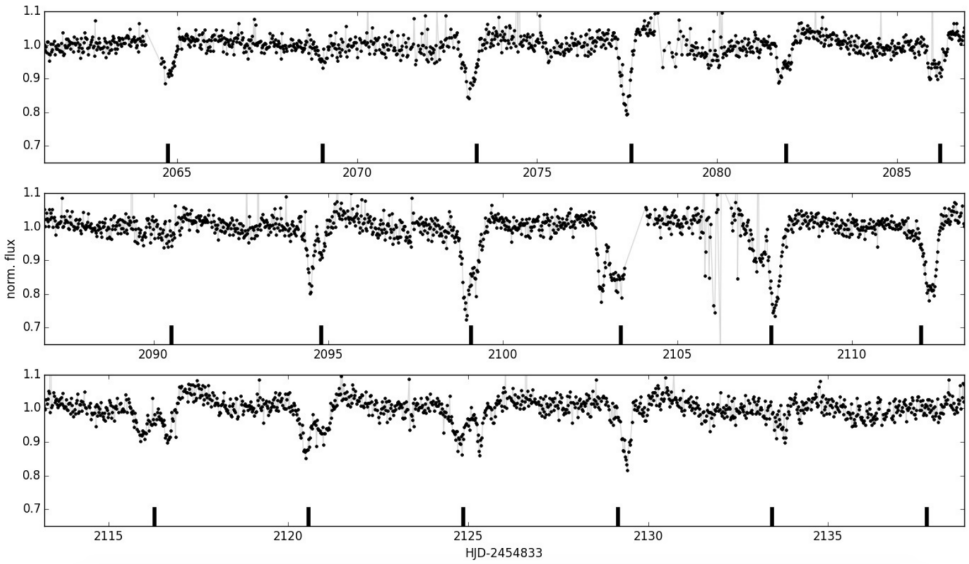


Figure C.1: K2 data for GY326: the normalised light-curve contains quasi-periodic eclipses that differ in depth and duration with a period of 4.3 days. The eclipses are sometimes double-peaked, or have leading or trailing edges, or sometimes vanish altogether.

We then analysed these spectra for radial velocity shifts and markers of accretion in order to better constrain the possibilities for this system.

C.1.1 Background: GY326 and Dippers

T-Tauri stars are young, pre-main sequence stars which exhibit pronounced variability from stellar activity, disk dynamics, and possibly protoplanetary formation (Wood et al., 1996). These stars have similar temperatures to their counterparts on the main sequence, yet are significantly more luminous, and not yet powered by thermonuclear fusion in their core, but still from the heat of gravitational contraction. GY326 is one such variable young T-Tauri star in the ρ Oph molecular cloud, the nearest star-forming region to earth, and has been categorized as a 1 Myr class II member of the cluster with an M2 spectral type (Wilking et al., 2005; Natta et al., 2006). With its weak infrared excess and silicate features, it is thought to have a transition disk rather than an envelope or photosphere (McClure et al., 2010). Its basic characteristics can be seen in Table C.1.

While T-Tauri stars are variable, the light curve of GY326 is especially unusual and the origin of its irregular dips presents a bit of a mystery. For example,

Stellar Parameters	
Name	ρ-Oph-ISO 172
RA/DEC (J2000.0)	16 27 42.70, -24 38 50.60
Lg Luminosity	-0.56
Lg T_{eff}	3.49
Lg M_*	-0.72
L(Pa beta)	<-4.82
M accreting ($M_\odot$/yr)	<-9.12

Table C.1: GY326 stellar characteristics and accretion rates from Natta et al. (2006).

starspots on younger stars can produce significant photometric variability with greater amplitudes than what is observed for our own sun (Basri et al., 2011). However the photometric features of GY326 are sharper and deeper than what would typically be expected for star spots. The features are also too irregular to result from a normal eclipsing binary or a classic planet. On the other hand, they are too regular to be something like an exocomet, which, with its typically highly eccentric orbits, would likely lead to non-periodic eclipses (Zieba et al., 2019).

Other possibilities for the configuration of GY326 include a three body system with one primary and two smaller bound companions, such as pictured in Figure C.2, or else, given the irregular limbs, a protoplanet with leading and trailing accreting edges and forming proto-moons. Such configurations could possibly explain the double eclipses sometime observed in the K2 data.

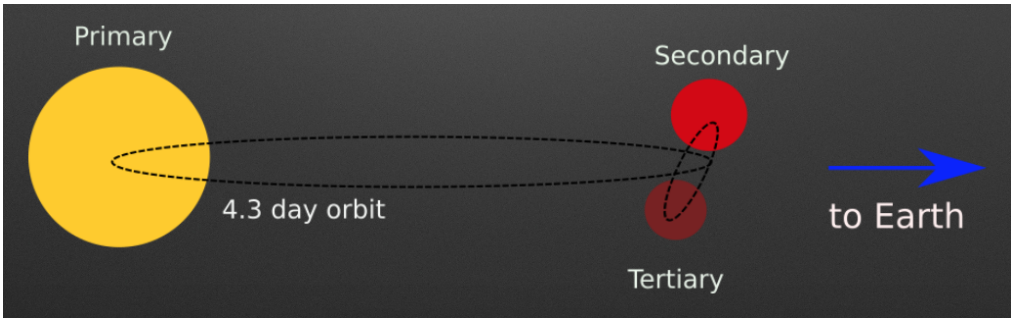


Figure C.2: A possible three body configuration, where two tightly orbiting secondary and tertiary bodies orbit their star. This could explain occasional double eclipses as the smaller star(s) or planet(s) move along their orbit in or out of the line of sight to earth.

A further, strong possibility for the system's unusual light curve is that GY326 is a "dipper" object. Dipper objects have been categorized previously as young

objects in which occultations, too deep to be star spots, are thought to result from warps or accretion columns in the inner edge of a circumstellar disk (Hedges et al., 2018). A significant fraction of young stars are dippers, with Cody et al. (2014) and Alencar (2010) finding that to be the case for about 20% to 30% of T Tauri stars in NGC 2264. Because circumstellar disks are thin and have an estimated aspect ratio of around 0.1, this suggests that material must be lifted high above the plane of the disk in order to occult its star and produce such large numbers of dippers. Bodman et al. (2017) proposes an model of magnetospheric truncation with a misaligned magnetic field, which would cause the star's accretion disk to pile up at the truncation radius, as shown in Figure C.1. Increased pressure at this radius would push gas out of the midplane to form a warp or a stream, which would then be observed as a dip from an observer perspective.

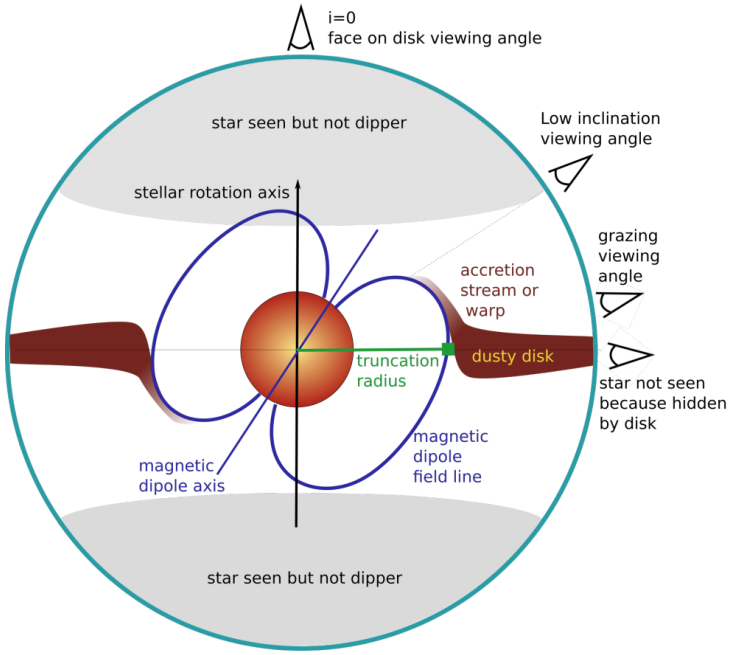


Figure C.3: Dipper Geometry, from (Bodman et al., 2017).

Spectroscopy has the potential to disentangle a good deal of these possibilities. For a dipper scenario with a disk and one or more streams of infalling material, we would expect to see markers of accretion. In accreting systems, material from the inner edge of a stellar disk is magnetically channeled along field lines to fall onto the

star at nearly free-fall velocity (Safier, 1998). This creates a hotspot on the star that changes the stellar spectrum, increasing both continuum emission and line emission. Often, this increase in the continuum emission in the visible and infrared produces a spectral feature called "veiling", which is a good measure of disk accretion. However, the Ophiuchus cluster in which GY326 is located has high extinction, which makes veiling measurements particularly difficult to obtain. Yet even with high extinction, hydrogen recombination lines such as Pa-β, Br-γ, Balmer emission, as well as other lines such as Ca II and He I originate in the accretion columns themselves and can often be seen (Calvet & Hartmannet, 2001; Harries & Symington, 2006; Bouvier et al., 2006). While a 2006 study by Natta et al. (2006) found GY326 to have a relatively low accretion rate compared to most other stars assessed in the cluster, follow-up examination of characteristic lines might give us a clearer picture.

Spectroscopy can also enable us to discern whether GY326 is in fact an eclipsing binary, or three-star system. A similar system with unusual eclipsing behaviour was KH 15D, a T-Tauri star with a binary companion where one or both stars periodically disappeared behind the inner edge of their disks, until the disk precessed and the eclipses vanished (Winn et al., 2003; Herbst et al., 2002). If GY326 is indeed part of a multi-star system, we would expect time series spectroscopy to reveal significant radial velocity changes, and for lines in the infrared to appear as double or triple. Finally, evidence for systems like comets, or transient or forming systems could come in the form of prominent spectral features that change in time (Kiefer et al., 2014).

Detailed modeling of K2 light curves combined with the X-Shooter medium-resolution time series spectroscopy should be able to confirm or constrain some of these possibilities for GY326. These data and their analysis are described in the following section.

C.1.2 Analysis

K2 Observations

GY326 was observed in K2's Campaign 2, an approximately 80 day long observing period in 2015. The data were processed using VARCAT to extract and detrend

the light curve (Armstrong et al., 2016), which appears in Figure C.1, and shows periodic, irregularly shaped eclipses. When fit with a Lomb-Scargle Periodogram, the best-fit period comes out to 4.32875 days as seen in figure C.4.

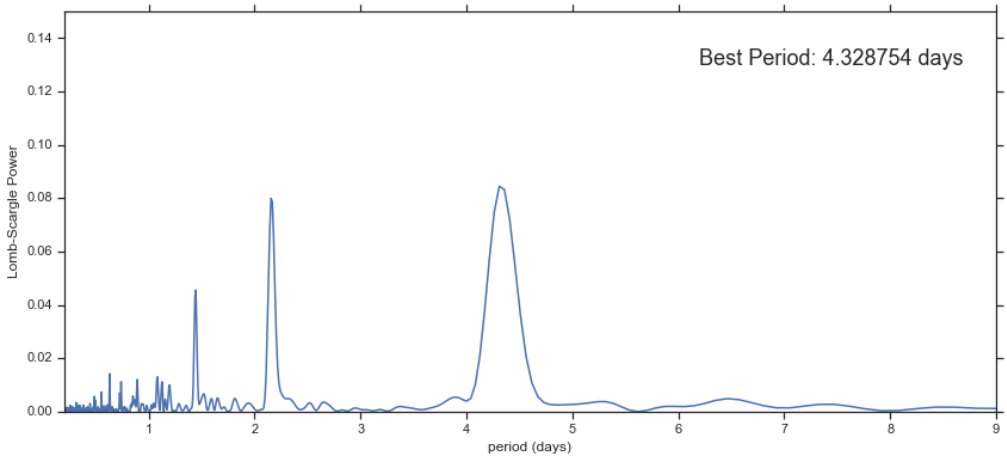


Figure C.4: A Lomb-Scargle Periodogram caclulated with 80 days of K2 data processed with VARCAT (Armstrong et al., 2016)

When these data are then phase-folded on the period, they appear in Figure C.5. This shows the clear differences in depth, shape and duration from eclipse to eclipse, and notably does not show any obvious directional time evolution.

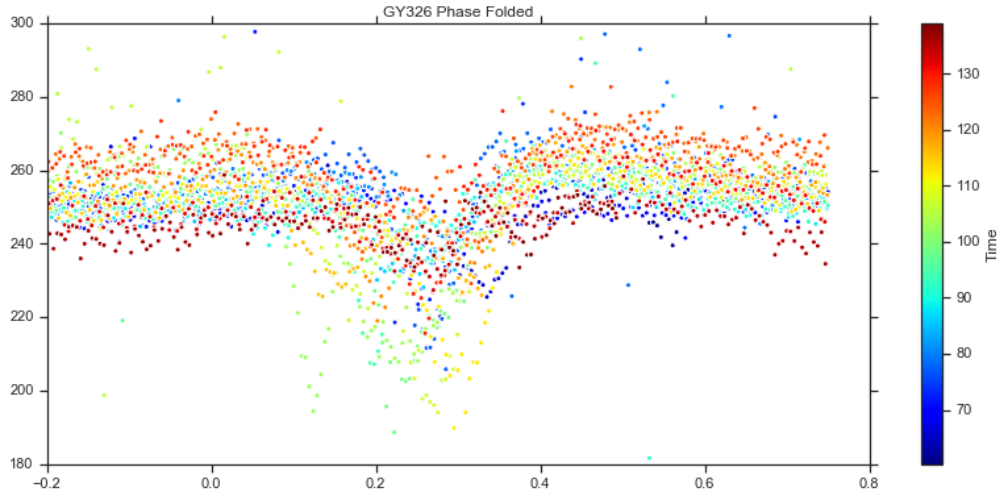


Figure C.5: GY326 phase-folded. The color bar indicates the day of observation. While the eclipse depth and duration vary, there does not appear to be any obvious progression over time.

X-Shooter Spectra: Pipeline and Tellurics

X-Shooter can provide moderate resolution spectra in both visible and near-IR (NIR) which makes it ideal for examining multiple emission lines that would be diagnostic of accretion, magnetic fields, disk dynamics, and chromospheric activity. Observations were requested 1-2 epochs a night for a period spanning at least two periods of eclipses. This resulted in a series of 18 observations in both the visible and NIR, of which 16 are usable, spread over 80 days. These observations were first reduced through the XSHOOTER pipeline using the EsoRex tool and processed separately for each spectrograph arm. This process included bias and flat field correction, wavelength calibration, flux calibration and merging of orders. A typical spectrum can be seen in Figure C.6.

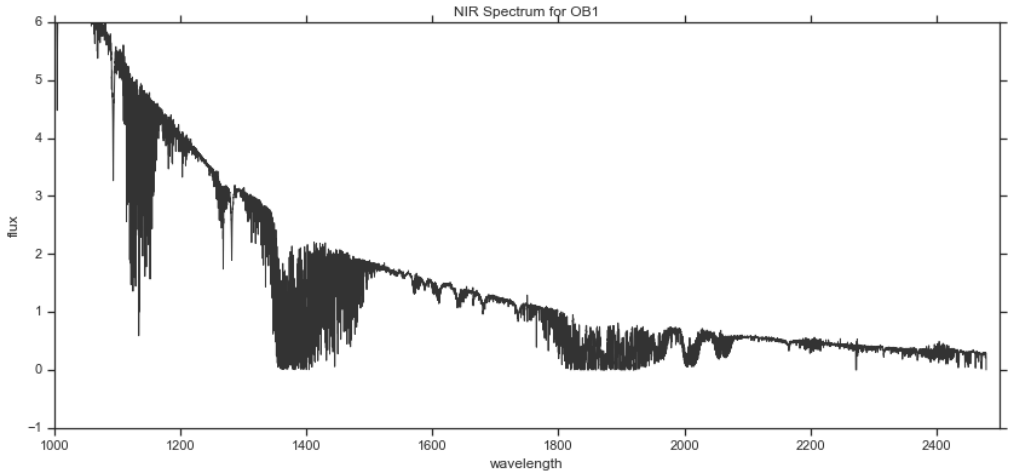


Figure C.6: Observation 1 in the NIR. Three wavelength regions are nearly saturated with telluric molecular absorption (mostly H_2O) and are excluded from correction with molecfit and from subsequent spectral analysis.

Telluric correction was then carried out with molecfit, which uses atmospheric profiles to feed into radiative transfer code, simulating atmospheric emission and transmission spectrum using a molecular spectroscopic database (Smette et al., 2015; Kausch et al., 2015). Molecfit allows the user to set which molecules to include in the radiative transfer code as well as define inclusion and exclusion regions of wavelengths. For the NIR, a nearby telluric standard star was corrected using molecfit and then the results applied to GY326. Only two sets of two observations

(5 & 18 and 14 & 17) used the same telluric standards, and were therefore used as a test of molecfit. Upon inspection, all corrected spectra looked similar to one another and it was not possible to distinguish which corrected observations relied on the same standard star. For the visible spectrum, which contains fewer and less significant telluric features, the correction was done using the GY326 spectrum itself. The correction was successful at all wavelengths, with only three regions in the NIR reaching saturation (1110-1160, 1340-1500, and 1750-1950) which were excluded from molecfit fitting and analysis. Figure C.7shows an example of a molecfit correction applied to GY326.

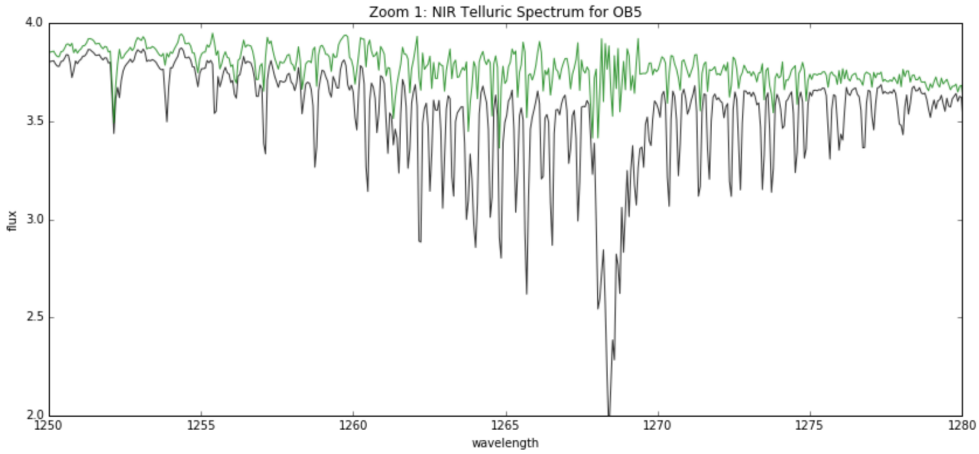


Figure C.7: Close-up of a molecfit correction (shown in green) applied to Observation 5 in the NIR.

Radial Velocity

All spectra were corrected for barycentric velocity offset as reported at the time of observation. Radial velocity variation was then calculated in two ways. In the first, notable absorption features in the shifted spectra were shifted step-wise at gradations of 1/10th a pixel and cross correlated to a PHOENIX model spectrum for an M2 star (Baraffe et al., 2015; Husser et al., 2013). Where the cross correlation function peaked was taken to be the velocity shift for that feature, and for each observation, shifts across ten features in differing parts of the NIR spectrum were averaged to arrive at the final average velocity shift and error (standard error on the velocity mean). The results of this fit are shown in Figure C.8.

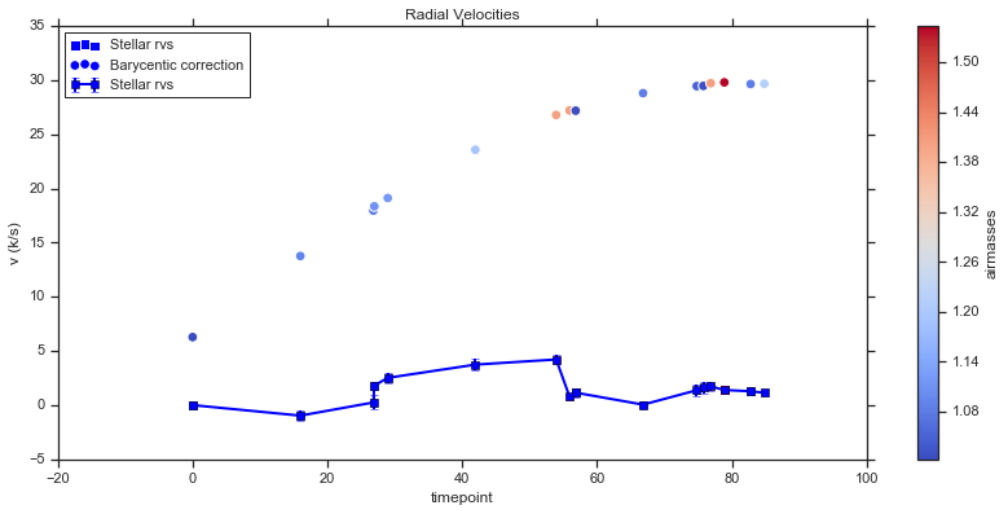


Figure C.8: Barycentric velocities are shown color-coded to air mass. Radial velocities calculated from the line-fitting method are shown below in blue with error bars representing standard error on the velocity mean calculation.

As a check of this first method and as an independent measurement, we used a gaussian process (GP) through the George package to fit 14 regions of molecfit-corrected spectrum, each with a pixel window of 120 pixels (Kreidberg et al., 2014b). The regions were chosen to contain distinct lines, and to be free of strong telluric features or regions of variation (to be defined below). In this way, not only known lines, but all parts of the spectrum can be used to provide more accurate radial velocity measures. Further, there appeared to be a radial velocity offset that was determined to be due to the instrument itself (magnitude of about 5km/s). This was found using the GP method and corrected for in subsequent analysis.

Spectral Lines

We searched for several lines that are known to be markers of accretion, wind, or variability. For the ones that were identifiable, we fit a gaussian to the line to get the velocity of maximum penetration, the full width at half max (FWHM), redward edge, blueward edge, and equivalent width. Several lines were in regions of very low flux, especially in the visible, or were in regions of high telluric absorption, especially in the NIR. These lines were excluded from analysis.

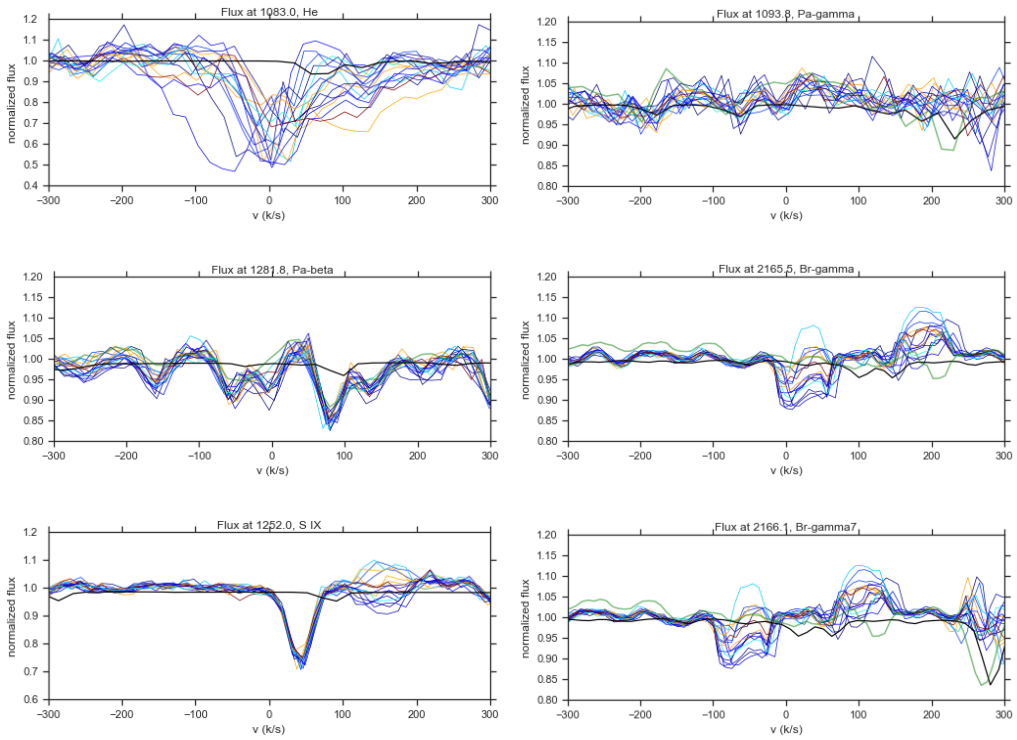


Figure C.9: Lines in the NIR: the above are regions in which common lines would appear. Each observation is shown in a colour corresponding to the air-mass at the time of observations (to show no obvious correlation between line depth and air-mass). Some, such as He and S IX are prominent, while others are seemingly absent. The black line indicates molecfit-calculated absorption. These lines are not near any absorption features. Also visible in the plots are the "variable regions" discussed in section 2.2.5

There was a notable lack of prominent lines of typical markers of accretion. In the visible region of the spectrum, several common lines are notably missing, including H-alpha, Paschen alpha, beta and gamma, Na D and O lines. Several of these, such as H-alpha fall into regions of very low flux for this faint star. In stacking spectra, an H-alpha line is discernible as can be seen in Figure C.10. Other lines such as the Ca triplet, Si IX and He are more pronounced. Prominent lines in the NIR and Visible are shown in Figures C.9 and C.10 respectively. Some lines were not observable because they were in regions of high telluric absorption: Pa-δ 1004.9, Pa-α 1875.1, Si X 1420.0, Si XI 1932.0, and Si VI 1962.0 in the NIR. In the visible, some lines were either in faint parts of the spectrum or were notably absent, such as He-I i 501.6, NaI D 589.0, He-I ii 587.6, He-I iii 667.8, He-I iv 706.5, O-I i 777.3, O-I ii 844.6, O2 A 686.7, and O2 B 759.4.



Figure C.10: Lines in the Visible: the above are regions in which common lines would appear. Because GY326 is so dim in the visible and it is difficult to discern lines in individual observations, spectra are stacked to show the presence of lines.

It is not uncommon for stars in this cluster to have undetectable Pa β or Br γ, and while when NIR hydrogen recombination emission lines are present, they can be a good indicator of accretion (since they are restricted to objects with circumstellar disks), their absence does not indicate a lack of accretion (Natta et al., 2006).

The most prominent and notable line in GY326 is the Helium line HeI 1083.0 (see Figure C.9). These lines appears deep in absorption with a large variance between observations as can be seen in Figure C.11. The helium line is a common marker of stellar winds- its blue-shifted and red-shifted absorption components can only be explained by wind outside the magnetosphere (Calvet & Hartmannet, 2001; Romanova & Harries, 2011).

Gas falling in along accretion streams to a star of mass M_* and radius R_* would have a free-fall speed at a distance r of

$$v_{ff} = \left[\frac{2GM_*}{R_*}\left(\frac{R_*}{r} - \frac{R_*}{R}\right)\right]^{1/2}$$

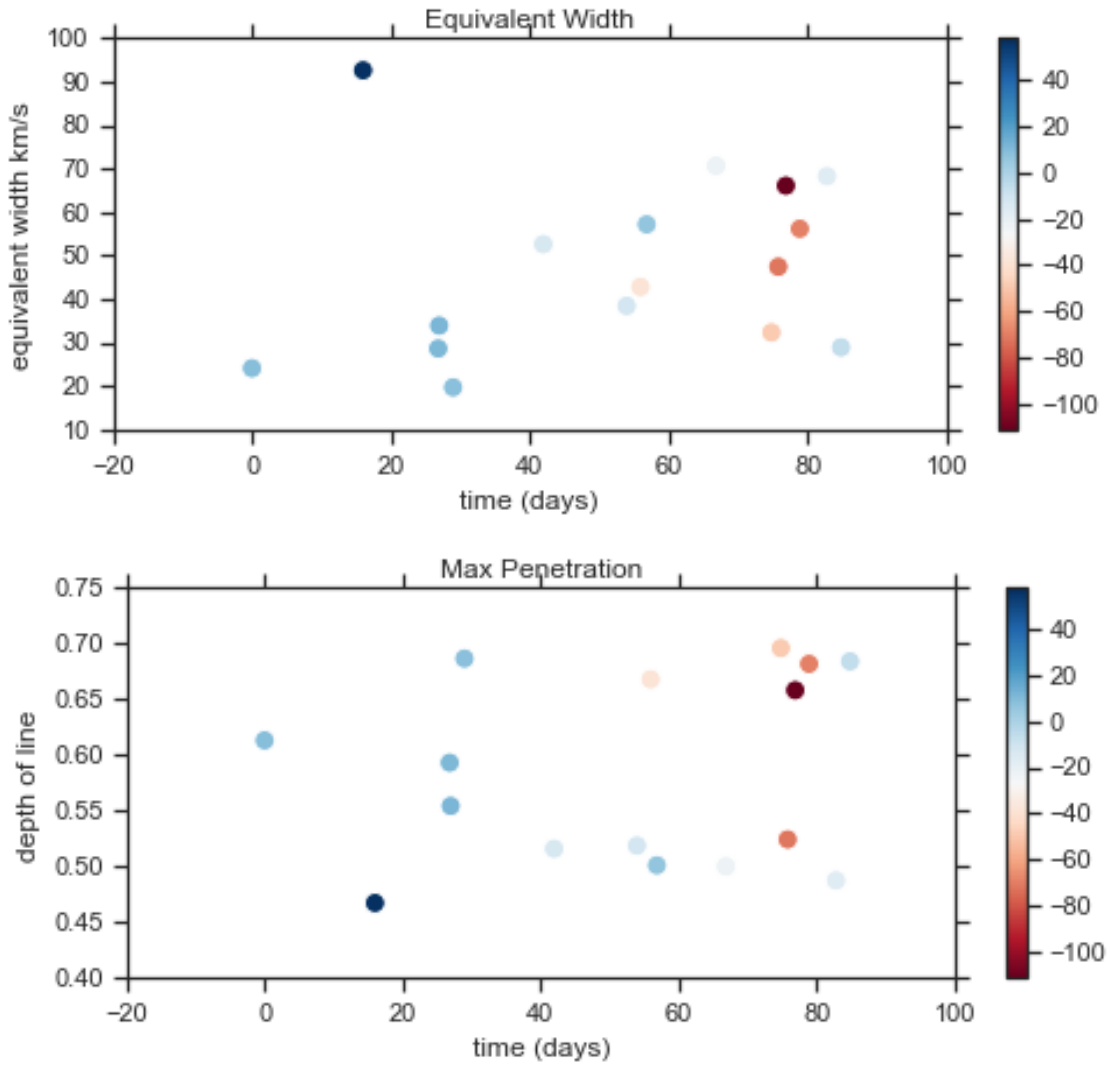


Figure C.11: Helium line diagnostics. The colour-bars indicate the centroid velocity (red shifted or blue shifted). There are a clustering of points around day 78 that appear significantly more red-shifted than the others, and which possibly correspond to a an increased equivalent width

$$V_{esc}\left(\frac{R_*}{r}-\frac{R_*}{R}\right)^{1/2}$$

The largest infall velocity (the most red-shifted part of the absorption line) therefore corresponds to the material right before it impacts the star, and can thus be used to find the radius of origin for the infall (the inner edge of the disk). Most stars have a radius 1.2-4 $R_\star$ (Fischer et al., 2011), and from the redmost velocities in the helium lines of GY326, the average radius of infall is about 3.9 x 10^6 km or 2.6

$R_\star$. This enables us to form a better picture of the possible geometries of the system.

Instrument Artifacts

Notable in these spectra are "regions of variability" (ROV) which are features that appear as emission or absorption differently across different observations. Examples are shown in Figure C.12. These features often contain multiple peaks and have velocity spreads from 50-200 km/s. These features do not correlate to large telluric corrections, as calculated by molecfit, nor do they correspond to lists of known skylines (Oliva et al., 2015).

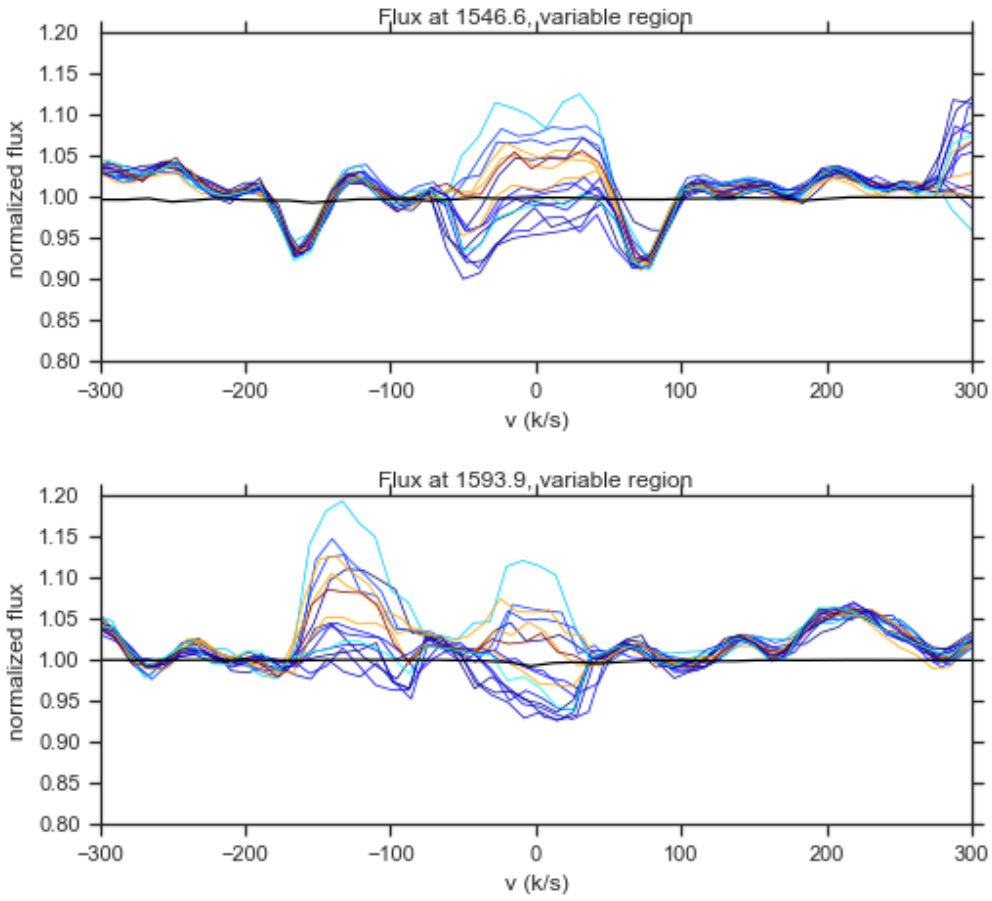


Figure C.12: Variable Regions (expand).

The strongest possibility is that they are artifacts from the instrument; in examining the dark images of these X-Shooter observations, there are small lines that appear in the 2D spectra that could possibly be roughly correlated to the

appearance of the variable regions. However, no report of these sorts of artifacts in X-Shooter has appeared before.

Another possibility is that they correspond to phenomena in the GY326 system itself as GY326 can be expected to have a highly variable spectrum, though further confirmation of this, possibly in other instruments, would be neccesary.

C.1.3 Concluding GY326

Accretion disks are common around young stars less than $3M_{\odot}$. These disks are the birthplace of a system's planets and disk dynamics have a major influence on planetary evolution and formation. Understanding systems like GY326 can give us more insight into these early stellar and planetary processes.

While the spectral evidence from X-Shooter is somewhat inconclusive, it enables us to check for patterns or the notable lack of patterns in line behavior and assess system radial velocities to a medium sensitivity. On the basis of this work, it is quite possible that GY326 has a disk with columns of accreting dust. A lack of significant radial velocity changes and double or triple lines appears to rule out an eclipsing binary or 3-star system, though high-resolution spectroscopy might be able to better detect smaller changes, as might be expected for a forming planetary system. The error bars on our radial velocity measurements are on the order of 1 km/s, beyond which detection of planetary companions is still very possible.

These results point to the likelihood of GY326 being some form of dipper system, though a more slowly accreting one, though they do not rule out the possibility of forming planetesimals. While follow-up spectroscopy and further photometric data for GY326 would help, its dimness makes it a poor target for follow-up observations. However, it is possible that future surveys and more sensitive instruments will cast further light on this elusive system.

C.2 Cloudie: Searching for inhomogeneous cloud cover on hot Jupiters

Introduction

Clouds are highly ubiquitous across planetary bodies both inside and beyond our solar system, and many ongoing investigations attempt to determine the distribution and composition of clouds in exoplanets. Currently, most transmission spectral studies that examine the atmospheres of exoplanets assume temperature, chemical abundances, and cloud composition that are latitudinally and longitudinally homogeneous for computing atmospheric models. Failing to factor in asymmetries in cloud cover can greatly impact the success of these models to accurately predict exoplanet atmospheres (Kreidberg et al., 2014a).

Two main physical mechanisms have been identified to form partial cloud cover: either polar accumulation due to meridianal circulation of cloud particles, occurring in tidally locked planets (Parmentier et al., 2013; Charnay et al., 2015), or morning side accumulation, owing to the large horizontal temperature contrast in hot Jupiters, dominant at equilibrium temperatures of around 1500K (Parmentier et al., 2016). By measuring the cloud coverage, we can place more accurate priors when performing atmospheric retrievals, breaking degeneracies between partial clouds and atmospheric abundances (Line & Parmentier, 2016).

Evidence for such configurations come so far in the form of asymmetric optical phase curves, which have been observed in several exoplanets to date (Muñoz & Isaak, 2015; Demory et al., 2016; Esteves et al., 2013; Webber et al., 2015). However, some of these phase curve asymmetries might be due instead to an asymmetry in scattering properties (von Paris et al., 2016), leaving us with a less reliable way of determining true cloud cover. Calculations by Line & Parmentier (2016), and Powell et al. (2019) predict that these asymmetries could be observed as residuals in transit light curves that are fit to cloudless models, on the order of $\sim$ 100-200 ppm, so long as the transit timing is known to seconds, as can be seen in Figure C.13. To date, a sole study by von Paris et al. (2016) examines the Kepler transits of two such planets (Kepler 7b and HAT-P-7b) by searching for asymmetries in the ingress and egress.

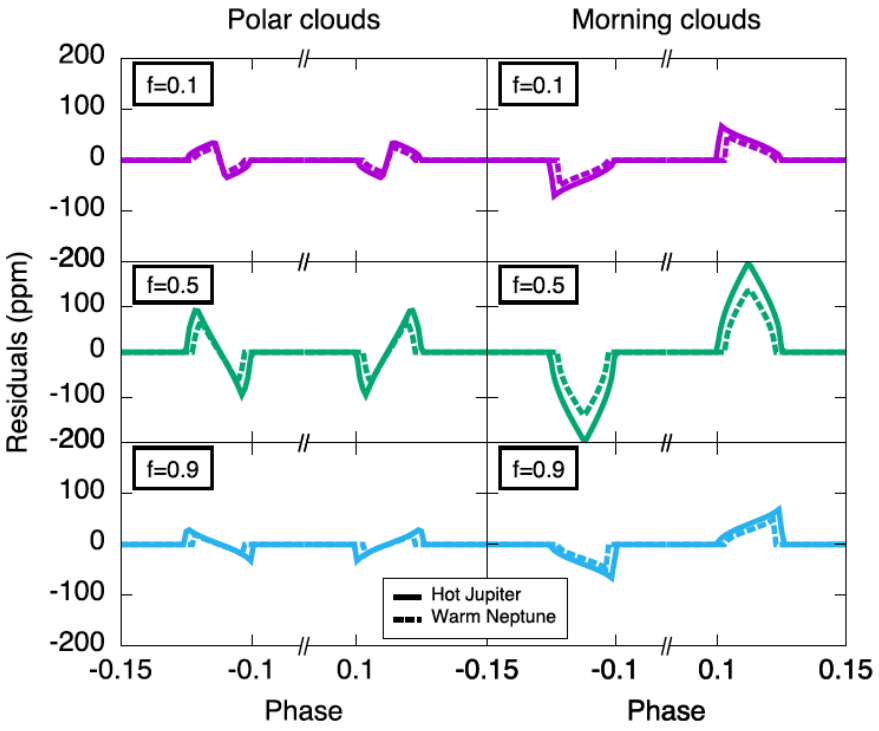


Figure C.13: Transit curves of hot Jupiters and warm Neptunes with inhomogeneous cloud cover will produce residuals when fit to classic models that do not take inhomogeneity into account. This figure from Line & Parmentier (2016), depicts these residuals for the polar and morning side cases at different cloud fractions (f). Even in the optimal case of a cloud fraction of 0.5, good signal to noise is needed to observe a residual at 100-200ppm. Further, as these residuals only occur on the limbs, with a time scale of several minutes, higher cadence (20 sec) observations are better able to probe this effect, as seen in Figures C.21 and C.22.

While they were unable to find conclusive signatures of inhomogeneous clouds from asymmetry alone, their model fitting suggested a better fit to light curves that incorporated inhomogeneous clouds. However, Kepler 7b is not a bright star and HAT-P-7b has a relatively high surface gravity (and therefore low scale height).

An effect of this size might be detectable in large, close in planets that have high signal to noise. HAT-P-11 b is a warm Neptune (5.07 $R_{\oplus}$) with a period of approximately 4.3 days, and is likely to be tidally locked, making it a prime candidate for inhomogeneous morning-side cloud cover Bakos et al. (2010), Huber et al. (2017). As HAT-P-11 is a particularly bright star (V=9.587), observed through 13 Kepler viewing periods, it is an ideal candidate for obtaining the level of precision necessary to detect clouds.

Below, I describe the search for asymmetries in the transit light curve of HAT-P-11 b that would indicate the presence of inhomogeneous clouds and discuss and simulate other targets that would be interesting to explore in search of this effect.

C.2.1 Analysis

Kepler light curves for HAT-P-11 b were obtained from 13 quarters and in the format of short cadence simple aperture photometry (SAP) provided by the Kepler pipeline reduction. HAT-P-11 b is highly active as seen in Figure C.14 and therefore needed to be normalized in order to extract the transits themselves.

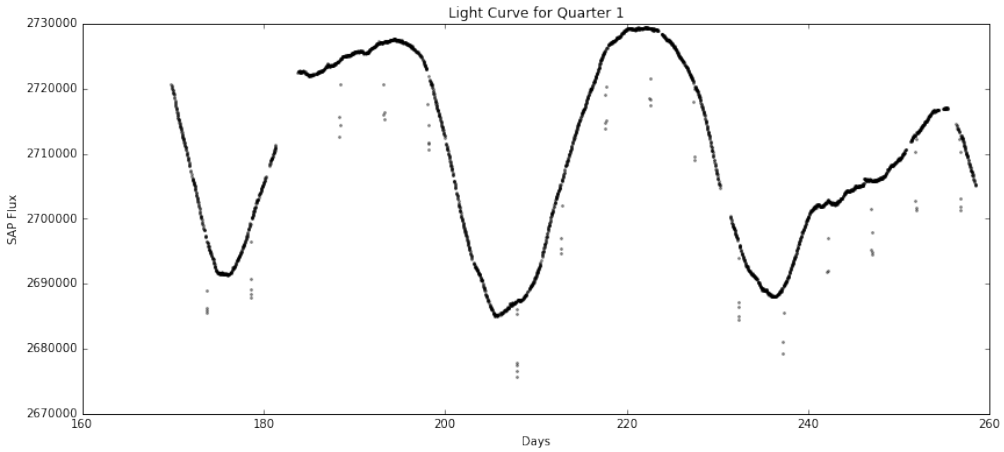


Figure C.14: HAT-P-11 is young and highly variable. Displayed is long cadence data for quarter 1. Eclipses are clearly visible amongst the stellar variability.

We first masked out the planetary transits and used the George package for a Gaussian process with squared exponential kernel to fit each quarter of the light curves Kreidberg et al. (2014b). We further applied a linear correction to each transit using the flux within a 0.03 phase window, while masking the transit, as an additional correction.

Light curve fitting was performed using BATMAN, which was described in previous chapters, as a python package that fits planet transits with radially symmetric stellar limb-darkening Kriedberg (2015). An initial fit using a Chi-square error function, was followed by fitting to arrive at a posterior distribution through MCMC using the python package emcee Foreman-Mackey et al. (2013b). HAT-P-11 has star spots which appear prominently in its transit curves themselves as seen in

Figure C.15. These arise as the planet passes in front of a peri-equatorial starspot and therefore increases the overall flux during the eclipse as shown in Figure number C.16. These present a problem both to fitting, and to looking for traces of clouds in the transits and therefore needed to be removed. While star spots can be removed by hand Sanchis-Ojeda & Winn (2011), we chose to automate this process by first fitting a transit that was free from starspots using a BATMAN light curve. If a data point was an outlier from this "starspot-free estimate" by more than 3.0 sigma, it was excluded, as were the points in the same 0.002 phase window. Upon visual inspection, this appears to conservatively remove all starspots in 208 eclipses. The final phase folded flux diagram is shown in Figure C.15.

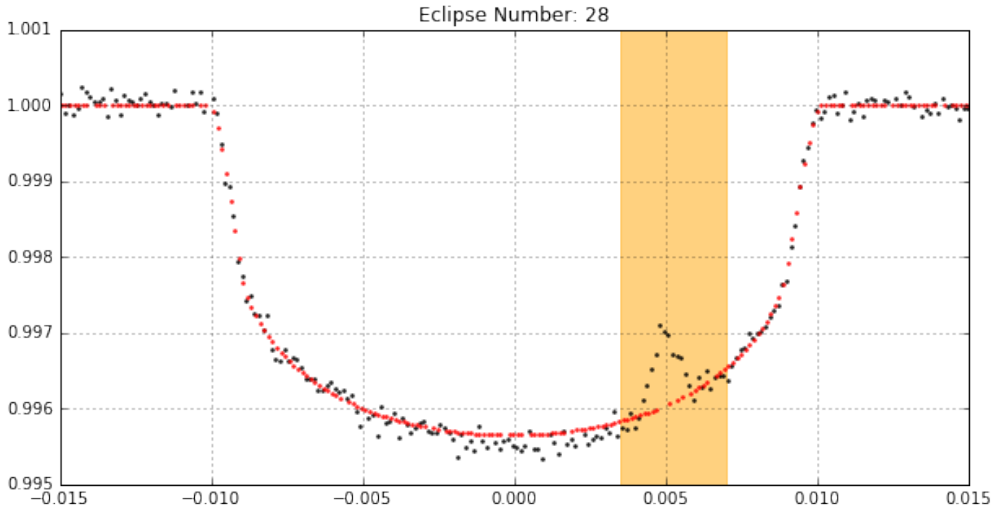


Figure C.15: An eclipse that displays a prominent starspot. Most eclipses display one or more starspots on either side of the midline.

Cloud Residuals

After star spot removal, phase-folded transits were then fit to a BATMAN light curve to arrive at an average curve for the system. Values for these initial guesses as well as results of the fit are shown in Table C.2.

We then subtracted the best-fit light curve to examine the residuals. The residuals were binned into 150 bins across a phase spread of +/- 0.04. Taking the bin median and standard error results in the binned residuals shown in Figure C.17.

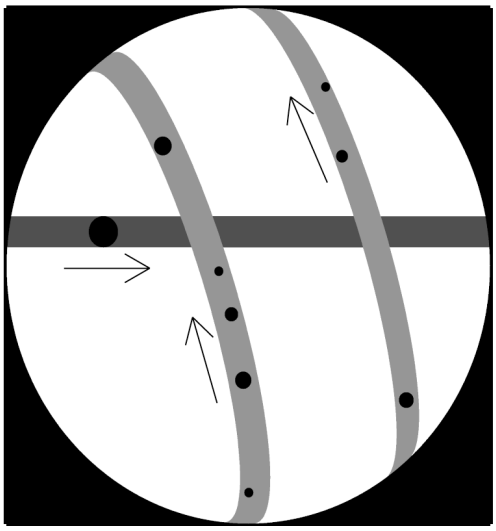


Figure C.16: The planetary alignment necessary to produce the starspot pattern seen in HAT-P-11 b shown in Figure 6 of Sanchis-Ojeda 2011, in which the planet crosses at a very high inclination, passing two equatorial bands of rotating starspots.
Sanchis-Ojeda & Winn (2011)

Parameter	Initial Value	Least Squares	MCMC
T_0	124.812464	124.813199	$124.81318720^{+0.00000996}_{-0.00000953}$
Period (days)	4.8878049	4.88780244	$4.88780250^{+0.00000004}_{-0.00000004}$
R_p/R_*	0.05862	0.0588053	$0.05880092^{+0.00004403}_{-0.00004593}$
b	0.132	0.20168	$0.21599086^{+0.01781215}_{-0.01727969}$
a/R_*	15.6	14.7929045	$13.76327715^{+0.44259263}_{-0.53357303}$
$u1$	0.599	0.629861	$0.62932426^{+0.00305956}_{-0.00305366}$
$u2$	0.073	0.0656307	$0.06628997^{+0.00598942}_{-0.00601836}$

Table C.2: The initial input parameters as reported by Sanchis-Ojeda, 2011 Sanchis-Ojeda & Winn (2011) along with results of the least-squares fit and the MCMC with 2 sigma uncertainties. The parameters are: planet-to-star radius, R_p/R_*; Impact parameter, b; scaled semimajor axis, a/R_*; Linear limb-darkening coefficient, $u1$, and quadratic limb-darkening coefficient, $u2$

Another obvious test for asymmetry in cloud cover is to fold the phase curve over itself (ingress over egress) and look for asymmetric residuals. Figure C.18, shows a small but possible asymmetry in the ingress and egress.

While this early work with HAT-P-11 hints at a possible effect of cloud coverage, the results are not yet conclusive and a few seconds of transit timing error (error in T_0) can largely negate the effect of clouds, reducing residuals by nearly an order of magnitude Line & Parmentier (2016). In order to test this effect and determine

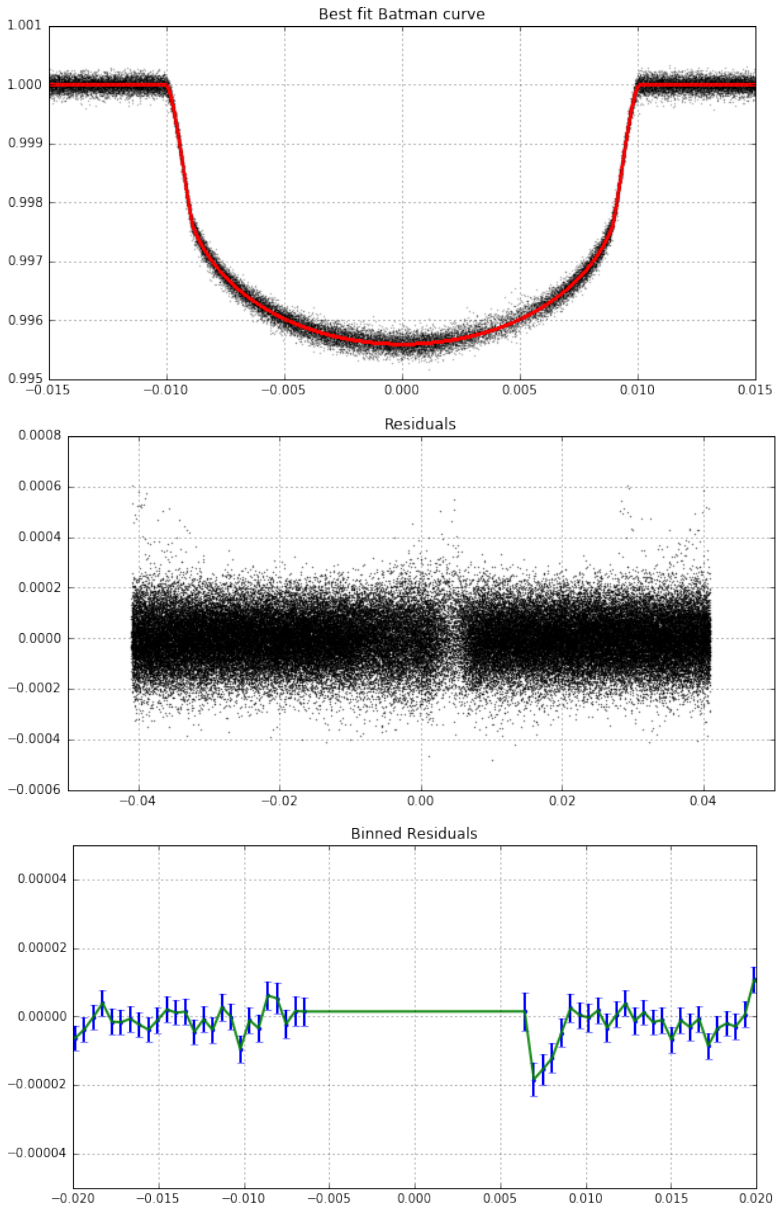


Figure C.17: The top panel shows the best-fit BATMAN curve in red after starspots were removed. The middle panel shows residuals after the best-fit BATMAN curve is subtracted. There are no obvious traces of excess or asymmetric residuals in this image. The visibly sparse patches indicate the removal of starspots in these regions. The bottom panel shows the median of binned residuals. The middle region is removed for clarity of showing the ingress and egress, which is where we would expect to see cloud signatures as a positive or negative excess. Due to data-point losses though starspot removals, this middle area is noisier.

whether the effects of inhomogeneous clouds would still be detectable if T_0 is allowed to vary, we adapted the BATMAN transit curve to model varying fractions of inhomogeneous morning cloud cover. As described in equations 11-15 of Line &

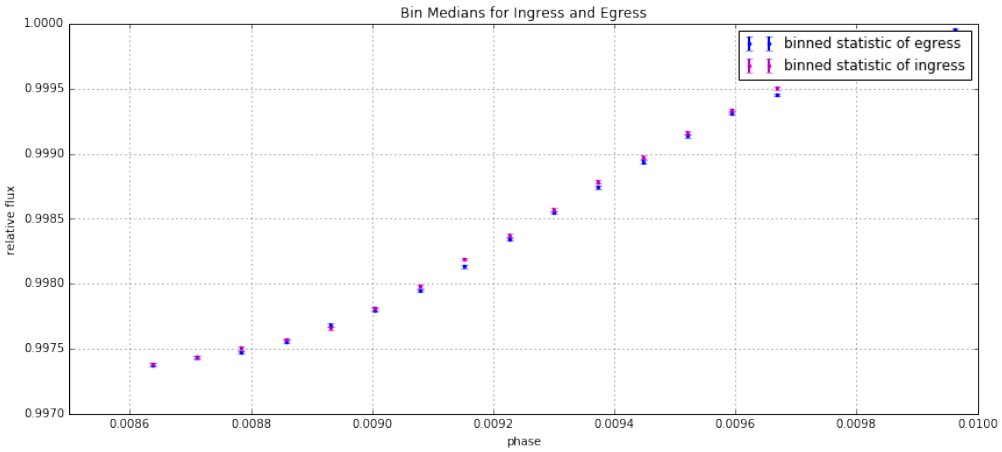


Figure C.18: Showing binned statistics Small error bars show a small but pronounced asymmetry between the shapes of the ingress and egress limbs of the transit.

Parmentier (2016), a cloud layer can be modeled combining the transit curve of a planet with a clear atmosphere and that of a planet with a cloudy atmosphere. For a HAT-P-11 b-like planet, an idealised curve with 50% morning cloud cover would appear like it does in Figure C.19, quite similar to the that of Figure C.13.

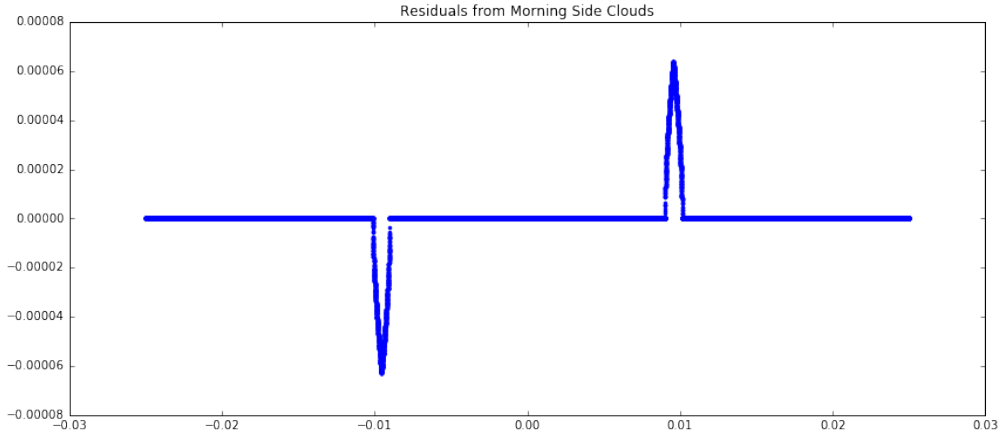


Figure C.19: Residuals expected from inhomogeneous cloud transit curve subtracted from a symmetric model.

At this point, we chose to expand our modelling to include two other planets, chosen for their temperatures, large scale heights, and observability in TESS. First, WASP-62, is an F type star with temperature of 6230K and a TESS magnitude of 9.7109. WASP-62b has a radius of 1.32 $R_{\rm Jup}$, a mass of about 0.5 $M_{\rm Jup}$, which gives it an ideally low surface gravity (Hellier et al., 2012). Combined with a calculated

equilibrium temperature of 1475K, it is likely to have a large scale height. Further its period of about 4.4 days and its location in the TESS continuous viewing zone would allow for many transits and a relatively large amount of data to be collected.

Next, WASP-126, is a G type star with temperature of 5800K and TESS magnitude of 10.6103. With 0.96 $R_{\rm Jup}$, 0.28 $M_{\rm Jup}$, and a calculated equilibrium temperature of 1480K, WASP-126b is also likely to have a large scale height (Maxted et al., 2016). With a period of 3.29 days and its location in the TESS continuous viewing zone it is another excellent candidate for achieving the data collection necessary to observe the subtle effect of inhomogeneous clouds.

We then modeled the expected transits which will be observed for each of these three systems, taking into account previously reported values of planetary parameters as well as TESS noise at 20s cadence, with an injection of expected inhomogeneous cloud cover. Similar to HAT-P-11, for WASP 62b and WASP 126b, we can see visible residuals in transit curves that are fit to models of inhomogeneous clouds (Figure C.21) that are likewise similar in appearance to the predicted residuals in Figure C.13. We then simulated data to attempt to recover all initial parameters, modelling a HAT-P-11 b-like planet with inhomogeneous cloud cover, seen in Figure C.20, and adding the same level of noise as is present in its Kepler data.

Modeled data was successfully fit with an MCMC to retrieve close approximations to input values, as can be seen in Figure C.22. However, the walkers tend to settle into several local likelihood maxima, and while the posterior distribution is not too far off, and reflects input parameters across most planetary parameters, it does not yet sufficiently constrain cloud fraction.

C.2.2 Continuing Work

The next steps of this work would be to obtain observations of these and other targets and to develop further tools to assess such cloud cover. For example, instead of MCMC fitting, cross correlation could be performed on simulated light curves to assess whether a template of symmetric verses asymmetric cloud cover might produce a significantly offset peak. Searches could also be performed in publicly

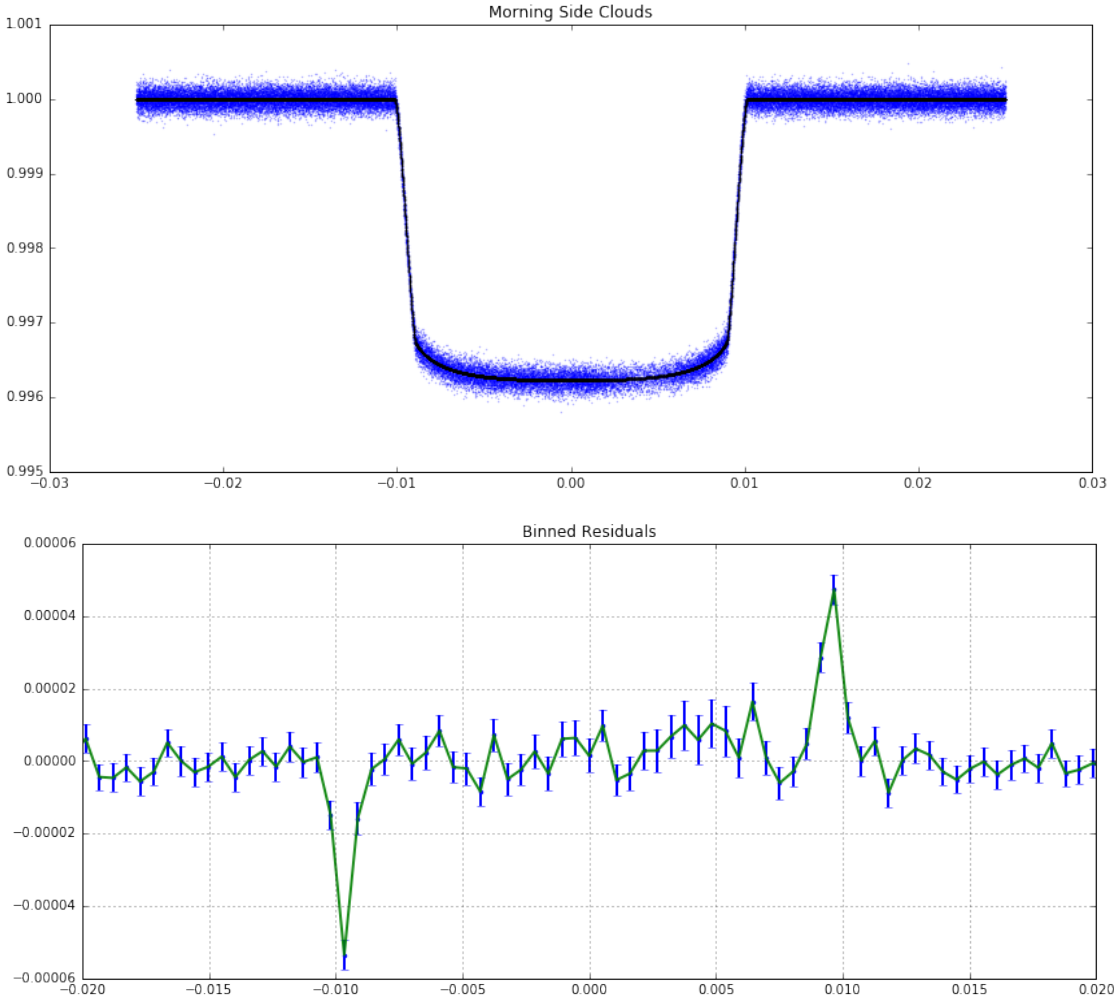


Figure C.20: The left shows simulated data of a HAT-P-11 b-like planet (though notably less limb darkening). The right part of the figure shows expected binned residuals if the data are fit with a model that does not take into account the inhomogeneous clouds.

available light curves, which were not available at the time this work was commenced. One possibility is the detection of inhomogeneous cloud cover without the ability to constrain a specific cloud fraction. This would still provide valuable insight into cloud and climate patterns on these alien worlds.

In conclusion, future high cadence TESS data from these bright targets might enable us to uncover the geometry of cloud cover for these objects specifically, or will at least enable us to place constraints on their scale heights and cloud geometry. This information would factor heavily into future atmospheric characterisation of these targets, as well as provide proof of concept for further studies on inhomogeneous

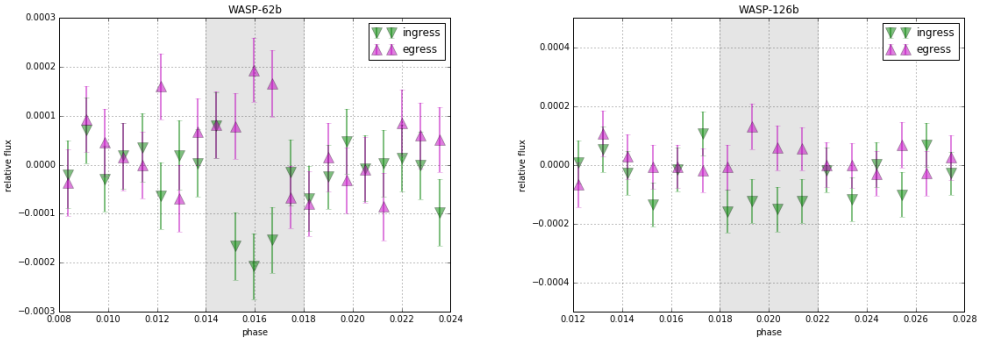


Figure C.21: Binned residuals after simulated data with homogeneous clouds are subtracted from cloud-free transit curves with ingress folded over egress. The shaded areas show the limbs, with pronounced differences between the two.

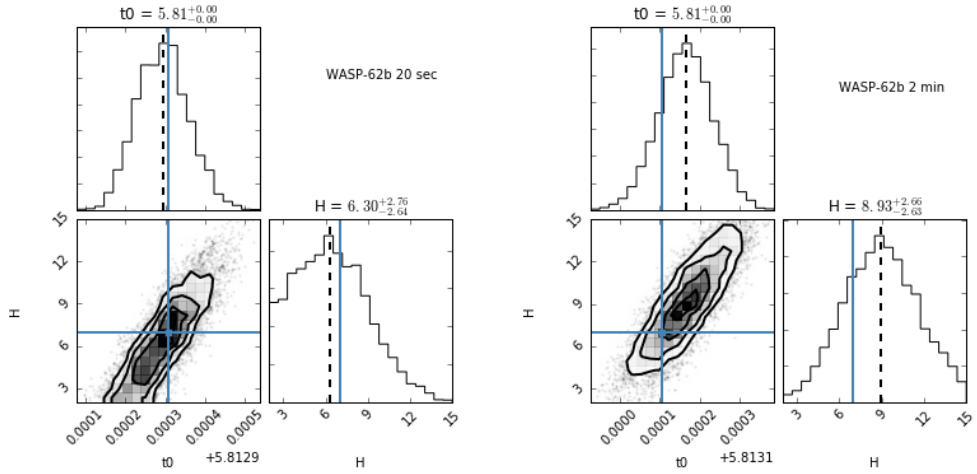
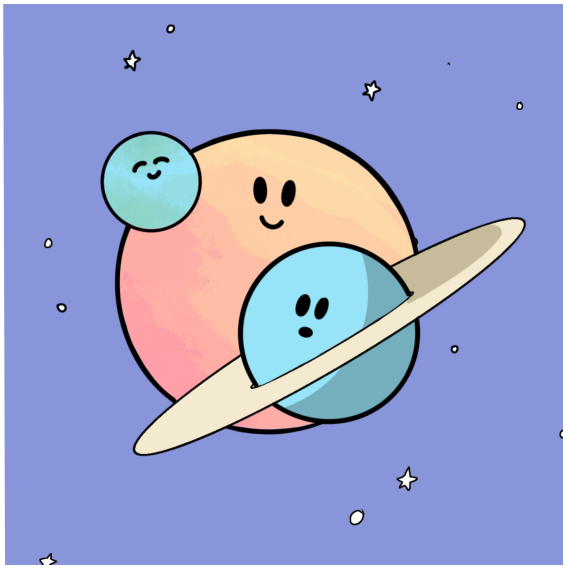


Figure C.22: MCMC results show a pronounced benefit in accuracy at constraining cloud parameters using 20s cadence data. Shown is the scale height (H) relation to T_0, with true values shown in blue.

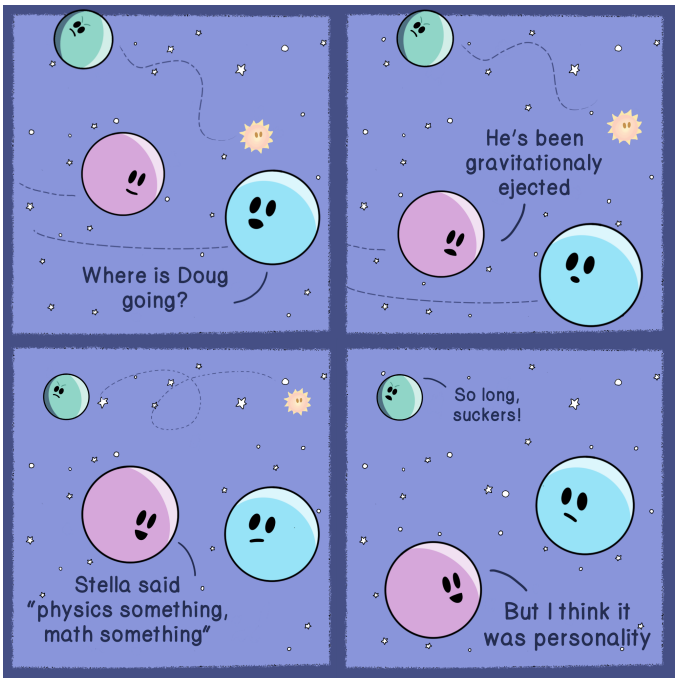
cloud cover. This methodology would enable us and other investigators to make predictions for future high signal to noise projects such as the James Webb Space Telescope.

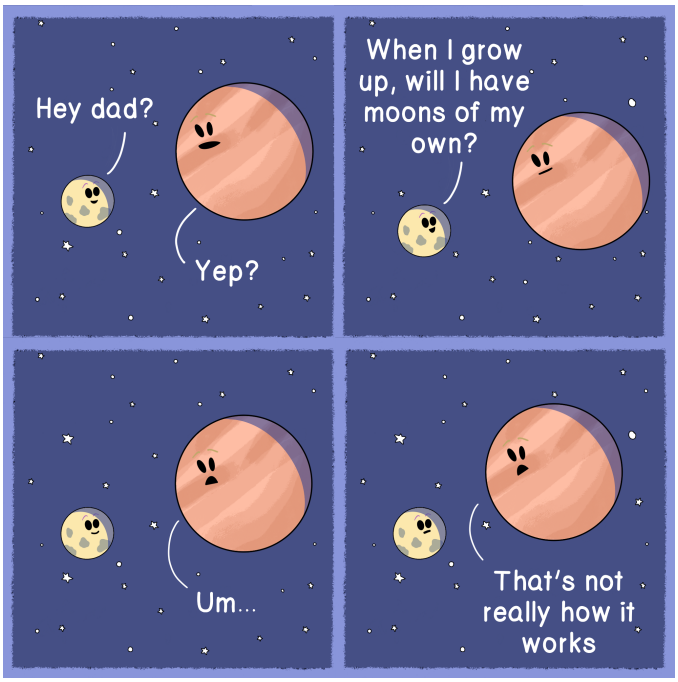
APPENDIX D

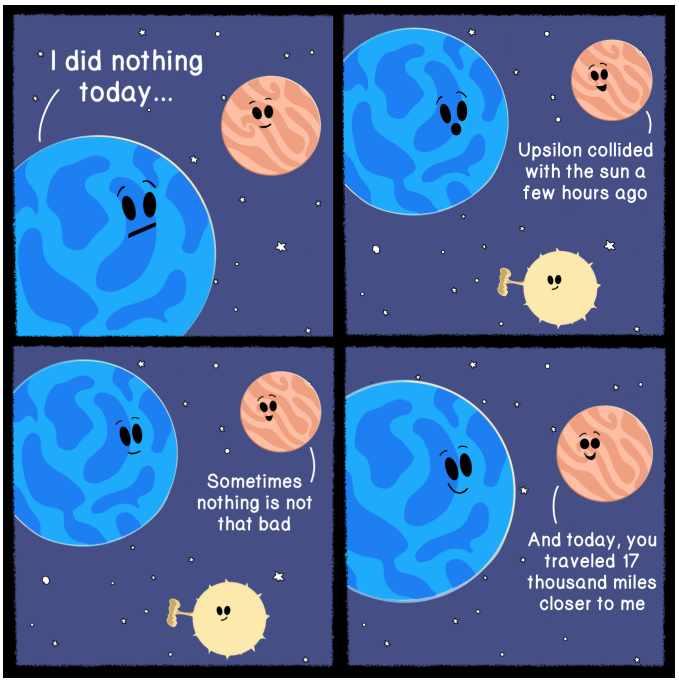
Meet the Planets

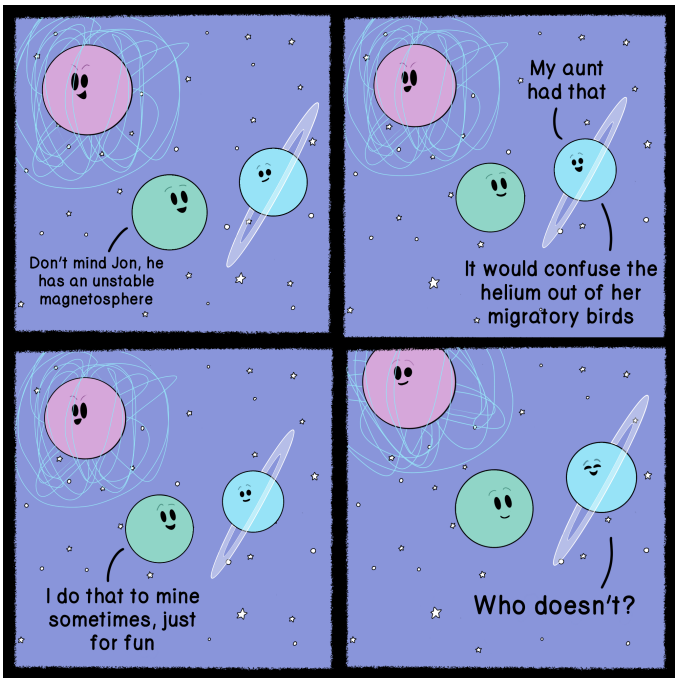


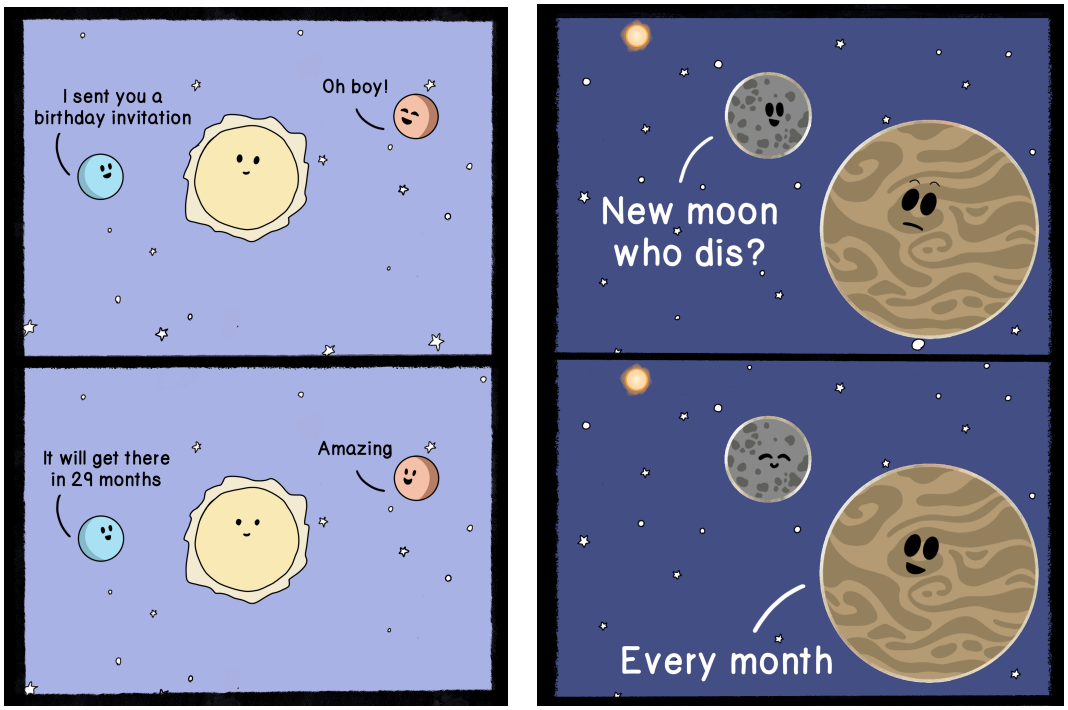
A short visit with our favourite floating family

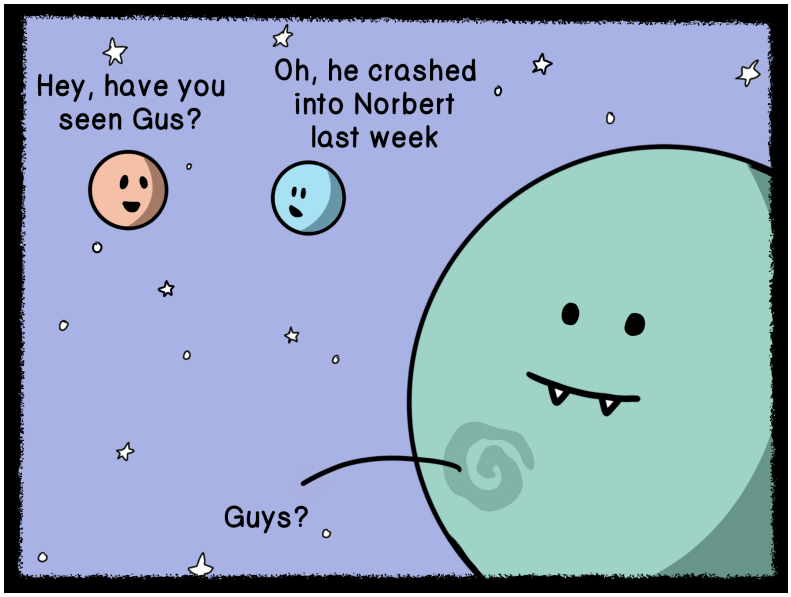

Where is Doug going?
He's been gravitationaly ejected
Stella said "physics something, math something"
So long, suckers!
But I think it was personality

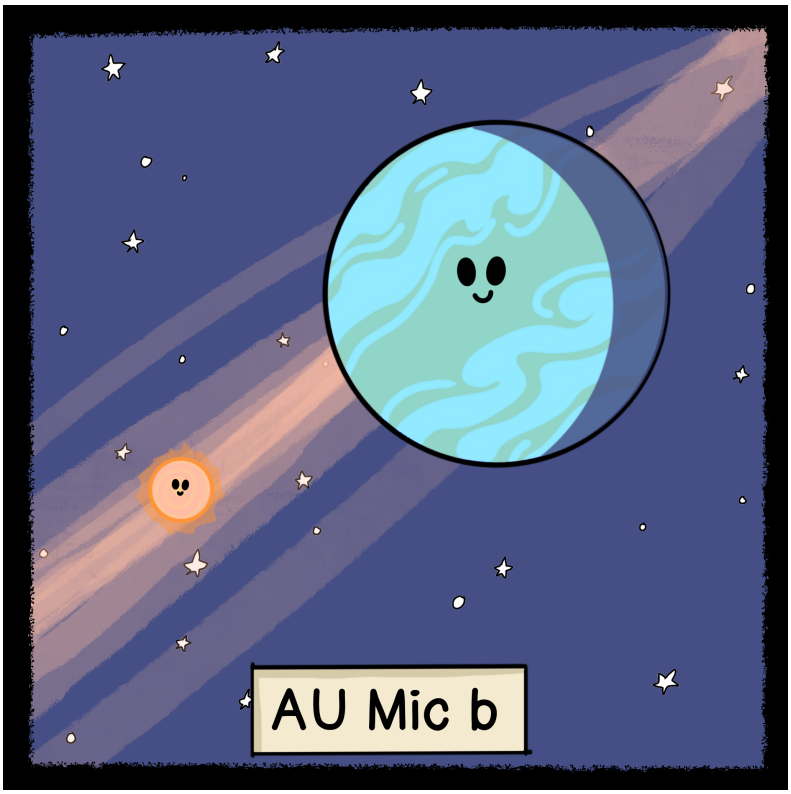

Hey dad?
Yep?
When I grow up, will I have moons of my own?
Um...
That's not really how it works

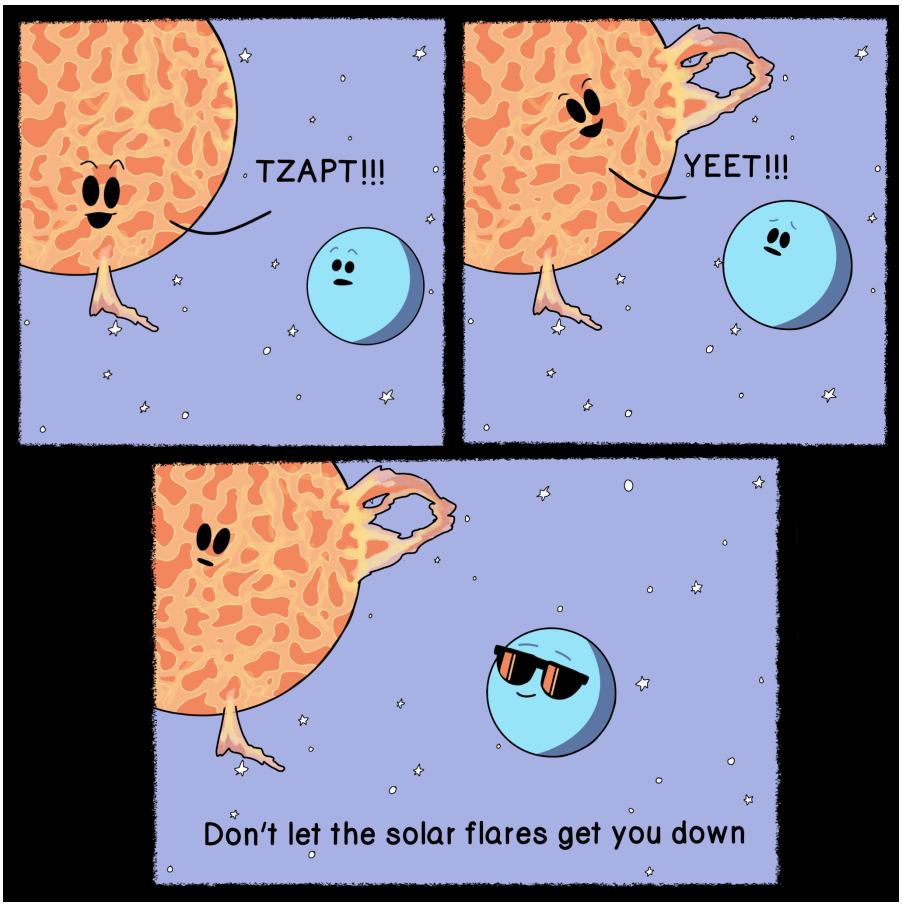

I did nothing today...
Upsilon collided with the sun a few hours ago
Sometimes nothing is not that bad
And today, you traveled 17 thousand miles closer to me


Don't mind Jon, he has an unstable magnetosphere
My aunt had that
It would confuse the helium out of her migratory birds
I do that to mine sometimes, just for fun
Who doesn't?


I sent you a birthday invitation
Oh boy!
It will get there in 29 months
Amazing
New moon who dis?
Every month


Hey, have you seen Gus?
Oh, he crashed into Norbert last week
Guys?


AU Mic b


TZAPT!!!
YEET!!!
Don't let the solar flares get you down

Bibliography

Abe L., et al., 2013, A&A, 553, A49

Agol E., Deck K., 2016, ApJ, 818, 177

Agol E., Fabrycky D. C., 2018, Transit-Timing and Duration Variations for the Discovery and Characterization of Exoplanets. p. 7, doi:10.1007/978-3-319-55333-7_7

Agol E., Steffen J., Sari R., Clarkson W., 2005, MNRAS, 359, 567

Agol E., et al., 2020, arXiv e-prints, p. arXiv:2010.01074

Agol E., et al., 2021, , 2, 1

Aguirre V. S., et al., 2015, MNRAS, 452, 2127

Aigrain S., Irwin M., 2004, MNRAS, 350, 331

Aigrain S., Parviainen H., Pope B. J. S., 2016a, MNRAS, p. stw706

Aigrain S., Parviainen H., Pope B. J. S., 2016b, MNRAS, p. stw706

Akana Murphy J. M., et al., 2021, AJ, 162, 294

Akeson R. L., et al., 2013, PASP, 125, 989

Alencar S., 2010, A&A, 000, 000

Almenara J. M., Dí az R. F., Mardling R., Barros S. C. C., Damiani C., Bruno G., Bonfils X., Deleuil M., 2015, MNRAS, 453, 2645

Alonso-Floriano F. J., et al., 2019, A&A, 629, A110

Alonso R., Aigrain S., Pont F., and T. M., 2008, Proceedings of the International Astronomical Union, 4, 91

Ambikasaran S., Foreman-Mackey D., Greengard L., Hogg D. W., O'Neil M., 2014

Applegate J. H., 1992, ApJ, 385, 621

Armstrong D. J., et al., 2015, A&A, 582, A33

Armstrong D., Kirk J., Lam K. W. F., McCormac J., 2016, MNRAS, 456, 2260

Bakos G., Noyes R. W., Kovács G., Stanek K. Z., Sasselov D. D., Domsa I., 2004, PASP, 116, 266

Bakos G. Á., et al., 2010, ApJ, 710, 1724

Ballard S., et al., 2011, ApJ, 743, 200

Baraffe I., Chabrier G., Barman T., 2008, A&A, 482, 315

Baraffe I., Homeier D., Allard F., Chabrier G., 2015, A&A

Barbary K., 2016, Journal of Open Source Software, 1, 58

Barnes J. W., Linscott E., Shporer A., 2011, APJS, 197, 10

Barnes J. W., van Eyken J. C., Jackson B. K., Ciardi D. R., Fortney J. J., 2013, ApJ, 774, 53

Barragán O., et al., 2019, MNRAS, 490, 698

Basri G., et al., 2011, AJ, 141, 20

Batalha N. E., et al., 2017, PASP, 129, 064501

Batalha N. E., Lewis N. K., Line M. R., Valenti J., Stevenson K., 2018, ApJL, 856, L34

Batalha N. E., Lewis T., Fortney J. J., Batalha N. M., Kempton E., Lewis N. K., Line M. R., 2019, ApJL, 885, L25

Battley M. P., Kunimoto M., Armstrong D. J., Pollacco D., 2021, MNRAS, 503, 4092

Bean J. L., Raymond S. N., Owen J. E., 2021, Journal of Geophysical Research: Planets, 126

Beck J. G., 2000, , 191, 47

Becker J. C., Vanderburg A., Adams F. C., Rappaport S. A., Schwengeler H. M., 2015, ApJL, 812, L18

Berger T. A., Huber D., Gaidos E., van Saders J. L., 2018, ApJ, 866, 99

Bertin E., Arnouts S., 1996, A&AS, 117, 393

Birkby J. L., et al., 2014, MNRAS, 440, 1470

Bodman E. H. L., et al., 2017, MNRAS, 470, 202

Boley A. C., Laerhoven C. V., Contreras A. P. G., 2020, AJ, 159, 207

Bolmont E., Raymond S. N., Leconte J., Hersant F., Correia A. C. M., 2015, A&A, 583, A116

Bolmont E., Demory B.-O., Blanco-Cuaresma S., Agol E., Grimm S. L., Auclair-Desrotour P., Selsis F., Leleu A., 2020, A&A, 635, A117

Bond I. A., et al., 2001, MNRAS, 327, 868

Bond I. A., et al., 2004, ApJ, 606, L155

Bonomo A. S., et al., 2017, A&A, 602, A107

Borkovits, T. Érdi, B. Forgács-Dajka, E. Kovács, T. 2003, A&A, 398, 1091

Borsato L., Marzari F., Nascimbeni V., Piotto G., Granata V., Bedin L. R., Malavolta L., 2014, A&A, 571, A38

Borsato L., et al., 2019, MNRAS, 484, 3233–3243

Borucki W. J., et al., 2010, Science, 327, 977

Borucki W. J., et al., 2013, Science, 340, 587

Bouvier J., Alencar S. H. P., Harries T. J., Johns-Krull C. M., Romanova M. M., 2006

Brahm R., et al., 2018, MNRAS, 477, 2572

Brakensiek J., Ragozzine D., 2016, ApJ, 821, 47

Brogi M., Line M. R., 2019, AJ, 157, 114

Brown T. M., 2001, ApJ, 553, 1006

Brown T. M., Gilliland R. L., 1994, ARA&A, 32, 37

Brown T. M., Latham D. W., Everett M. E., Esquerdo G. A., 2011, AJ, 142, 112

Brown T. M., et al., 2013, PASP, 125, 1031

Bryant E. M., et al., 2020, MNRAS, 494, 5872

Buchhave L. A., et al., 2012, Nature, 486, 375

Böker T., et al., 2023, PASP, 135, 038001

Cale B. L., et al., 2021, AJ, 162, 295

Calvet J. M. N., Hartmannet L., 2001, ApJ, 550, 944

Carter J. A., et al., 2012, Science, 337, 556

Cassan A., et al., 2012, Nature, 481, 167

Castro González A., et al., 2020, MNRAS, 499, 5416

Castro-González A., et al., 2022, MNRAS, 509, 1075

Charbonneau D., Brown T. M., Latham D. W., Mayor M., 2000, ApJL, 529, L45

Charbonneau D., et al., 2005, ApJ, 626, 523

Charnay B., Meadows V., Leconte J., 2015, ApJ, 813, 15

Chatterjee S., Ford E. B., Matsumura S., Rasio F. A., 2008, ApJ, 686, 580

Chontos A., et al., 2019, AJ, 157, 192

Christ C. N., Montet B. T., Fabrycky D. C., 2019, AJ, 157, 235

Christensen-Dalsgaard J., et al., 2010, ApJL, 713, L164

Cincotta P. M., Simó C., 2000, A&AS, 147, 205

Claret A., 2000, A&A, 363, 1081

Claret A., Bloemen S., 2011, A&A, 529, A75

Cleveland W. S., 1979, Journal of the American Statistical Association, 74, 829

Cochran W. D., Hatzes A. P., Butler R. P., Marcy G. W., 1997, ApJ, 483, 457

Cochran W. D., et al., 2011, The Astrophysical Journal Supplement Series, 197, 7

Cody A. M., Hillenbrand L. A., 2018, AJ, 156, 71

Cody A. M., et al., 2014, AJ, 147, 82

Collins K. A., Kielkopf J. F., Stassun K. G., Hessman F. V., 2017, AJ, 153, 77

Cranmer M., Tamayo D., Rein H., Battaglia P., Hadden S., Armitage P. J., Ho S., Spergel D. N., 2021, arXiv e-prints, p. arXiv:2101.04117

Crossfield I. J. M., et al., 2016, APJS, 226, 7

Crossfield I., et al., 2018, Spitzer Transits of New TESS Planets, Spitzer Proposal

David T. J., et al., 2018, AJ, 156, 302

Dawson R. I., et al., 2014, ApJ, 791, 89

Dawson R. I., et al., 2019, AJ, 158, 65

Deck K., Agol E., 2014, ApJ

Deck K. M., Agol E., 2016, ApJ, 821, 96

Deck K. M., Agol E., Holman M. J., Nesvorný D., 2014a, ApJ, 787, 132

Deck K. M., Agol E., Holman M. J., Nesvorný D., 2014b, ApJ, 787, 132

Deming D., Seager S., Richardson L. J., Harrington J., 2005, Nature, 434, 740

Deming D., et al., 2015, ApJ, 805, 132

Demory B.-O., et al., 2013, ApJL, 776, L25

Demory B.-O., et al., 2016, Nature, 532, 207

Demory B. O., et al., 2020, A&A, 642, A49

Désert J.-M., et al., 2011, APJS, 197, 14

Doyle L. R., et al., 2011, Science, 333, 1602

Dreizler S., Ofir A., 2014, Kepler-9 revisited 60more data (arXiv:1403.1372)

Duck A., Harada C. K., Harrell J., Morris R. R. A., Williams E., Crossfield I., Werner M., Deming D., 2021, AJ, 162, 136

Eastman J., Gaudi B. S., Agol E., 2013, PASP, 125, 83

Eastman J. D., et al., 2019, EXOFASTv2: A public, generalized, publication-quality exoplanet modeling code (arXiv:1907.09480)

Eisner N. L., et al., 2020, MNRAS, 501, 4669

Eisner N. L., et al., 2021, MNRAS, 505, 1827

Esteves L. J., Mooij E. J. W. D., Jayawardhana R., 2013, ApJ, 772, 51

Fabrycky D. C., et al., 2014, ApJ, 790, 146

Fazio G. G., et al., 2004, APJS, 154, 10

Fischer D. A., et al., 2011, MNRAS, 419, 2900

Fischer D. A., et al., 2016, PASP, 128, 066001

Ford E. B., Rasio F. A., 2008, ApJ, 686, 621

Foreman-Mackey D., Hogg D. W., Lang D., Goodman J., 2013a, PASP, 125, 306

Foreman-Mackey D., Hogg D. W., Lang D., Goodman J., 2013b, PASP, 125, 306

Foreman-Mackey D., Agol E., Ambikasaran S., Angus R., 2017, AJ, 154, 220

Foreman-Mackey D., et al., 2019, The Journal of Open Source Software, 4, 1864

Fouesneau M., et al., 2023, A&A, 674, A28

Freudenthal J., et al., 2018, A&A, 618, A41

Fulton B. J., et al., 2017, AJ, 154, 109

Gaia Collaboration et al., 2016a, A&A, 595, A1

Gaia Collaboration et al., 2016b, A&A, 595, A2

Gaia Collaboration Brown A. G. A., Vallenari A., Prusti T., de Bruijne J. H. J., Babusiaux C., Bailer-Jones C. A. L., 2018, preprint, (arXiv:1804.09365)

Gaia Collaboration et al., 2023, A&A, 674, A1

Garai Z., Pribulla T., Komžík R., Kundra E., Hambálek , Szabó G. M., 2019, MNRAS

García R. A., Ballot J., 2019, Living Reviews in Solar Physics, 16, 4

Gardner J. P., et al., 2006, Space Science Reviews, 123, 485

Gilbert G. J., Fabrycky D. C., 2020, AJ, 159, 281

Gilbert E. A., et al., 2022, AJ, 163, 147

Giles H. A. C., et al., 2018, MNRAS, 475, 1809

Gilliland R. L., et al., 2010, PASP, 122, 131

Gillon M., Jehin E., Fumel A., Magain P., Queloz D., 2013, in European Physical Journal Web of Conferences. p. 03001, doi:10.1051/epjconf/20134703001

Gillon M., et al., 2017, Nature, 542, 456

Giménez A., 2006, A&A, 450, 1231

Ginzburg S., Schlichting H. E., Sari R., 2018, MNRAS, 476, 759

Glindemann A., 2011, Principles of Stellar Interferometry, doi:10.1007/978-3-642-15028-9.

Goldberg M., Hadden S., Payne M. J., Holman M. J., 2019, AJ, 157, 142

Gould A., et al., 2006, ApJ, 644, L37

Griest K., Safizadeh N., 1998, ApJ, 500, 37

Griffith C. A., 2014, Philosophical Transactions of the Royal Society of London Series A, 372, 20130086

Grimm, Simon L. et al., 2018, A&A, 613, A68

Grunblatt S. K., et al., 2017, AJ, 154, 254

Guillot T., Burrows A., Hubbard W. B., Lunine J. I., Saumon D., 1996, ApJL, 459, L35

Guillot T., et al., 2015, Astronomische Nachrichten, 336, 638

Günther M., Pozuelos F., Dittmann J. e. a., 2020, Nature Astronomy, 1099

Hadden S., Lithwick Y., 2016, AJ, 154

Harries R. K. T., Symington N., 2006, Mon. Not. R. Astron. Soc. PASP, 370, 580–596

Haynes K., 2015, in American Astronomical Society Meeting Abstracts #225. p. 219.02

Hébrard G., et al., 2014, A&A, 572, A93

Hedges C., Hodgkin S., Kennedy G., 2018, MNRAS, 476, 2968

Hedges C., Saunders N., Barentsen G., Coughlin J. L., Cardoso J. V. d. M., Kostov V. B., Dotson J., Cody A. M., 2019, ApJL, 880, L5

Hellier C., et al., 2012, MNRAS, 426, 739

Henry G. W., Marcy G. W., Butler R. P., Vogt S. S., 2000, ApJL, 529, L41

Herbst W., et al., 2002, PASP, 114, 1167

Herschel W., Dreyer J. L. E., 1912, The Scientific Papers of Sir William Herschel, Including Early Papers Hitherto Unpublished

Heyrovsky D., 2007, ApJ, 656, 483

Hippke M., 2015, ApJ, 810

Hippke M., David T. J., Mulders G. D., Heller R., 2019, AJ, 158, 143

Hirano T., et al., 2016, ApJ, 825, 53

Hirano T., et al., 2018, AJ, 155, 127

Holczer T., et al., 2016, The Astrophysical Journal Supplement Series, 225, 9

Holl B., et al., 2023, A&A, 674, A10

Holman M. J., Murray N. W., 2005, Science, 307, 1288

Holman M. J., et al., 2010, Science, 330, 51

Hood C. E., et al., 2021, in American Astronomical Society Meeting Abstracts. p. 428.04

Howell S. B., et al., 2014, PASP, 126, 398

Huber D., et al., 2013, ApJ, 767, 127

Huber K. F., Czesla S., Schmitt J. H. M. M., 2017, Astronomy &amp$$ Astrophysics, 597, A113

Husser T.-O., von Berg S. W., Dreizler S., Homeier D., Reiners A., Barman T., Hauschildt P. H., 2013, A&A, 553, A6

Hwang K. H., et al., 2015, arXiv e-prints, p. arXiv:1507.05361

Ida S., Lin D. N. C., 2004, ApJ, 604, 388

Ikwut-Ukwa M., et al., 2020, AJ, 160, 209

Ingalls J. G., Krick J. E., Carey S. J., Laine S., Surace J. A., Glaccum W. J., Grillmair C. C., Lowrance P. J., 2012, in Proc. SPIE 5487. p. 84421Y, doi:10.1117/12.926947

Jaffe T. J. Barclay T., 2017, Zenodo

Jehin E., et al., 2011, The Messenger, 145, 2

Jenkins J. M., 2002, ApJ, 575, 493

Jenkins J. M., 2017, Technical report, Kepler Data Processing Handbook

Jenkins J. M., et al., 2010, in Software and Cyberinfrastructure for Astronomy. p. 77400D, doi:10.1117/12.856764

Jenkins J. M., et al., 2016, in Software and Cyberinfrastructure for Astronomy IV. p. 99133E, doi:10.1117/12.2233418

Jensen E., 2013, Tapir: A web interface for transit/eclipse observability, Astrophysics Source Code Library (ascl:1306.007)

Johnson M. C., et al., 2016, AJ, 151, 171

Johnson J. A., et al., 2017, AJ, 154, 108

Jontof-Hutter D., et al., 2016, ApJ, 820, 39

Jurić M., Tremaine S., 2008, ApJ, 686, 603

Kalas P., Liu M. C., Matthews B. C., 2004, Science, 303, 1990

Kane M., Ragozzine D., Flowers X., Holczer T., Mazeh T., Relles H. M., 2019, AJ, 157, 171

Kausch W., Noll S., Smette A., Kimeswenger S., 2015, A&A, 576

Kaye L., et al., 2022, MNRAS, 510, 5464

Kempton E. M.-R., et al., 2018, PASP, 130, 114401

Kiefer E., des Etangs A. L., Boissier J., 2014, Nature, 514, 462

Kim D.-W., Protopapas P., Alcock C., Byun Y.-I., Bianco F. B., 2009, MNRAS, 397, 558

Kipping D., Nesvorný D., Hartman J., Torres G., Bakos G., Jansen T., Teachey A., 2019, MNRAS, 486, 4980

Kley W., Nelson R. P., 2012, ARA&A, 50, 211

Kopparapu R. K., Ramirez R. M., SchottelKotte J., Kasting J. F., Domagal-Goldman S., Eymet V., 2014, ApJL, 787, L29

Korth J., et al., 2019, MNRAS, 482, 1807

Kovács G., Zucker S., Mazeh T., 2002, A&A, 391, 369

Kovács G., Bakos G., Noyes R. W., 2005, MNRAS, 356, 557

Kreidberg L., 2015, batman: BAsic Transit Model cAlculatioN in Python (ascl:1510.002)

Kreidberg L., et al., 2014a, Nature, 505, 69

Kreidberg L., et al., 2014b, Nature, 505, 69

Kriedberg L., 2015, PASP, 127, 1161

Lammer H., Selsis F., Ribas I., Guinan E. F., Bauer S. J., Weiss W. W., 2003, ApJL, 598, L121

Lanotte A. A., et al., 2014, A&A, 572, A73

Latham D. W., et al., 2011, ApJ, 732, L24

Lecavelier Des Etangs A., 2007, A&A, 461, 1185

Lee E. J., Chiang E., 2015, ApJ, 811, 41

Libby-Roberts J. E., et al., 2020, AJ, 159, 57

Lillo-Box J., et al., 2016, A&A, 594, A50

Line M., Parmentier V., 2016, ApJ, 000, 000

Lithwick Y., Xie J., Wu Y., 2012, ApJ, 761, 122

Livingston J. H., et al., 2018, AJ, 156, 277

Lopez E. D., Fortney J. J., 2014, ApJ, 792, 1

Luger R., Agol E., Kruse E., Barnes R., Becker A., Foreman-Mackey D., Deming D., 2016, AJ, 152, 100

Luger R., Kruse E., Foreman-Mackey D., Agol E., Saunders N., 2018, AJ, 156, 99

Lund M. N., Handberg R., Davies G. R., Chaplin W. J., Jones C. D., 2015, ApJ, 806, 30

Lundkvist M. S., et al., 2016, Nature Communications, 7

Lustig-Yaeger J., Meadows V. S., Lincowski A. P., 2019, AJ, 158, 27

MacDonald M. G., et al., 2016, AJ, 152, 105

Macintosh B., et al., 2007, Comptes Rendus Physique - C R PHYS, 8, 365

Malavolta L., et al., 2017, AJ, 153, 224

Mandel K., Agol E., 2002, ApJL, 580, L171

Marconi A., et al., 2021, Published in The Messenger vol. 182, pp. 27-32, March 2021.

Marcy G. W., Butler R. P., Fischer D. A., 1999, in American Astronomical Society Meeting Abstracts #194. p. 14.02

Marois C., Zuckerman B., Konopacky Q. M., Macintosh B., Barman T., 2010, Nature, 468, 1080

Martioli E., Hé brard G., Correia A. C. M., Laskar J., des Etangs A. L., 2021, Astronomy &amp$$ Astrophysics, 649, A177

Masuda K., Hirano T., Taruya A., Nagasawa M., Suto Y., 2013, ApJ, 778, 185

Maxted P. F. L., et al., 2016, A&A, 591, A55

Mayer P., 1971, Bulletin of the Astronomical Institutes of Czechoslovakia, 22, 168

Mayo A. W., et al., 2018, AJ, 155, 136

Mayor M., Queloz D., 1995, Nature, 378, 355

Mazeh T., et al., 2013, The Astrophysical Journal Supplement Series, 208, 16

McClure M., et al., 2010, The Astrophysical Journal Supplement Series, 188, 75

McCormac J., Pollacco D., Skillen I., Faedi F., Todd I., Watson C. A., 2013, PASP, 125, 548

McCully C., Volgenau N. H., Harbeck D.-R., Lister T. A., Saunders E. S., Turner M. L., Siiverd R. J., Bowman M., 2018, in Proc. SPIE 5487. p. 107070K (arXiv:1811.04163), doi:10.1117/12.2314340

McQuillan A., Mazeh T., Aigrain S., 2013, ApJL, 775, L11

Mékarnia D., et al., 2016, MNRAS, 463, 45

Meschiari S., Wolf A. S., Rivera E., Laughlin G., Vogt S., Butler P., 2009, PASP, 121, 1016

Millholland S., Laughlin G., 2018, ApJ, 869, L15

Mills S. M., Fabrycky D. C., 2017, AJ, 153, 45

Mills S. M., Mazeh T., 2017, ApJ, 839, L8

Mills S. M., Fabrycky D. C., Migaszewski C., Ford E. B., Petigura E., Isaacson H., 2016a, Nature, 533, 509

Mills S. M., Fabrycky D. C., Migaszewski C., Ford E. B., Petigura E., Isaacson H., 2016b, Nature, 533, 509–512

Miner E., Wessen R., 2002, Neptune. The planet, rings and satellites. Springer

Montet B. T., Johnson J. A., 2012, ApJ, 762, 112

Mordasini C., Alibert Y., Benz W., 2009, A&A, 501, 1139

Morton T. D., Bryson S. T., Coughlin J. L., Rowe J. F., Ravichandran G., Petigura E. A., Haas M. R., Batalha N. M., 2016, ApJ, 822, 86

Murray C. D., Correia A. C. M., 2010, Keplerian Orbits and Dynamics of Exoplanets. pp 15–23

Murray C. D., Dermott S. F., 1999, Solar system dynamics

Muterspaugh M. W., et al., 2010, AJ, 140, 1657

Muñoz A., Isaak K., 2015, PNAS, 112, 13461–13466

Narita N., et al., 2019, J. Astron. Telesc. Instruments, Syst., 5, 015001

Nascimbeni V., et al., 2022, Astronomy &amp$$ Astrophysics, 658, A31

Natta A., Testi L., Randich S., 2006, Astronomy &amp$$ Astrophysics, 452, 245

Nespral D., et al., 2017, A&A, 601, A128

Nesvorný D., Beaugé C., 2010, ApJ, 709, L44

Nesvorný D., Vokrouhlický D., 2014, ApJ, 790, 58

Nesvorný D., Vokrouhlický D., 2016, ApJ, 823, 72

Nesvorný D., 2009, ApJ, 701, 1116

Nesvorný D., Morbidelli A., 2008, ApJ, 688, 636

Nesvorný D., Kipping D. M., Buchhave L. A., Bakos G. , Hartman J., Schmitt A. R., 2012, Science, 336, 1133

Niţu I. C., Keith M. J., Stappers B. W., Lyne A. G., Mickaliger M. B., 2022, MNRAS, 512, 2446

Oliva E., et al., 2015, A&A, 581, A47

Owen J. E., Jackson A. P., 2012, MNRAS, 425, 2931

Owen J. E., Wu Y., 2017, ApJ, 847, 29

Papaloizou J. C. B., Terquem C., 2005, Reports on Progress in Physics, 69, 119

Papaloizou J. C. B., Nelson R. P., Kley W., Masset F. S., Artymowicz P., 2006, Disk-Planet Interactions During Planet Formation (arXiv:astro-ph/0603196)

Parmentier V., Showman A. P., Lian Y., 2013, A&A, 558, A91

Parmentier V., Fortney J. J., Showman A. P., Morley C., Marley M. S., 2016, ApJ, 828, 22

Parmentier V., et al., 2019, Seeing through the haze of two mini-Neptunes with Spitzer, Spitzer Proposal

Parviainen H., 2015, MNRAS, 450, 3233

Parviainen H., Aigrain S., 2015, MNRAS, 453, 3821

Parviainen H., et al., 2019, A&A, 630, A89

Patra K. C., Winn J. N., Holman M. J., Yu L., Deming D., Dai F., 2017, AJ, 154, 4

Pearson K. A., Palafox L., Griffith C. A., 2017, MNRAS, 474, 478

Pepe F., et al., 2000, in Iye M., Moorwood A. F. M., eds, Vol. 4008, Optical and IR Telescope Instrumentation and Detectors. SPIE, pp 582 – 592, doi:10.1117/12.395516, https://doi.org/10.1117/12.395516

Pepe F., et al., 2021a, A&A, 645, A96

Pepe F., et al., 2021b, A&A, 645, A96

Pepper J., et al., 2007, PASP, 119, 923

Petigura E. A., Howard A. W., Marcy G. W., 2013, Proceedings of the National Academy of Science, 110, 19273

Petigura E. A., et al., 2017, AJ, 154, 107

Petigura E., et al., 2018, AJ, 156, 89

Petigura E. A., et al., 2020, AJ, 159, 2

Petit A. C., Pichierri G., Davies M. B., Johansen A., 2020, A&A, 641, A176

Pigulski A., Pojmanski G., Pilecki B., Szczygiel D., 2009, 59

Plavchan P., et al., 2020, Nature, 582, 497

Pollacco D. L., et al., 2006, PASP, 118, 1407

Pont F., et al., 2007, A&A, 476, 1347

Powell D., Louden T., Kreidberg L., Zhang X., Gao P., Parmentier V., 2019, ApJ, 887, 170

Quillen A. C., 2011, MNRAS, 418, 1043

Quirrenbach A., et al., 2014, in Ramsay S. K., McLean I. S., Takami H., eds, Society of Photo-Optical Instrumentation Engineers (SPIE) Conference Series Vol. 9147, Ground-based and Airborne Instrumentation for Astronomy V. p. 91471F, doi:10.1117/12.2056453

Rabus M., et al., 2009, A&A, 494, 391

Ragozzine D., Wolf A. S., 2009, ApJ, 698, 1778

Rampalli R., et al., 2019, AJ, 158, 62

Rasmussen C. G. G., 2001, Advances in Neural Information Processing Systems 14 (NIPS 2001)

Rauer H., et al., 2009, A&A, 506, 281

Rauer H., et al., 2014, Experimental Astronomy, 38, 249

Rein H., Liu S., 2012a, A&A, 537, A128

Rein H., Liu S. F., 2012b, A&A, 537, A128

Rein H., Spiegel D. S., 2015, MNRAS, 446, 1424

Rein H., Tamayo D., 2016, MNRAS, 459, 2275

Ricker G. R., et al., 2014, in Proc. SPIE 5487. p. 914320 (arXiv:1406.0151), doi:10.1117/12.2063489

Romanova R. K. M., Harries T., 2011, Mon. Not. R. Astron. Soc. PASP, 416, 2623–2639

Rosário N., Barros S., Demangeon O., Santos N., 2022

Saad-Olivera X., Nesvorný D., Kipping D. M., Roig F., 2017, AJ, 153, 198

Safier P., 1998, ApJ, 494, 336

Sahlmann J., Lazorenko P. F., Ségransan D., Martín E. L., Mayor M., Queloz D., Udry S., 2015, A&A, 577, A15

Sanchis-Ojeda R., Winn J., 2011, ApJ, 0, 000

Sanchis-Ojeda R., et al., 2012, Nature, 487, 449

Sarkis P., et al., 2018, AJ, 155, 257

Savitzky A., Golay M. J. E., 1964, Analytical Chemistry, 36, 1627

Schmitt J. R., et al., 2014, ApJ, 795, 167

Shevchenko I. I., 2017, The Lidov-Kozai Effect - Applications in Exoplanet Research and Dynamical Astronomy. Vol. 441, doi:10.1007/978-3-319-43522-0,

Showman A. P., Guillot T., 2002, A&A, 385, 166

Shporer A., et al., 2014, ApJ, 788, 92

Smette A., et al., 2015, A&A, 576, A77

Smith J. C., et al., 2012, PASP, 124, 1000

Smith A. M. S., et al., 2019, AcA, 69, 135

Smith A. M. S., et al., 2020, Astronomische Nachrichten, 341, 273

Spalding C., Batygin K., 2015, ApJ, 811, 82

Steffen J. H., Agol E., 2005, Monthly Notices of the Royal Astronomical Society: Letters, 364, L96

Steffen J., et al., 2012, MNRAS, 421, 2342

Sterken C., 2005, in Sterken C., ed., Astronomical Society of the Pacific Conference Series Vol. 335, The Light-Time Effect in Astrophysics: Causes and cures of the O-C diagram. p. 3

Stumpe M. C., et al., 2012, PASP, 124, 985

Stumpe M. C., Smith J. C., Catanzarite J. H., Van Cleve J. E., Jenkins J. M., Twicken J. D., Girouard F. R., 2014, PASP, 126, 100

Sumi T., et al., 2011, Nature, 473, 349

Szabó G. M., Pál A., Derekas A., Simon A. E., Szalai T., Kiss L. L., 2012, Monthly Notices of the Royal Astronomical Society: Letters, 421, L122

Szabó G. M., et al., 2021, A&A, 654, A159

Tamayo D., et al., 2020, Proceedings of the National Academy of Science, 117, 18194

Tamuz O., Mazeh T., North P., 2006, MNRAS, 367, 1521

Teyssandier J., Libert A.-S., 2020, A&A, 643, A11

Thompson S. E., Fraquelli D., Van Cleve J. E., Caldwell D. A., 2016, Kepler Archive Manual, Kepler Science Document KDMC-10008-006, id. 9. Edited by Faith Abney, Dwight Sanderfer, Michael R. Haas, and Steve B. Howell

Thompson S. E., et al., 2018, The Astrophysical Journal Supplement Series, 235, 38

Tinetti G., Liang M.-C., Vidal-Madjar A., Ehrenreich D., Lecavelier des Etangs A., Yung Y. L., 2007, ApJL, 654, L99

Tinetti G., et al., 2021, arXiv e-prints, p. arXiv:2104.04824

Torres C. A. O., Quast G. R., da Silva L., de la Reza R., Melo C. H. F., Sterzik M., 2006, A&A, 460, 695

Trifonov T., 2019, The Exo-Striker: Transit and radial velocity interactive fitting tool for orbital analysis and N-body simulations, Astrophysics Source Code Library, record ascl:1906.004 (ascl:1906.004)

Trifonov T., et al., 2021, arXiv e-prints, p. arXiv:2108.05323

Udalski A., Szymanski M. K., Kubiak M., Pietrzynski G., Soszynski I., Zebrun K., Szewczyk O., Wyrzykowski L., 2004, AcA, 54, 313

Usoskin I. G., Mursula K., Arlt R., Kovaltsov G. A., 2009, ApJ, 700, L154

Van Cleve J. E., Bryson S. T., 2017, K2 Handbook, Kepler Science Document KSCI-19116-001, id. 24. Edited by Doug Caldwell, Jeffrey L. Coughlin, and Jessie Dotson

Van Cleve J. E., Caldwell D. A., 2016, Kepler Instrument Handbook, Kepler Science Document KSCI-19033-002, id.1. Edited by Michael R. Haas and Steve B. Howell

Van Eylen V., Albrecht S., 2015, ApJ, 808, 126

Van Eylen V., et al., 2016, ApJ, 820, 56

Van Eylen V., Agentoft C., Lundkvist M. S., Kjeldsen H., Owen J. E., Fulton B. J., Petigura E., Snellen I., 2018, MNRAS, 479, 4786

Van Eylen V., et al., 2021, Masses and compositions of three small planets orbiting the nearby M dwarf L231-32 (TOI-270) and the M dwarf radius valley (arXiv:2101.01593)

Vanderburg A., Johnson J., 2014b, PASP, 126, 948

Vanderburg A., Johnson J. A., 2014a, PASP, 126, 948

Vanderburg A., et al., 2016, The Astrophysical Journal Supplement Series, 222, 14

Vidal-Madjar A., Des Etangs A. L., Désert J. M., Ballester G. E., R. F., Hébrard G., Mayor M., 2003, Nature, 422, 143

Vissapragada S., et al., 2022, The Astrophysical Journal Letters, 941, L31

Wang Z., Chakrabarty D., Kaplan D. L., 2006, Nature, 440, 772

Watson C. A., Marsh T. R., 2010, MNRAS, pp no–no

Webber M. W., Lewis N. K., Marley M., Morley C., Fortney J. J., Cahoy K., 2015, ApJ, 804, 94

Weiss L. M., Marcy G. W., 2014, in American Astronomical Society Meeting Abstracts #223. p. 105.04

Weiss L. M., et al., 2013, ApJ, 768, 14

Weiss L. M., et al., 2017, AJ, 153, 265

Wells R., Poppenhaeger K., Watson C. A., 2019, MNRAS, 487, 1865

Werner M. W., et al., 2004, The Astrophysical Journal Supplement Series, 154, 1

Wheatley P. J., et al., 2010, The thermal emission of the exoplanets WASP-1b and WASP-2b (arXiv:1004.0836)

Wheatley P. J., et al., 2018, MNRAS, 475, 4476

White J., Mishra I., Lewis N., 2021, in American Astronomical Society Meeting Abstracts. p. 531.03

Wilking B. A., Meyer M. R., Robinson J. G., Greene T. P., 2005, AJ, 130, 1733

Williams J. P., Cieza L. A., 2011, ARA&A, 49, 67

Wilson C., 1985, Arch. Rational Mech., 000, 000

Winn J. N., 2014, Transits and Occultations (arXiv:1001.2010)

Winn J. N., Garnavich P. M., Stanek K. Z., Sasselov D. D., 2003, ApJ, 593, L121

Wittenmyer R. A., Tinney C. G., Butler R. P., O'Toole S. J., Jones H. R. A., Carter B. D., Bailey J., Horner J., 2011, ApJ, 738, 81

Wittrock J. M., et al., 2022, AJ, 164, 27

Wolszczan A., 1997, in Soderblom D., ed., Astronomical Society of the Pacific Conference Series Vol. 119, Planets Beyond the Solar System and the Next Generation of Space Missions. p. 135

Wolszczan A., Frail D., 1992, Nature, 355, 145–147

Wood K., Kenyon S. J., Whitney B. A., Bjorkman J. E., 1996, ApJL, 458, L79

Wu Y., Murray N., 2003, ApJ, 589, 605

Yelle R. V., 2004, , 170, 167

Yoder C. F., Peale S. J., 1981, , 47, 1

Yoffe G., Ofir A., Aharonson O., 2021, ApJ, 908, 114

Zhang Z., Zhou Y., Rackham B. V., Apai D., 2018, AJ, 156, 178

Zicher N., et al., 2022, MNRAS, 512, 3060

Zieba S., Zwintz K., Kenworthy M. A., Kennedy G. M., 2019, A&A, 625, L13

Zucker S., Giryes R., 2018, AJ, 155, 147

de Leon J. P., et al., 2021, MNRAS, 508, 195

de Wit J., et al., 2016, Nature, 537, 69

von Paris P., Gratier P., Bordé P., Leconte J., Selsis F., 2016, A&A, 589, A52